2023

# Development of Redox-Gel Electrolyte for Wearable Thermocells

Yuetong Zhou

**Australian Research Council Centre of Excellence for Electromaterials Science**

**Intelligent Polymer Research Institute**

**Australian Institute for Innovative Materials**

# Development of Redox-Gel Electrolyte for Wearable Thermocells

**Yuetong Zhou**

**This thesis is presented as part of the requirements for the**

**Award of the Degree of Doctor of Philosophy of**

**The University of Wollongong**

**March 2023**

# Certification

I, Yuetong Zhou, declare that this thesis submitted in fulfilment of the requirements for the conferral of Doctor of Philosophy, from the University of Wollongong, is wholly my own work unless otherwise referenced or acknowledged. This document has not been submitted for qualifications at any other academic institution.

Yuetong Zhou

March 2023

# ACKNOWLEDGEMENTS

This work would not have been completed without the assistance and support from my family, my supervisors, workmates, and friends over the past four years.

First, I would like to extend my greatest appreciation to all my supervisors, Prof. Jun Chen and Prof. Gordon Wallace for their excellent supervision and great help. I also show true gratitude and respect to my principal supervisor Prof. Jun Chen, who provided me with an opportunity to pursue the academic career and supported me at the high research level platform, which valuable experience will become the wealth of whole my life.

Thanks for the help from my team members: Dr. Yuqing Liu, Dr. Yuyang Hou, Dr. Shuai Zhang, Dr Chunyan Qin, Dr. Dandan Cui, Lisha Jia. I would like to give special you to my friends in IPRI, who provided me huge help and constant encouragement throughout the PhD period in academic work, Dr. Liangxu Lin, Dr Guangzhi Dong, Dr. Chang Wu, Qilong Wu, Yeqing Xu, Zhiqi Chen, Dr. Kezhong Wang, Dr. Yunfeng Chao and Dr. Jinshuo Zou, with their help during these 4 years in life work and all my friends in Australia and China, thank you for all the encouragement you gave me.

Here, I want to give a special appreciation to Ms. Yan Zhang, who almost mentally accompanied me for nearly six years, and I hardly describe how huge and unimaginable impact she made on my life path. She has been continuously giving

me encouragement and courage, and I can not do this achievement without her effort. I really give the most honest acknowledgment and respect to her.

Finally, I sincerely thank my parents Mrs Shuo Zhang and Mr Zhihua Zhou for who give me love and faith for many years. I also give the truest gratitude to dear Ms. Chenxu Guo, who enriched my life, especially the wealth of the mind. Her patience and inclusiveness prompted me to have more critical thinking and made me more sophisticated. I could not be at your side to accompany since I arrived in Australia. You are always my most beloved.

# PUBLICATIONS

[1] **Y. Zhou**, S. Zhang, Y. Liu, G.G. Wallace, J. Chen, Highly stretchable double-network gel electrolyte integrated with textile electrodes for Thermo-Electrochemical Cells. (**Under review**)

[2] **Y. Zhou**, S. Zhang, M.A. Buckingham, L. Aldous, S. Beirne, C. Wu, Y. Liu, G.G. Wallace, J. Chen, Novel Porous Thermosensitive Gel Electrolytes for Wearable Thermo-Electrochemical Cells, Chem. Eng. J. (2022) 137775.

[3] **Y. Zhou**, Y. Liu, M.A. Buckingham, S. Zhang, L. Aldous, S. Beirne, G. Wallace, J. Chen, Electrochemistry Communications The significance of supporting electrolyte on poly (vinyl alcohol) - iron (II)/ iron (III) solid-state electrolytes for wearable thermo-electrochemical cells, Electrochem. Commun. 124 (2021) 106938.

[4] Y. Liu, S. Zhang, **Y. Zhou**, M.A. Buckingham, L. Aldous, P.C. Sherrell, G.G. Wallace, G. Ryder, S. Faisal, D.L. Officer, S. Beirne, J. Chen, Advanced Wearable Thermocells for Body Heat Harvesting, Adv. Energy Mater. 10 (2020) 2002539.

[5] S. Zhang, **Y. Zhou**, Y. Liu, G.G. Wallace, S. Beirne, J. Chen, All-polymer wearable thermoelectrochemical cells harvesting body heat, IScience. 24 (2021).

[6] Y. Liu, S. Zhang, S. Beirne, K. Kim, C. Qin, Y. Du, **Y. Zhou**, Z. Cheng, G. Wallace, J. Chen, Wearable Photo-Thermo-Electrochemical Cells (PTECs) Harvesting Solar Energy, Macromol. Rapid Commun. 43 (2022) 1-9.

# ABSTRACT

The thermo-electrochemical cells (TECs, known as thermocells) provide a new potential for self-powered devices by converting heat energy into electricity through redox reactions driven by the presence of a temperature gradient. Among multiple power sources, human body heat has attracted the attention in last decades due to its continuously releasing heat energy. For harvesting body waste heat, the wearable thermocell is urgent to develop, where the gel electrolyte is the most essential component. Wearable thermocell devices could be twisted or stretched during realistic applications, therefore flexible gel-based solid-state electrolytes are the ideal candidate to avoid the leakage issue and maintain integrity while deformations. Tremendous progress has been achieved in developing flexible gel electrolytes, however, challenges are still remained in compatibility, mechanical strength and electrochemical performance. In this thesis, the primary purpose is to develop high performance gel electrolytes for wearable thermal-electrochemical cells. Initially, the suitable polymer will match the unique redox couple. Additionally, the effort should focus on improving electrochemical properties especially the issue of ion transfer limited by the gel system. Meanwhile, the mechanical strength of gel electrolytes is also needed to pursue to satisfy the movement of human limbs.

In chapter 3, low-grade heat from the human body can be harvested using thermocells containing a suitable electrolyte, such as the iron(II)/iron(III) chloride ($FeCl_2/FeCl_3$)redox couple housed in polyvinyl alcohol (PVA). In this work, stretchable PVA-Fe gel electrolytes were designed, which achieved up to 100%

tensile strain. However, conventionally the thermo-electrochemical performance of gelled electrolytes is poor, due to slow ionic transport and high charge transfer resistance. Here, hydrochloric acid has been found to synergistically decrease the charge transfer resistance of the redox reaction, whilst doubling the tensile properties of the gel housing. The Fe-HCl-based thermocell exhibited excellent thermo-electrochemical performance with a $S_e$ of 0.8 ± 0.02 mV $K^{-1}$, current density of 16.1 A $m^{-2}$ and power density of 63.7 mW $m^{-2}$ at a ΔT of 20 K. Moreover, individual thermocells can be connected in parallel to enhance current output, where the current increased roughly 100% (20 ± 1 A $m^{-2}$) in parallel connection compared with individual cells, and the open circuit voltage ($V_{oc}$) maintained the identical value (8.0 ± 0.2 mV), which paved the way for N- and P-type thermocells connected in series in the next research.

In the following work, to address the problems about the flexible, solid-state gelled electrolytes used in wearable thermocell devices suffer from poor mass transport of electrolytes. A novel porous gel is developed via sodium acetate (NaAc) templates and freeze-drying treatment that is applied in p-type gelled electrolyte: poly-acrylamide (PAM) - $K_{3/4}[Fe(CN)_6]$ and integrated into platinum (Pt) electrodes for wearable devices. Moreover, the guanidinium ($[Gdm]^+$) is initially introduced into gelled electrolytes, and the p-type cell effectively boosts the maximum power density from 4.01 to 7.68 mW $m^{-2}$ at ΔT = 10 ℃, and exhibits a quick thermosensitive response under a broad temperature range (15 - 55 ℃), which is sufficient for working conditions of wearable devices. The optimised porous gel host was also utilized in series with an n-type: PAM-$FeCl_{2/3}$-HCl gelled electrolyte. The multiple thermocells (12 pairs) were further fabricated into a device by alternating p-

and n-type cells in series. This device was found to output nearly 0.23 volt (V) at ΔT = 10 ℃, and was manufactured into a flexible wearable device that was demonstrated to successfully harvest human body heat by both charging a supercapacitor (100 mF), and illuminating an Light emitting diode (LED), demonstrating the potential of actual application of our n-p type in series devices.

However, challenges still remain in the fabrication of flexible and tough gel electrolytes, and their compatibility with redox actives. To achieve this aim, a robust, neutral and biocompatible hydrogel with outstanding stretchability and recoverability is developed via double network crosslinked carboxymethyl chitosan sodium (CMCs) and polyacrylamide (PAM) by covalent bonds, which accommodated both N ($FeCl_2/FeCl_3$) and P-type ($K_3[Fe(CN)_6]/K_4[Fe(CN)_6]$) redox couple. Moreover, PEDOT:PSS textile electrodes with a porous structure are integrated into gel electrolytes that effectively boost the $P_{max}$ of N- and P-type thermocell by 76% and 26%, respectively, under the larger electrochemical active area and the ionic coordination effect with $Fe^{3+}$. Optimized 10 wt.% 1-2 N-type gel electrolyte provided a Seebeck coefficient of -1.4 mV $K^{-1}$, current density ($J_{sc}$) of 2.3 A $m^{-2}$ and the maximum power density ($P_{max}$) of 5.3 mW $m^{-2}$ at ΔT = 10 ℃. P-type gel generated a Seebeck coefficient of 0.9 mV $K^{-1}$, comparable $J_{sc}$ value of 2.0 A $m^{-2}$ and $P_{max}$ of 7.1 mW $m^{-2}$. The $P_{max}$ of N and P-type thermocells showed power density of 4.42 and 4.79 mW $m^{-2}$ respectively at 4 mm (releasing state), while $P_{max}$ increased to 6.26 and 7.98 mW $m^{-2}$ at 1 mm (compressing state) individually. The optimized thermocells exhibits a quick current density response and is continually fully operational under deformations, which satisfies the working conditions of wearable devices. The multiple thermocells (4 pairs) were fabricated in alternating single N

and P-type cells in series and outputted nearly 74.3 millivolt (mV) at $\Delta T = 10$ ℃. The wearable device was manufactured into a soft pack thermocells to successfully harvest human body heat and illuminate an LED, demonstrating the potential of the actual application of the thermocell device.

# ABBREVIATIONS

| | |
|---|---|
| A | Ampere |
| mA | Milliampere |
| V | Volt |
| mV | Millivolt |
| m | Metre |
| cm | Centimetre |
| nm | Nanometre |
| T | Time (usually in seconds unless otherwise stated) |
| h | Hour |
| min | Minute |
| s | Second |
| M | Mole per litre |
| Raman | Raman spectroscopy |
| SEM | Scanning electron microscopy |
| CV | Cyclic voltammetry |
| D | Diffusion coefficient |
| EIS | Electrochemical impedance spectroscopy |
| $R_{\Omega}$ | mass transport resistance |
| $R_{et}$ | Electrical transfer resistance |
| CA | Chronoamperometry/Chronocoulometry |

| | |
|---|---|
| LSV | Linear Sweep Voltammetry |
| $\Delta T$ | Temperature difference |
| $S_e$ | Seebeck coefficient |
| $V_{oc}$ | Open circuit voltage |
| $J_{sc}$ | Short circuit current |
| Pa | Pascal |
| W | Watt |
| **Ω** | Ohm |
| μ | Micro |
| Pt | Platinum |
| Pt-textile | Platinum and textile electrode |
| LED | Light emitting diode |
| $FeCl_2 \cdot 4H_2O$ | Iron(II) chloride tetrahydrate |
| $FeCl_3$ | Iron(III) chloride |
| $K_4Fe(CN)_6 \cdot 3H_2O$ | Potassium hexacyanoferrate |
| $K_3Fe(CN)_6$ | Potassium ferricyanide |
| PDMS | Poly (dimethylsiloxane) |
| PEDOT/PSS (PEDOT:PSS) | Poly(3,4-ethylenedioxythiophene)/polystyrene sulfonate |
| PVA | Poly (vinyl alcohol) |
| CMC | Carboxymethyl cellulose |
| CMCs | Carboxymethyl Chitosan sodium |
| GA | Glutaraldehyde solution (25 wt.% in $H_2O$) |
| PAM | Polyacrylamide |

| | |
|---|---|
| APS | Ammonium persulfate |
| HCl | Hydrochloric acid solution (32%) |
| $H_3PO_4$ | Phosphoric acid |
| KCl | Potassium chloride |
| AM | Acrylamide |
| MBA | N,N′-Methylenebis acrylamide |
| NaAc | Sodium acetate |
| GdmCl | Guanidinium chloride |
| DEG | Diethylene glycol |

# TABLE OF CONTENTS

# LIST OF FIGURES

# LIST OF TABLES

# Chapter 1 Introduction

## 1.1 Overview of thermo-electrochemical cells

Tremendous efforts have been devoted toward harvesting waste heat energy and energy generators, such as thermosdiffusion cells (TDC) [1], thermoelectric devices (TEs) [2–4] and thermo-electrochemical cells (TECs) [5–13], can effectively harvest waste heat sources and convert it into electricity [6,14]. Thermosdiffusion cells (TDC) are a type of electrochemical cell that leverage the phenomenon of thermophoresis, also known as the Soret effect, to generate electrical energy, which operates based on the principle that ions can migrate in response to a temperature gradient and benefit from no application of external pressure or the use of chemicals. This makes them environmentally friendly and reduces the risk of contamination in the separated components. However, these cells are also limited by lower efficiency, power output and a narrow temperature range compared with thermocells, and these cells also require complicated, leakage proof cell structures to accommodate the gas-phase components, which depreciates their practical feasibility [15]. TE devices are comprised of multiple thermoelectric couples, including n-type (containing free electrons) and p-type (containing free holes) units electrically connected in series. Heat flow drives an electric load through the external circuit [16]. Unfortunately, the power output of TEs is limited by their low Seebeck coefficient ($S_e$) (on the order of $\mu V\ K^{-1}$) [14]. When compared to traditional TEs, TEC devices contain redox couples inside the electrolyte and the temperature gradient ($\Delta T$) powers the occurrence of redox reactions and induce electrochemical potential disequilibrium between electrodes [17–19], which drives electrons through an external circuit, thereby allowing the generation of current and power [20,21]. The higher $S_e$ exhibited by TECs (on the order of $mV\ K^{-1}$) supplies energy for facilities used in everyday life, such as remote micro-sensors, health monitoring devices, and smart cards [22].

### 1.1.1 Principle of thermo-electrochemical cells

A schematic diagram of the thermocell mechanism is shown in Figure 1.1 [23]. These cells typically consist of electrodes and redox couples within the electrolyte, in which the two electrodes are deliberately maintained at ΔT [24]. This relies on the entropy difference of the redox processes and therefore, a potential difference (ΔE) can be generated across the two electrodes, which is directly proportional to ΔT and the overall or total entropy change resulting from the redox processes [25]. ΔE drives the redox reactions at the electrodes, resulting in ion transfer between the electrode and electrolyte, which causes an electric current through the external circuit. Subsequently, a concentration gradient is established in the electrolyte, which drives the flow of ions through the electrolyte, completing the circuit and maintaining the current flow.

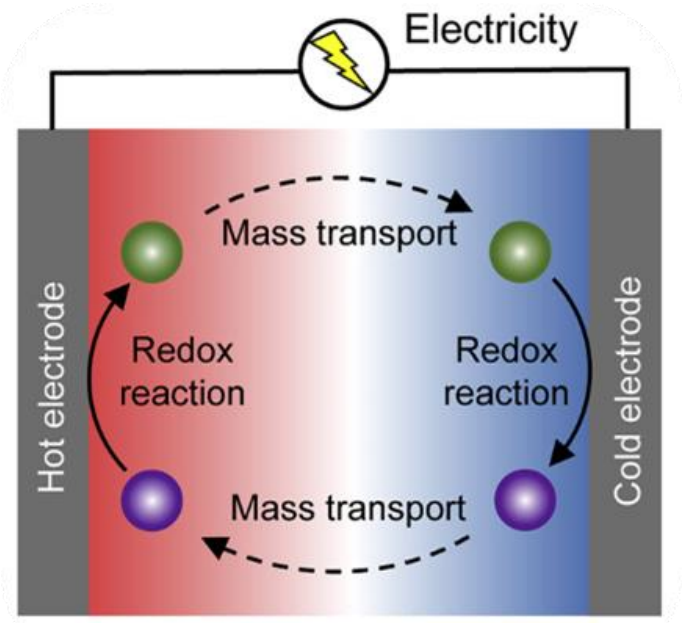


Figure 1.1 The configuration and working mechanism of an electrochemical-cell device.

## 1.1.2 Evaluation of thermo-electrochemical cells

*1.1.2.1 Seebeck coefficient*

The Seebeck coefficient ($S_e$) is an essential parameter for the evaluation of a thermocell and is related to the entropy of the redox reaction. Assuming that the hypothetical redox system (A+ $ne^- \leftrightarrow$ B) occurs in the thermocell, $S_e$ can be expressed using equation (1):

$$S_e = V_{oc}/\Delta T = \Delta S/nF \quad (1)$$

where $V_{oc}$ is the open-circuit voltage, ΔT is the temperature gradient, ΔS is the standard redox reaction entropy, n is the number of electrons involved in the reaction, and F is the Faraday constant (96,485 C/mol) [13,26].

The entropy change can be rewritten as follows [27]:

$$\Delta S = (S_B + S^*_B) - (S_A + S^*_A) - n\overline{\overline{S_e}} \quad (2)$$

where $S_A$ and $S_B$ are the partial molar entropies of redox couples A and B with their Eastman entropies of transport denoted by $S^*_A$ and $S^*_B$, respectively, n is the number of electrons involved in the redox reaction, F is Faraday's constant, and $\overline{\overline{S_e}}$ is the transported entropy of electrons in the electrodes.

Systems with an appropriate $S_e$ that is large enough to be useful in thermocells have small Eastman entropy of transport when compared with their partial molar entropies. $\overline{\overline{S_e}}$ is extremely small in most thermocells. for example, copper results in $< 2\mu V/K$ [28]. Therefore, equation (2) can be simplified into equation (3):

$$\Delta S = S_B - S_A \quad (3)$$

From equation (1-3), $S_e$ is directly influenced by the redox couple of the entropies, as shown in equation (4) and (5):

$$S_e = \frac{(S_B - S_A)}{nF} \tag{4}$$

$$V_{oc} = \frac{(S_B - S_A)\Delta T}{nF} \tag{5}$$

*1.1.2.2 Thermal conductivity*

The ΔT between the two electrodes is another significant parameter that is related to the thermal conductivity (*K*) of the thermocells. ΔT can be expressed using equation (6) [28]:

$$\Delta T = \frac{\partial Q}{\partial t} \cdot \frac{d}{AK} \tag{6}$$

where *K* is the thermal conductivity of the electrolyte, A is the electrode cross-sectional area, d is the separation between the two electrodes, and $\partial Q/\partial t$ is the thermal flow through the thermocell. Therefore, a smaller *K* is ideal in order to achieve a larger ΔT.

*1.1.2.3 Electrical conductivity*

$$P_\varepsilon = P_r + P_R \tag{7}$$

$$P_R = I^2 R = \frac{\varepsilon^2 R}{(R + r)^2} \tag{8}$$

where $P_\varepsilon$ is the total power generated by the electromotive force of the thermocell, $P_r$ is the internal resistance power consumption, r is the internal resistance, $P_R$ is the useful power output, R is the external resistance, I is the current through an external resistor with resistance (R), and $\varepsilon$ is the electromotive force.

When $y = P_R/(\varepsilon^2/r)$ and $x = R/r$, equation (8) can be rewritten as follows:

$$y = \frac{x}{(1+x)^2} \tag{9}$$

The function y(x) increases monotonically from zero upon increasing x in the range of 0 < x < 1, which attains a maximum value of 1/4 at x = 1, and then decreases monotonically when x >1. In other words, if the load resistance (R) is varied at constant $\varepsilon$ and r, then the transferred power attains its maximum value, as shown in equation (10):

$$(P_R)_{max} = \frac{\varepsilon^2}{4r} \tag{10}$$

where $V_{oc}$ is the open circuit voltage and $I_{sc}$ is the short circuit current.

$$U = \varepsilon\frac{R}{R+r} \tag{11}$$

$$I = \frac{\varepsilon}{R+r} \tag{12}$$

where U is the potential of the external resistance R and I is the current through the external circuit. When R is infinite in equation (11), $U = \varepsilon = V_{oc}$; when R approaches 0 in equation (12), $I = I_{sc} = \frac{\varepsilon}{r}$. Therefore, equation (10) can be rewritten as follows:

$$(P_R)_{max} = \frac{1}{4} V_{oc} I_{sc} \quad (13)$$

Therefore, when r = R, the power of the thermocell reaches its maximum value. In other words, $(P_R)_{max}$ can be improved when the internal r is small (electrical conductivity (σ) is large).

*1.1.2.4 Power conversion efficiency*

The power conversion efficiency (Φ) of a thermocell is given by equation (14) [29]:

$$\Phi = \frac{\text{Electrical power output}}{\text{Thermal power fl}u\text{xing through the cell}} \quad (14)$$

Based on equation (5) and (13), Φ can be given as follows:

$$\Phi = \frac{0.25 V_{oc} I_{sc}}{KA(\Delta T/d)} \quad (15)$$

Based on these findings, $S_e$, K, σ, A, and d are the most important parameters.

The ohmic overpotential is dictated by the electrolyte resistance and the mass transport overpotential is maximized at a large electrode separation value. Upon decreasing the inter-electrode separation, an increase in the short-circuit current is observed, resulting in larger amounts of generated power, which can be attributed to the decrease in both the ohmic and mass transport overpotentials. However, the power conversion efficiency will be decreased due to the higher thermal flux flowing from the hot to cold side of the

cell, i.e., it will be more difficult to maintain the thermal gradient [30]. Therefore, a thermocell should be designed to balance the resistance and thermal gradient.

Another challenge for the thermocell is to balance the concentration of the redox couple. Romano et al. reported that K is inversely proportional to the concentration of the redox couple, resulting in different ΔT values between the two electrodes. However, a larger redox couple concentration also results in a higher power output and short-circuit current density [31]. In this study, we found the possibility of a reliable power source to support energy for portable and smart devices.

### 1.1.3 Redox couple

The redox couple can be divided into N- and P-types corresponding to positive and negative $S_e$, respectively. The opposite $S_e$ is caused by the opposite types of ions (anions and cations). For example, Iron(II) chloride tetrahydrate/Iron(III) chloride ($Fecl_2$/$Fecl_3$) and potassium ferricyanide/potassium hexacyanoferrate ($K_3[Fe(CN)_6]$/$K_4[Fe(CN)_6]$) are commonly used as N- and P-type redox couples, respectively. When a temperature gradient is applied across a P-type material in a thermocell, the oxidation of $Fe(CN)_6^{4-}$ to $Fe(CN)_6^{3-}$ occurs at the hot electrode (i.e., anode) and the reduction of $Fe(CN)_6^{3-}$ to $Fe(CN)_6^{4-}$ occurs at the cold electrode (i.e., cathode). The migration of anions results the negative $S_e$ observed for P-type materials. In the same way, the N-type $Fe^{2+}$/$Fe^{3+}$ redox couple shows positive $S_e$. Redox couples are the main components of the redox reactions and cause entropy changes, which directly affect the $S_e$ and ionic conductivity.

#### *1.1.3.1 P-type redox couple*

For P-type electrolytes, the $K_{3/4}[Fe(CN)_6]$ aqueous system has been arguably the most common redox couple used in thermocells for harvesting low-degree heat due it exhibiting the best TECs performance among the P-type redox couples reported to date. The concentration of the redox couple is an important direction for investigation because $S_e$ is highly dependent on concentration and is more sensitive to the ratio of $[Fe(CN)_6]^{3-}$ to $[Fe(CN)_6]^{4-}$ [32]. The $S_e$ of the 0.4 M $K_{3/4}[Fe(CN)_6]$ redox couple, which is close to saturation, can reach +1.4 mV $K^{-1}$ using carbon-based electrodes. Numerous attempts have been made to optimize the $S_e$ and ionic conductivities of the $K_{3/4}[Fe(CN)_6]$ redox couple in thermocells.

Buckingham et al. have systematically investigated the inherent physiochemical limitations of the $[Fe(CN)_6]^{3-/4-}$ redox couple and increased the concentration of $[Fe(CN)_6]^{3-/4-}$ ($K_3[Fe(CN)_6]$ and $Na_4[Fe(CN)_6]$) to 1.6 M; a 400% increase compared to conventional 0.4 M $K_{3/4}[Fe(CN)_6]$ systems, leading to a 166% increase in the thermogalvanic $P_{max,}$ and found a plateau of $P_{max}$ when the concentration was >1 M [33].

Mark et al. identified 0.4 M $K_{3/4}[Fe(CN)_6]$ as the optimal concentration for thermocells because the $V_{oc}$ values of $K_{3/4}[Fe(CN)_6]$ in the range of 0.1 - 0.4 M were almost identical (Figure 1.2 a). Furthermore, a higher concentration results in lower thermal conductivity and higher power conversion (Figure 1.2 b). Therefore, 0.4 M $K_{3/4}[Fe(CN)_6]$ should be selected for further investigations [31]. Hyeongwook et al. designed a thermocell for harvesting waste heat from the human body. They used a 0.4 M $K_{3/4}[Fe(CN)_6]$ aqueous solution as the electrolyte and carbon nanotube (CNT)-coated activated carbon textile (ACT) as the electrodes to fabricate thermocells. The $S_e$ of the thermocell was ~1.4 mV

$K^{-1}$ (Figure 1.2 c). The authors also measured the current density to be 0.39 A $m^{-2}$ and $P_{max}$ was 0.46 mW $m^{-2}$ at $\Delta T$ = 3.4 ℃ (Figure 1.2 d).

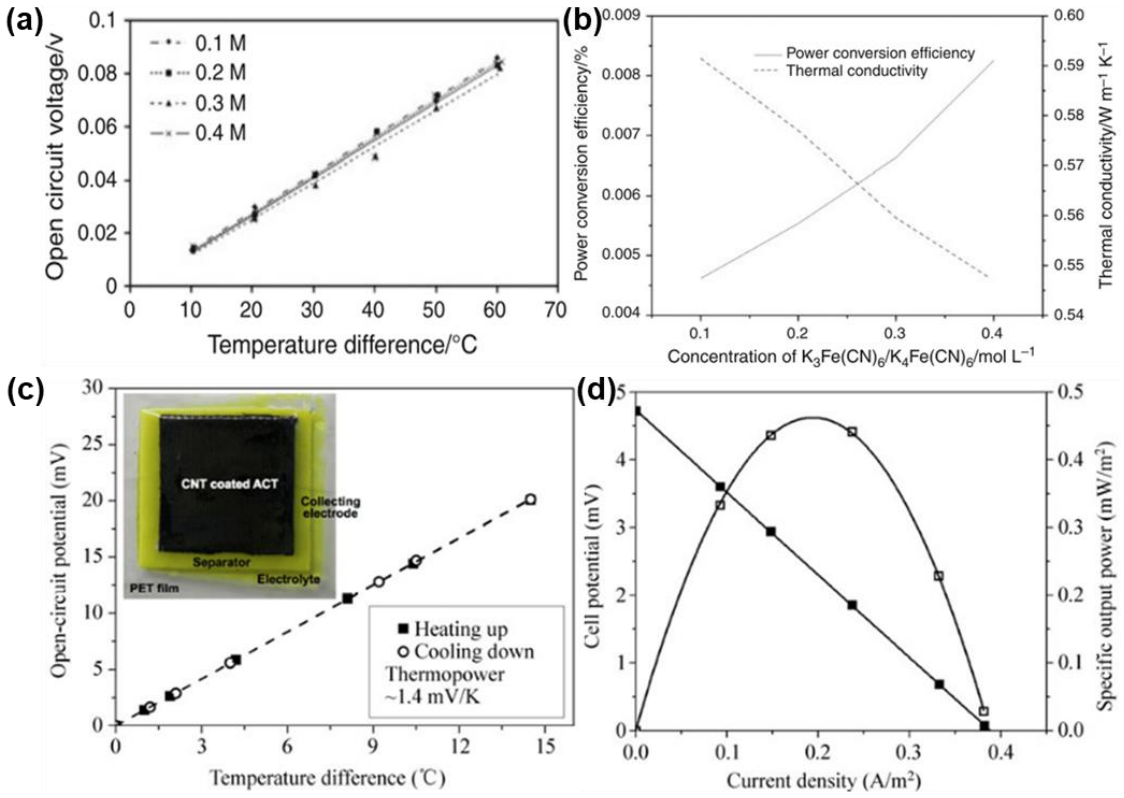


Figure 1.2 Open circuit voltage (a) power conversion efficiency and thermal conductivity (b) changes with varying concentrations of $[Fe(CN)_6]^{3-/4-}$. (c) The $V_{oc}$ of thermocell changed from the temperature difference. The insert is the image of thermocell. (d) The current and power output of the thermocell at $\Delta T$ = 3.4 ℃.

Duan et al. reported that amide derivatives (urea) and guanidinium cations ($Gdm^+$) effectively boost the $S_e$ of $[Fe(CN)_6]^{3-/4-}$ from +1.4 to +4.2 mV $K^{-1}$ by synergistically increasing the entropy difference of the redox couple [34] in liquid-state thermocells. The redox couples $[Fe(CN)_6]^{3-}$ and $[Fe(CN)_6]^{4-}$ are able to coordinate with the most typical chaotropic cation, $Gdm^+$. Sufficient $Gdm^+$ cations gather and complex with $[Fe(CN)_6]^{4-}$,

resulting in the rearrangement of its solvation shell, but are less affected by $[Fe(CN)_6]^{3-}$, which considerably increases the entropy difference (ΔS) between $[Fe(CN)_6]^{3-}$ and $[Fe(CN)_6]^{4-}$. Furthermore, urea is a cost-effective amide that dramatically affects the hydrogen-bonding network and hydration shell of ions in an aqueous solution. The authors also fabricated a prototype that generated an outstanding $V_{oc}$ of 3.4 volt (V) at ΔT = 18 °C. Yu et al. also employed 3 M $Gdm^+$ in a 0.4 M $K_{3/4}[Fe(CN)_6]$ aqueous electrolyte based on this theoretical mechanism. The liquid-state thermocell (LTC) was placed in the vertical direction with the cold electrode at the top and the hot electrode at the bottom. Crystals of $Gdm^+$ and $[Fe(CN)_6]^{4-}$ crystallized at the cold electrode (upper) due to the low temperature, which then precipitate and gradually redissolve on the hot side (bottom) (Figure 1.3 a). The concentration ratio difference (ΔCr) and ΔS between the anode and cathode drives the $S_e$ from 1.4 mV $K^{-1}$ to an extraordinarily high 3.73 mV $K^{-1}$ (Figure 1.3 b). The scalable thermocell device comprised of the LTC reached a Carnot-relative efficiency ($\eta_r$) of ~5% [35].

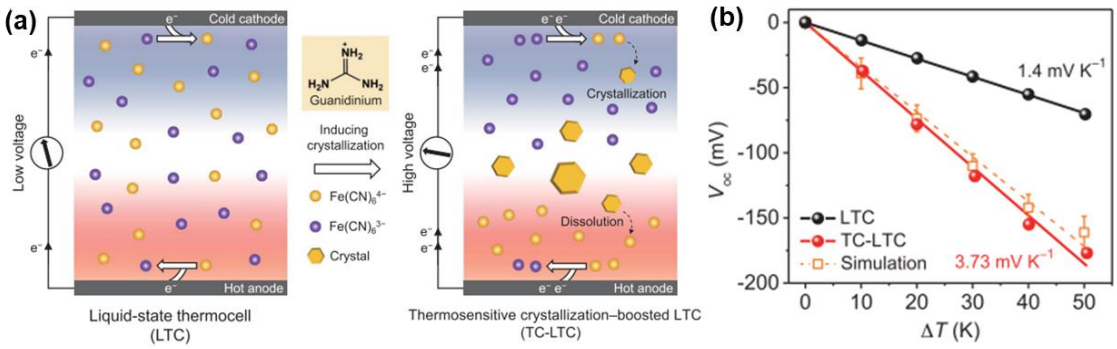


Figure 1.3 (a) A schematic representation of $Gdm^+$ inducing $[Fe(CN)_6]^{4-}$ crystallization and enhancement of the ΔS in the 0.4 M $K_3Fe(CN)_6/K_4Fe(CN)_6$ system. (b) Open-circuit voltage ($V_{oc}$) of the LTC and TC-LTC at different ΔT values. The simulated

result (dashed line) is consistent with the experimental result. The Seebeck coefficient ($S_e$) is calculated from the slope of the $V_{oc}$ - $\Delta T$ curves.

Ionic liquids (ILs) are liquid-state solutions at room temperature, but their physicochemical properties are the same as molten salts at high temperature [36]. ILs are attractive candidates for thermocell applications due to their inherent high thermal stability, non-volatility, non-flammability, and thermal stability [37]. Russo et al. incorporated various ionic liquids into gel electrolytes containing $K_{3/4}[Fe(CN)_6]$ to enhance the ionic conductivity and thermo-electrochemical performance. However, a fairly low power output was observed after the introduction of ILs, which was attributed to their high viscosity, resulting in prohibitively low diffusion coefficients and relatively low redox couple concentrations (Figure 1.4). Currently, ILs are not suitable for $K_{3/4}Fe(CN)_6$ redox couple systems and further work will focus on ILs with low viscosity that increase the redox couple solubility in order to improve the thermo-electrochemical output [38].

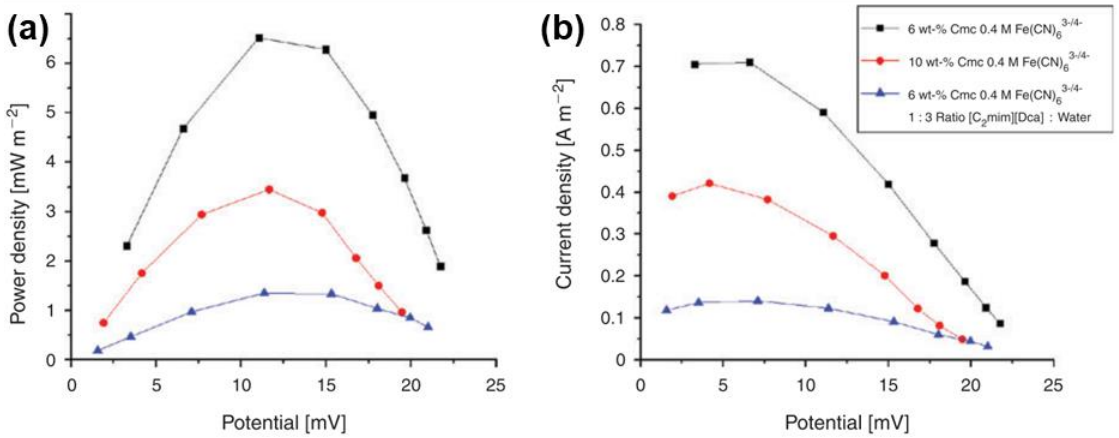


Figure 1.4 (a) Power and (b) current density of 6 wt.% and 10 wt.% CMC with 0.4 M $Fe(CN)_6^{3-/4-}$ hydrogel, and 6 wt.% CMC 0.4 M $Fe(CN)_6^{3-/4-}$ $[C_2mim][Dca]$ : water (1 : 3) gel electrolytes at $T_h$ = 35 °C, $T_c$ = 20 °C.

### *1.1.3.2 N-type redox couple*

*$Co^{2+}/Co^{3+}$*

The cobalt (III/II) tris-bipyridyl is a common cation that combines with varying anions that are used as a different type of redox couple. The $Co^{II/III}(bpy)_3(NTf_2)_{2/3}$ is a normally used redox couple based on ionic liquid (ILs), whose $S_e$ can reach 1.5 - 1.9 mV $K^{-1}$ in 3-methoxypropionitrile (MPN) solvent. Because of the low vapor pressure of ILs, the $Co^{II/III}(bpy)_3(NTf_2)_{2/3}$ could be utilized to harvest waste heat up to 130 °C, thereby achieving high power densities [7]. Abuzar Taheri et al. firstly reported the non-aqueous gel electrolytes that consist with $Co^{II/III}(bpy)_3(NTf_2)_{2/3}$ redox couple in MPN gelled with PVDF (Figure 1.5 a). They also fabricated thermocells with Pt electrodes, 0.1 M $Co^{II/III}(bpy)_3(NTf_2)_{2/3}$ and 5 wt% PVDF gel electrolytes. The authors systematically studied the performance of cells by decreasing the distance between the

two electrodes from 10 mm to 5 mm, 2.5 mm and 1 mm, and found the $P_{max}$ can reach 14 mW $m^{-2}$ at 1 mm separation (Figure 1.5 b) [39].

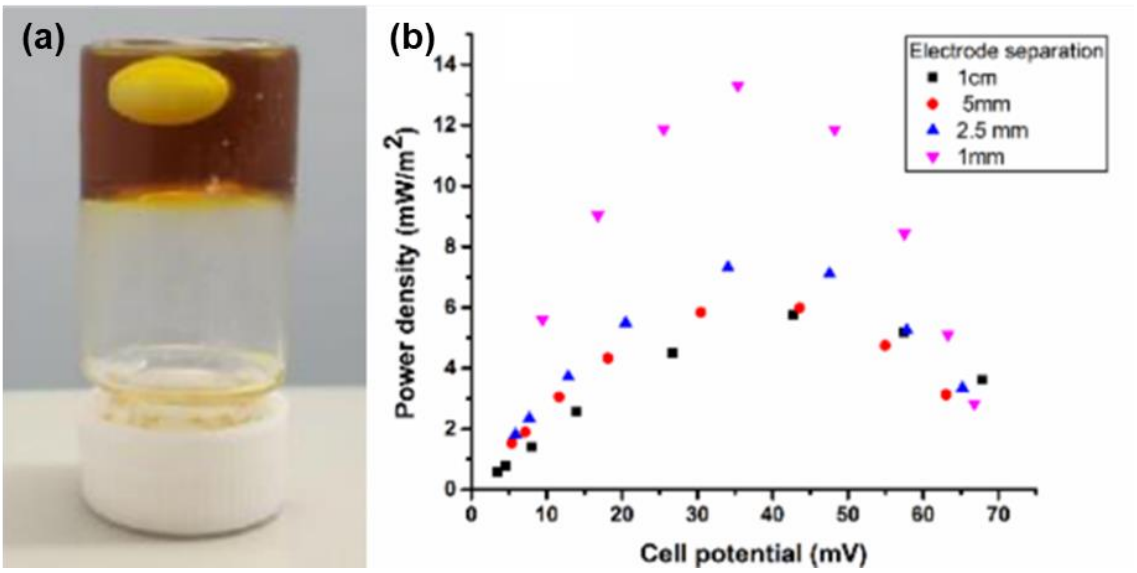


Figure 1.5 (a) Quasi-solid-state electrolytes containing 0.05 M $[Co(bpy)_3]^{2+/3+}[NTf_2^-]_{2/3}$ in MPN gelled with 5 wt% PVDF. The effect of electrode separation on (b) Power density of cells using polymer gel electrolyte (5 wt% PVDF, 0.05 M $[Co(bpy)_3]^{2+/3+}[NTf_2^-]_{2/3}$ in MPN, $T_c$ = 20 °C, $T_h$ = 60 °C).

*KI/KI₃*

Because host-guest interaction provides a concentration gradient of redox ion pairs between two electrodes (Figure 1.6 a). The $I_3^-$ was encapsulated by supramolecular α-Cyclodextrin (α-CD) surrounding the cold electrode side, which altered the equilibrium toward the oxidation process of $I^-$ to $I_3^-$ due to the reduced relative concentration gradient of $I_3^-$. Meanwhile, the α-CD-$I_3^-$ complexes were expected to dissociate near the hot electrode side and shifted the equilibrium of the reduction reaction ($I_3^-$ to $I^-$). The host−guest interaction yielded 70% increase in the $S_e$ of ca. 2.0 mV $K^{-1}$ around ambient

temperatures (Figure 1.6 b). Zhou et al. also assembled thermocells by $I_3^-/I^-$ with α-CD as electrolytes and Pt wire as electrodes. Moreover, the KCl served as supporting electrolytes, contributing to increasing the ionic conductivity of the electrolyte solution and balancing the static electric field generated by the redox reaction. The salt-induced segregation of solid K[α-$CD_2$-$I_5$] complexes at the cold electrode side resulting a decrease in the concentration of free $I_3$ anions, which host-guest interactions boosted the TECs performance (Figure 1.6 c and d) [13].

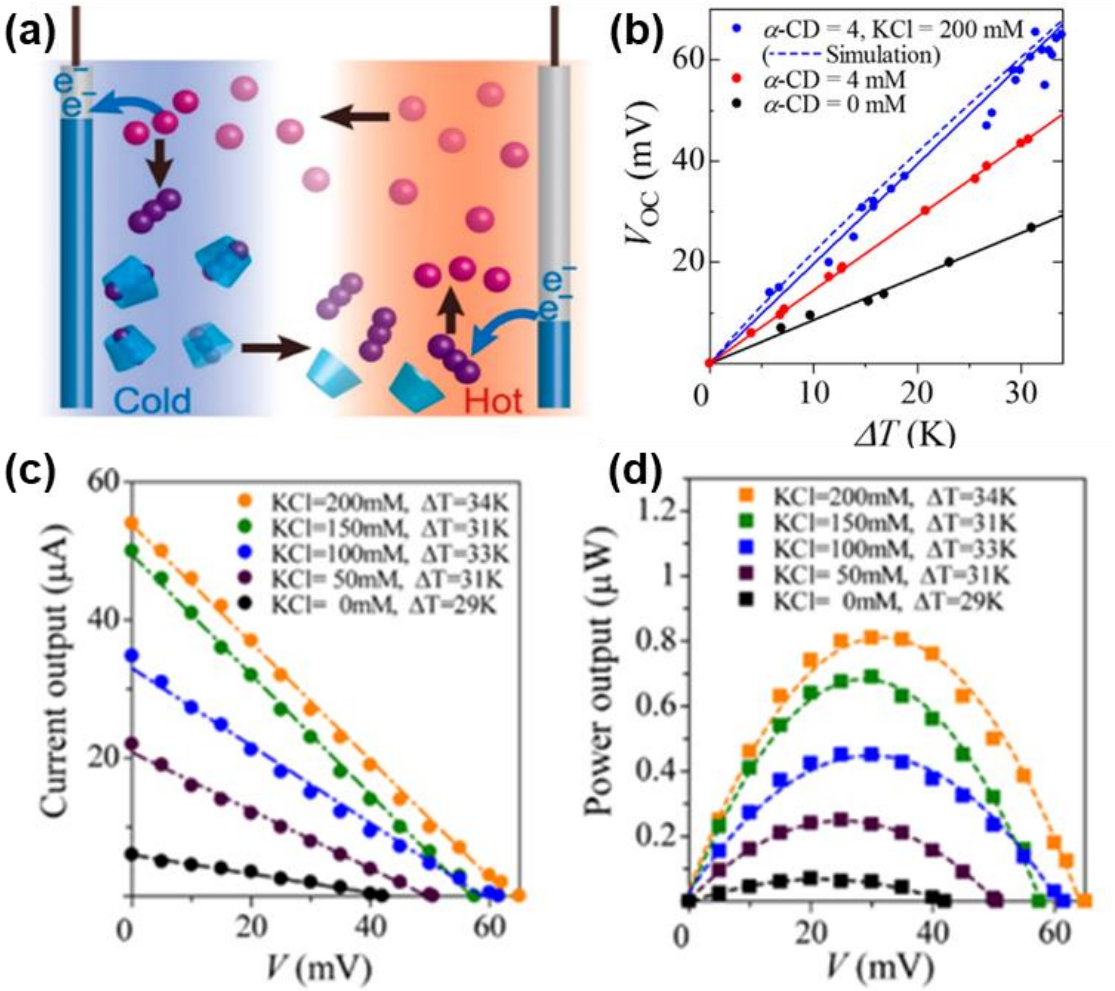


Figure 1.6 (a) The combination of α-CD and $I_3^-/I^-$ redox couple; (b) Linear increase of $V_{oc}$ with ΔT in $I_3^-/I^-$. Current output (c) and power output (d) changes of TECs with varying concentration of KCl.

$Fe^{2+}/Fe^{3+}$

Iron ions ($Fe^{2+}/Fe^{3+}$) are the widely used redox couples in thermocells, which have advantages over $Co^{2+}/Co^{3+}$ and $KI/KI_3$ because of their higher Seebeck coefficient and power output. Many anions can be combined with iron ions to form N-type redox couples, such as $FeCl_2/FeCl_3$, $Fe(ClO_4)_2/Fe(ClO_4)_3$, and $Fe(SO_4)_2/Fe_2(SO_4)_3$. These iron compounds exhibit different $S_e$ values due to hydrolysis or ionization effects. Two significant chemical equilibria exist in the Fe(II)/Fe(III) redox couple system.

$$[Fe(H_2O)_6]^{3+} \rightleftarrows [Fe(OH)(H_2O)_5]^{2+} + H^+ \quad (16)$$

$$Fe^{3+} + [SO_4]^{2-} \rightleftarrows [FeSO_4]^+ \quad (17)$$

In equation (16), the $Fe^{3+}$ cation combines with $H_2O$ to generate its hydrate, $[Fe(H_2O)_6)]^{3+}$. $[Fe(H_2O)_6)]^{3+}$ will hydrolyze into $[Fe(OH)(H_2O)_5]^{2+}$ and $H^+$, which is why most $Fe^{2+/3+}$ aqueous solutions are acidic. A decrease in the pH will encourage more hexaaqua $Fe^{3+}$ to be present (as opposed to species such as $[Fe(OH)]^{2+}$) [40,41]. Equation (17) is in competition with equation (16), and the anion is dominant. In other words, a smaller $pK_a$ indicates a greater degree of ionization of the inorganic acid (i.e., a smaller degree of hydrolysis) for monovalent anions. For divalent acids, every ionization step must be considered. To decrease the degree of ion pairing, anions whose conjugate acids exhibit low $pK_a$ values should be chosen, such as HBr (-9.00), HCl (-8.0), $HClO_4$ (-10), $HNO_3$ (-1.3), and $CF_3SO_3H$ (-14) [40]. For the Fe(II)/Fe(III) redox couple, more free redox couples should be present in the system rather than ion-pairing or iron hydrate; for example, $[FeSO_4]^+$ or $[Fe(OH)]^{2+}$ will lead to a low $S_e$. $FeCl_{2/3}$ is a commonly applied redox couple due to the lower $pK_a$ value of hydrochloric acid (HCl) [40] and therefore, more $Fe^{2+/3+}$ ions can be ionized from the $FeCl_{2/3}$ aqueous solution and

exhibit a relatively higher $S_e$ (1.02 mV $K^{-1}$) [42]. In addition, the solubility of $FeCl_{2/3}$ in water can be as high as 3 M. Due to the hydrolysis effect, the aqueous solution of the redox couple is acidic and thus, polymers that can be crosslinked under acidic conditions should be selected as the framework for gel electrolytes.

Mark et al. selected four Fe(II)/Fe(III) salt systems ($[NH_4]_2Fe(II)[SO_4]_2/[NH_4]Fe(III)[SO_4]_2$ as '$[NH_4]FeSO_4$', $Fe(II)SO_4/Fe(III)[SO_4]_{1.5}$ as '$FeSO_4$', $Fe(II)[NO_3]_2/Fe(III)[NO_3]_3$ as '$FeNO_3$', and $Fe(II)[CF_3SO_3]_2/Fe(III)[CF_3SO_3]_3$ as '$FeCF_3SO_3$') and investigated the effect of pH and anions on the current, power output, and $S_e$ [40]. Among the four iron salt systems, the sulfate-based systems demonstrate high pH sensitivity because the acidic system can effectively reduce the ion-pairing. For the monovalent anion system, the dissociation of water during hydration has a more dominant effect than ion pairing (Figure 1.7 a). The concentration of acidic protons correlated with the $S_e$ value. Since equation (16) only influences the minority of redox-active species across the systems, equation (17) is assumed to dominate the overall trend in $S_e$ observed (Figure 1.7 b). In addition, the power curves obtained for both $FeSO_4$ and $[NH_4]FeSO_4$ were strongly altered by the addition of acid, resulting in ~10- and ~20-fold increases in the power output for the $[NH_4]FeSO_4$ and $FeSO_4$ systems, respectively (Figure 1.7 c&d).

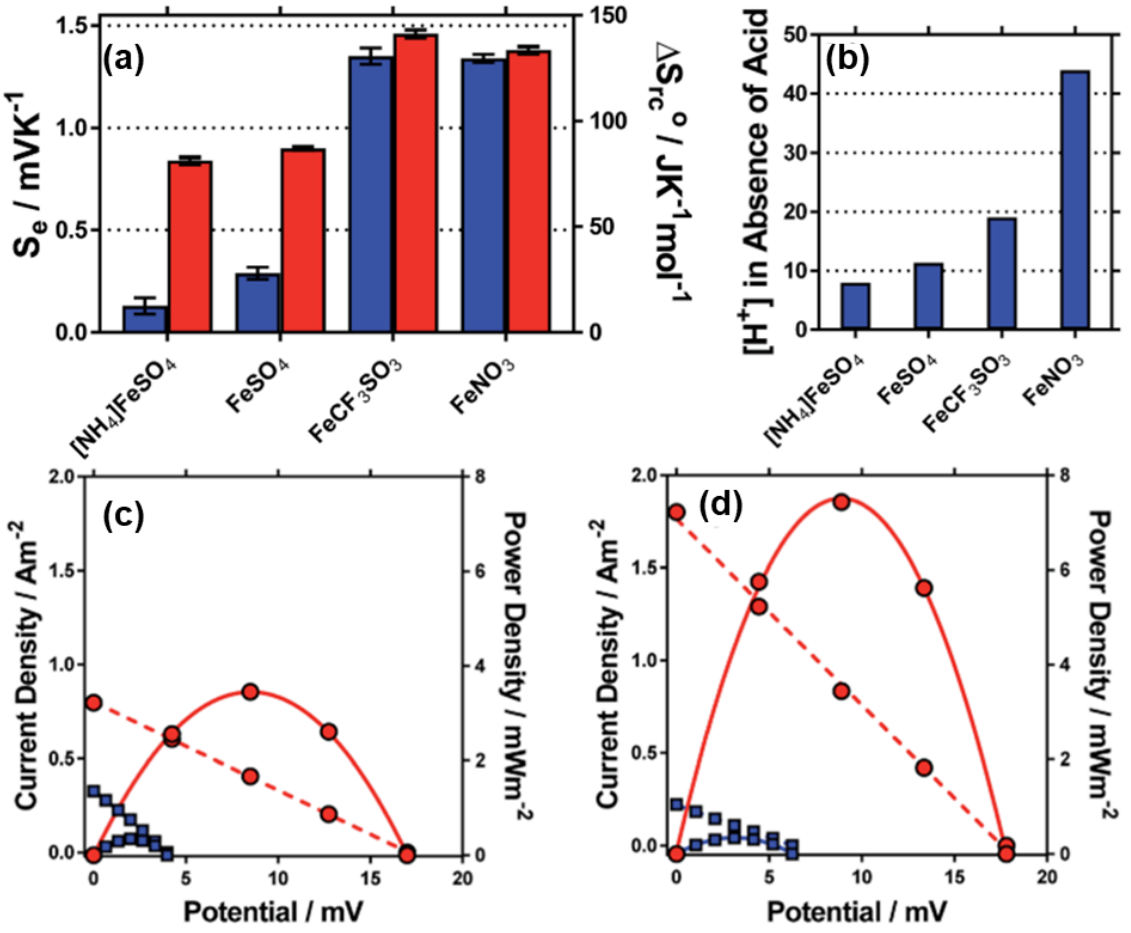


Figure 1.7 (a) Bar chart showing the Seebeck coefficient ($S_e$) and entropy values $\Delta Src^o$ for various Fe(II)/Fe(III) systems; (b) the concentration of protons, $[H^+]$, present in solution for the unacidified systems (present indicates the extent to equation (16), i.e. $[Fe(OH)(H_2O)_5]^{2+} + H^+$) occurs); current and power densities plots vs. potential for (c) $[NH_4]FeSO_4$, (d) $FeSO_4$ in the absence (blue) and presence (red) of 1 M conjugate acid.

Kim et al. demonstrated a novel N-type electrolyte using iron(II/III) perchlorate as the redox couple, in which $S_e$ can reach up to +1.76 mV K$^{-1}$ when using platinum electrodes (Figure 1.8 a). They found that both the thermal and ionic conductivities decrease upon increasing the concentration (Figure 1.8 b and c). Finally, the authors connected an N-type electrolyte (0.8 M $Fe^{2+}/Fe^{3+}$) and P-type electrolyte (0.4 M $Fe(CN)_6^{3-}/Fe(CN)_6^{4-}$) in

series as TECs to measure the power output at ΔT = 20 ℃ using platinum (Pt) electrodes (Figure 1.8 d) [43].

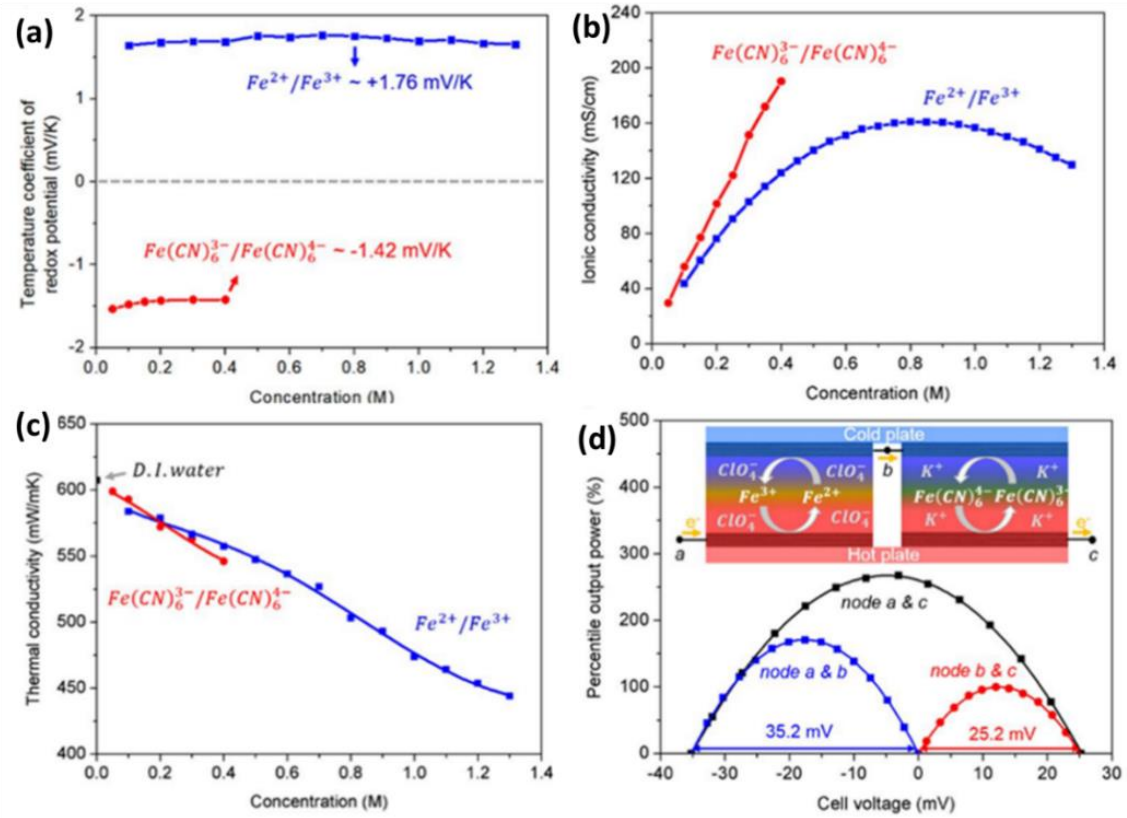


Figure 1.8 (a) A comparison of $V_{oc}$ of $Fe(CN)_6^{3-}/Fe(CN)_6^{4-}$ and $Fe^{2+}/Fe^{3+}$ redox couple solution with varying concentration. (b) Ionic and (c) thermal conductivity changes with different concentrations of redox couple. (d) The electrochemical performance of TECs assembled using 0.4 M $Fe(CN)_6^{3-}/Fe(CN)_6^{4-}$ and 0.8 M $Fe^{2+}/Fe^{3+}$ in series.

## 1.2 Wearable thermo-electrochemical cells

Wearable thermocells are designed to harvest waste heat from human bodies, which can convert thermal energy from human bodies into electric power without any detrimental by-products [44]. Human body heat has attracted a lot of attention as a potentially

extensive and sustainable energy source in recent years because it consistently maintains a core temperature of ~37 ℃ and continually releases *ca.* 100 W of thermal energy to the surroundings per day even if we do nothing at home or sleep, which is part of the energy we never consider [6]. With the increasing aging population, health monitoring systems are expected to be in high demand and the global market is expected to reach $1.7 billion by 2025. Therefore, sustainable energy conversion devices that harvest human body heat have been extensively investigated [2]. Wearable thermocell devices may satisfy the requirements for potential wireless health monitoring and diagnosis because integrated circuits and microsensors only require energy consumption in the range of 100 nW to 10 mW. Portability and miniaturization are the trend for next-generation electronic devices. Therefore, the flexibility, bendability, and stretchability of self-charging wearable power supplies have been widely highlighted.

### 1.2.1 Requirements of wearable thermo-electrochemical devices

The configuration of a wearable thermocell is similar to that of traditional TECs with the exception that wearable TECs require sufficient flexibility. Therefore, wearable thermocell devices normally use flexible electrolytes because they are stretched, compressed, or twisted during their actual application. Gel electrolytes meet these requirements very well, which promotes the application of thermocells in wearable devices [2,9,14,42]. First, utilizing gelated rather than liquid electrolytes can help prevent leakage issues, which is safe for wearable devices. Second, thermocells may be twisted and deformed for the practical use in wearable devices. Gelled electrolytes can maintain unity and larger temperature gradients by frustrating the thermal convection mechanism [14,25]. The desired gel electrolytes should have minimal internal resistance, and thermal

conductivity, and higher $S_e$. However, gel electrolytes are also limited by their high viscosity and low conductivity when compared with liquid electrolytes, which is a significant aspect of their breakthrough.

Figure 1.9 shows wearable thermoelectrochemical devices typically consist of two flexible electrodes sandwiching a redox-active gel electrolyte [17,18]. The thermocell is encapsulated by polydimethylsiloxane (PDMS) or low-weight and high-flexibility membrane materials [45–50]. The package materials must have good thermal conductivity and transfer heat from the human body to the electrodes. The black layers are flexible electrode materials. The yellow part is the bendable gel electrolyte, in which the polymer matrix acts as the host, which can provide sufficient mechanical properties for gel electrolytes. However, they do not normally participate in redox reactions. Therefore, the two key elements for assembling wearable TECs are flexible electrode materials and bendable gel electrolytes.

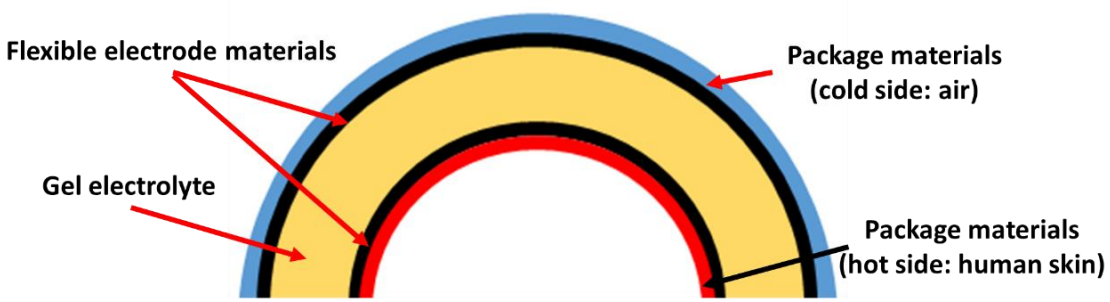


Figure 1.9 Configuration of wearable thermo-electrochemical cells.

## 1.2.2 Flexible electrodes

Electrodes in wearable thermocell devices should have a high surface area, high electrical conductivity, and porous architecture with low tortuosity and high thermal conductivity. However, it is difficult to simultaneously achieve these four requirements. The main challenge for the development of wearable thermocells is the preparation of flexible electrodes with high thermal conductivity and porosity. The most commonly used materials in wearable thermocell devices are conducting polymer-based electrodes due to their intrinsic flexibility, low cost, low weight, and ease of preparation [10,14,51]. Poly(3,4-ethylenedioxythiophene):poly(styrenesulfonate) (PEDOT:PSS) is a well-known intrinsically conductive polymer widely used in active electrode materials [52–56]. The melting material (PEDOT:PSS) can solve the problem of the poor solubility of PEDOT and has high conductivity (up to ~1000 s/cm), good air stability, and water processability. Furthermore, PEDOT:PSS is a promising active material for use in flexible electrodes. Liu et al. synthesized a large-scale freestanding and flexible PEDOT:PSS film, in which diethylene glycol (DEG) was used as a dopant to improve the conductivity (Figure 1.10 a). Moreover, flexible rGO-Poly(3,4-ethylenedioxythiophene)/polystyrene sulfonate (PEDOT/PSS) was assembled using solid electrolytes as a wearable solid-state supercapacitor (Figure 1.10 b) [57]. However, polymer-based electrodes suffer when using 2D film materials, which limit their electrochemical performance. The 2D film material needs porosity (microscale and macroscale) to guarantee that the viscous gel electrolyte penetrates the inner surface of the electrode materials, which can be further researched by 3D printing and laser cutting methods.

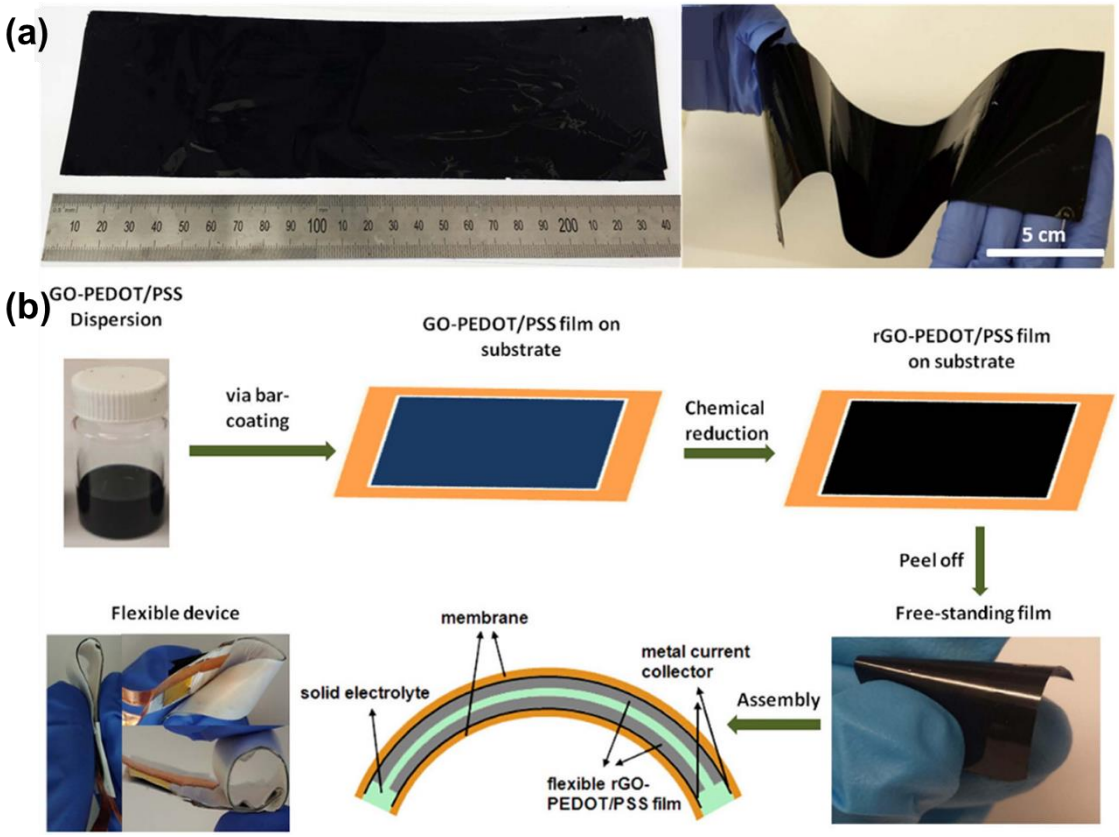


Figure 1.10 (a) Photographs of the as-prepared scaled, free-standing, and highly flexible PEDOT/PSS film. (b) Schematic illustration of the preparation process of rGO-PEDOT/PSS films and the structure of the assembled supercapacitor devices.

### 1.2.3 Gel electrolytes

Gel electrolytes typically consist of a polymetric framework as the host, crosslinker, solvent, redox couple as the most significant part participating in redox reactions, and salt or acid as the supporting electrolyte. The desired gel electrolyte should have high ionic conductivity, low thermal conductivity, good mechanical properties, and compatibility between the redox couple and polymers. However, there is a trade-off between the mechanical properties and high electrochemical performance. The two key elements of gel electrolytes are balancing the mechanical properties and high

electrochemical performance, and maintaining the redox couple within the polymer matrix. The concentration and molecular weight of the polymer are the main aspects of further investigation and suitable hydrogel hosts should be selected depending on the different chemical properties of the N- and P-type redox couples used.

#### *1.2.3.1 Crosslinking strategies*

Cross-linking is a stabilization process in polymer chemistry that leads to a multidimensional extension of the polymeric chains, resulting in network structures. The cross-linking process is a bonding process that links one polymer chain to another, and changes from the liquid state to 'solid' or 'gel'state by restricting its ability to move [58]. Based on this mechanism, the polymerization process can be classified into physical and chemical crosslinking.

Physical crosslinking involves entangled chains, hydrogen bonding, hydrophobic interactions, and crystallite formation (Figure 1.11 a) [59]. The gel formed via physical crosslinking is considered reversible and may decompose at a high temperature. However, the inert crosslinking process without involving any crosslinkers or chemical modifications is beneficial for the incorporation of some highly chemically activated redox couples [60].

Chemical crosslinking is termed a permanent or irreversible process due to the combination of covalent bonds, which may occur via the polymerization of monomers or condensation reactions between polymer chains containing more than two functional groups, which can be classified as chain-growth polymerization, addition, and condensation (Figure 1.11 b) [59]. Chain-growth polymerization includes free radical

polymerization and requires an oxidant, which is detrimental to the stability of the redox couples.

Crosslinking strategies are highly dependent on the chemical properties of the polymers and redox couples used. The selection of polymers and crosslinking methods differs depending on the type of redox couple used ($Fe^{2+/3+}$ or $[Fe(CN)_6]^{3-/4-}$). The redox couple $FeCl_{2/3}$ can coexist with acidic polymers or in a crosslinking process carried out in the presence of acid. Conversely, the $[Fe(CN)_6]^{3-/4-}$ redox couple accommodates only neutral polymers and crosslinking methods. In conclusion, the main challenge is the compatibility of redox couples and polymers. Furthermore, the concentration and molecular weight of the polymers are essential for determining the maximum thermoelectrochemical performance. For the development of hydrogel hosts for solid-state electrolytes used in thermocells, multifunctional hydrogels (*e.g.* both N- and P-type compatibility, porous structures, and excellent mechanical properties) are required for a diverse range of application environments.

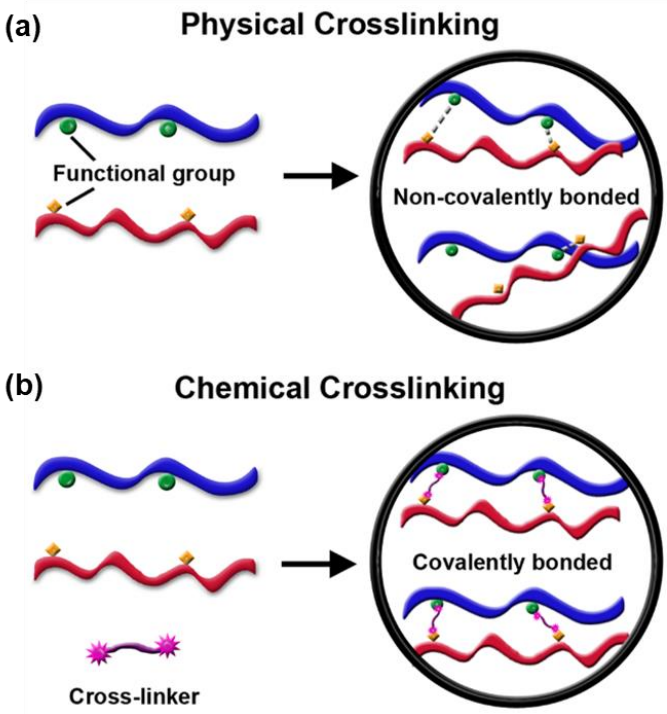


Figure 1.11 Graphical representation of physical and chemical cross-linking illustrating the type of bonding within the material.

### *1.2.3.2 Polymers for P-type redox couples*

Great efforts have been made to develop gel electrolytes as an alternative to aqueous systems. However, the coexistence of redox couples and polymers is a priority issue to consider. The pH is a significant factor for evaluating the compatibility of the polymer matrix with the redox couple because decomposition occurs for $[Fe(CN)_6]^{3-/4-}$ in the presence of acidic or alkaline conditions. Moreover, the redox couple $[Fe(CN)_6]^{3-/4-}$ also suffers from low solubility in most polymer aqueous solutions, resulting in undesirable TEC performance [38]. To overcome these challenges, inert and harmless crosslinking processes are required due to the high chemical activity of $[Fe(CN)_6]^{3-/4-}$. Therefore,

neutral polymers with high $[Fe(CN)_6]^{3-/4-}$ solubility should be applied as frameworks for gel electrolytes.

Cellulose (Figure 1.12 a) is a type of glucose that is insoluble in water and other conventional solvents. Therefore, the hydroxyl groups in cellulose are usually etherified by hydrophilic methyl and ethyl units [61]. Cellulose-based polymers are commonly used to prepare solid electrolytes due to their high ionic conductivity ($1.07 \times 10^{-2}$ mS $cm^{-1}$ at 30 °C) [62]. Among the many derivatives available, sodium carboxymethylcellulose (CMC) (Figure 1.12 b) has been proven to be an ideal mediator for matching $[Fe(CN)_6]^{3-/4-}$ due to the neutral pH, low-cost, and high solubility of $[Fe(CN)_6]^{3-/4-}$ (0.4 M) as well as its sufficient number of hydroxy and carboxylic groups that retain moisture [63]. Russo et al. designed a P-type gel electrolyte comprised of polyvinyl alcohol (PVA) - $[Fe(CN)_6]^{3-/4-}$, however, the redox couple suffered from low solubility (0.05 M $[Fe(CN)_6]^{3-/4-}$ in PVA aqueous solution). The polyacrylamide (PAM) polymer can improve the solubility up to 0.4 M, which can lead to higher power and current densities at ~ 6 mV $m^{-2}$ [38].

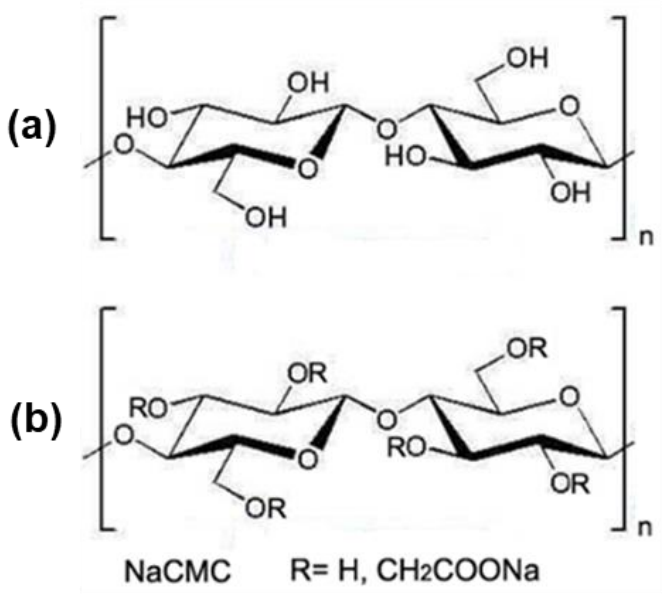


Figure 1.12 (a) Identical two units of cellulose. (b) Identical two units of cellulose derivatives. The group "R" is substituted in CMC.

Notably, PAM is also widely used in electronic devices due to its high ionic conductivity, excellent mechanical properties, and good compatibility with metal salts [64,65]. Typically, polyacrylamide (PAM) hydrogels are prepared *via* free-radical polymerization using acrylamide (AM, monomer), where the oxidizing agent (initiator, *e.g.* ammonium persulfate (APS)) and crosslinker (*e.g.* N,N′-methylenebis(acrylamide) (MBA)) are essential for chemical crosslinking (Figure 1.13). In addition, free-standing PAM gel electrolytes can be physically crosslinked via hydrogen bonding, hydrophobic interactions, or electrostatic interactions. Our research group introduced 0.4 M $Fe(CN)_6]^{3-/4-}$ into mechanically robust PAM hydrogels (100% strain) *via* an ion exchange process. The thermocell achieved an $S_e$ of -1.25 mV $K^{-1}$ and $P_{max}$ 29.03 mW $m^{-2}$ at $\Delta T = 20$ °C [11].

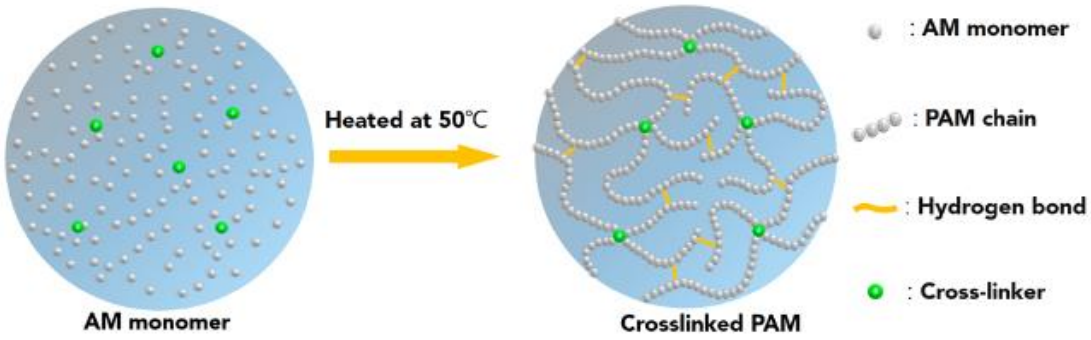


Figure 1.13 A schematic representation of the fabrication of the cross-linked PAM-based electrolytes.

Commercial neutral hydrogels are another promising candidate for use as gel electrolytes. Jimmy et al. used commercial gelated products (sodium polyacrylate beads, agar gels, and gelatin) as gelators for gel electrolytes. The authors also studied the TEC performance of 0.1 M $K_{3/4}[Fe(CN)_6]$ with 5.5 wt.% sodium polyacrylate gel electrolyte (Figure 1.14 a and b) at $\Delta T$ = 5, 15, and 25 ℃ (cold side: 10, 20, and 30 ℃ /hot side: 35 ℃) at the stainless-steel electrodes used in CR2032 battery casings (Figure 1.14 c) [25]. In this study, agar and gelatin gels were found to be unfavorable for $[Fe(CN)_6]^{3-/4-}$ thermocells. Conventional gelatin gels melts at a relatively low temperature of 35 ℃ and agar gels suffered from low current density values when compared to liquid electrolytes. Conversely, the poly(sodium acrylate) hydrogel was more appropriate with mechanically robust and unchanged diffusion coefficients. In addition, the authors also differentiated the gelated electrolytes and quasi-solid-state electrolytes using an "inversion" test method, where the flow phenomena occurred in the liquid (even a viscous liquid) while the container was turned upside down. Ultimately, they also demonstrated the stable power output of the gel electrolytes when compared to liquid electrolytes caused by the accommodation of the CR2032 housings in the thermocells. Hassan et al. used commercial sodium polyacrylate spheres as the polymer host soaked

in an excess volume of 0.4 M $K_{3/4}[Fe(CN)_6]$ aqueous solution for 24 h as a gel electrolytes (Figure 1.14 d), which avoids the poor solubility of $[Fe(CN)_6]^{3-/4-}$ in the most commonly used polymer aqueous solutions. However, the concentration of $[Fe(CN)_6]^{3-/4-}$ penetrating the gel is difficult to determine and control. The authors also used gold nanoparticles (AuNP) as the supporting electrolyte at the gel/electrode interface or throughout the gel, AuNP@surface and AuNP@gel, respectively (Figure 1.14 e and f) to reduce resistance to electron transfer. However, the distribution of AuNPs throughout the gel is unstable in the $[Fe(CN)_6]^{3-/4-}$ gel electrolyte over time, which can decrease the power output of the thermocell (Figure 1.14 g and h) [17]. A detailed comparison of the different p-type gel electrolytes is provided in Table 1.1.

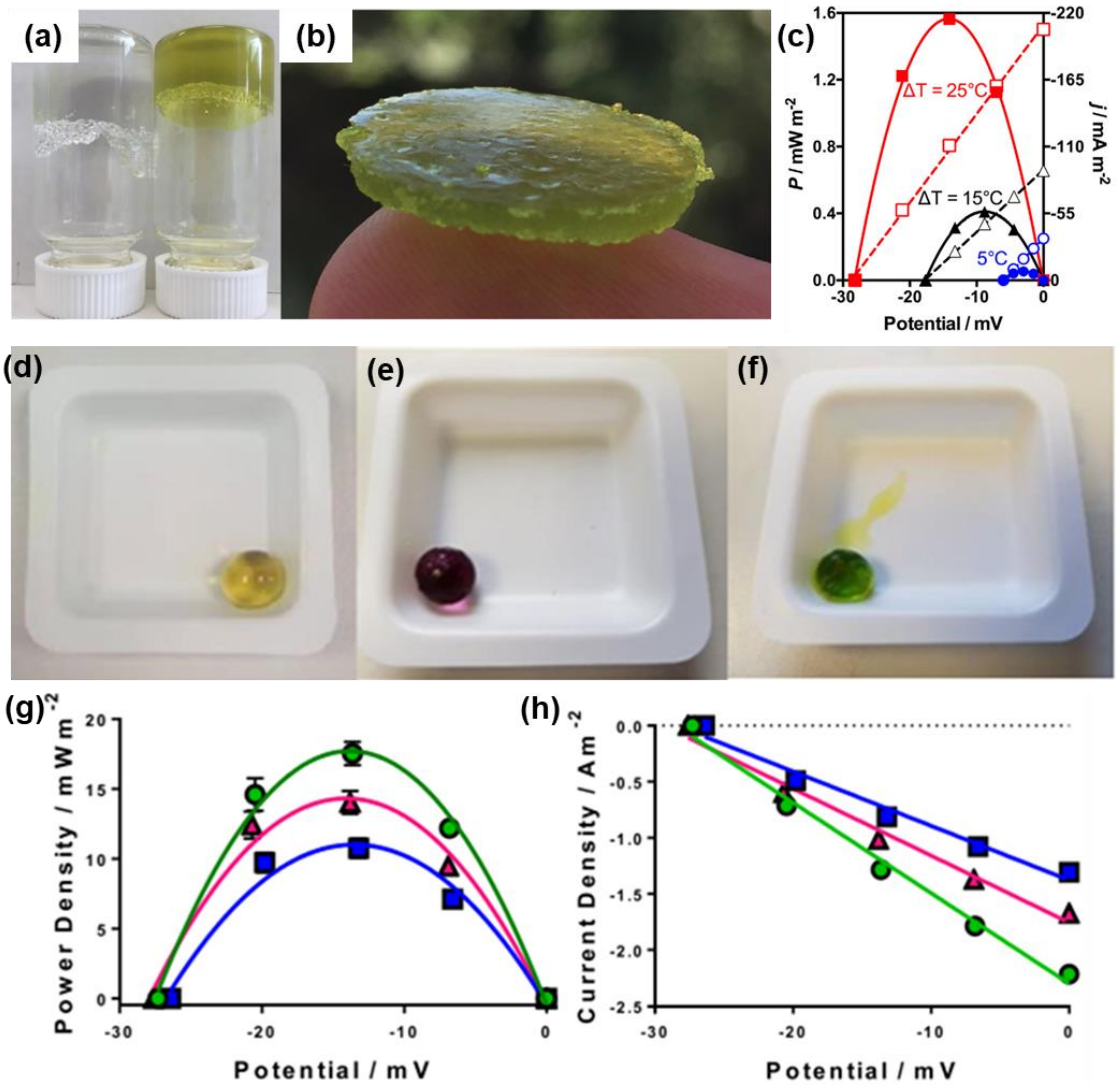


Figure 1.14 Photographs of (a) gels was prepared by 5.5 wt.% poly(sodium acrylate) with just water (transparent) and with 0.1 M $K_3[Fe(CN)_6]$/0.1 M $K_4[Fe(CN)_6]$ (yellow), and (b) freestanding gel on a fingertip prepared with 5.5 wt.% agar-agar and 0.1 M $K_3[Fe(CN)_6]$/0.1 M $K_4[Fe(CN)_6]$, cut to size for the CR2032 internal cavity. (c) The power output of the thermocell when $T_h$ = 35 °C, and $T_c$ is varied to give ΔT = 25 °C (■), 15 °C triangles (▲) and 5 °C (●). Hollow symbols display current density and filled symbols the overall power output. Picture (d) represents the gelled sphere after being soaked in 0.4 M $[Fe(CN)_6]^{3-/4-}$, showing the yellow colour (gel-cell), picture (e) is a gelled sphere containing immobilised AuNP (AuNP@gel), picture (f) is the AuNP@gel

after thermogalvanic measurement, the colour turns to deep green because of a gold analogue of Prussian blue. The graphs also show the representative (g) power curves and (h) I-V plots for (pink) gel-cell, (green) AuNP@surface and (blue) AuNP@gel systems.

Table 1.1 The preparation of P-type gel electrolytes with crosslinking and post-treatment methods.

| **Polymer** | **Crosslinking method (crosslinker)** | **Concentration of redox couple** | **Post-treatment** | $S_e$ **[mV K$^{-1}$]** | **Reference** |
|---|---|---|---|---|---|
| PVA | Dry in the air | 0.1 M $K_3[Fe(CN)_6]$/0.1 M $K_4[Fe(CN)_6]$ | - | -1.2 | [66] |
| PVA | - | 0.1 M $K_3[Fe(CN)_6]$/0.1 M $K_4[Fe(CN)_6]$ | - | -1.21 | [42] |
| PVA | Physical crosslinking (freeze-thawing) | 0.05 M $K_3[Fe(CN)_6]$/0.05 M $K_4[Fe(CN)_6]$ | | -1.47 ± 0.03 | [38] |
| PAM | Chemical crosslinking (MBA) | 0.1 M $K_3[Fe(CN)_6]$/0.1 M $K_4[Fe(CN)_6]$ | - | -1.24 | [67] |
| PAM | Chemical crosslinking (MBA) | 0.4 M $K_3[Fe(CN)_6]$/0.4 M $K_4[Fe(CN)_6]$ | 0.1 M $Gdm^+$ | -1.25 | [11] |
| CMC | - | 0.4 M $K_3[Fe(CN)_6]$/0.4 M $K_4[Fe(CN)_6]$ | - | -1.17 | [14][68] |
| CMC | - | 0.4 M $K_3[Fe(CN)_6]$/0.4 M $K_4[Fe(CN)_6]$ | - | -1.25 ± 0.04 | [38] |
| Gelatin | - | 0.25 M $K_3[Fe(CN)_6]$/0.42 M $K_4[Fe(CN)_6]$ | 0.8 M KCl | -12.7 - -17.0 | [24] |

| | | | | | |
|---|---|---|---|---|---|
| PAM | Chemical crosslinking (MBA) | 0.4 M $K_3[Fe(CN)_6]$/0.4 M $K_4[Fe(CN)_6]$ | Citric acid monohydrate (CA) | -1.37 | [69] |
| PAM | Chemical crosslinking (MBA) | 0.4 M $K_3[Fe(CN)_6]$/0.4 M $K_4[Fe(CN)_6]$ | - | -1.34 ±0.02 - 1.43 ±0.03 | [38] |
| AMPS:AM | Chemical crosslinking-UV curing (MBA, PEGDA) | 0.4 M $K_3[Fe(CN)_6]$/0.4 M $K_4[Fe(CN)_6]$ | 1 M NaCl | -1.4 | [70] |
| PAA (50% potassium neutralized by KOH) | Chemical crosslinking (MBA) | 0.4M $K_3[Fe(CN)_6]$/0.4 M $K_4[Fe(CN)_6]$ | - | -1.26 | [71] |

#### *1.2.3.3 Polymers for N-type redox couples*

For N-type electrolytes, the $FeCl_2/FeCl_3$ redox couple is widely used in thermoelectric cells because it has a large $S_e$, which means it can produce significantly more electrical energy from a temperature gradient when compared to other N-type redox couples. In addition, $FeCl_2$ and $FeCl_3$ are both readily accessible and inexpensive, making them attractive choices for thermos-electrochemical applications. The compatibility of $FeCl_2/FeCl_3$ and polymers should also be considered during the selection of the polymer, in which the acidic properties of the $FeCl_2/FeCl_3$ aqueous solution requires neutral and acidic polymers. Moreover, $FeCl_2/FeCl_3$ can be dissolved in a majority of the polymer aqueous solutions reported to date, which is not similar to P-type redox couples.

Polyvinyl alcohol (PVA) is a synthetic polymer that is typically used as the host polymer due to its inherent characteristics, such as excellent mechanical strength, non-toxicity, cost-effectiveness, good optical properties, high-temperature resistance, and hydrophilicity [72–74]. PVA can be chemically or physically crosslinked. Glutaraldehyde (GA) is a general crosslinker with two aldehyde groups in each molecule, which undergoes an aldol condensation reaction with the hydroxyl groups in PVA in the presence of an acidic environment to generate 3D network structures [75]. Coincidentally, the redox couple ($Fe^{2+}/Fe^{3+}$) exhibits highly acidic properties in a PVA aqueous solution, which facilitates the crosslinking of PVA and GA to generate stretchable gel electrolytes and avoids the introduction of extra ions. In addition, Yang et al. employed PVA to synthesize remarkable gel electrolytes for use as n-type gel electrolytes. The gels are quasi-solid-state gels, which have good moldability and can be made into films with significant mechanical strength. The samples tested (15 mm × 8 mm × 1 mm)

exhibit mechanical strength of up to 0.1 MPa and excellent tensile properties, and can be stretched 2 to 4 times their original length (Figure 1.15 a). These properties make the gels suitable for use in wearable electronic systems. The wearable thermocell was attached to a hand, which generated an open-circuit voltage ($V_{oc}$) and short-circuit current ($J_{sc}$) of ~0.7 V and ~2 μA, respectively at an ambient temperature of 5 °C [42].

The freeze-thaw technique is a commonly used physical crosslinking method that establishes abundant intermolecular hydrogen-bonded network structures comprised of PVA chains and avoids the remaining crosslink remnants [76,77]. Bai et al. fabricated an excellent flexible self-powered body temperature monitoring device using a PVA-$FeCl_{2/3}$ gel electrolyte obtained after the freezing-thawing process (Figure 1.15 b) [78]. Multiple individual thermocells were connected in parallel to fabricate a patch that was attached to the forehead and used to monitor body temperature through real-time current measurements and effectively cool fever in patients. The stretchability of the PVA gel electrolyte was 2-3 times the original length and the mechanical strength reached 25 KPa. When 25 thermoelectric units were integrated, the $V_{oc}$ and $J_{sc}$ can reach 0.5 V and 100 μA at the temperature difference of 30 °C in series and parallel, respectively. Moreover, the device was also thermally sensitive and exhibited a quick response and recovery in the temperature detection limit of 0.1 K. A detailed comparison of the different N-type gel electrolytes is provided in Table 1.2.

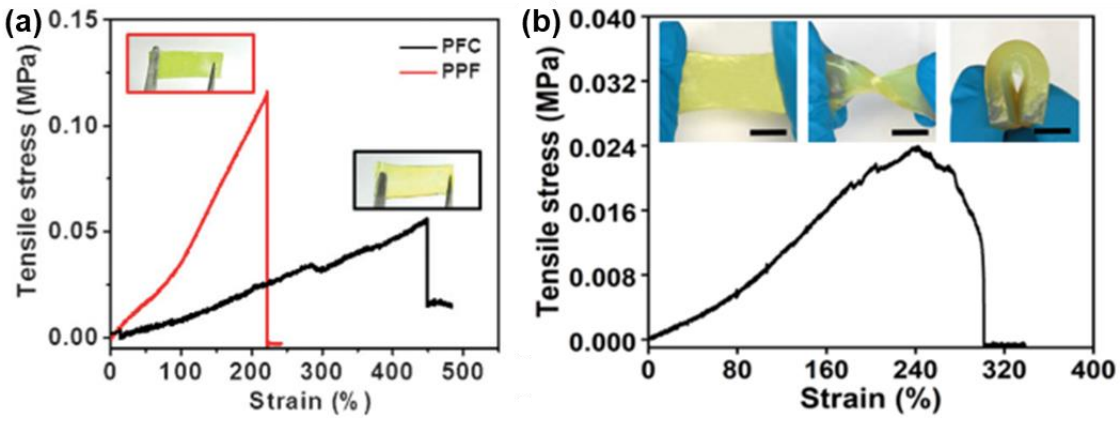


Figure 1.15 (a) Stress-strain curves for PFC and PPF gel films. The tests were carried out at a stretching rate of 5 mm $min^{-1}$ (at ca. 23 ℃ and a relative humidity (RH) of ca. 65%). Insets: Photographs of films made from PFC and PPF gels. (b) Stress-strain curves for thermogalvanic gel films. The tests were carried out at a stretching rate of 5 mm $min^{-1}$ at indoor (20 ℃, RH 50%). Insets: Photograph of PVA that has been stretched, twisted, and bent (scale bar: 1 centimetre, cm).

Table 1.2 The preparation of N-type gel electrolytes with crosslinking and post-treatment methods.

| **Polymer** | **Crosslinking method (crosslinker)** | **Concentration of redox couple** | **Post-treatment** | $S_e$ **[mV K$^{-1}$]** | **Reference** |
|---|---|---|---|---|---|
| PVA | Quasi-solid state | 0.1 M $FeCl_2$/0.1 M $FeCl_3$ | 1 mL of 36 wt.% HCl →10 mL of 0.1 M $FeCl_{2/3}$ | 1.02 | [42] |
| PVA | Chemical crosslinking (GA) | 1 M $FeCl_2$/1 M $FeCl_3$ | 0.08 M HCl | 0.85 | [9,11,14] |
| PVA | Chemical crosslinking (GA) | 1 M $FeCl_2$/1 M $FeCl_3$ | 0.1 M HCl | 0.8 ±0.02 | [9] |
| PVA | Physical crosslinking (freeze-thawing) | 0.1 M $FeCl_2$/0.1 M $FeCl_3$ | 1 mL of 36 wt.% HCl →10 mL of 0.1 M $FeCl_{2/3}$ | 0.79 | [78] |
| PAM | Chemical crosslinking | 0.1 M $FeCl_2$/0.1 M $FeCl_3$ | - | 1.05 | [67] |

| | | | | | |
|---|---|---|---|---|---|
| | (MBA) | | | | |
| METAC | Chemical crosslinking (MBA) | 0.4 M $FeCl_2$/0.4 M $FeCl_3$ | - | 1.12 | [71] |

*1.2.3.4 Polymers for both N and P-type redox couples*

The selection of a suitable gel electrolyte is crucial for the appropriate operation of thermocells. The gel electrolyte acts as a medium for ion transport and provides mechanical stability to the cell. For the N-type redox couple, the $FeCl_2/FeCl_3$ redox couple, which exhibits acidic properties, is commonly used as the redox species. On the other hand, for P-type redox couples, the $K_3[Fe(CN)_6/K_4[Fe(CN)_6]$ redox couple is chemically sensitive toward the pH conditions and redox reaction used in the crosslinking processes. A suitable gel electrolyte for both N- and P-type TECs must have high ionic conductivity, chemical stability towards redox couples, and electrochemical inertness.

Polyacrylamide (PAM) hydrogel is a promising material for use as a host material in thermocells and has been found to be a suitable host for both N- and P-type thermocells due to its low cost, high ionic conductivity, chemical stability towards the redox couple, and ease of preparation. PAM hydrogels can be prepared via the free radical polymerization of acrylamide in the presence of a crosslinker, such as N,N'-methylenebisacrylamide (BIS), or ionic crosslinker, such as citric acid (CA), in the presence of a neutral aqueous solution (Figure 1.16 a). The resulting PAM hydrogel has a porous structure and high water content, making it ideal for ion transport and improving the durability of TECs. Xu et al. demonstrated that a PAM-based ultra-stretchable hydrogel can be used as a superior candidate matrix suitable for both N- and P-type redox couples in flexible and stretchable thermocells [69]. Two PAM-based gel electrolytes (PAM-FeCN and PAM-Fe) have been prepared via solvent exchange with the redox ion pair solutions ($[Fe(CN)_6]^{4-}/[Fe(CN)_6]^{3-}$ and $Fe^{3+}/Fe^{2+}$) (Figure 1.16 b).

Figure 1.16 c shows both PAM-FeCN and PAM-Fe gel electrolytes demonstrate excellent stretchability of >1000% strain with a Young's modulus of 32 kPa.

Natural neutral polymer carboxymethyl chitosan (CMCs) is a highly versatile material with several advantages when used as a gel electrolyte in thermocells, in which the biocompatibility of the CMCs make them especially suitable for wearable thermocell devices. Moreover, CMCs hydrogels have been found to be chemically stable towards various redox couples, such as $FeCl_2/FeCl_3$ and $K_3[Fe(CN)_6/K_4[Fe(CN)_6]$, which ensures that the redox reaction proceeds smoothly without any side reactions.

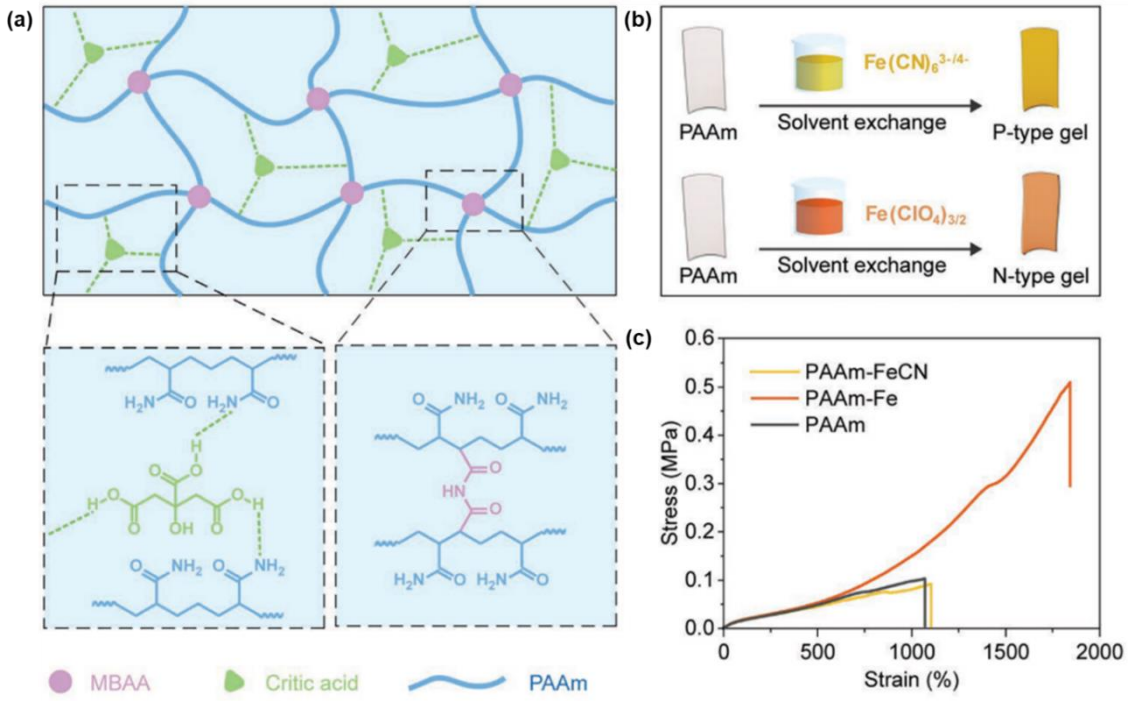


Figure 1.16 The preparation of electrolyte hydrogel. (a) Schematic illustration of the structure of PAAm hydrogel. (b) The preparation of hydrogels contained redox ion-pair electrolytes. (c) Stress-strain curves for PAM, PAM-FeCN, and PAM-Fe hydrogels.

## 1.3 Research progress in gel electrolytes

### 1.3.1 Porous structures

Gel electrolytes are generally limited by mass transport when compared to liquid systems. Therefore, porous structures are highly attractive in solid-state electrolytes because the oriented channels facilitate ionic transfer and abundant surface area is beneficial for mass loading [79]. Gel electrolytes with porous structures have promising applications in energy-storage devices, supercapacitors, and thermocells.

Considerable research efforts have been focused on the design of anisotropic gel electrolytes using a directional freezing method (Figure 1.17 a) [80–84]. Zhao and co-workers were inspired by the macroporous channels inherent in the structure of wood and designed the morphological tuning of aligned hydrogels suitable for supercapacitors using directional freezing methods. An aligned structure was formed along the freezing direction after the ice was removed (Figure 1.17 b) [79]. Wei et al. used $NaAc{\cdot}3H_2O$ crystal templates at ambient temperature (as hot-ice templates) to enlarge the aligned pores of PAM hydrogels (Figure 1.17 c). Needle-like $NaAc{\cdot}3H_2O$ crystals were arranged in parallel inside the hydrogels after removing the crystal templates, maintaining a pore size of ~50 μm (Figure 1.17 d) [85]. We also synthesized PAM gel electrolytes with porous structures using sodium acetate (NaAc) templates and a freeze-drying method for use in thermocells and boosted the maximum power density from 4.01 to 7.68 mW $m^{-2}$ at $\Delta T = 10$ °C [11].

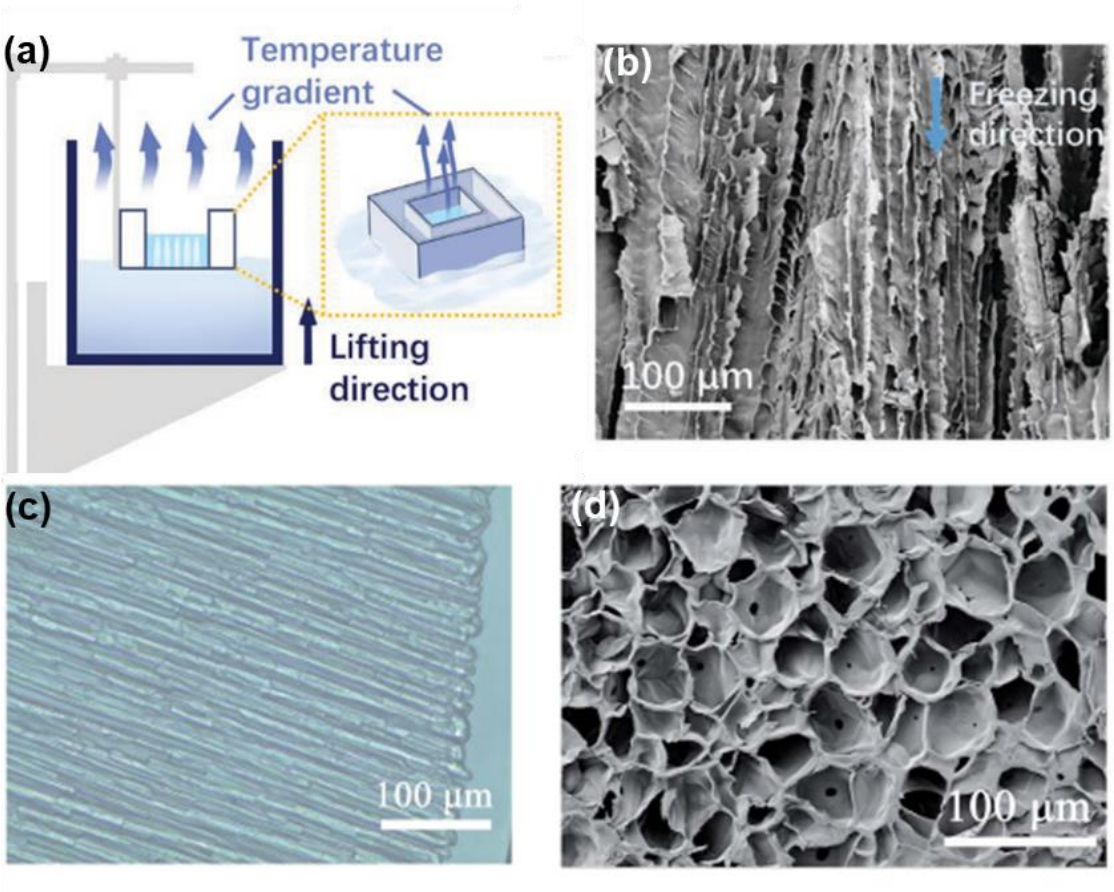


Figure 1.17 (a) A schematic representation of the directional freezing setup. The inset shows the mold which remains hollow in between the inner precursor solution and outer liquid nitrogen, enabling the preferably vertical temperature gradient. (b) SEM images of cross-sections along the alignment (freezing) direction. (c) Optical microscopy image of the aligned $NaAc{\cdot}3H_2O$ crystals. (d) SEM image of the aligned porous structures in the vertical pore direction.

### 1.3.2 Stretchability

Sodium alginate (SA) is a natural polymer typically used to synthesize neutral gels. Lili et al. prepared extremely high-concentration SA gels (25 wt.%) when compared with the reported values (3-7 wt.%) using the water evaporation crosslinking method (WEC)

(Figure 1.18 a). Free water is evaporated from the pre-gel solution until it became homogenous to maintain the maximum concentration of the polymer. Ultra-strong hydrogels were synthesized under the double effect of hydrogen bonding and ionic bonds with $Ca^{2+}$ [86]. A concentration of 15 wt.% SA demonstrated outstanding comprehensive mechanical properties (Figure 1.18 b). Furthermore, the author employed the WEC method on κ-carrageenan and agar polymers using only hydrogen bonding, resulting in a significant improvement in the mechanical performance.

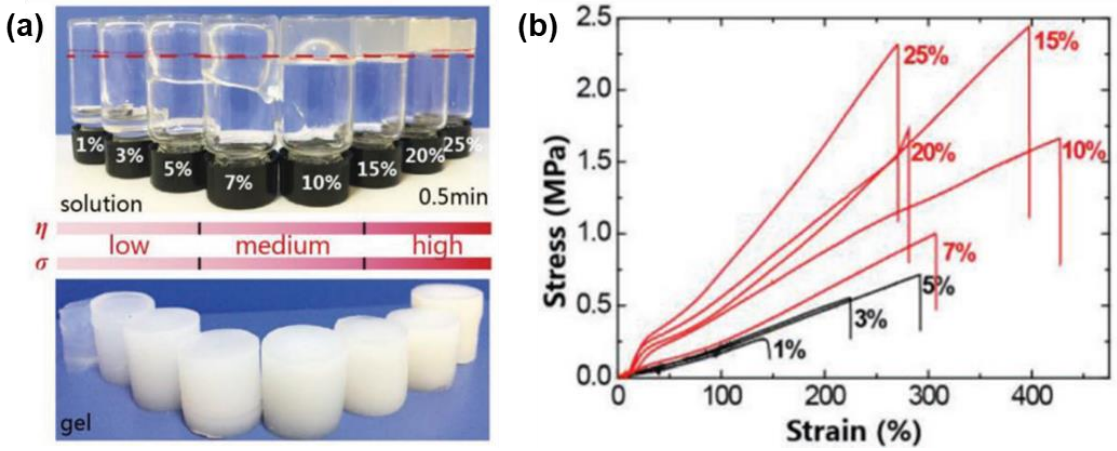


Figure 1.18 (a) Comparison of before and after crosslinking with SA concentration ranging from 1 wt.% to 25 wt.%, (b) The tension test of varying concentration of SA gels (length: 10 mm and speed of tension: 20 mm $min^{-1}$) [86].

Double-network (DN) crosslinking is an effective strategy for a range of diverse applications [87]. Normally, the DN hydrogel is synthesized using a two-step method, wherein rigid and fragile sacrificial bonds are generated in the first network to dissipate energy and the second network provides elasticity to the hydrogels [88]. As introduced in Section 1.4.2, PAM is a desirable polymer host for wearable thermocell devices and therefore, numerous investigations have been devoted to PAM hydrogels. Zhang et al.

designed a DN hydrogel comprised of PAM and CMCs-grafted-polyaniline with high stretchability (~1100%), which was used to assemble a self-powered strain sensor to detect human motions [89]. Duan et al. fabricated DN hydrogels via ionic crosslinking between alginate and calcium sulfate, and the copolymerization of CMCs and PAM via covalent bonds, which exhibited excellent stretchability with a frustration point at 1150%. A novel hybrid hydrogel comprised of CMCs, dialdehyde cellulose nanocrystals (DACNC), and PAM was prepared, which can also be repeatedly stretched to 400% and recovered to original shape after 90% compression [88]. Wang et al. designed a sewable Zn-$MnO_2$ battery based on PAM/nanofibrillated cellulose (NFC) hydrogels. The solid-state electrolyte NFC is a hydrophilic polymer, which reached 1100% strain (Figure 1.19 a) [64]. Sun et al. introduced a novel stretchable, electrically conductive, and robust hydrogel with promising applications in wearable devices, human health monitoring, advanced intelligent systems, and energy harvesting. Stretchable and conductive hydrogels were prepared *via* the synergistic effect of physical and chemical crosslinking between PAM and gelatin (Figure 1.19 b) [90]. Yan et al. demonstrated a novel supercapacitor made from PAM-vinyl hybrid silica nanoparticle (VSNPs) hydrogels, which could be stretched to 1500% strain and exhibited good ionic conductivity (Figure 1.19 c) [91]. Choudhury et al. reported a PVA/polyacrylic acid (PAA) blended hydrogel electrolyte that was chemically crosslinked using GA. The blended PVA/PAA hydrogel has film integrity and good mechanical properties, and the PAA aqueous solution also provided acidic conditions for the crosslinking process [92].

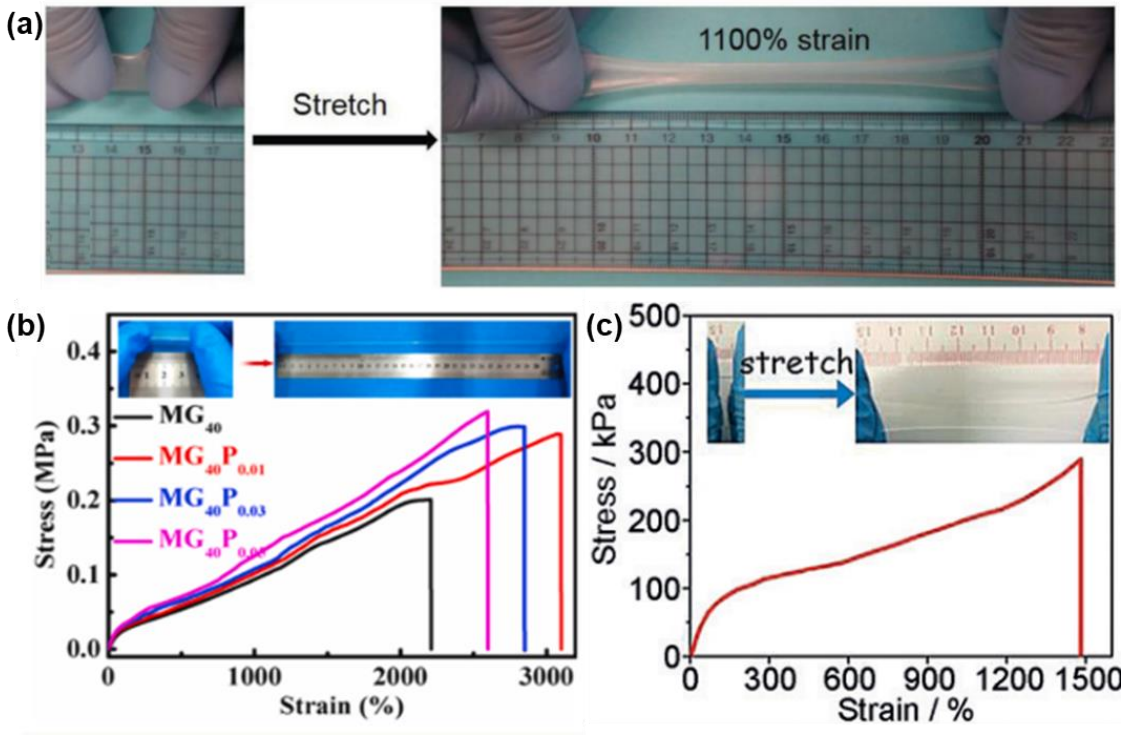


Figure 1.19 (a) Relaxed (left) and elongated (right) state of the NFC/PAM, exhibiting excellent stretchability. (b) Typical tensile stress-strain curves of PAM-gelatin hydrogels. The inset is the image of hydrogel that directly stretched to 1000% strain. (c) Stress-strain curve of as-synthesized VSNPs-PAM under stretching. Insets: relaxed (left) and elongated (right) states of the VSNPs-PAM exhibit excellent stretchability.

## 1.4 Device fabrication of wearable thermo-electrochemical cells

Wearable thermocells typically consist of single N-type and P-type units in series rather than parallel to avoid thermal short-circuits and improve the $V_{oc}$ to levels suitable for practical application [6]. Yang et al. synthesized N-type and P-type electrolytes based on 8 wt.% PVA - 0.02 M $FeCl_{2/3}$ (PFC) and 8 wt.% PVA - 0.02 M $[Fe(CN)_6]^{3-/4-}$ (PPF), respectively, which were alternately connected in series using Au/Cr electrodes (Figure 1.20 a) [42]. The result showed the $S_e$ of PFC and PPF are +1.02 mV $K^{-1}$ and -1.21 mV $K^{-}$

[1] (Figure 1.20 b), indicating that a relatively close $V_{oc}$ can be maintained. However, the current density of the PPF was lower than that of the PFC. The inset images in Figure 1.20 c showed the current density of PFC and PPF continuously increased until a stable value 1.3 A $m^{-2}$ and 0.4 A $m^{-2}$ respectively and immediately dropped when the heating was removed. The tandem N-P cells delivered $V_{oc}$ of 23 mV at $\Delta T$ = 10 °C (Figure 1.20 d), which was almost twice that of the individual specimens. The current output only reached 3 μA owing to the mismatch of the P and N current outputs, which was detrimental to chasing the maximum power output.

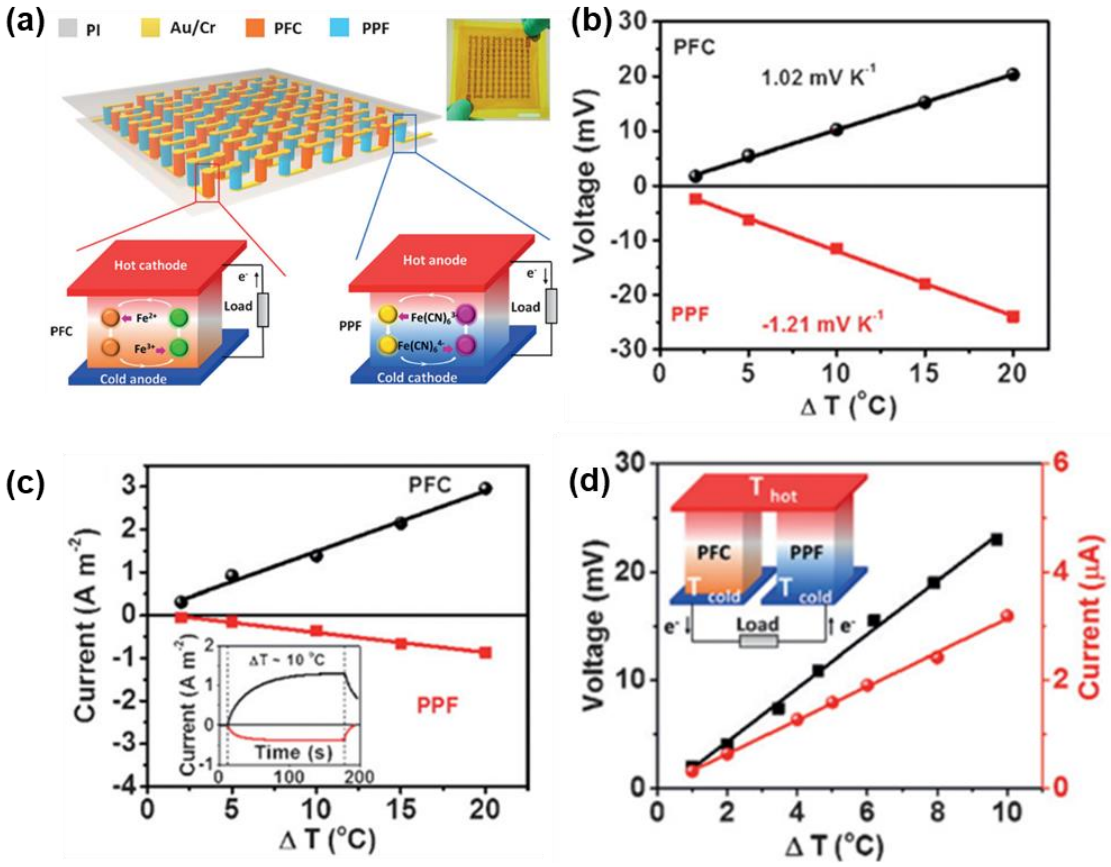


Figure 1.20 (a) The integrated gel-based array thermocells. Both the PFC and PPF gels were sandwiched between two flexible substrates (polyimide, PI). With alternating top and bottom interconnections, the PFC and PPF gels are connected sequentially in series.

The magnified insets illustrate the operation mechanism of the gel-based thermocells. At a certain temperature difference, the thermo-voltage polarity of PFC and PPF is exactly reversed. The top right inset is a photograph of the integrated device (scale bar: 2 cm). The $V_{oc}$ (b) and current density (c) of individual N-type or P-type thermocell at different temperatures. (d) The $V_{oc}$ and current output of tandem thermocell at different temperatures. The inset is thermocell consists of N-P-type in series.

Developing a wearable device that can maintain or adapt to temperature gradients in thermo-electrochemical cells (TECs) requires addressing the challenges posed by fluctuating temperature gradients. To achieve steady operation, some effort has been made such as, temperature stabilization, energy storage and buffering, and system optimization, where one of the primary objectives is to stabilize the temperature gradient across the TECs. This can be achieved through various means, such as incorporating insulation materials to minimize heat loss or the use of active cooling methods to dissipate excess heat. The insulation layer can act as a barrier between the hot and cold sides of the device, reducing undesired heat transfer. Next, integrating energy storage components, such as batteries or supercapacitors, can help buffer the electrical output from the TECs. During periods of fluctuating temperature gradients, the wearable device can still operate steadily by utilizing the stored energy. This ensures a constant power supply to the device, despite variations in temperature conditions. Finally, careful design and optimization of the overall system are crucial for maintaining a steady operation. This includes selecting thermally efficient materials, improving thermal conductivity, and minimizing thermal losses within the device. Furthermore, optimizing the placement and configuration of the TECs in the wearable device can help reduce the impact of fluctuations in the temperature gradient. These

principles ensure that the devices can operate steadily even in the presence of fluctuating temperature conditions, improving their efficiency and reliability.

The fluctuation limit of the temperature difference between the hot and cold electrodes in TECs for wearable devices depends on several factors, including the materials and the usage scenarios of TECs. Typically, TECs operate most efficiently and reliably when the temperature difference across the device remains within a certain range. This range is mainly determined by characteristics of the materials of electrodes and electrolytes. In addition, generally speaking, it is advantageous to minimize the fluctuations in the temperature difference to ensure stable power supply. However, in practice, the specific fluctuation limit may vary and should be determined through experimentation and testing for each TEC design and application. Therefore, in this thesis, textile (polyester-PEDOT:PSS) and platinum electrodes, and hydrogel electrolytes were used, which satisfied requirements of harvesting human body heat. Moreover, the temperature range of 15 ℃ - 55 ℃ (to achieve $\Delta T$=20℃) was applied for evaluating the operational temperatures of TECs, which is for simulating the practical situations of harvesting human body temperatures to ensure that the wearable TECs device is fully operational under a broad temperature range.

## 1.5 Thesis objectives

The goal of this project was to develop and optimize gel electrolytes for wearable thermocells. As described in this comprehensive literature review, wearable thermocell devices have made significant progress due to the development of gel electrolytes with multiple applications in recent decades. Nevertheless, gel electrolytes still suffer from

compatibility limitations between the polymer host, redox couples, and ion transfer. Therefore, the purpose of this thesis was to investigate novel multifunctional gel electrolytes for use in thermocell devices (acidic crosslinking, porous structures, and high stretchability). The thermo-electrochemical performance was further optimized *via* altering the polymer concentrations, introducing supporting electrolytes, use of porous gel electrolytes, and expanding the electrochemical surface area.

In Chapter 3, PVA was selected as the hydrogel host to be compatible with the acidic $FeCl_{2/3}$ redox couple, which was crosslinked with glutaraldehyde. Furthermore, multiple supporting electrolytes were used to enhance the mechanical strength and electrochemical performance. Finally, two individual PVA-$FeCl_{2/3}$ hydrogels were connected in electrical parallel to double the current output to identify the working potential for wearable applications.

In Chapter 4, the porous structure of the freeze-dried PAM gel electrolyte was synthesized in order to explore a gel that accommodates both N- and P-type redox couples and facilitates ion transfer. Gel electrolytes with porous structures are mainly based on the PAM polymer, which is prepared via the free-radical polymerization of AM monomer. The concentration of AM was comprehensively investigated to balance the mechanical stretchability and electrochemical performance. The pores inside the gel electrolyte were generated by removing the needle-like NaAc crystals that crystallized during the crosslinking process. In addition, $Gdm^+$ was initially adapted as a supporting electrolyte in the porous gelated electrolyte systems to boost the $S_e$. Meanwhile, the migration of crystals in gel electrolytes was incomparable with liquid electrolytes and in order to avoid precipitation inhibiting the porous channels and decreasing the

thermocell output, the optimal concentration of $Gdm^+$ was also investigated to achieve a high power output. Finally, the N- and P-type thermocells were alternately connected in series and a band-shaped wearable device that can harvest human body heat to light an Light emitting diode (LED) was fabricated.

In Chapter 5, a novel highly stretchable double-network carboxymethyl chitosan – polyacrylamide (CMCs-PAM) gel electrolyte was prepared, which accommodated both N- and P-type redox couples, in order to achieve outstanding stretchability of gel electrolytes suitable for body movements, in which a double-network crosslinking technique was used to generate ultra-stretchable gel electrolytes and the electrochemical performance was maintained at a comparable level. CMCs and PAM are neutral polymers that can be crosslinked under a neutral environment and are desirable candidates as gel electrolytes for wearable devices due to their excellent mechanical tensile properties, which can be attached to the skin and bent with the movement of joints. Moreover, a PEDOT:PSS textile electrode was also developed, which was integrated with gel electrolytes to further improve the electrochemical performance of the thermocells. The integral stretchable thermocell was evaluated under deformation to simulate its realistic utility and was manufactured as a soft-packing wearable device that harvested human body heat to illuminate an LED.

## 1.6 Reference


[1] R. Hu, D. Xu, X. Luo, *Matter* **2020**, *3*, 1400.

[2] R. Tian, Y. Liu, K. Koumoto, J. Chen, *Joule* **2019**, *3*, 1399.

[3] Z. Liu, *Mater. Lab* **2022**, *1*, 1.

[4] L. Zhao, *Mater. Lab* **2022**, *1*, 1.

[5] M. S. Romano, J. M. Razal, D. Antiohos, G. Wallace, J. Chen, *J. Nanosci. Nanotechnol.* **2015**, *15*, 1.

[6] H. Im, H. G. Moon, J. S. Lee, I. Y. Chung, T. J. Kang, Y. H. Kim, *Nano Res.* **2014**, *7*, 1.

[7] T. J. Abraham, D. R. MacFarlane, J. M. Pringle, *Energy Environ. Sci.* **2013**, *6*, 2639.

[8] M. M. I. M. Hasnan, N. Abdullah, S. M. Said, M. F. M. Salleh, S. A. M. Hussin, N. M. Shah, *Electrochim. Acta* **2018**, *261*, 330.

[9] Y. Zhou, Y. Liu, M. A. Buckingham, S. Zhang, L. Aldous, S. Beirne, G. Wallace, J. Chen, *Electrochem. commun.* **2021**, *124*, 106938.

[10] Y. Liu, H. Wang, P. C. Sherrell, L. Liu, Y. Wang, J. Chen, *Adv. Sci.* **2021**, *8*, 1.

[11] Y. Zhou, S. Zhang, M. A. Buckingham, L. Aldous, S. Beirne, C. Wu, Y. Liu, G. Wallace, J. Chen, *Chem. Eng. J.* **2022**, *449*, 137775.

[12] A. Shindrov, D. Artyukhov, M. Vikulova, N. Spirin, N. Nikitina, N. Savin, N. Gorshkov, I. Burmistrov, in *AIP Conf. Proc.*, **2017**, p. 020016.

[13] H. Zhou, T. Yamada, N. Kimizuka, *J. Am. Chem. Soc.* **2016**, *138*, 10502.

[14] R. E. Del Sesto, T. M. McCleskey, A. K. Burrell, G. A. Baker, J. D. Thompson, B. L. Scott, J. S. Wilkes, P. Williams, *Chem. Commun.* **2008**, *10*, 447.

[15] K. Kim, J. Kang, H. Lee, *Chem. Eng. J.* **2021**, *426*, 131797.

[16] G. J. Snyder, E. S. Toberer, *Nat. Mater.* **2008**, *7*, 105.

[17] H. A. H. Alzahrani, M. A. Buckingham, F. Marken, L. Aldous, *Electrochem. commun.* **2019**, *102*, 41.

[18] M. F. Dupont, D. R. MacFarlane, J. M. Pringle, *Chem. Commun.* **2017**, *53*, 6288.

[19] S. W. Hasan, S. M. Said, M. F. M. Sabri, A. S. A. Bakar, N. A. Hashim, M. M. I. M. Hasnan, J. M. Pringle, D. R. MacFarlane, *Sci. Rep.* **2016**, *6*, 1.

[20] T. J. Kang, S. Fang, M. E. Kozlov, C. S. Haines, N. Li, Y. H. Kim, Y. Chen, R. H. Baughman, *Adv. Funct. Mater.* **2012**, *22*, 477.

[21] P. F. Salazar, S. Kumar, B. a. Cola, *J. Electrochem. Soc.* **2012**, *159*, B483.

[22] D. Qi, Y. Liu, Z. Liu, L. Zhang, X. Chen, *Adv. Mater.* **2017**, *29*, 1602802.

[23] J. Duan, B. Yu, L. Huang, B. Hu, M. Xu, G. Feng, J. Zhou, *Joule* **2021**, *5*, 768.

[24] C.-G. Han, X. Qian, Q. Li, B. Deng, Y. Zhu, Z. Han, W. Zhang, W. Wang, S.-P. Feng, G. Chen, W. Liu, *Science (80-. ).* **2020**, *368*, 1091.

[25] J. Wu, J. J. Black, L. Aldous, *Electrochim. Acta* **2017**, *225*, 482.

[26] A. H. Kazim, B. A. Cola, *J. Electrochem. Soc.* **2016**, *163*, F867.

[27] T. I. Quickenden, Y. Mua, *J. Electrochem. Soc.* **1995**, *142*, 3985.

[28] T. I. Quickenden, C. F. Vernon, *Sol. Energy* **1986**, *36*, 63.

[29] A. V. Sokirko, *Electrochim. Acta* **1994**, *39*, 597.

[30] Y. Mua, T. I. Quickenden, *J. Electrochem. Soc.* **1996**, *143*, 2558.

[31] M. S. Romano, S. Gambhir, J. M. Razal, A. Gestos, G. G. Wallace, J. Chen, *J. Therm. Anal. Calorim.* **2012**, *109*, 1229.

[32] M. A. Buckingham, S. Hammoud, H. Li, C. J. Beale, J. T. Sengel, L. Aldous, *Sustain. Energy Fuels* **2020**, *4*, 3388.

[33] M. A. Buckingham, K. Laws, H. Li, Y. Kuang, L. Aldous, *Cell Reports Phys. Sci.* **2021**, *2*, 100510.

[34] J. Duan, G. Feng, B. Yu, J. Li, M. Chen, P. Yang, J. Feng, K. Liu, J. Zhou, *Nat. Commun.* **2018**, *9*, 5146.

[35] B. Yu, J. Duan, H. Cong, W. Xie, R. Liu, X. Zhuang, H. Wang, B. Qi, M. Xu, Z. L. Wang, J. Zhou, *Science (80-. ).* **2020**, *370*, 342.

[36] M. Galiński, A. Lewandowski, I. Stepniak, *Electrochim. Acta* **2006**, *51*, 5567.

[37] A. Taheri, D. R. MacFarlane, C. Pozo-Gonzalo, J. M. Pringle, *Aust. J. Chem.* **2019**, *72*, 709.

[38] M. Russo, H. Warren, G. M. Spinks, D. R. MacFarlane, J. M. Pringle, *Aust. J. Chem.* **2019**, *72*, 112.

[39] A. Taheri, D. R. MacFarlane, C. Pozo-Gonzalo, J. M. Pringle, *ChemSusChem* **2018**, *11*, 2788.

[40] M. A. Buckingham, F. Marken, L. Aldous, *Sustain. Energy Fuels* **2018**, *2*, 2717.

[41] C. C. A. Loures, M. A. K. Alcântara, H. J. I. Filho, A. C. S. C. Teixeira, F. T. Silva, T. C. B. Paiva, G. R. L. Samanamud, *Int. Rev. Chem. Eng.* **2013**, *5*, 102.

[42] P. Yang, K. Liu, Q. Chen, X. Mo, Y. Zhou, S. Li, G. Feng, J. Zhou, *Angew. Chemie - Int. Ed.* **2016**, *55*, 12050.

[43] J. H. Kim, J. H. Lee, R. R. Palem, M.-S. Suh, H. H. Lee, T. J. Kang, *Sci. Rep.* **2019**, *9*, 8706.

[44] W. Li, J. Ma, J. Qiu, S. Wang, *Mater. Today Energy J.* **2022**, 101032.

[45] M. Kaempgen, C. K. Chan, J. Ma, Y. Cui, G. Gruner, *Nano Lett.* **2009**, *9*, 1872.

[46] J. Ge, G. Cheng, L. Chen, *Nanoscale* **2011**, *3*, 3084.

[47] Z. Niu, J. Du, X. Cao, Y. Sun, W. Zhou, H. H. Hng, J. Ma, X. Chen, S. Xie, *Small* **2012**, *8*, 3201.

[48] J. Han, Y. Dou, J. Zhao, M. Wei, D. G. Evans, X. Duan, *Small* **2013**, *9*, 98.

[49] X. Li, X. Li, G. Wang, X. Wang, J. Ji, *J. Mater. Chem. A* **2013**, *1*, 10103.

[50] Z. Zhang, T. Zhai, X. Lu, M. Yu, Y. Tong, K. Mai, *J. Mater. Chem. A* **2013**, *1*, 505.

[51] Y. Wang, M. Mukaida, K. Kirihara, L. Lyu, Q. Wei, *Energy Technol.* **2020**, *8*, 1.

[52] M. Fabretto, C. Jariego-Moncunill, J.-P. Autere, A. Michelmore, R. D. Short, P. Murphy, *Polymer (Guildf).* **2011**, *52*, 1725.

[53] P. Hojati-Talemi, C. Bächler, M. Fabretto, P. Murphy, D. Evans, *ACS Appl. Mater. Interfaces* **2013**, *5*, 11654.

[54] O. Bubnova, Z. U. Khan, H. Wang, S. Braun, D. R. Evans, M. Fabretto, P. Hojati-Talemi, D. Dagnelund, J. B. Arlin, Y. H. Geerts, S. Desbief, D. W. Breiby, J. W. Andreasen, R. Lazzaroni, W. M. Chen, I. Zozoulenko, M. Fahlman, P. J. Murphy, M. Berggren, X. Crispin, *Nat. Mater.* **2014**, *13*, 190.

[55] M. Culebras, C. M. Gómez, A. Cantarero, *J. Mater. Chem. A* **2014**, *2*, 10109.

[56] L. Manjakkal, A. Pullanchiyodan, N. Yogeswaran, E. S. Hosseini, R. Dahiya, *Adv. Mater.* **2020**, *32*, 1907254.

[57] Y. Liu, B. Weng, J. M. Razal, Q. Xu, C. Zhao, Y. Hou, S. Seyedin, R. Jalili, G. G. Wallace, J. Chen, *Sci. Rep.* **2015**, *5*, 1.

[58] J. Maitra, V. K. Shukla, *Am. J. Polym. Sci.* **2014**, *4*, 25.

[59] R. Ramachandran, D. Jung, A. M. Spokoyny, *NPG Asia Mater.* **2019**, *11*, 9.

[60] R. parhi, *Adv. Pharm. Bull.* **2017**, *7*, 515.

[61] A. Sannino, C. Demitri, M. Madaghiele, *Materials (Basel).* **2009**, *2*, 353.

[62] P. K. Varshney, S. Gupta, *Ionics (Kiel).* **2011**, *17*, 479.

[63] K. M. El Salmawi, *J. Macromol. Sci. Part A Pure Appl. Chem.* **2007**, *44*, 619.

[64] D. Wang, H. Li, Z. Liu, Z. Tang, G. Liang, F. Mo, Q. Yang, L. Ma, C. Zhi, *Small* **2018**, *14*, 1.

[65] H. Li, Z. Liu, G. Liang, Y. Huang, Y. Huang, M. Zhu, Z. Pei, Q. Xue, Z. Tang, Y. Wang, B. Li, C. Zhi, *ACS Nano* **2018**, *12*, 3140.

[66] A. Kundu, T. S. Fisher, *Electrochim. Acta* **2018**, *281*, 357.

[67] T. Ding, Y. Zhou, X. Q. Wang, C. Zhang, T. Li, Y. Cheng, W. Lu, J. He, G. W. Ho, *Adv. Energy Mater.* **2021**, *11*, 1.

[68] S. Zhang, Y. Zhou, Y. Liu, G. G. Wallace, S. Beirne, J. Chen, *iScience* **2021**, *24*, 103466.

[69] C. Xu, Y. Sun, J. Zhang, W. Xu, H. Tian, *Adv. Energy Mater.* **2022**, *12*, 2201542.

[70] Z. Lei, W. Gao, P. Wu, *Joule* **2021**, *5*, 2211.

[71] M. A. Buckingham, S. Zhang, Y. Liu, J. Chen, F. Marken, L. Aldous, *ACS Appl. Energy Mater.* **2021**, *4*, 11204.

[72] C. O. Dasenbrock, T. H. Ridgway, C. J. Seliskar, W. R. Heineman, *Electrochim. Acta* **1998**, *43*, 3497.

[73] M. Y. Jen, Z. W. Hung, C. Y. Chun, *J. Memb. Sci.* **2008**, *322*, 74.

[74] C. C. Yang, G. M. Wu, *Mater. Chem. Phys.* **2009**, *114*, 948.

[75] C. Tang, C. D. Saquing, J. R. Harding, S. A. Khan, *Macromolecules* **2010**, *43*, 630.

[76] C. Chang, A. Lue, L. Zhang, *Macromol. Chem. Phys.* **2008**, *209*, 1266.

[77] Y. Guan, J. Bian, F. Peng, X. M. Zhang, R. C. Sun, *Carbohydr. Polym.* **2014**, *101*, 272.

[78] C. Bai, Z. Wang, S. Yang, X. Cui, X. Li, Y. Yin, M. Zhang, T. Wang, S. Sang, W. Zhang, *ACS Appl. Mater. Interfaces* **2021**, *13*, 37316.

[79] Y. Zhao, Y. Alsaid, B. Yao, Y. Zhang, B. Zhang, N. Bhuskute, S. Wu, X. He, *Adv. Funct. Mater.* **2020**, *1909133*, 1.

[80] W. Kong, C. Wang, C. Jia, Y. Kuang, G. Pastel, C. Chen, G. Chen, S. He, H. Huang, J. Zhang, S. Wang, L. Hu, *Adv. Mater.* **2018**, *30*, 1.

[81] J. Zhou, D. Wu, C. Wu, G. Wei, J. Wei, Z. Tai, S. Xi, S. Shen, Q. Wang, Y. Chen, *J. Mater. Chem. A* **2019**, *7*, 19753.

[82] X. Liu, O. O. Taiwo, C. Yin, M. Ouyang, R. Chowdhury, B. Wang, H. Wang, B. Wu, N. P. Brandon, Q. Wang, S. J. Cooper, *Adv. Sci.* **2019**, *6*, 1.

[83] W. Li, X. Li, X. Zhang, J. Wu, X. Tian, M. J. Zeng, J. Qu, Z. Z. Yu, *ACS Appl. Energy Mater.* **2020**, *3*, 9408.

[84] G. Shao, D. A. H. Hanaor, X. Shen, A. Gurlo, *Adv. Mater.* **2020**, *32*, 1907176.

[85] J. Wei, C. Yin, H. Wang, Q. Wang, *J. Mater. Chem. A* **2017**, *6*, 58.

[86] L. Wang, X. Zhang, Y. Xia, X. Zhao, Z. Xue, K. Sui, X. Dong, D. Wang, *Adv. Mater.* **2019**, *31*, 1902381.

[87] X. Huang, J. Li, J. Luo, Q. Gao, A. Mao, J. Li, *Mater. Today Commun.* **2021**, *29*, 102757.

[88] W. Huang, Y. Wang, L. M. McMullen, M. T. McDermott, H. Deng, Y. Du, L. Chen, L. Zhang, *Carbohydr. Polym.* **2019**, *222*, 114977.

[89] H. Zhang, H. Shen, J. Lan, H. Wu, L. Wang, J. Zhou, *Carbohydr. Polym.* **2022**, *295*, 119848.

[90] H. Sun, Y. Zhao, C. Wang, K. Zhou, C. Yan, G. Zheng, J. Huang, K. Dai, C. Liu, C. Shen, *Nano Energy* **2020**, *76*, 105035.

[91] Y. Huang, M. Zhong, F. Shi, X. Liu, Z. Tang, Y. Wang, Y. Huang, H. Hou, X. Xie, C. Zhi, *Angew. Chemie - Int. Ed.* **2017**, *56*, 9141.

[92] N. A. Choudhury, S. Sampath, A. K. Shukla, *Energy Environ. Sci.* **2009**, *2*, 55.

# Chapter 2 Experiment

## 2.1 Chemicals and Materials

The chemical reagents and materials used in this work are listed in Table 2.1

Table 2.1 List of chemical reagents and materials used in this work.

| **Chemicals/Materials** | **Grade** | **Company** |
|---|---|---|
| Iron (II) chloride tetrahydrate ($FeCl_2$) | AR | Sigma-Aldrich |
| Iron (III) chloride ($FeCl_3$) | AR | Sigma-Aldrich |
| Potassium ferricyanide ($K_3[Fe(CN)_6]$) | AR | Sigma-Aldrich |
| Potassium hexacyanoferrate (II) ($K_4[Fe(CN)_6]\cdot 3H_2O$) | AR | Sigma-Aldrich |
| Poly(vinyl alcohol) (PVA) | AR | Sigma-Aldrich |
| Glutaraldehyde solution (GA, 25 wt.% in $H_2O$) | AR | Sigma-Aldrich |
| Hydrochloric acid (HCl, 32%) | AR | Sigma-Aldrich |
| Phosphoric acid ($H_3PO_4$, 85% in $H_2O$) | AR | Sigma-Aldrich |
| Potassium chloride (KCl) | AR | Sigma-Aldrich |
| Acrylamide (AM) | AR | Sigma-Aldrich |
| N,N′-Methylenebis acrylamide (MBA) | AR | Sigma-Aldrich |
| Ammonium persulfate (APS) | AR | Chem-Supply |
| Sodium acetate (NaAc) | AR | Chem-Supply |
| Guanidinium chloride (GdmCl) | AR | Chem-Supply |

| | | |
|---|---|---|
| Carboxymethyl Chitosan sodium (CMCs) | AR | Sigma-Aldrich |
| Poly(3,4-ethylenedioxythiophene)-poly(styrenesulfonate) (PEDOT:PSS) | AR | Sigma-Aldrich |
| Diethylene glycol (DEG) | AR | Sigma-Aldrich |
| Polyester fiber | | |

## 2.2 Sample preparation

### 2.2.1 Metal sputter coater

The EDWARDS FTM6 Auto 306 (Figure 2.1 a) was performed as a sputter coater in this research. A thin layer of platinum of 5 nanometre (nm) was sputter-coated onto freeze-dried hydrogel samples before SEM characteristic. Moreover, for fabricating the flexible electrodes of wearable devices, 200 nm of platinum (Pt) was sputter-coated onto a substrate of Kapton-tape (Figure 2.1 b) as electrodes for thermo-electrochemical measurement (Figure 2.1 c).

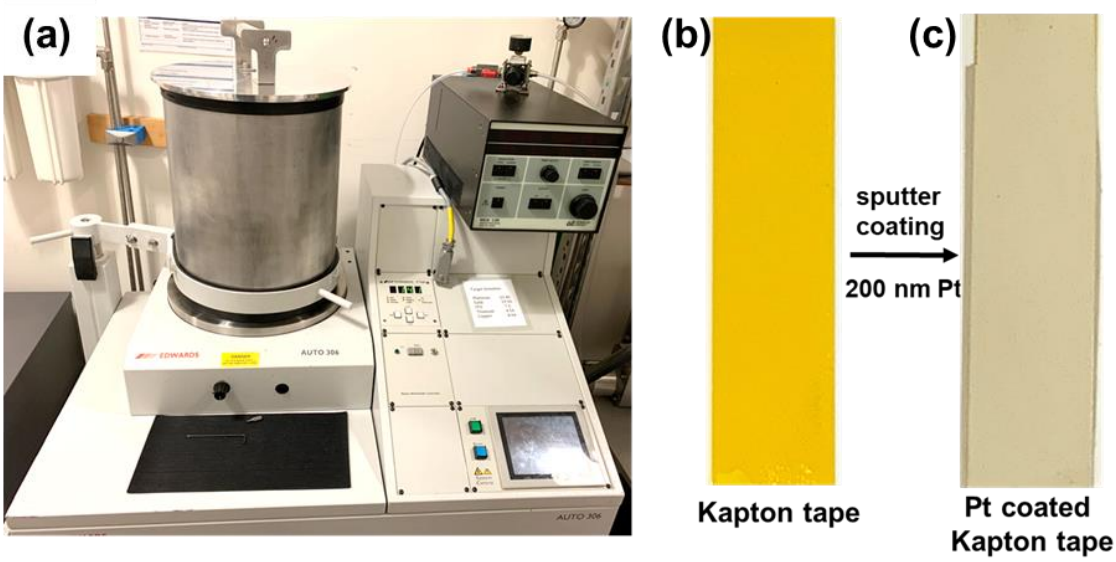


Figure 2.1 (a) Photographs of Edwards FTM6 Auto 306 Sputter coater, a Kapton tape before (b) and after (c) platinum (Pt) coating.

### 2.2.2 Ultra-sonication

Bath sonication is a common facility that used ultra-sonication techniques to disperse materials in the solvent (*e.g.* water). In this work, A John Morris DL 514 BH ultrasonic bath (Figure 2.2 a) was used to disperse materials uniformly (*e.g.* Graphene oxide and PEDOT:PSS aqueous solution). As shown in Figure 2.2 b, an rGO and PEDOT:PSS can be dispersed in water after bath sonication. It was used in a 100% intensity for 30 min. Varying sonication times and amplitude were used for different materials.

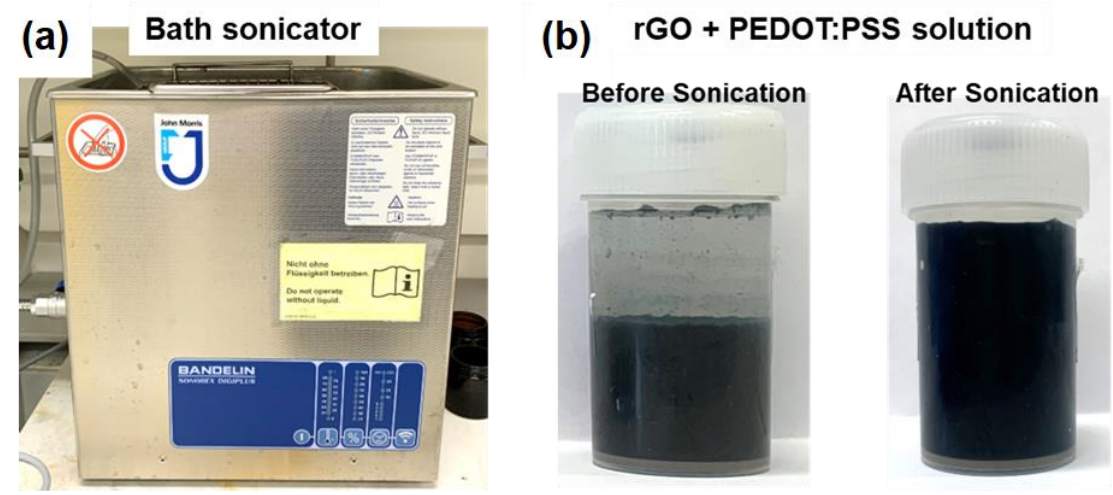


Figure 2.2 (a) Photographs of John Morris DL 514 BH ultrasonic bath, (b) sonicated rGO + PEDOT:PSS dispersion.

### 2.2.3 Plasma treatment

Plasma treatment is one of the most widely utilized techniques to modify surfaces to have a strong attraction to water [1]. It was used in this work to increase the hydrophilicity of polyester substrate, in which the ink material can penetrate and be absorbed well by the polyester fibre. It was conducted by a Harrick Plasma Cleaner PDC-32G-2 and Plasmaflo PDC-FMG (Figure 2.3 a) with a process pressure 0.75 Pa and a deposited time of 30 mins. As shown in Figure 2.3 b&c, the plasma treatment effectively increased the hydrophilicity of polyester fiber. The contact angle between polyester fibres and PEDOT:PSS aqueous ink decreased from 45.8$^{o}$ to spreading after plasma treatment, indicating that the oxygen plasma greatly increased the wettability of polyester fibres.

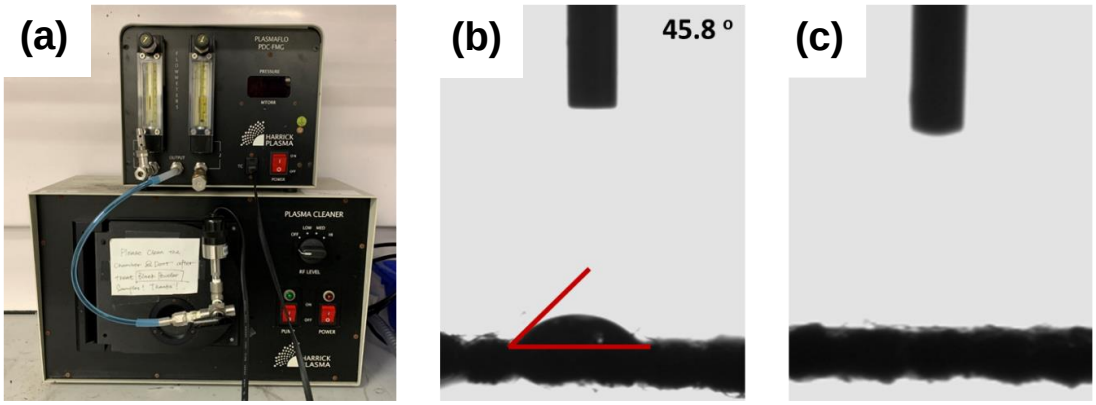


Figure 2.3 (a) Photographs of Plasma Cleaner PDC-32G-2 and Plasmaflo PDC-FMG. Photographs of 20 mg/mL PEDOT:PSS aqueous solution dropped on the polyester fiber before (b) and after (c) hydrophilic treatment.

### 2.2.4 Freeze-dry

Freeze-dry technique was used to remove the water contained in hydrogels, which was performed using Martin Christ Alpha 1-4 LSCbasic (Figure 2.4 a). As shown in Figure 2.4 b&c, the PAM hydrogel shirked after the freeze-drying. Compared with the air drying, the freeze-drying technique would maintain the skeleton 3D network structure of hydrogels. The freeze-dried sample was sputter-coated with a 5 nm layer of platinum. After that, the surface structure was characterized by the scanning electron microscope (JSM-7500FA, JEOL, Tokyo, Japan)

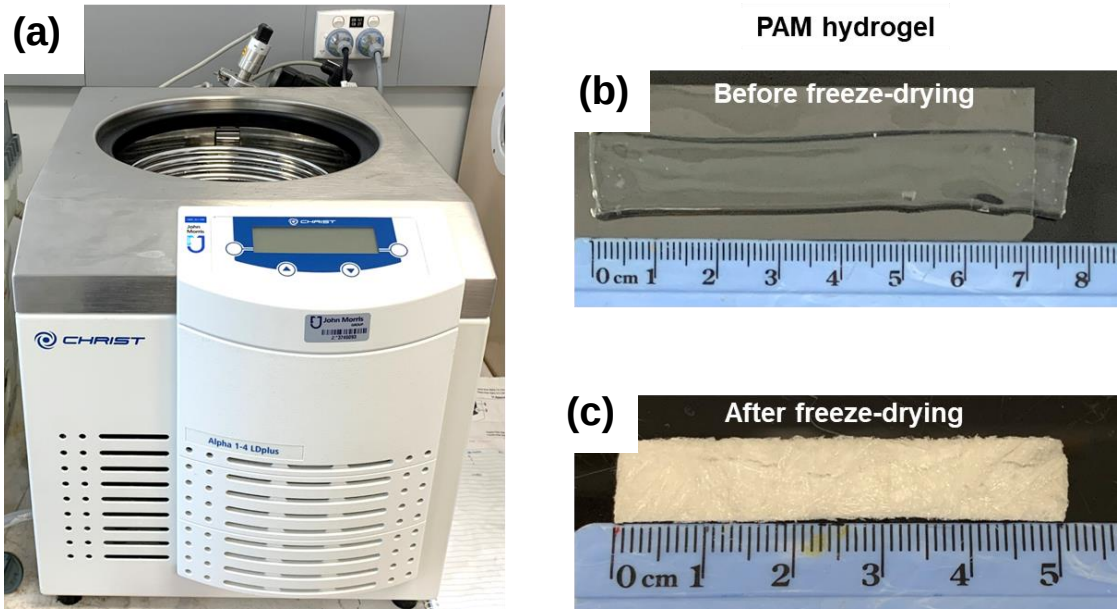


Figure 2.4 (a) Photograph of the freeze-drier Martin Christ Alpha 1-4 LSCbasic, PAM hydrogel before (b) and after (c) freeze-drying.

## 2.3 Physical characterization techniques

### 2.3.1 Scanning electron microscopy (SEM)

A scanning electron microscope (SEM) is a surface imaging method in which an incoming electron beam travels over the sample surface and interacts with it to produce backscattered and secondary electrons, which are then utilised to form a picture of the sample [2]. In this work, A JEOL JSM-7500FA field emission SEM (Figure 2.5 a) was used to observe the 3D network structure of hydrogels and textile electrodes. Freeze-dried hydrogel samples were sputter-coated with a 5 nm layer of platinum. Samples were mounted to the sample holder using conductive carbon tape and silver for observation. After that, the surface structure was characterized by the SEM an

acceleration voltage of 5 KV, emission current of 10 milliampere (mA) and the working distance of 8 mm. As shown in the Figure 2.5 b is a SEM image of PAM hydrogel porous 3D network structure.

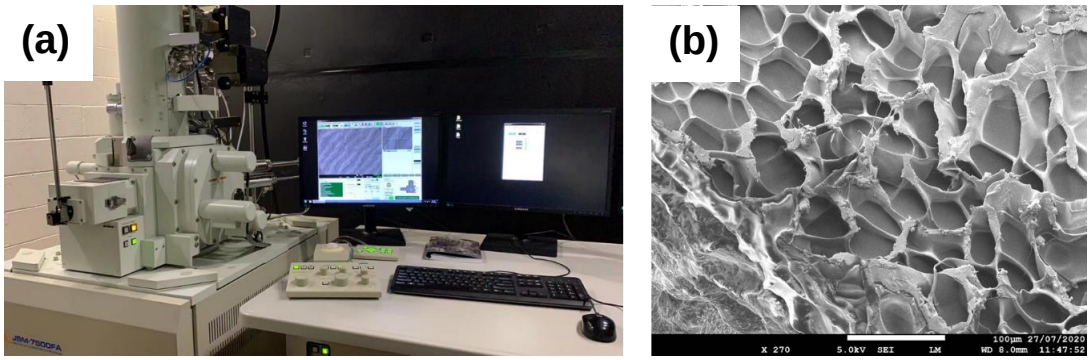


Figure 2.5 (a) Photograph of JEOL-7500FA field emission gun scanning electron microscope (SEM) and (b) SEM image of PAM hydrogel.

### 2.3.2 Ultraviolet-visible spectroscopy (UVs)

UV-Vis spectroscopy is a wildly used identification and quantification technique that detected the absorbance spectra of compounds at specific wavelengths of ultra violet or visible light [3]. In this work, the presentence of redox couple was analyzed by the Shimadzu UV-3600 Spectrophotometer (Figure 2.6 a) and UV probe 2.52 software. Figure 2.6 b shows the UV-Vis spectre of individual $Fe(CN)_6^{4-}$ and $Fe(CN)_6^{3-}$ aqueous solution, and the mixed redox couple aqueous solution.

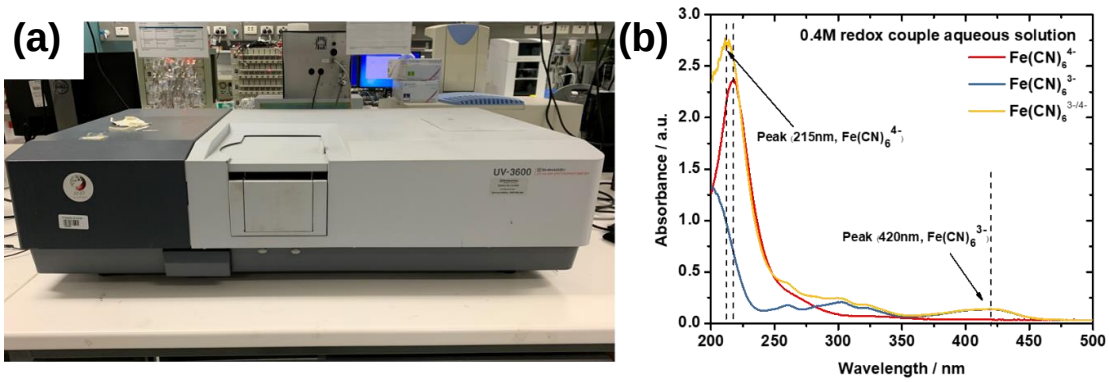


Figure 2.6 (a) Photograph of the Shimadzu UV-3600 spectrophotometer, and (b) the UV-Vis spectrum of $K_{3/4}[Fe(CN)_6]$ redox couple aqueous solution.

### 2.3.3 Raman spectroscopy

Raman spectroscopy is a technique that can provide information about the structure of molecules, and quantitative and qualitative analysis of the individual compounds [4]. In this work, Raman spectroscopy was utilized to analyse the existence of chemical bonds in the 3D network bonds of polyacrylamide hydrogel. It was carried out on a Jobin-Yvon Horiba 800 using a 632.81 nm laser (Figure 2.7 a) and Labspec V.5.45.09 software. Shown in Figure 2.7 b is the Raman spectrum of the freeze-dried polyacrylamide hydrogel and the signature peaks for chemical bonds were detected.

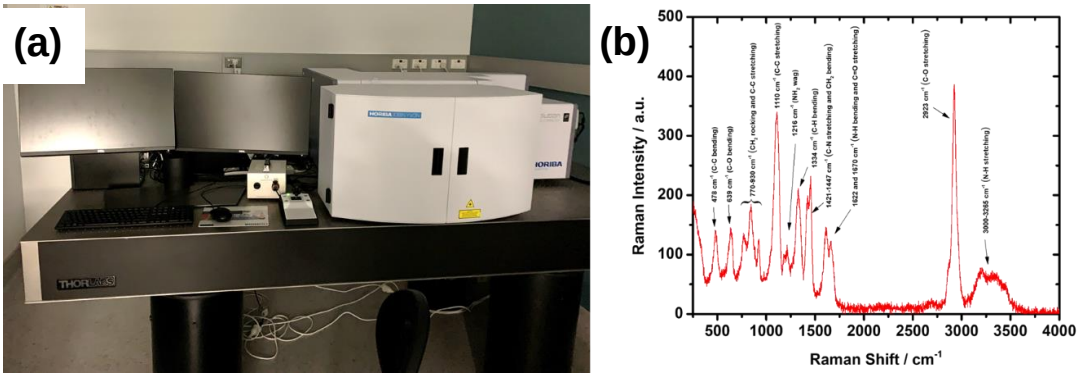

Figure 2.7 (a) Photograph of Raman spectroscopy apparatus, Jobin-Yvon Horbia 800 and (b) Raman spectrum of PAM hydrogel.

### 2.3.4 Thermal conductivity

Thermal conductivity (*k*) is a parameter to evaluate the ability of a material to conduct heat [5]. In this work, thermal conductivity of gel electrolytes directly influenced the temperature differences between electrodes and the open circuit voltage of thermocells. The thermal conductivity of hydrogel samples (20 mm diameter; 5 mm thickness) was measured by TCI Thermal conductivity analyser (TCI-2-A, Figure 2.8 a) and each measurement was repeated five times to calculate an average value. As shown in Figure 2.8 b, the thermal conductivity measurement of the PAM gel with and without redox couple and AM aqueous solution demonstrated that the *k* increased after the crosslinking.

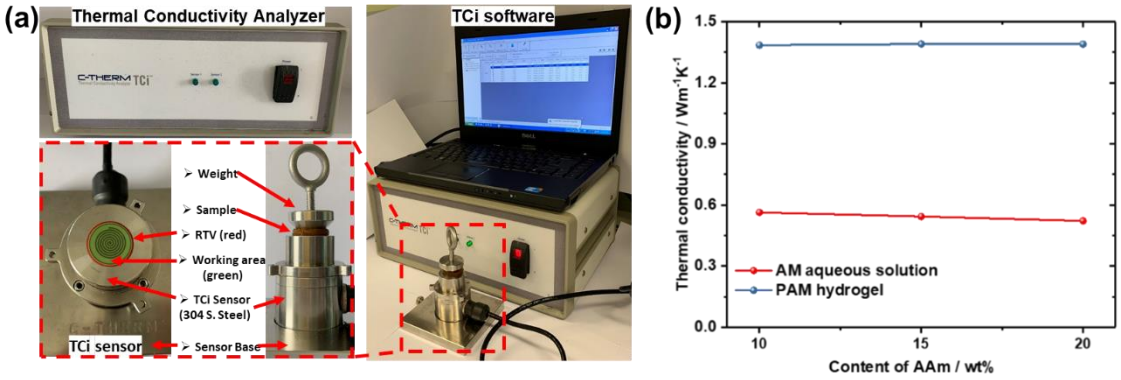


Figure 2.8 (a) Photographs of TCI Thermal conductivity analyser and the setup for gel electrolytes, and (b) the thermal conductivity of AM aqueous solution, PAM gel with and without redox couple.

### 2.3.5 Mechanical properties

The mechanical properties of gel electrolytes are essential because the deformation of wearable devices caused by human activities such as stretching, and twisting is common in practical applications. Therefore, the Shimadzu EZ mechanical tester (Figure 2.9 a) was used to measure the stress-strain curve in this work. Hydrogel samples were tailored in a rectangle shape (50 mm in length, 10 mm in width and 2 mm in thickness) in a tensile test with a 10 N load cell and a tensile speed of 25 mm $min^{-1}$. In a compressed test, the hydrogel samples were prepared in cylinder size. The PAM gel electrolyte was undergoing tensile testing (Figure 2.9 b). Shown in Figure 2.9 c is the strain-stress curve of the 5 wt% PVA-1 M $FeCl_{2/3}$ gel electrolyte in the presence and absence of HCl supporting electrolytes.

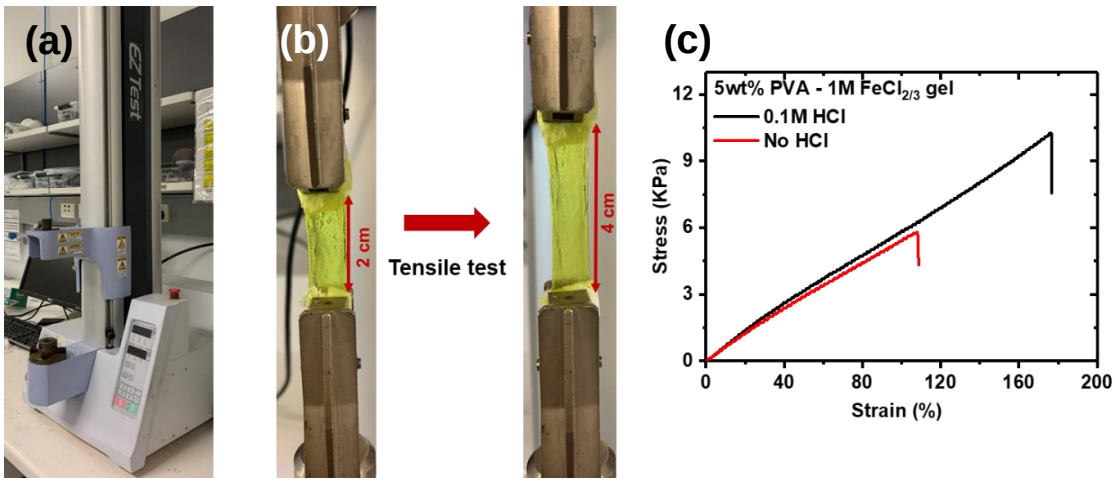


Figure 2.9 (a) Photograph of the Shimadzu EZ mechanical tester, (b) the PAM gel electrolytes before and after strain and (c) the strain-stress curves of PVA-$FeCl_{2/3}$ gel electrolyte with and without HCl supporting electrolytes.

### 2.3.6 Swelling ratio

In this work, the swelling ratio represents the ability of the hydrogel to absorb redox couples. The original weight ($W$) of hydrogels (L × W × T: 10 × 10 × 2 mm) was recorded, then the gels were swollen by immersion in a sufficient volume of the redox couple aqueous solution until swelling equilibrium was reached. Swollen hydrogels ($W_0$) were measured after gently removing the hydrogel from the solution at different time points (and drying the excess surface solution of the gels by tissue). The swelling ratio ($Q$) - reported as the average of three samples was calculated as $Q = W/W_0 \times 100\%$ [6].

## 2.4 Electrochemical analysis techniques

Electrochemical performances of gel electrolytes and fabricated thermocell devices were investigated by the following techniques including cyclic voltammetry (CV), electrochemical impedance spectroscopy (EIS), diffusion coefficient ($D$), open-circuit voltage ($V_{oc}$), linear sweep voltammetry (LSV), and chronoamperometry (CA) in either a three-electrode or two electrode set-up. All electrochemical activities measurements including CV and EIS were performed in a three-electrode system using thin-film platinum electrodes (ED-SE1-Pt, Micrux) where platinum was used as both the reference and counter electrodes. Gelled electrolyte samples were sliced into 2 x 2 x 2 mm cubes for positioning on top of the three Pt electrode setup (Figure 2.10 a). The platform of thin-film platinum electrodes was connected to the potentiostat by the miniUSB–type connector and a universal cable (Figure 2.10 b & c). The data was collected through a VSP potentiostat (Bio-logic) (Figure 2.11) and EC-lab software (11.21).

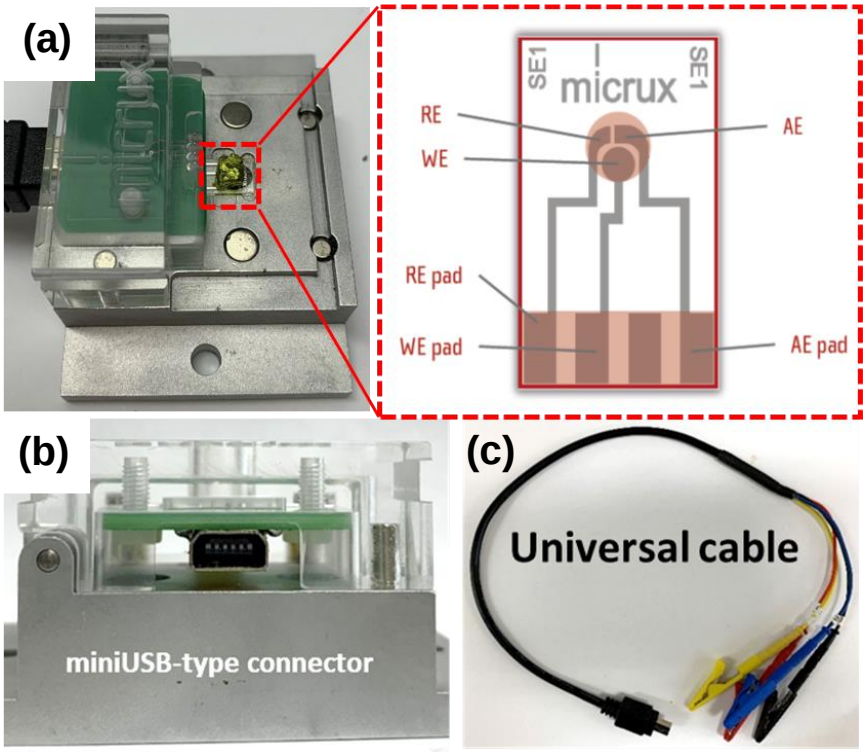


Figure 2.10 (a) The setup of the electrochemical activities measurements of gel electrolyte, (b) the connection of the platform of thin-film electrode, and (c) the universal cable for connection.

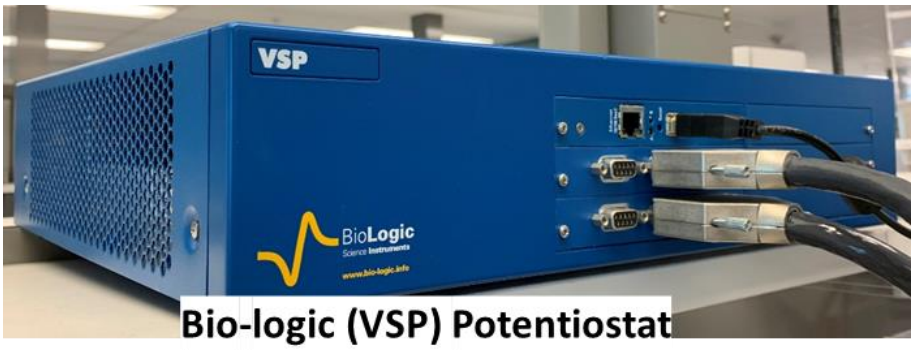


Figure 2.11 The photograph of Bio-logic VSP potentiostat.

### 2.4.1 Cyclic voltammetry (CV)

Cyclic voltammetry (CV) is the most widely used technique for acquiring qualitative information about electrochemical reactions, which provides information on the redox processes, heterogeneous electron-transfer reactions and absorption processes. CV consists of scanning linearly the potential of a stationary working electrode using a triangular potential waveform, the current resulting from electrochemical reactions [7]. In this work, the CV technique is used for investigating the redox potential and the reversibility of the electroactive species in gel electrolytes. CV curves of PVA-$FeCl_{2/3}$ gel electrolyte with and without HCl supporting electrolytes were measured by the VSP potentiostat (Bio-logic) from -0.5 V to +0.5 V at scan rates 50 mV $s^{-1}$ (Figure 2.12 a).

Moreover, the peak current in the CV test also determined the diffusion coefficient ($D$) that reflected the redox ions transfer between two electrodes within gel electrolyte system, which is calculated based upon the Randles-Sevcik equation at 25 $^{o}$C.

$$ip = (2.69 \times 10^{5}) n^{\frac{3}{2}} A D^{\frac{1}{2}} C v^{\frac{1}{2}}$$

Where $ip$ is the peak current in the CV measurement, $n$ is the number of electrons, $A$ is the electrode surface area, $C$ is the redox couple concentration, $v$ is the scan rate and $D$ is the electrolyte diffusion coefficient. The $D$ of redox species can be qualitatively analysed under the same system. The linear relationship of peak currents versus square root of scan rates (10 - 100 mV $s^{-1}$) is shown in Figure 2.12 b.

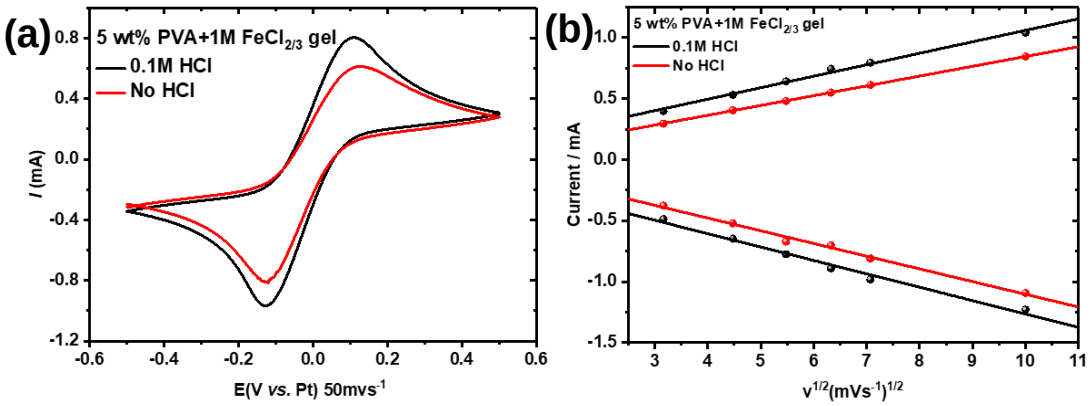


Figure 2.12 The electrochemical activities of PVA-$FeCl_{2/3}$ gel electrolyte with and without HCl supporting electrolytes in terms of (a) the CV curves and (b) the linear relationship of peak currents versus square root of scan rates (10 - 100 mV $s^{-1}$).

### 2.4.2 Electrochemical impedance spectroscopy (EIS)

Electrochemical impedance spectroscopy (EIS) experiments perform impedance measurements in applying an AC potential to an electrochemical cell and then measuring the current through the cell [8]. In this work, the EIS reveals the ohmic resistance and charge transfer resistance of gel electrolytes in the three-electrode system, which was obtained by the VSP potentiostat (Bio-logic) in triplicate at the equilibrium potential using a frequency range of 1000 kHz to 10 mHz and an amplitude of 10 mV. Furthermore, EIS is an electrochemical activities performance test for analysing the ohmic overpotential and charge transfer resistance. As shown in Figure 2.13, Nyquist plots of the comparison of PVA-$FeCl_{2/3}$ gel electrolyte and $FeCl_{2/3}$ aqueous solution.

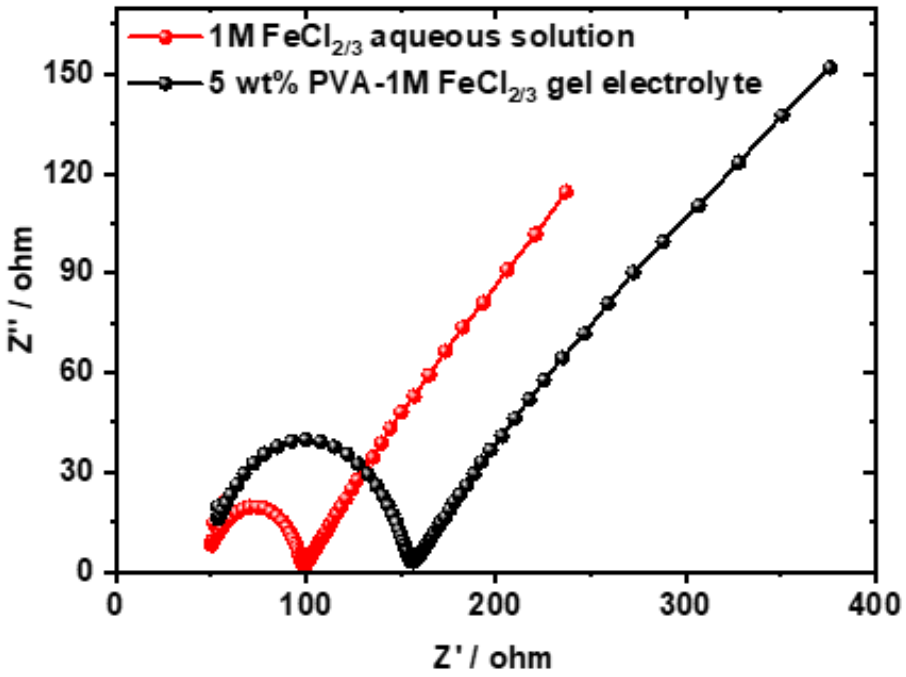


Figure 2.13 A comparison between $FeCl_{2/3}$ aqueous (concentration: 1 M) and PVA-$FeCl_{2/3}$ gel electrolyte (PVA content: 5 wt.%, $FeCl_{2/3}$ concentration: 1 M) in terms of electrochemical impedance spectra.

### 2.4.3 Open-circuit voltage ($V_{oc}$)

The open circuit voltage ($V_{oc}$) is the maximum voltage available from the thermocells when no potential or current is applied to the circuit [9]. The $V_{oc}$ of thermocells is greatly determined by multiple parameters (the type of redox couple, electrode materials, the thickness of thermocells, thermal conductivity), which directly reflects the Seebeck coefficient ($S_e$) based on the equation $S_e = V_{oc}/\Delta T$, and the increase of $V_{oc}$ theoretically promotes the current output and power output of thermocells, therefore, a higher $V_{oc}$ when maintaining the temperature gradient ($\Delta T$) is pursued in this work. The $V_{oc}$ is measured for 10 mins until the stable condition property of thermocells. As shown in Figure 2.14, The $V_{oc}$ of PVA-$FeCl_{2/3}$ gel electrolyte under varied $\Delta T$.

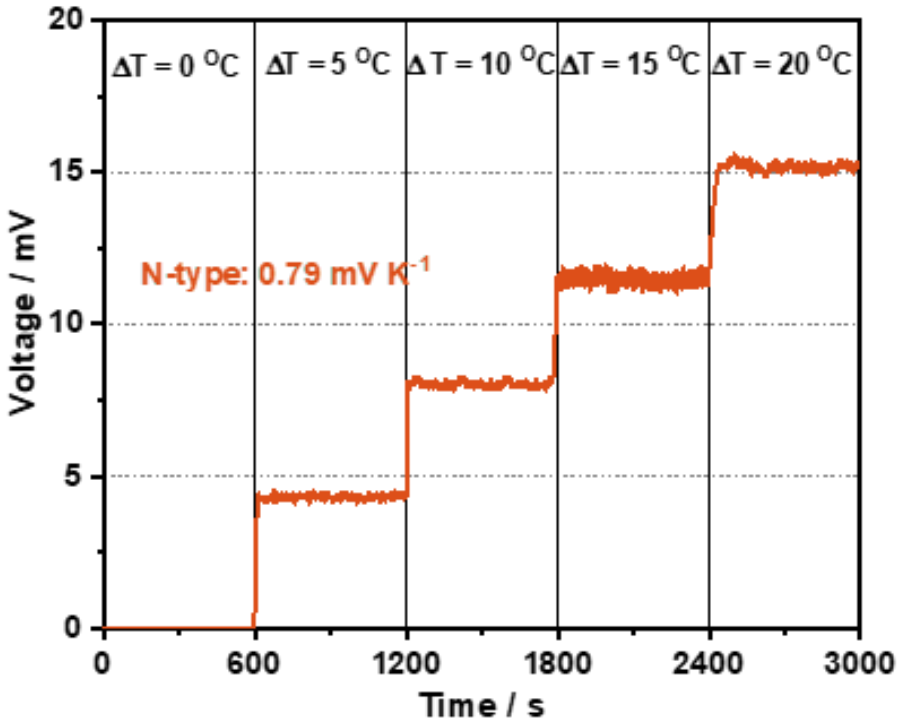


Figure 2.14 The $V_{oc}$ of PVA-$FeCl_{2/3}$ gel electrolyte under varied ΔT.

### 2.4.4 Linear sweep voltammetry (LSV)

The linear sweep voltammetry technique is a standard electrochemical method for measuring current, where the potential was applied between the working electrode and a reference electrode is swept linearly in time [10]. Unlike the CV, no backward scan is done, only the forward scan is applied. The LSV technique used in this work is targeted to measure the short-term current density of thermocells that are consisted of various gel electrolytes and electrodes. As shown in Figure 2.15, LSV plots of 1 M $FeCl_{2/3}$ aqueous solution.

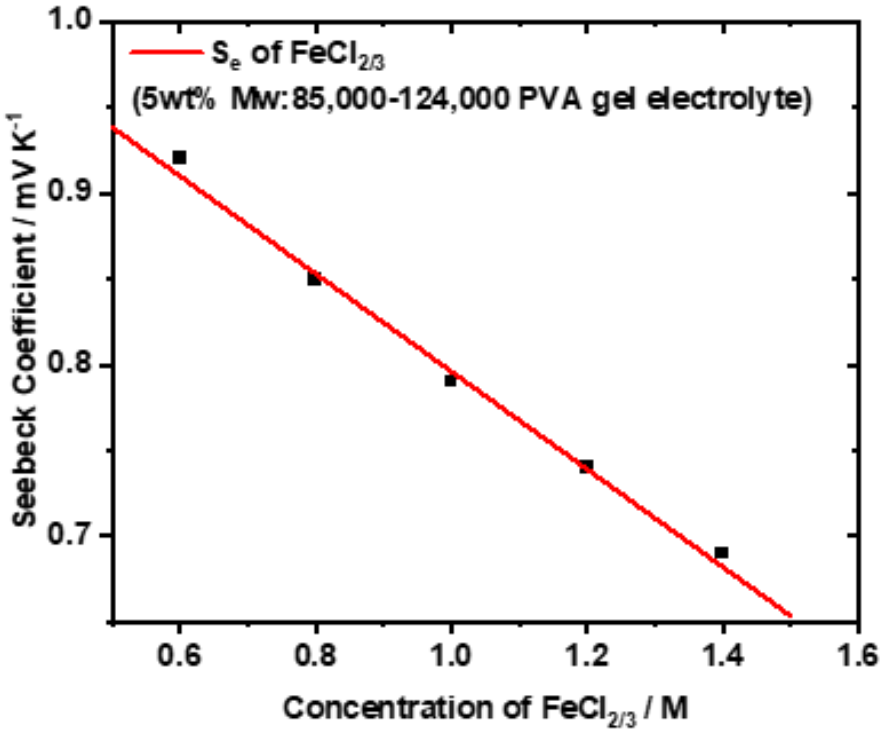


Figure 2.15 LSV plots of 1 M $FeCl_{2/3}$ aqueous solution.

### 2.4.5 Chronoamperometry (CA)

Chronoamperometry is a technique of square-wave potential applied to the working electrode depending on the time [11]. Chronoamperometry involves stepping the potential of the working electrode from an initial potential, at which (generally) no faradic reaction occurs, to a potential Ei at which the faradic reaction occurs. The external potential applied in thermocells is employed as the electrical components in the realistic circuit. The constant potential method was employed to measure the current-potential relationship $(I - V)$ [12]. Firstly, the open-circuit voltage ($V_{oc}$) was recorded for 600s until values stabilize and the averaged data of last 300 s was used. Then, the $V_{oc}$ was divided into 5 segments: $V_{oc}$ ($I$ = 0 A), $0.75V_{oc}$, $0.5V_{oc}$, $0.25V_{oc}$, $0V_{oc}$ ($I = J_{sc}$, short-circuit current density), and the current was measured at each potential for 600 s with

the final averaged 300 s data was recorded as the current density ($J$). Lastly, power density ($P$) was calculated by the $P = JV$[3]. The stability tests to study the long-term performance of the paired N- and P-type thermocells were conducted for 12 h, and the $j_{sc}$ and $V_{oc}$ were recorded every 30 mins. As shown in Figure 2.16, thermo-electrochemical performance of 5 wt.% PVA - 1 M $FeCl_{2/3}$ gel electrolyte.

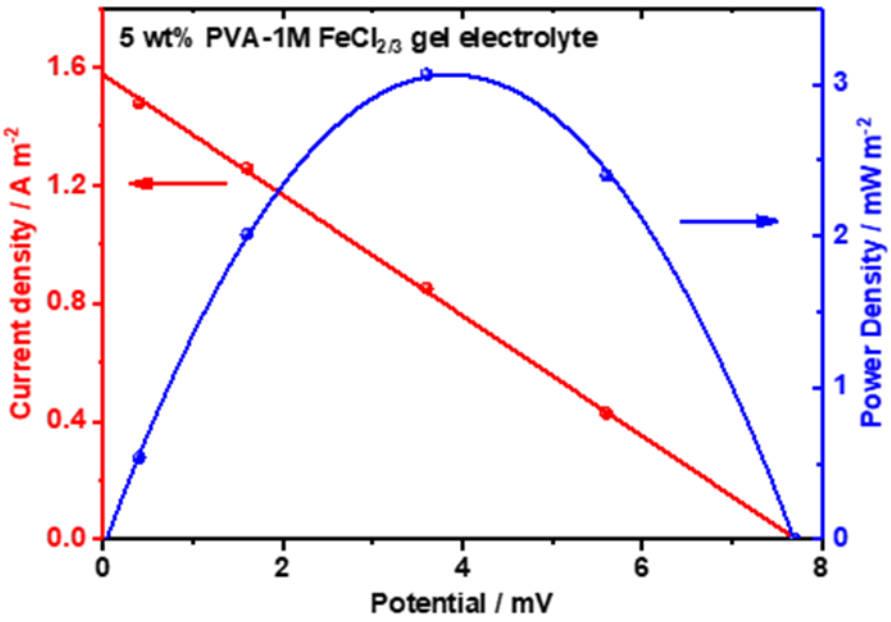


Figure 2.16 Thermo-electrochemical performance of 5 wt.% PVA - 1 M $FeCl_{2/3}$ gel electrolyte: current and power versus voltage.

## 2.5 Preparation of gel electrolytes and electrodes

### 2.5.1 Synthesis of PVA-$FeCl_{2/3}$ hydrogel electrolytes

Initially, $FeCl_2 \cdot 4H_2O$ and $FeCl_3$ powder were added to pre-prepared PVA aqueous solution (3, 5, 8, and 10 wt.%) with magnetic stirring until dissolved thoroughly (0.1, 0.2, 0.5, 1, or 2 M $FeCl_{2/3}$). Next, 5 wt.% GA aqueous solution (mass ratio PVA:GA =

40:1) was added (as the cross-linker) into the above solutions while stirring and immediately dropped into a PDMS mould or thermocell device and allowed to crosslink at room temperature for 1 h. The resulting gelled electrolyte can be peeled off ready to use. For performance enhancement, HCl (hydrochloric acid solution 32%), $H_3PO_4$ (phosphoric acid) and KCl (potassium chloride) as supporting electrolyte with the final concentration varying from 0.02 to 0.3 M was added into the PVA-$FeCl_{2/3}$ solutions before the addition of chemical cross-linker (GA).

### 2.5.2 Synthesis of porous structure PAM gel electrolytes

Initially, varied amounts of AM (10, 15, 20 wt.%), MBA (0.1 wt.%) and NaAc (saturated solubility at each temperature) were added into 10 mL of deionised water with a magnetic stirrer (250 rpm). These reagents were added at different temperatures (either 60, 70, 80 or 90 ℃) for 10 minutes until completely dissolved. Then, APS (5 wt.%) was immediately blended into the solution and stirred vigorously for 10 s (1000 rpm). The supersaturated NaAc precursor solution is obtained and cools down to room temperature without disturbance. Needle-like NaAc crystallization generates from the solution surface and further extends to the bottom after dropping NaAc crystal seed. The polymerization process occurs surrounding NaAc crystallization under ambient conditions for 24 hours. Consequently, gels were soaked in deionised water for 24 hours, replacing the original synthetic solution with deionised water, this process was repeated five times until the NaAc crystallization was removed. Finally, porous gels were freeze dried (Scientz-10N, China) for two days and ready to use for p- and n-type cells. The p-type gelled electrolyte was made *via* immersing freeze-dried porous gel into 0.4 M $K_3Fe(CN)_6/K_4Fe(CN)_6$ (mole ratio 1:1) containing varying concentrations of

guanidinium chloride (GdmCl) (0.1 - 0.5 M) for 48 hours at 35 ℃ (simulation of average surface skin temperature), and n-type gelled electrolyte was produced in the identical process except replacing the $K_{3/4}Fe(CN)_6$-GdmCl electrolyte with 1 M $FeCl_2/FeCl_3$ (mole ratio 1:1) - 0.08 M HCl aqueous solution [4]. The porous PAM gel electrolyte was obtained by the same process except that there is no freeze-drying treatment. As a comparison, the non-porous gel electrolyte was prepared by the following method: varied amount AM (10, 15, 20 wt.%), MBA (0.1 wt.%) and APS (5 wt.%) were added into 10 mL deionised water with a magnetic stirrer (250 rpm), until a homogeneous solution was formed. The precursor solution was placed in a 50 ℃ oven for 4 hours. Finally, the hydrogel was soaked in identical aqueous solution containing the redox couple as above for 48 hours, to obtain the final, non-porous gel.

### 2.5.3 Synthesis of double-network CMCs:PAM gel electrolytes

Initially, varied contents (5 wt.% - 20 wt.%) and the weight ratio of AM and CMCs (1:2 - 1:5) were added to 5 mL of deionised water. Then, 5 mg MBA was blended into above solution with a magnetic stirrer (250 rpm) until a homogeneous solution was obtained. Next, 100 μl GA aqueous solution (1.25%) and 100 μl APS aqueous solution (50 wt.%) was added to the above solution by sequence and immediately transferred into the PDMS mold (L × W × T: 50 × 10 × 2 mm) after shaking with a vortex mixer for 10 s. The precursor solution was placed in an oven (50 ℃) for 4 h for the first crosslinking. After that, the semi-finished hydrogel was immersed in 20 mL mixed aqueous solution (2.5 g AM, 3.08 mg APS and 60 mg MBA) for 24 h, subsequently, the soaked gel was sealed in a container and underwent the second crosslinking (50 ℃ oven, 4 h). Finally, the double-network gel was ready to immersed in redox couple aqueous solution (P-

type: 0.4 M [$K_3Fe(CN)_6$] and 0.4 M $K_4Fe(CN)_6 \cdot 3H_2O$; N-type: 1 M $FeCl_2$, 1 M $FeCl_3$ and 0.08 M HCl) for 48 h to prepare gel electrolytes.

### 2.5.4 Preparation of platinum electrode (Pt electrode)

The Kapton tape is electrical insulation and flexible material, meanwhile remaining stable across a wide range of temperatures [13]. Pt electrodes that were prepared through the sputter coating 200 nm Pt on the Kapton tape were employed for the measurement of thermal-electrochemical performance and the interconnection of multiple arrays of N-P cells connected in series (Figure 2.17).

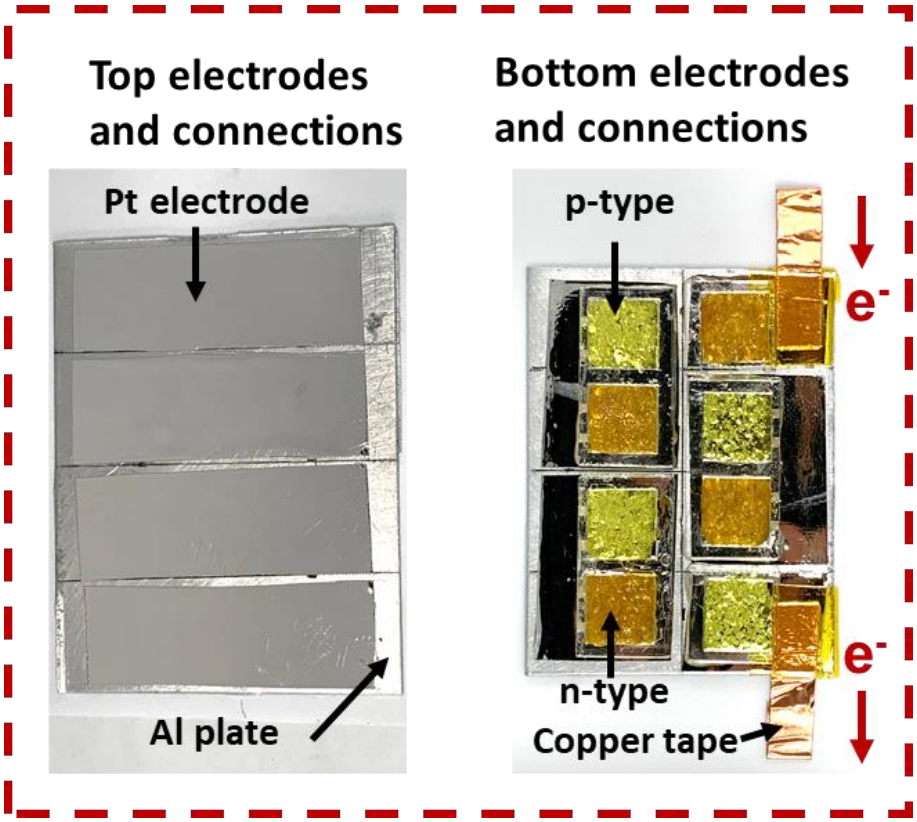


Figure 2.17 Photographs of 4 pairs N-P cells connected in series by Pt electrodes for the thermo-electrochemical test.

### 2.5.5 Preparation of textile electrode (specified to Chapter 5)

The elastic polyester fabric was used as a host of textile electrodes (10 cm × 5 cm) and hydrophilized by plasma treatment 30 min on each side. The elastic polyester fabric was used as a host of textile electrodes, was tailored in 50 mm × 20 mm rectangle and processed by plasma treatment for 10 min (Figure 2.18 a). The varied concentration of PEDOT:PSS (10 mg/mL – 100 mg/mL) and DEG (fixed ratio: 100 mg PEDOT:PSS in 166 µl DEG) was dissolved in 20 ml DI water, then the mixed materials were blended by a magnetic stir to form a uniform slurry. Hydrophilic polyester fabrics were immersed into PEDOT:PSS aqueous solution for 1 h (Figure 2.18 b) and dried in an oven (50 $^{o}$C, 1 h) with hanging to guarantee the uniform coating of PEDOT:PSS on both sides of polyester (Figure 2.18 c). This process was repeated 1 - 6 times and then the textile electrode was tailored to a suitable size to integrate with gel electrolytes.


Figure 2.18 Illustration of the fabrication of the textile electrodes.

## 2.6 Device fabrication

In this work, the temperature was controlled by TEC temperature Controller-1091 (Meerstetter Engineering GmbH, Switzerland) and TEC software V3.10. Kapton tape with 200 nm sputter-coated Pt (Pt-Kt) was used as both electrodes.

### 2.6.1 Device assembly with PVA-$FeCl_{2/3}$ gel electrolytes (specified to Chapter 3)

N-type thermocells connected in parallel was prepared in this work. The acrylic framework (10 × 10 × 2 mm) and Pt electrodes were assembled using epoxy glue (dashed area in Figure 2.19 a). The framework was used to maintain the size and shape of the gelled electrolyte during the curing process. The precursor solution was then injected into the frame from the top holes and left to crosslink. The thermocell device was placed between the hot and cold electrodes to provide a temperature gradient (Figure 2.19 b).

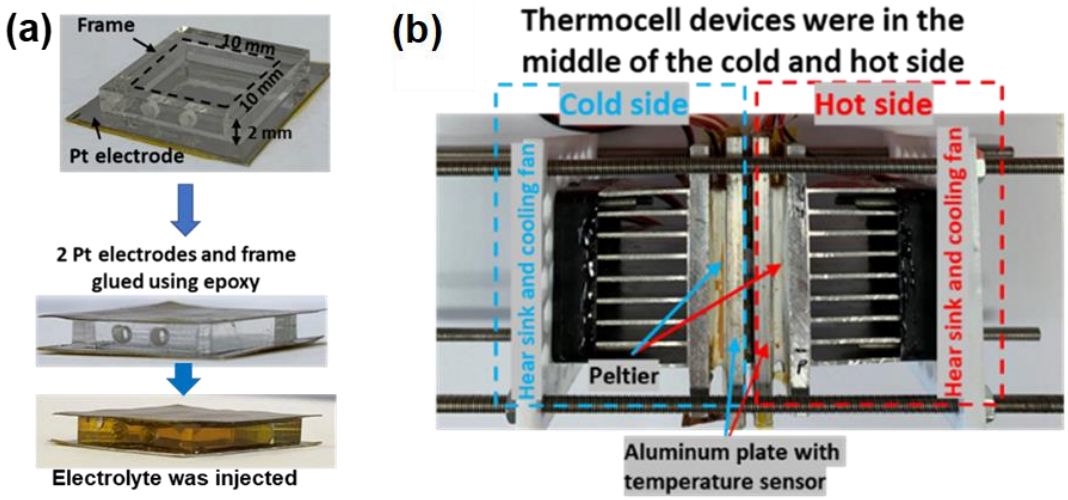


Figure 2.19 (a) An illustration of the fabrication of thermocell devices, (b) photograph of the temperature controller setup.

### 2.6.2 Device assembly with porous structure gel electrolytes (specified to Chapter 4)

The framework was made of Poly (methyl methacrylate) (PMMA) with a 10 x 10 mm cell size and an inter-electrodes distance of 2 mm. The gel electrolyte was tailored to 10

× 10 × 2.1 mm (L × W × T) to guarantee solid contact between electrodes and gel electrolytes (Figure 2.20). Thermocells were placed in the middle of two Peltier devices (hot and cold side). During the test, the cell model was vertically oriented (cold side: top; hot side: bottom), and the hot electrode ($T_h$) and the cold electrode ($T_c$) were varied in the range of 15 ℃ - 55 ℃.

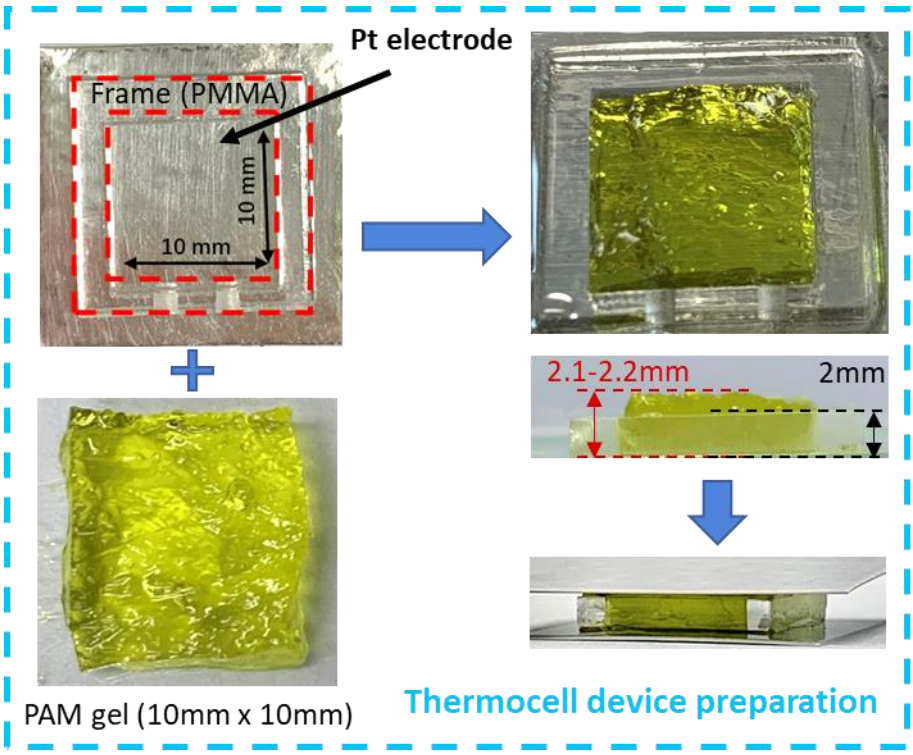


Figure 2.20 An illustration of the fabrication of thermocell devices.

### 2.6.3 Device assembly with stretchable double-network gel electrolytes (specified to Chapter 5)

Once gel electrolytes and textile electrodes had been optimized, the thermocell was taken to the thermo-electrochemical performance analysis and the fabrication process is illustrated in Figure 2.21 The thermocell prepared with textile electrodes was tailored

into 1 × 1 cm square and assembled with Pt electrodes. Two acrylic frameworks (1 - 4 mm thickness) were placed at the side of thermocells to control the distance of electrodes. The thermocell device was then placed between the hot and cold Peltier instruments to provide a temperature gradient. For the thermocell without textile electrodes, all procedures are similar except for the thermocell was replaced by the gel electrolyte. For simulating the working situation of the wearable device, the hot electrode stayed at 35 ℃ as the temperature of human skin, while the cold electrode was set from 15 ℃ - 30 ℃ as the changing ambient environmental temperature.

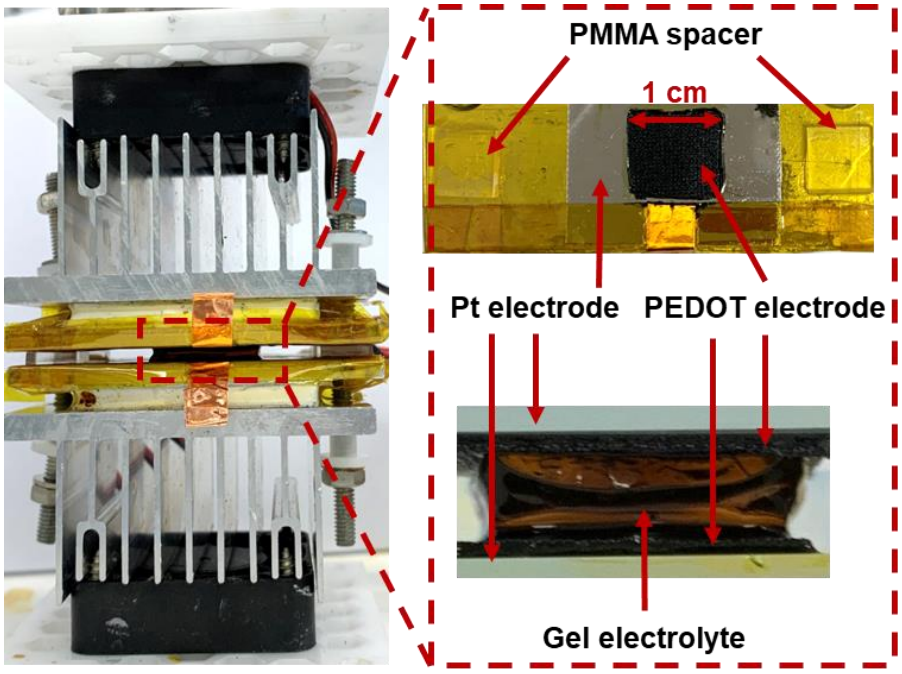


Figure 2.21 An illustration of the temperature control setup and fabrication of the thermocell devices.

## 2.7 Reference

[1] “What is Oxygen Plasma” from https://www.thierry-corp.com/plasma-knowledgebase/hydrophilic-treatment

[2] Z. Ji, Sci. Bull. 2016, 61, 755.

[3] "What is Ultraviolet–visible spectroscopy " from https://en.wikipedia.org/wiki/Ultraviolet%E2%80%93visible_spectroscopy

[4] “What is Raman Spectroscopy?” from http://www.inphotonics.com/raman.htm.

[5] “What is Thermal conductivity?” from https://en.wikipedia.org/wiki/Thermal_conductivity

[6] H. Kamata, Y. Akagi, Y. Kayasuga-kariya, U. Chung, T. Sakai, Science. 2014, 343, 873.

[7] “What is Thermal conductivity?” from https://en.wikipedia.org/wiki/Cyclic_voltammetry

[8] “What is Electrochemical Impedance Spectroscopy?” from https://www.biologic.net/topics/what-is-eis/

[9] “What is Open Circuit Voltage?” from https://en.wikipedia.org/wiki/Open-circuit_voltage#:~:text=Open%2Dcircuit%20voltage%20(abbreviated%20as,current%20flows%20between%20the%20terminals

[10] “What is Linear sweep voltammetry?” from https://en.wikipedia.org/wiki/Linear_sweep_voltammetry

[11] “What is Chronoamperometry?” from https://en.wikipedia.org/wiki/Chronoamperometry

[12] M. A. Buckingham, L. Aldous, J. Electroanal. Chem. 2020, 872, 114280.

[13] “What is Kapton tape?” from https://en.wikipedia.org/wiki/Kapton

# Chapter 3 Advanced wearable thermocells based on PVA gel electrolytes

*This chapter is adapted from articles:*

*"The significance of supporting electrolyte on poly (vinyl alcohol)-iron(II)/iron(III) solid-state electrolytes for wearable thermo-electrochemical cells", by Yuetong Zhou , Yuqing Liu, Mark A. Buckingham, Shuai Zhang, Leigh Aldous, Stephen Beirne, Gordon Wallace and Jun Chen, that was published in Electrochemistry Communications (2021). Adapted with permission from Elsevier Publishing Group.*

*"Advanced Wearable Thermocells for Body Heat Harvesting", by Yuqing Liu, Shuai Zhang, Yuetong Zhou, Mark A. Buckingham, Leigh Aldous, Peter C. Sherrell, Gordon G. Wallace, Gregory Ryder, Shaikh Faisal, David L. Officer, Stephen Beirne, and Jun Chen, that was published in Advanced Energy Materials (2020). Adapted with permission from Wiley Publishing Group.*

## 3.1 Introduction

This research is driven by the rapid development of wearable devices, which require a reliable power supply. Gelled electrolytes have received significant attention as TECs due to avoiding leakage of electrolyte [1]. The polymer and redox couple need to provide suitable mechanical properties, as well as generate a suitable $S_e$ when a temperature gradient is applied, to act as a solid-state electrolyte.

The $FeCl_2$ and $FeCl_3$ are a commonly used redox couple in TECs [2]. Yang *et al.* reported the relatively high $S_e$ (+1.02 mV $K^{-1}$) for 0.1 M $FeCl_{2/3}$ [3]. Kim *et al.* reported a $S_e$ of +1.04 mV $K^{-1}$ for aqueous $FeCl_{2/3}$ [4]. Because of the hydrolysis effect, the aqueous solution of the redox couple is a strong acid (0.5 M $FeCl_{2/3}$, pH = 0.75) [4], thus, a polymer that can be crosslinked under acidic conditions is potentially optimal to host the gelled $FeCl_{2/3}$ electrolyte.

Poly(vinyl alcohol) (PVA) can be chemically cross-linked with glutaraldehyde (GA) under the acid catalysis (e.g. by inherently acidic solutes like $FeCl_2$ and $FeCl_3$). PVA has been widely used in supercapacitors, [5] lithium batteries [6] and fuel cells [7] due to good mechanical strength, non-toxicity of the components, cost-effectiveness of materials, good optical properties, high-temperature resistance and high hydrophilicity of the gel [8,9].

Solid-state electrolytes suffer from lower ionic conductivity due to poor ionic transport in the solid-state. Russo *et al.* employed an ionic liquid to increase ionic conductivity and thermo-electrochemical performance [10]. However, the ionic liquid reduced the mass transport and redox couple concentration due to the high viscosity, which leads to

fairly low thermo-electrochemical performances [10]. To resolve this problem, some researchers have widely employed supporting electrolytes to reduce the internal resistance of TECs by enhancing ionic strength, and thus reducing ohmic resistance within the thermocell, even when not directly interfering with redox reaction [10]. Buckingham *et al.* reported that the conjugate acid of iron salts can be used as supporting electrolyte to decrease the internal resistance and improve the thermo-electrochemical performance of a range of aqueous iron(II/III) redox couple thermocells [2]. Kim *et al.* has also reported that the internal resistance of $Fe^{2+/3+}$ TECs was decreased from 14.4 to 9.8 Ω after adding 1 M HCl [4]. Phosphoric acid ($H_3PO_4$) has been reported to significantly increase the ionic conductivity from $10^{-9}$ to $10^{-4}$ S $cm^{-1}$ of PVA based polymer electrolytes [11]. Hongyao *et al.* reported that ionic conductivity increases with the increasing KCl concentration and shows a linear relationship in the α-CD-$I_3^-/I^-$ system [12].

Here, we investigate the mechanical strength and thermo-electrochemical performance of PVA-$FeCl_{2/3}$ gel electrolyte with HCl, $H_3PO_4$ and KCl supporting electrolyte (hereafter named Fe-KCl, Fe-$H_3PO_4$ and Fe-HCl, respectively). For comparison, PVA-$FeCl_{2/3}$ gel electrolyte in the absence of any supporting electrolyte was also investigated as a "blank" equivalent. We also report thermo-electrochemical performance of the thermocells under various temperature gradients, and the ability to increase current output of these thermoelectrochemical cells by connecting the individual thermocells in parallel.

## 3.2 Experiment

### 3.2.1 Synthesis of PVA-$FeCl_{2/3}$ hydrogel electrolytes

The synthetic processes of PVA-$FeCl_{2/3}$ hydrogel electrolytes were described in Chapter 2.5.1

### 3.2.2 Preparation of platinum electrodes

The Pt electrode for the thermal-electrochemical performance and the paralleled device were described in Chapter 2.5.4

### 3.2.3 Device Assembly

The flexible wearable thermocell devices were assembled using the PVA-$FeCl_{2/3}$ gel electrolytes and Pt electrodes as described in Chapter 2.6.1

## 3.3 Results and Discussions

### 3.3.1 Investigation of the component of PVA-$FeCl_{2/3}$ gel electrolytes

GA is known to react with the hydroxyl functional groups of PVA chains to form acetal bonds under acidic catalysis (Figure 3.1 a) [13]. Figure 3.1 b shows that the gelled electrolytes were extremely twistable and stretchable, which can be rotated through 360 degrees three times and elongated to twice of their original length without any deformation or break. These robust mechanical properties of the gel electrolyte are important because it can endure deformations like twist and stretch during practical utilization when integrated into wearable devices.

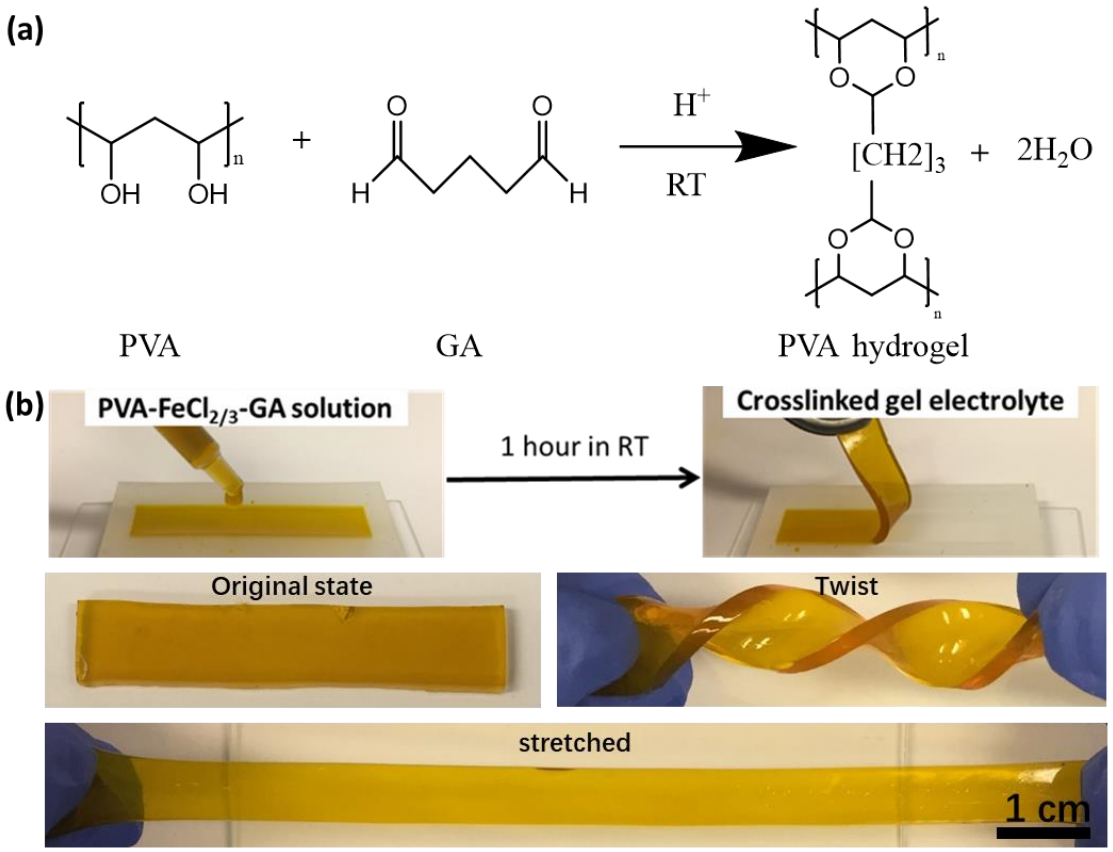


Figure 3.1 (a) The cross-linking mechanism of PVA by GA, (b) photographs of the stretchable gelled electrolyte.

*3.3.1.1 Molecule weight and concentration of PVA*

The molecular weight and concentration of PVA were investigated to achieve a trade-off between gel formation, mechanical properties, and TE performance. PVA with various molecular weights (31 - 50 kDa, 85- 124 kDa, 146 - 186 kDa) and concentrations from 3 wt.% to 8 wt.% can be used to form a homogeneous gel electrolyte (Figure 3.2 a and Figure 3.2 c). The gels produced using PVA molecular weights >85 - 124 kDa and concentrations >5 wt.% exhibit elongation to over 100%

strain (Figure 3.2 b and Figure 3.2 d), and are suitable for use as stretchable components for wearable applications [10].

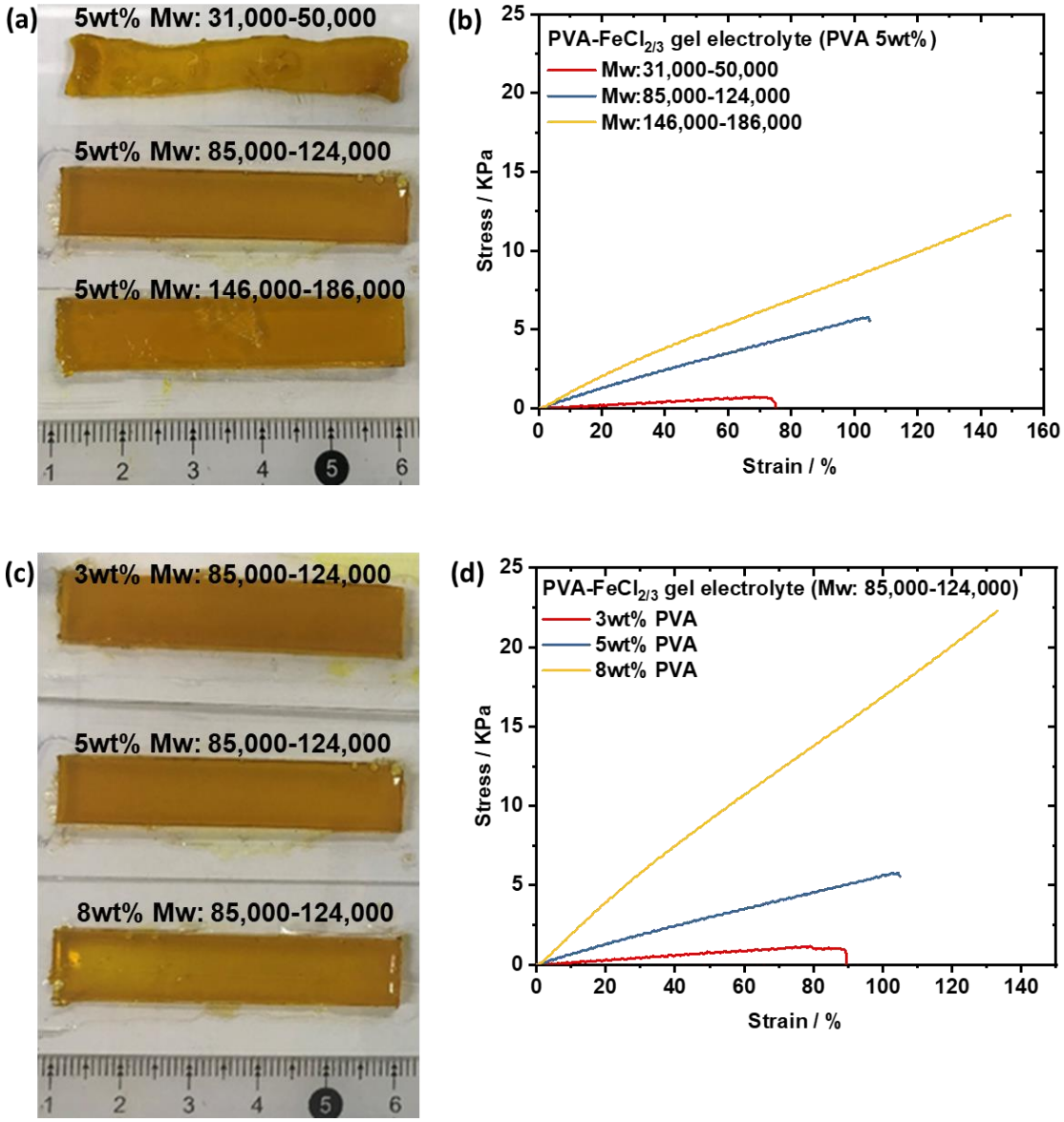


Figure 3.2 (a) Photographs and (b) strain and stress curves of PVA-$FeCl_{2/3}$ (PVA content: 5 wt.%, $FeCl_{2/3}$ concentration: 1 M) gel electrolyte with different molecular of 31,000 ~ 50,000, 85,000 ~ 124,000, 146,000 ~ 186,000. (c) Photographs and (d) strain and stress curves of PVA- $FeCl_{2/3}$ (PVA Mw: 85,000 ~ 124,000, $FeCl_{2/3}$ concentration: 1 M) gel electrolyte with different PVA content.

To limit the inhibition of ion diffusion and transfer by high molecular weight and densely packed PVA networks (Figure 3.3), the low PVA molecular weight and concentration with suitable elasticity (85 - 124 kDa, 5 wt.%) was selected for in depth study of thermo-cell performance.

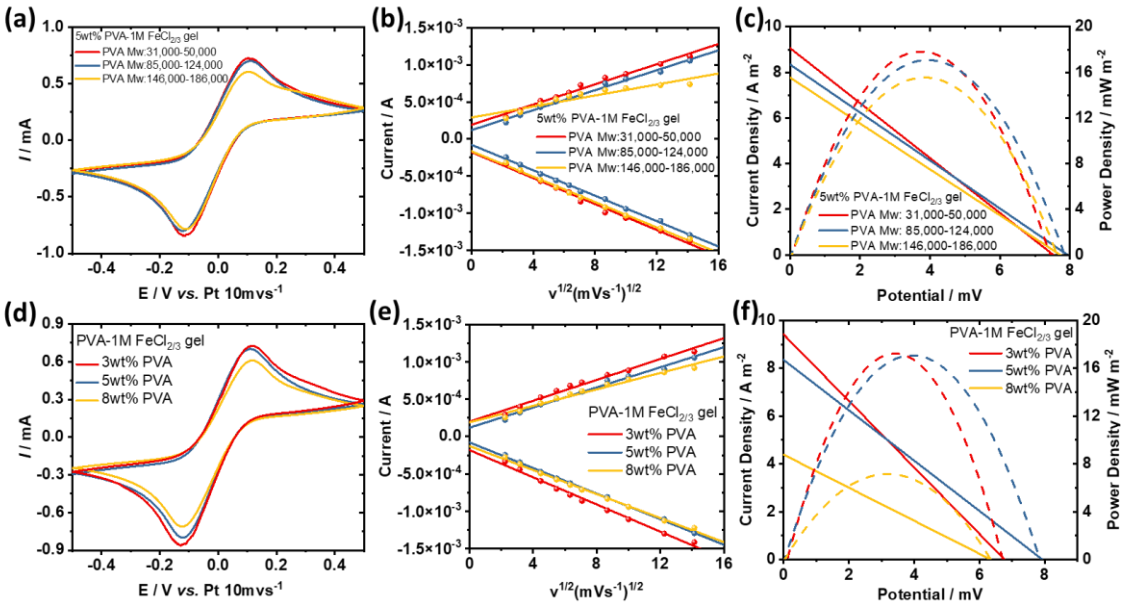


Figure 3.3 A comparison between PVA-$FeCl_{2/3}$ (PVA content: 5 wt.%, $FeCl_{2/3}$ concentration: 1 M) gel electrolyte with different molecular of 31,000 ~ 50,000, 85,000 ~ 124,000, 146,000 ~ 186,000. (a) CV at 50 mV $s^{-1}$, (b) peak current versus scan rate square-rooted, and (c) thermo-electrochemical performance ($\Delta T$ = 10 ℃): current (solid line) and power (dash line) vs voltage. A comparison between PVA - $FeCl_{2/3}$ (PVA Mw: 85,000 ~ 124,000, $FeCl_{2/3}$ concentration: 1 M) gel electrolyte with different PVA content (d) CV at 50 mV $s^{-1}$, (e) peak current versus the square root of scan rate, and (f) thermo-electrochemical performance ($\Delta T$ = 10 ℃): current (solid line) and power (dash line) vs voltage.

*3.3.1.2 Concentration of redox couple*

The performance of the PVA-$FeCl_{2/3}$ gel was also investigated as a function of the concentration of redox couples ranging from 0.1 to 2.0 M (Figure 3.4 a). The color of the gel electrolytes darkened as the concentration of redox couple increased. A completed gel electrolyte was a failure to format at 0.1 M redox couple because the crosslinking reaction between PVA and GA occurs in an acidic environment, and a lower concentration of redox couple limited the acidity of gel precursor solution that did not satisfy the completely crosslinking of PVA. Figure 3.4 b and Figure 3.4 c demonstrated the CV curves and the diffusion coefficient of the PVA-$FeCl_{2/3}$ gel electrolyte within a different concentration of $FeCl_{2/3}$. The result is expected that a higher concentration of the redox couple sample has a much larger peak current in the CV measurement, which is caused by a higher ions concentration in the presence of the gel electrolyte that facilitates ionic diffusion in the PVA-based gelled electrolytes.

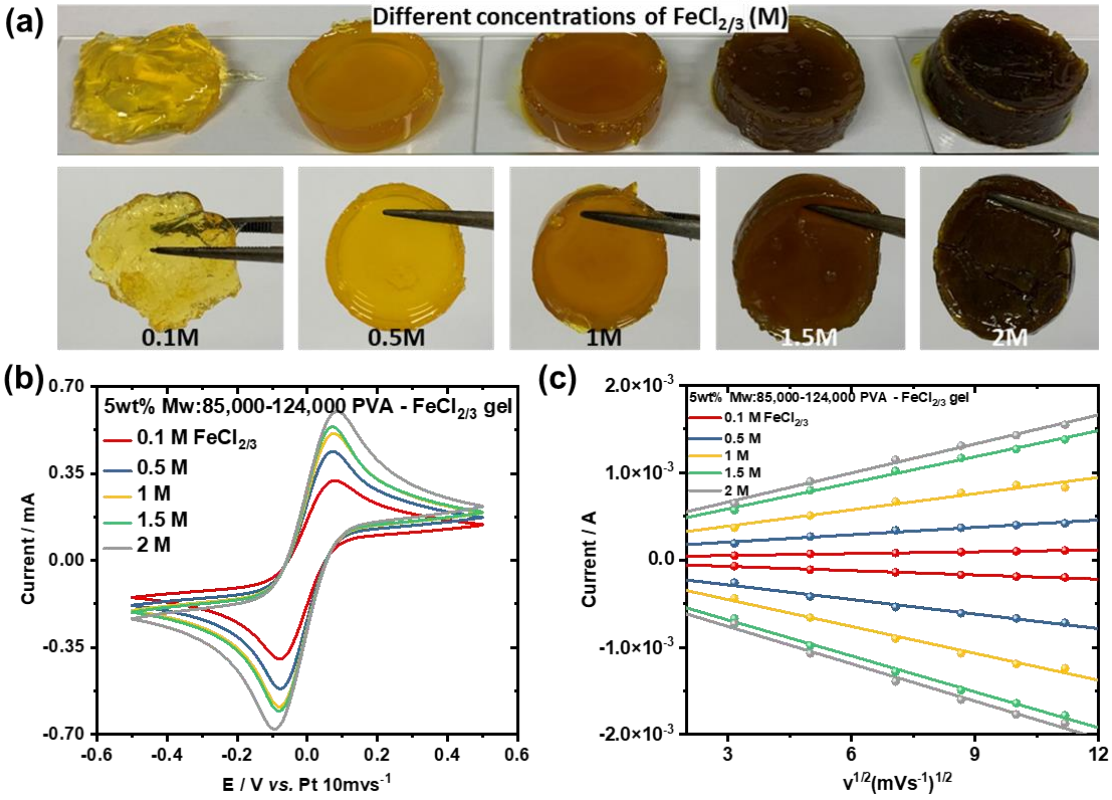

Figure 3.4 A comparison between PVA - $FeCl_{2/3}$ (5 wt.% PVA Mw: 85,000 ~ 124,000) gel electrolyte with different $FeCl_{2/3}$ concentration (0.1 - 2 M) (a) photos of PVA - $FeCl_{2/3}$ gel electrolytes, (b) comparison of CV curves at 10 mV $s^{-1}$, and (c) peak current *versus* the square root of scan rate.

The Seebeck coefficient dropped from 1.1 to 0.59 mV $K^{-1}$ with increasing concentration, which is in line with Debye-Hückel theory (*i.e.* there is a linear variation between the Eastman entropy of transport and the square root of the ionic strength) [14,15]. The output current increases with concentration reaching a plateau at 1.0 M, as a result of the decreased driving force from the decreased Seebeck coefficient (*i.e.* open circuit voltage). The maximum calculated power density was 17 mW $m^{-2}$, attained when the concentration of redox couple is 1 M, which we therefore take as the optimized concertation (Figure 3.5 a&b).

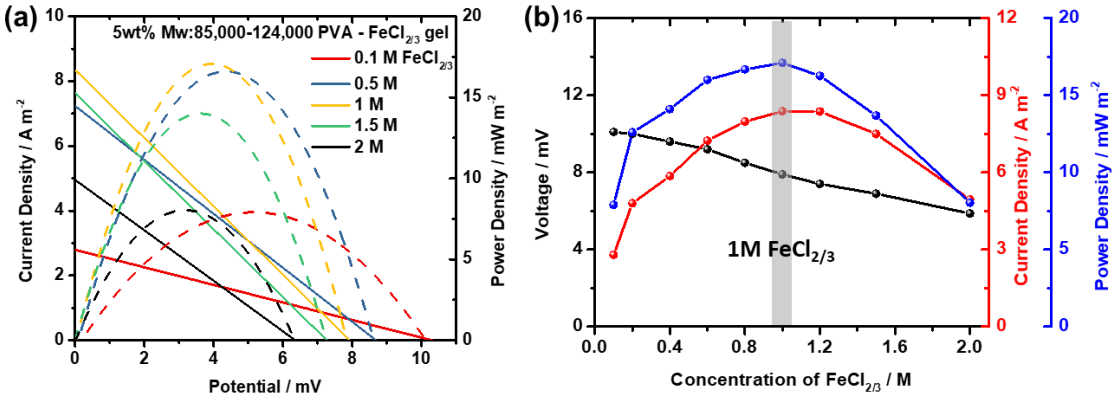


Figure 3.5 Thermo-electrochemical performance ($\Delta T$ = 10 °C) of PVA - $FeCl_{2/3}$ (PVA Mw: 85,000 ~ 124,000, PVA content: 5 wt.%) gel electrolytes with different $FeCl_{2/3}$ concentration (a) current (solid line) and power (dash line) vs voltage. (b) $V_{oc}$, $J_{sc}$, and $P_{max}$ as a function of $FeCl_{2/3}$ concentration.

### 3.3.2 Performance of PVA-$FeCl_{2/3}$ gel electrolytes containing supporting electrolyte

#### *3.3.2.1 Mechanical properties*

Figure 3.6 a&b shows the stress-strain curves of four gelled electrolytes used to test the fracture point of the gel electrolytes. Addition of acid was found to be highly beneficial to the mechanical strength of the gelled electrolyte, since the strains of Fe-HCl and Fe-$H_3PO_4$ were improved from 110% to nearly 180% and doubled the stress (from 6 KPa to 12 KPa) when compared to the gels in the absence of electrolyte, or with KCl supporting electrolyte. This is due to the higher crosslinking density of 0.88 in Fe-HCl sample than others (0.8, 0.68, and 0.67 for Fe-$H_3PO_4$, Fe-KCl and Blank samples respectively), which is quantitative evaluated from the strain-stress relationship:

$$E = 3v_eRT$$

where E = Young's modulus (Pa), $v_e$= crosslinking density (mol $m^{-3}$), R = molar gas constant and T = absolute temperature [22]. The abundant $H^+$ in Fe-HCl sample accelerates reaction rate, generates more C-O bonding, leads to difficult slippage of chains under loading, and therefore significantly modifies the polymer network and increases the mechanical strength [17-19]. After repeated cyclic stretching to 100% strain (Figure 3.6 c&d), the gel electrolyte shows less than 10% plastic deformation (over 60 cycles), indicating its excellent elasticity and cyclic stability [20].

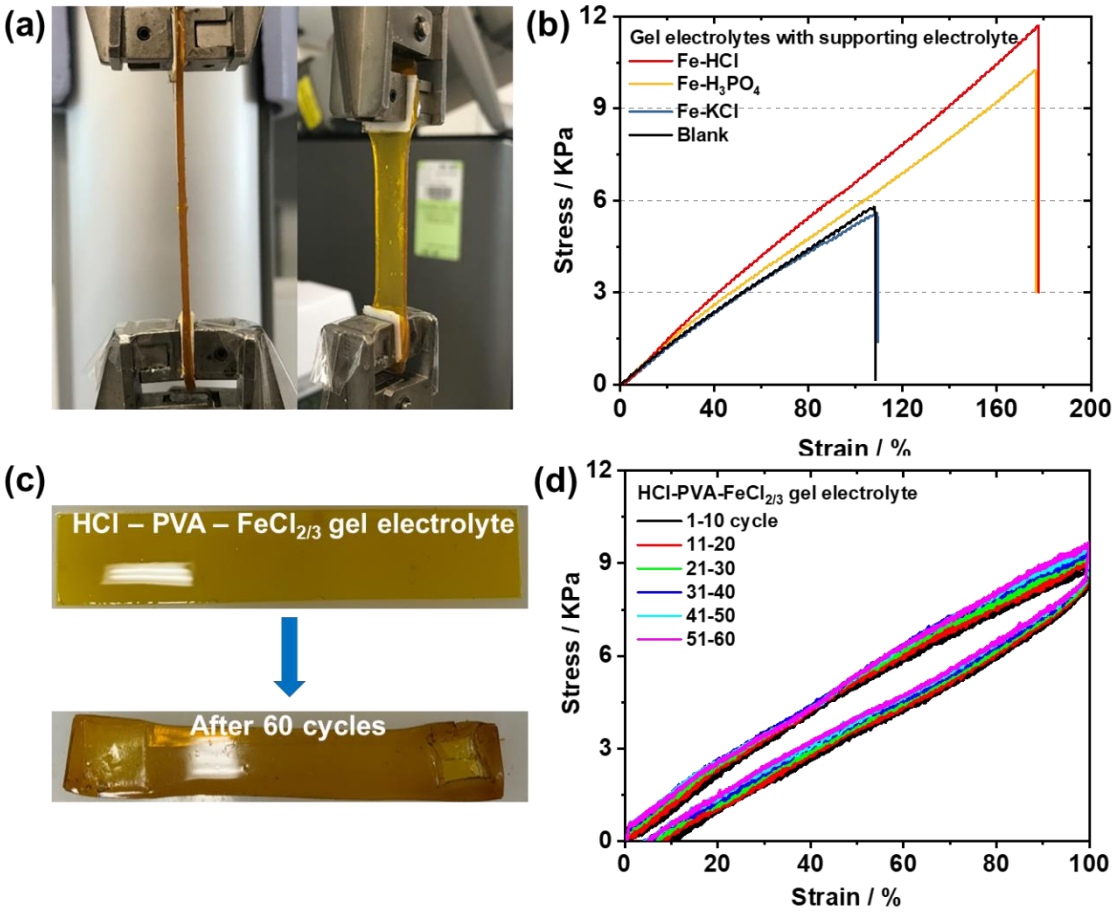


Figure 3.6 (a) Gel electrolytes undergoing the tensile test and (b) tensile stress-strain curves for the gel electrolytes. (c) The photograph of gel electrolyte before and after the cyclic test and (d) stress-strain curves of PVA - $FeCl_{2/3}$ gel electrolyte (PVA content: 5 wt.%, $FeCl_{2/3}$ concentration: 1 M, Mw = 85000 - 124000, HCl concentration: 0.08 M) during 100% cyclic strain.

### *3.3.2.2 Electrochemical properties*

Figure 3.7 a displays both current and power density curves of the four investigated thermocells. The power output ($P$) is calculated from Watt's power Law: $P = IV$, therefore with a linear IV (or $jV$ using current density), the power exhibits the expected

parabola. The maximum power output ($P_{max}$) is calculated by half of the open-circuit voltage (0.5 $V_{oc}$) and half of the short circuit current (0.5 $J_{sc}$) [21].

The supporting electrolytes at low concentration (0.1 M) hardly affected $S_e$. The parabola power output curve and potential-current liner relationship show the Fe-HCl has the $P_{max}$ of 21.2 mW $m^{-2}$ and $j_{sc}$ of 10.1 A $m^{-2}$, which was superior in performance than the thermocells containing $H_3PO_4$ and KCl as supporting electrolyte. This is due to the HCl reduced internal resistance of gel electrolyte (Figure 3.7 c), thereby improved the current and power output density.

Figure 3.7 b demonstrates the cyclic voltammogram (CVs) curves for four gel electrolytes. Peak-to-peak separations ($\Delta E_p$) of the four gelled electrolyte CVs were found to be nearly identical (236 - 251 mV), which indicates the reversibility of PVA-$FeCl_{2/3}$ gel electrolyte was not influenced by the type of supporting electrolyte. The CVs also demonstrate a significant improvement in the peak current ($i_p$) for the Fe-HCl gel electrolyte. This is indicative of facilitated ionic diffusion in the PVA-based gelled electrolytes electrolyte [22].

In order to investigate the effect of supporting electrolytes on internal resistance, electrochemical impedance spectroscopy (EIS) was employed. Figure 3.7 c shows the Nyquist plots for the four gelled electrolytes investigated with the electrolyte resistance ($R_\Omega$) and the electron transfer resistance ($R_{ET}$) calculated from EIS shown in Figure 3.7 d. The four gel electrolytes had relatively similar $R_\Omega$ (indicated by the intercept at the real axis). Notably, the supporting electrolyte effectively reduced the $R_{ET}$ of investigated systems (indicated by the semicircle diameter in Figure 3.8 c). The Fe-HCl mitigated the $R_{ET}$ to nearly half compared to the absence of supporting electrolyte (from 113 Ω to

57 Ω). Since the thermo-electrochemical performance of thermocells is highly influenced by the resistance in electron transfer [2], the observed trend in decreasing $R_{ET}$ is mirrored as an increase in thermogalvanic power. In summary, these results indicate that using HCl as supporting electrolyte in the these gelled thermocells facilitate reducing the internal resistance ($R_{ET}$ and ionic diffusion resistance) of gel electrolytes and promoted the thermo-electrochemical performance of thermocells.

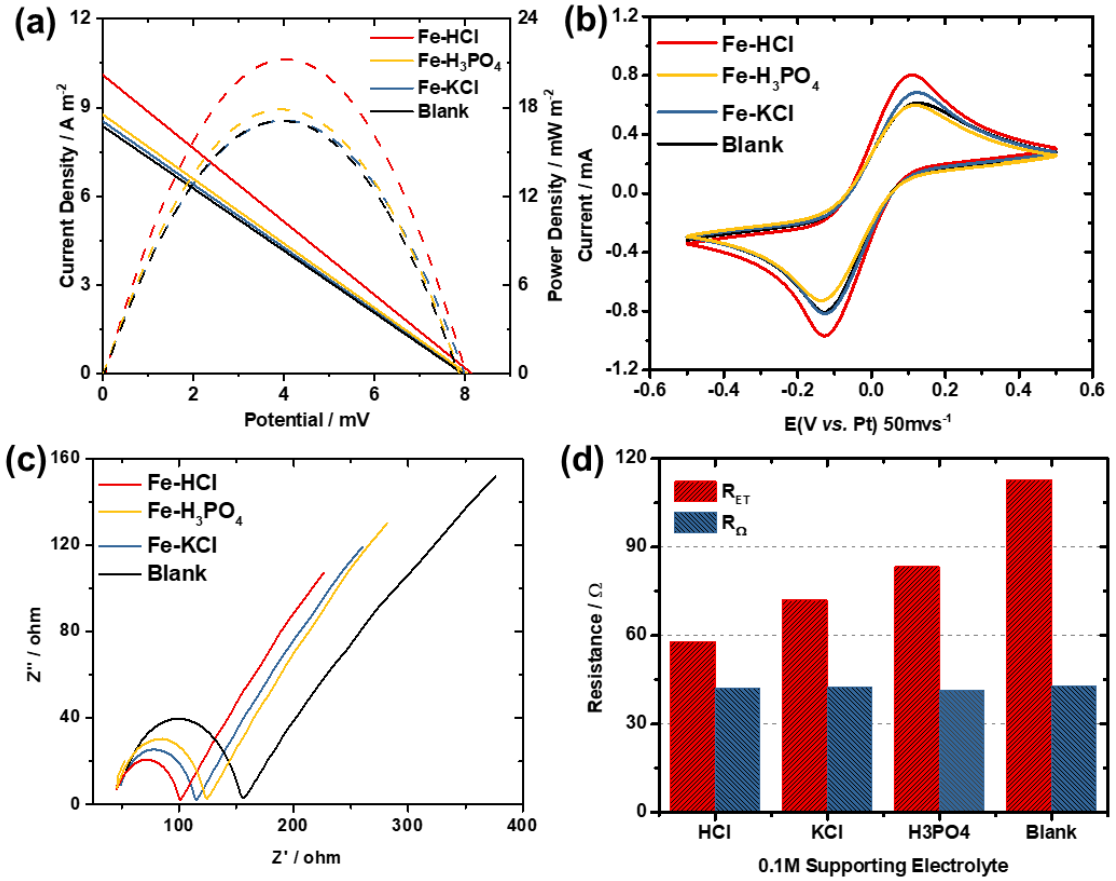


Figure 3.7 A comparison of the PVA - $FeCl_{2/3}$ gel electrolyte containing various 0.1 M supporting electrolytes. (a) Thermo-electrochemical performance at ΔT = 10 °C, (b) CV curves at scan rate 50 mV $s^{-1}$, (c) Nyquist plots, and (d) the electrolyte resistance ($R_\Omega$) and the electron transfer resistance ($R_{ET}$) determined by EIS (using the model described elsewhere [2]).

The addition of conjugate acid could enhance ion transport and electron transfer (shown in Figure 3.8 c with reduced $R_S$ and $R_{ET}$ in EIS analysis), so an optimized concentration of 0.08 M HCl was added in this gel electrolyte system to increase the $J_{sc}$ and $P_{max}$ to 9.9 A $m^{-2}$ and 21.3 mW $m^{-2}$, respectively (Figure 3.8 a&b) [23]. In addition, the cyclic performance stability of the optimized n-type gel electrolytes with 5 wt.% PVA, 1M $FeCl_{2/3}$ and 0.08 M HCl was tested over 4 days (Figure 3.8 d). The maximum power density remains almost unchanged even after 4 days (17.12 mW $m^{-2}$ at day 1, 15.74 mW $m^{-2}$ at day 4), indicating the excellent electrochemical and thermo-electrochemical stability of our n-type gel electrolyte.

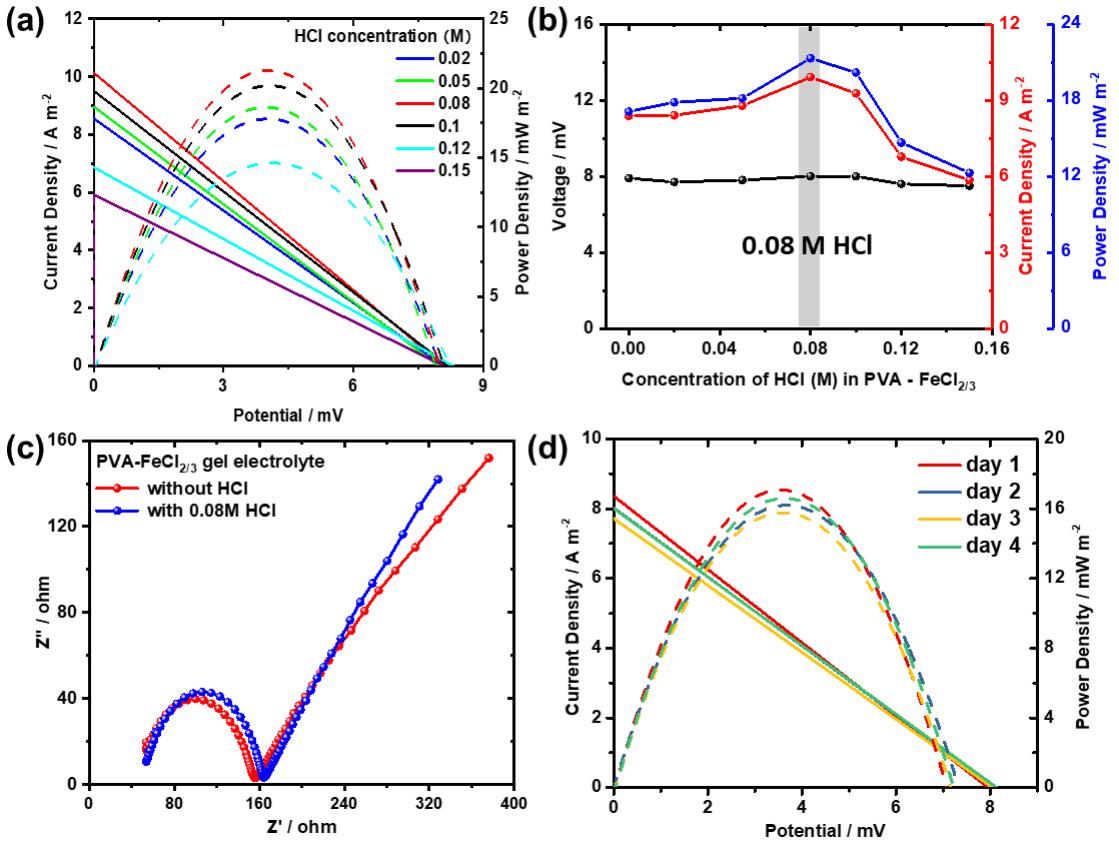


Figure 3.8 Thermo-electrochemical performance (ΔT = 10 °C) and electrochemical performance of PVA $FeCl_{2/3}$ (PVA Mw: 85,000 ~ 124,000, PVA content: 5 wt.%) gel

electrolytes with different $FeCl_{2/3}$ concentration. (a) Current (solid line) and power (dash line) vs voltage, (b) $V_{oc}$, $J_{sc}$, and $P_{max}$ as a function of $FeCl_{2/3}$ concentration, (c) EIS curves, and (d) current (solid line) and power (dash line) vs voltage of the optimized n-type gel electrolyte (5 wt.% PVA, 1M $FeCl_{2/3}$ and 0.08 M HCl) tested at the 1st, 2nd 3rd and 4th day after the device was assembled.

### 3.3.3 Electrochemical performance of N-type thermocells were connected in parallel

The open-circuit voltage ($V_{oc}$) of the single thermocell at varied ΔT is displayed in Figure 3.9 a. The potential of the thermocell was recorded for 600 s at ΔT = 0 ℃. Then the temperature of the hot electrode was increased in 5 ℃ increments for 600 s at each temperature until the ΔT = 20 ℃. The $V_{oc}$ increased linearly with ΔT, as expected. Figure 3.9 b displays the current and power output densities of the thermocell with varied ΔT (by increasing the temperature of the colder electrode). The $P_{max}$ and $V_{OC}$ reduced from 63.7 to 4.21 mW $m^{-2}$ and 14.6 to 3.5 mV respectively as expected as ΔT decreased from 20 ℃ to 5 ℃.

In order to effectively harvest waste heat, individual thermocells can be combined in series to increase potential output, or combined in parallel to increase current output [24,25]. Here, using only n-type thermocells, in order to avoid a thermal short circuit, alternating thermocells with identical $S_e$ are arranged both thermally and electrically in parallel (Figure 3.9 c&d) [2]. As expected, when in parallel the current increased 100% (20 ± 1 A $m^{-2}$) relative to individual cells, while the potential remained the same (8.0 ± 0.2 mV). The current of thermocells in parallel adds quantitatively with additional cells,

which provides the possibility to effectively connect TECs of a single type (either n- or p-type) in series for increased power output kinetics [24].

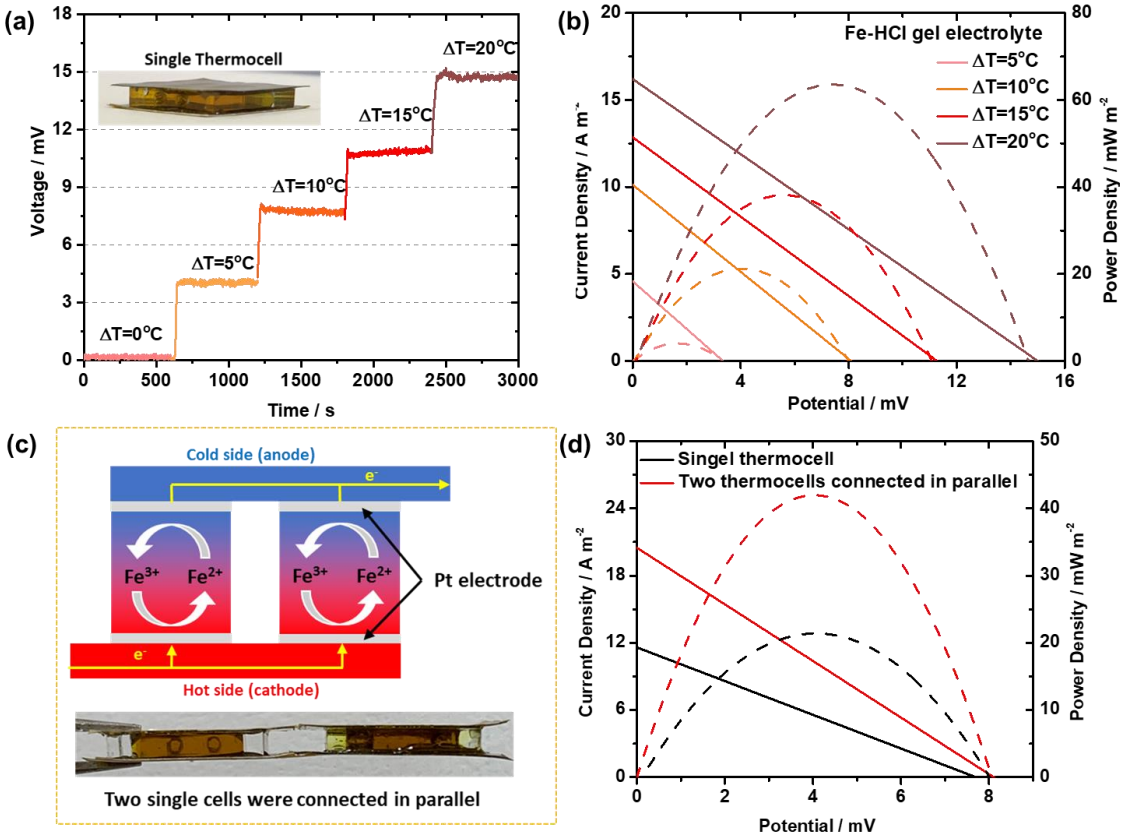


Figure 3.9 (a) $V_{oc}$ of thermocells when held for 600 s at each ΔT, (b) power and current output density at different temperature gradients (ΔT = 5, 10, 15 and 20 ℃), (c) photographs and schematics of two single thermocells electrically connected in parallel (connected by a hot-to-hot arrangement), and (d) thermo-electrochemical performance of an individual thermocell and two thermocells connected in parallel at ΔT = 10 ℃.

## 3.4 Conclusions

In summary, we have synthesized a novel PVA-$FeCl_{2/3}$ gelled electrolyte and systematically investigated the effect of polymer concentration, molecular weights and

supporting electrolytes on mechanical stress and electrochemical performance of gelled electrolytes. Results show that the supporting electrolyte of HCl has greatly enhanced mechanical strength and reduced charge transfer resistance. The Fe-HCl-based thermocell exhibited excellent thermo-electrochemical performance with a $S_e$ of 0.8 ± 0.02 mV $K^{-1}$, and current density of 16.1 A $m^{-2}$ and power density of 63.7 mW $m^{-2}$ at a ΔT of 20 K. Finally, the low current output observed by an individual thermocell was increased by the combining thermocells in parallel. This attempt at the synthesis of gel electrolytes and the fabrication of thermocells demonstrate the potential for realistic applications of wearable devices in the future. A type of neutral hydrogel host that satisfies requirements of both P-type and N-type and the fabrication of N-P type gel electrolyte connected in series are the next pursuit in chapter 4. Moreover, gel electrolytes with porous structures that facilitate ion transfer are also discussed in the next chapter.

## 3.5 References


[1] L. Jin, G. W. Greene, D. R. MacFarlane, J. M. Pringle, ACS Energy Lett. 2016, 1, 654.

[2] M. A. Buckingham, F. Marken, L. Aldous, Sustain. Energy Fuels 2018, 2, 2717.

[3] P. Yang, K. Liu, Q. Chen, X. Mo, Y. Zhou, S. Li, G. Feng, J. Zhou, Angew. Chemie - Int. Ed. 2016, 55, 12050.

[4] K. Kim, S. Hwang, H. Lee, Electrochim. Acta 2020, 335, 135651.

[5] H. Fei, C. Yang, H. Bao, G. Wang, J. Power Sources 2014, 266, 488.

[6] G. Hirankumar, N. Mehta, Heliyon 2018, 4, e00992.

[7] G. M. Liao, C. C. Yang, C. C. Hu, Y. L. Pai, S. J. Lue, J. Memb. Sci. 2015, 485, 17.

[8] M. Y. Jen, Z. W. Hung, C. Y. Chun, J. Memb. Sci. 2008, 322, 74.

[9] C. C. Yang, G. M. Wu, Mater. Chem. Phys. 2009, 114, 948.

[10] M. Russo, H. Warren, G. M. Spinks, D. R. MacFarlane, J. M. Pringle, Aust. J. Chem. 2019, 72, 112.

[11] M. Z. Kufian, S. R. Majid, A. K. Arof, Ionics (Kiel). 2007, 13, 231.

[12] H. Zhou, T. Yamada, N. Kimizuka, J. Am. Chem. Soc. 2016, 138, 10502.

[13] M. Li, S. Cheng, H. Yan, Green Chem. 2007, 9, 894.

[14] H. Im, T. Kim, H. Song, J. Choi, J. S. Park, R. Ovalle-Robles, H. D. Yang, K. D. Kihm, R. H. Baughman, H. H. Lee, T. J. Kang, Y. H. Kim, Nat. Commun. 2016, 7, 1.

[15] D. P. Dubal, N. R. Chodankar, D. H. Kim, P. Gomez-Romero, Chem. Soc. Rev. 2018, 47, 2065.

[16] S. G. Croll, J. Coatings Technol. Res. 2010, 7, 49.

[17] F. S. Matty, M. T. Sultan, A. K. Amine, Pure Appl. Sci. Ibn Al-Haitham Jour. Pure Appl. Sci 2015, 28.

[18] E. Marin, J. Rojas, Int. J. Pharm. Pharm. Sci. 2015, 7, 242.

[19] H. K. Purss, G. G. Qiao, D. H. Solomon, J. Appl. Polym. Sci. 2005, 96, 780.

[20] Q. Tang, M. Chen, G. Wang, H. Bao, P. Saha, J. Power Sources 2015, 284, 400.

[21] M. A. Buckingham, L. Aldous, J. Electroanal. Chem. 2020, 872, 114280.

[22] N. Elgrishi, K. J. Rountree, B. D. McCarthy, E. S. Rountree, T. T. Eisenhart, J. L. Dempsey, J. Chem. Educ. 2018, 95, 197.

[23] J. Duan, B. Yu, K. Liu, J. Li, P. Yang, W. Xie, G. Xue, R. Liu, H. Wang, J. Zhou, Nano Energy 2019, 57, 473.

[24] M. Al Maimani, J. J. Black, L. Aldous, Electrochem. commun. 2016, 72, 181.

[25] M. A. Buckingham, K. Laws, J. T. Sengel, L. Aldous, Green Chem. 2020, 22, 6062.

# Chapter 4 Porous structure PAM gel electrolytes for wearable thermo-electrochemical cells

*This chapter is adapted from articles:*

*"Novel porous thermosensitive gel electrolytes for wearable thermo-electrochemical cells", by Yuetong Zhou, Shuai Zhang, Mark A. Buckingham, Leigh Aldous, Stephen Beirne, Chang Wu, Yuqing Liu, Gordon Wallace and Jun Chen, that was published in Chemical Engineering Journal (2022). Adapted with permission from Elsevier Publishing Group.*

## 4.1 Introduction

In chapter 3, the thermogalvanic device was designed that comprised of N-type thermocells connected in parallel, where gel electrolytes were fabricated by polyvinyl alcohol (PVA)-$FeCl_{2/3}$[1]. However, to achieve the satisfied voltage output that enough to power electric device, N- and P-type gel electrolytes are designed to be connected in series.

The potassium ferricyanide/ferrocyanide ($K_{3/4}[Fe(CN)_6]$) redox couple is commonly used in thermocells due to the high $S_e$ of -1.4 mV $K^{-1}$ (as 0.4 M) in solid-state electrolytes[2]. However, considerable limitations can arise during the selection of polymers compatible with redox couples, including pH sensitivity, low electrolyte solubility and poor thermal stability and mechanical properties. The carboxymethyl cellulose (CMC) is a natural neutral polymer that coexists with pH sensitive $K_{3/4}[Fe(CN)_6]$, however, the poor stretchability of CMC-$K_{3/4}[Fe(CN)_6]$ gels limited its applications. The N-type redox couple $FeCl_{2/3}$ was also compatible with PVA polymer and had with a higher solubility (1 M). Conversely, the low solubility of $K_{3/4}[Fe(CN)_6]$ in PVA polymer solution (0.05 M) and neutral properties inhibited the crosslinking of PVA gels, which proved that PVA is not suitable for P-type redox couple. Therefore, the neutral gel host that is compatible with both N and P-type redox couple is also indeed to explore. Besides, the thermal-electrochemical performance was also limited by the gelled system, where the current output is significantly related with ion diffusions. Micro-channels in gel electrolytes that facilitate the mass transfer is also investigated in this chapter.

The hydrophilic polymer polyacrylamide (PAM) is an attractive polymer for thermocells as it is stable in the presence of metal salts, and demonstrates high ionic conductivity and exceptional mechanical properties[3,4]. However, gelled electrolytes commonly limit the mass transport of electrolyte, resulting in the lower thermo-electrochemical performance than liquid electrolytes. Zhao *et. al.* fabricated an aligned hydrogel based on PAM in an all-solid-state hydrogel supercapacitor through ice templating[5]. The Liu group combined the freeze casting and a solvent replacement method to prepare aligned ionogels with better electrochemical activities and strength modulus[6]. Wei *et. al.* utilized sodium acetate trihydrate ($NaAc{\cdot}3H_2O$) as a crystal template (hot ice template), which is safer and more facile method that freeze casting to prepare aligned PAM hydrogel for supercapacitors[7].

Significant progress has recently been made in wearable thermocells. One of the main targets of thermocell research is to achieve higher $S_e$, and this has been achieved by several methods: using redox couples with superior intrinsic $\Delta S$; replacing aqueous solvent with organic or ionic liquid solvents or inducing combined Seebeck and Soret effects. Ionic liquids (ILs) have been proposed as an alternative solvent for redox couples in thermocells, which has led to significantly enlarged $S_e$[8-11]. In addition, the Kim group doubled $S_e$ (from 1.43 to 2.9 mV $K^{-1}$) of $[Fe(CN)_6]^{3-/4-}$ through introducing organic solvent into aqueous systems[12]. Despite these advantages, the high viscosity of ILs (25 times or more than water) or organic solvents result in significant mass transfer limitations, which is a major obstacle to their utilization in thermocells[13,14]. Recently, the introduction of guanidinium cations ($[Gdm]^+$) and amide derivatives (-CONR′R″) effectively boosted the $S_e$ of the $[Fe(CN)_6]^{3-/4-}$ thermocell from 1.4 to 4.2 mV $K^{-1}$ through enhanced $\Delta S$ in an aqueous thermocell[15,16]. Guanidinium cations ($[Gdm]^+$)

could be associated with $Fe(CN)_6^{4-}$ and formed a thermosensitive crystal, which repetitive dissolved and crystallized based on the electrode temperature difference [16]. This approach, while compatible with liquid electrolytes has not been tested in a gelled electrolyte thermocell.

This chapter presents the process of manufacturing porous, gelled $K_{3/4}[Fe(CN)_6]$ electrolytes, combined with Pt electrodes as a p-type thermocell (PAM-$K_{3/4}Fe(CN)_6$). The optimized, freeze-dried porous gelled electrolytes were selected for further investigation. We also introduce GdmCl into the $K_{3/4}[Fe(CN)_6]$ thermocell, with the thermo-electrochemical properties measured at different GdmCl concentrations, temperature differences and electrode temperatures. Finally, the freeze-dried porous gelled thermocell is also combined in series with a PAM-$Fe^{2+}/Fe^{3+}$ thermocell, integrated with Pt electrodes as an n-type cell (PAM-$FeCl_{2/3}$-HCl). A demo device of paired p-type and n-type TECs (p-n cells) was fabricated to achieve higher voltage output, demonstrating the potential for practical applications by charging a supercapacitor and illuminating an LED.

## 4.2 Experiment

### 4.2.1 Synthesis of porous structure PAM gel electrolytes

The synthetic processes of porous structure PAM gel electrolytes were described in Chapter 2.5.2

### 4.2.2 Freeze-drying treatment

The freeze-drying treatment of porous structure PAM gel electrolytes were described in Chapter 2.2.4

### 4.2.3 Electrochemical measurement

All the electrochemical measurements were performed according to the procedures presented in Chapter 2.4

### 4.2.4 Preparation of platinum electrode

The Pt electrode for the thermal-electrochemical performance were described in Chapter 2.5.4

### 4.2.5 Thermal conductivity

The thermal conductivity measurement of porous structure PAM gel electrolytes were described in Chapter 2.3.4

### 4.2.6 Device assembly

The flexible wearable themocell devices were assembled using gel electrolytes and Pt electrodes as described in Chapter 2.6.2

## 4.3 Results and Discussion

### 4.3.1 Investigation of the component of PAM porous gel electrolytes

#### *4.3.1.1 The mechanism of crosslinking of PAM porous gel electrolytes*

A previously reported procedure [8] was adapted to prepare porous gels, which could subsequently be impregnated with a redox-active electrolyte, to prepare flexible materials suitable for wearable thermocells. The PAM gel was prepared *via* the free radical polymerization of the AM monomer, initiated by APS in the presence of MBA crosslinker (Figure 4.1 a). This process was conducted concurrently with NaAc crystallisation, which provides micrometre-sized diameter channels throughout the gel (Figure 4.1 b-f) [8], which were subsequently removed by rinsing and five immersion cycles in deionised water, forming the porous gel (Figure 4.2). Figure 4.1 g and h show SEM images of 10 wt.% AM porous gel in two directions (either vertical or parallel pores), which is mainly determined by the directional of NaAc crystal during the crystallization procure.

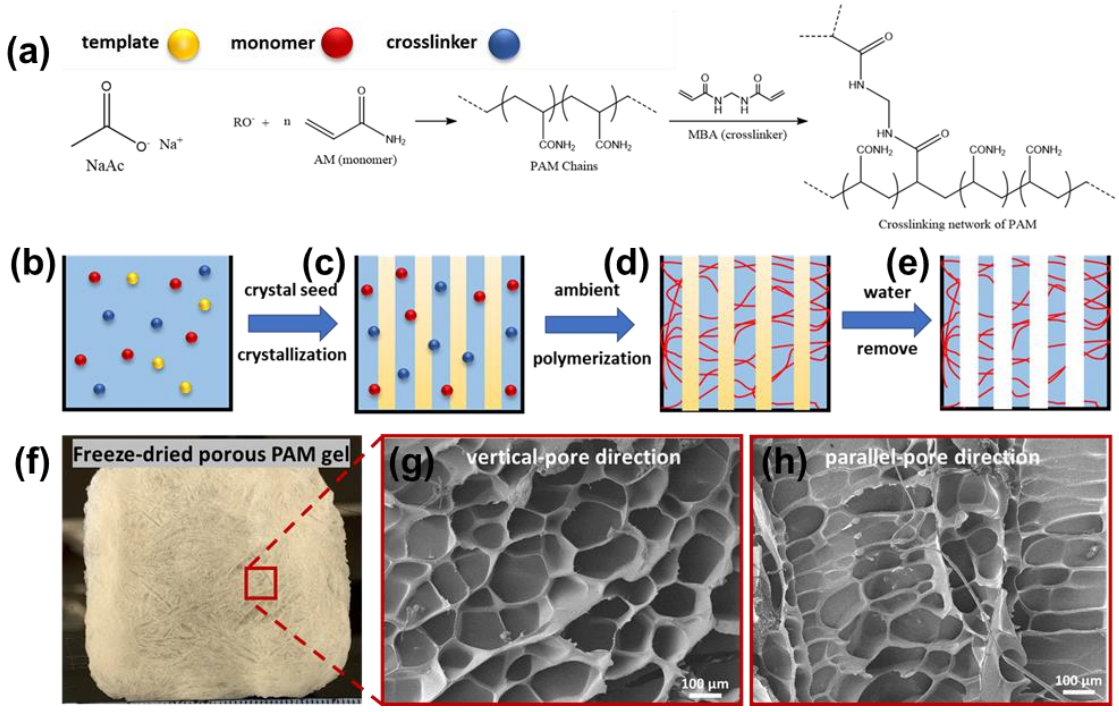


Figure 4.1 (a) The mechanism of AM polymerization reactions, (b-e) the schematic illustration of the NaAc presents in PAM gel and generates porous structure, (f) photos

of the freeze-dried porous PAM gel, SEM images (secondary electron) of cross-section of (g) vertical and (h) parallel pore direction of the porous structure.

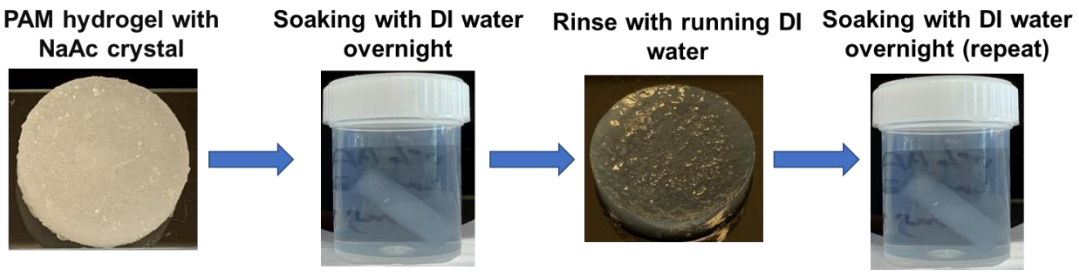


Figure 4.2 Photographs of the soaking process of PAM hydrogel with NaAc crystals.

As shown in Figure 4.3, the Raman spectrum of freeze-dried porous PAM gel shows a broad peak near 3000 $cm^{-1}$, corresponding to the stretching vibration of the N-H bond. The sharp peak at 2923 $cm^{-1}$ is assigned to C-H stretching. Peaks located at 1622 and 1670 $cm^{-1}$ represent primarily N-H bending and C=O stretching in the PAM. Complex peaks indicate C-N stretching and $CH_2$ bending (1447 $cm^{-1}$), C-C skeletal stretching (1110 $cm^{-1}$) and C-H bending (1334 $cm^{-1}$). The weak peak at 1216 $cm^{-1}$ is probably $NH_2$ wagging. Multipeaks in the range of 770 - 845 $cm^{-1}$ are maybe the C-C skeletal stretching (side chain) and $CH_2$ rocking. Two peaks in 639 $cm^{-1}$ and 478 $cm^{-1}$ are for C-O bending and C-C skeletal bending respectively[17-19].

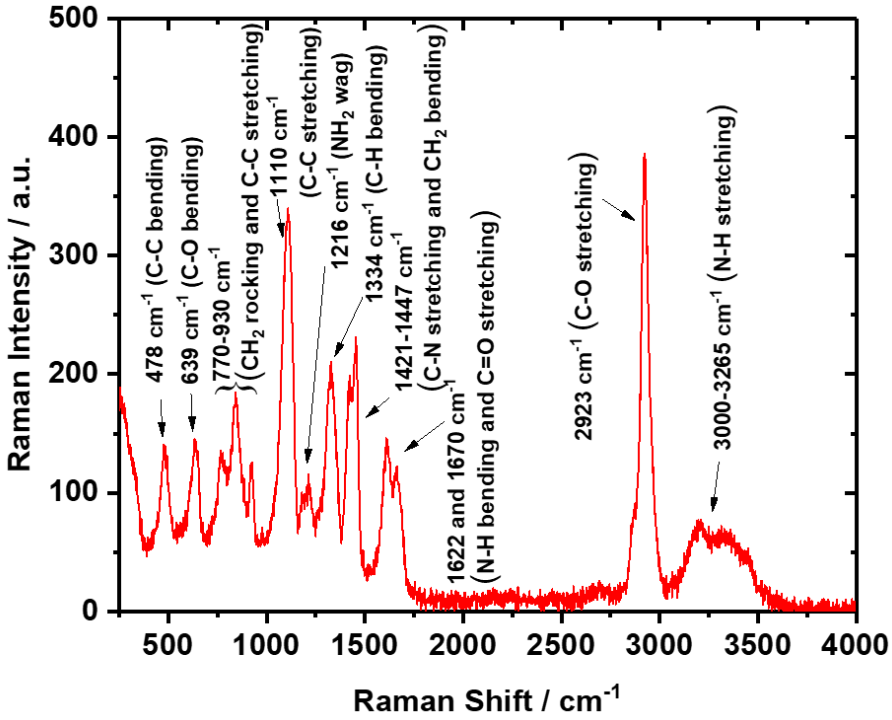


Figure 4.3 Raman spectra of freeze-dried porous polyacrylamide gel.

*4.3.1.2 Content of AM*

The same synthesis was repeated with various concentrations of AM monomer. This was conducted under the absence and presence of NaAc template, the size of the pores prepared with NaAc template (Figure 4.4 a-c) were found to be considerably larger than those prepared without NaAc (Figure 4.4 d-f). Furthermore, the pore size can also be controlled by modifying the concentration of AM, allowing a study of the effect of porosity. The 10 wt.% AM gel demonstrated a pore size of roughly 100 - 120 µm (Figure 4.1 g and Figure 4.4 a). The diameter of pore size correspondingly decreased to between 50 - 70 µm upon increasing AM to 15 wt.% or 20 wt.% (Figure 4.4 b-c).

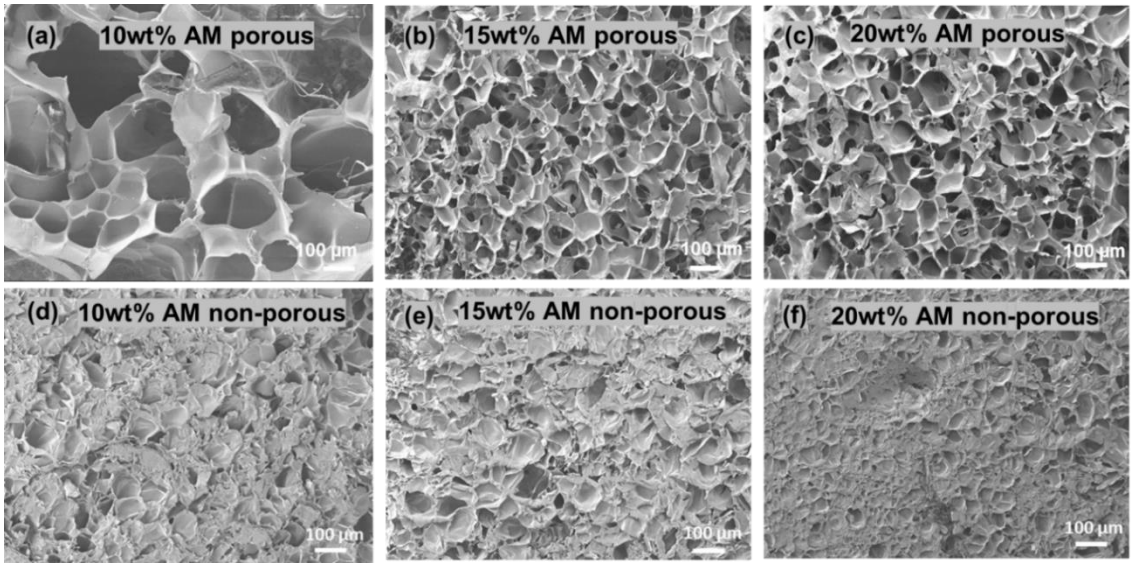


Figure 4.4 (a-c) Cross-sectional SEM image of porous hydrogel: (a) 10 wt.%, (b) 15 wt.%, and (c) 20 wt.% AM, (d-f) cross-sectional SEM image of non-porous hydrogel: (d) 10 wt.%, (e) 15 wt.%, and (f) 20 wt.% AM.

The gelled electrolyte with different pore size (synthesised with 10 wt.% - 20 wt.% AM) was also prepared, through which the gel forming ability, the mechanical properties and the thermo-electrochemical performance can be optimized (Figure 4.5). The ability of these synthesised gels to withstand stress increased from 8.3 KPa to 32 KPa by increasing the AM concentration from 10 wt.% to 20 wt.% (Figure 4.5 a). During this testing, the gels were found to be able to stretch double of the original length, due to the reinforcing crosslinking density between PAM chains[20,21],which is ideal for wearable devices[1]. Moreover, the pore size has minor impact on the thermal conductivity of gels, with the value ranging from 0.59 to 0.63 $Wm^{-1}K^{-1}$ (Figure 4.5 b). The gelled electrolyte synthesised with 10 wt.% AM achieved optimal electrochemical performance (in terms of EIS, CV, ion diffusion and ionic conductivity) and thermo-electrochemical

performance, which is attributed to the appropriate pore size[8] (Figure 4.5 c-h). Therefore, 10 wt.% AM was selected for further research.

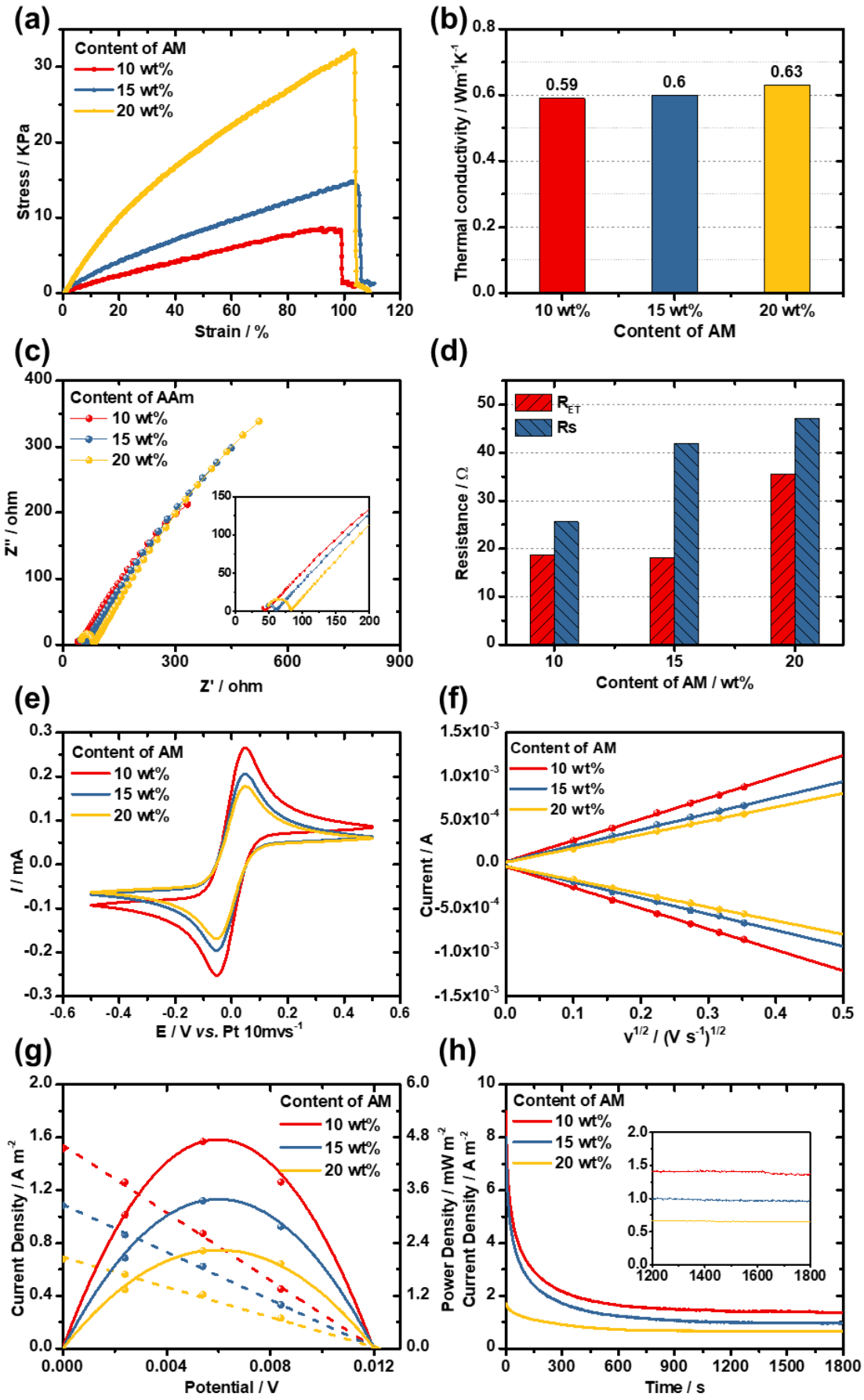
(a)
Content of AM
10 wt%
15 wt%
20 wt%
Stress / KPa
Strain / %
(b)
Thermal conductivity / Wm-1K-1
0.59
0.6
0.63
10 wt%
15 wt%
20 wt%
Content of AM
(c)
Content of AAm
10 wt%
15 wt%
20 wt%
Z'' / ohm
Z' / ohm
(d)
RET
Rs
Resistance / Ω
Content of AM / wt%
(e)
Content of AM
10 wt%
15 wt%
20 wt%
I / mA
E / V vs. Pt 10mvs-1
(f)
Content of AM
10 wt%
15 wt%
20 wt%
Current / A
v1/2 / (V s-1)1/2
(g)
Content of AM
10 wt%
15 wt%
20 wt%
Current Density / A m-2
Potential / V
(h)
Content of AM
10 wt%
15 wt%
20 wt%
Power Density / mW m-2
Current Density / A m-2
Time / s

Figure 4.5 A comparison among 10 wt.% (red), 15 wt.% (blue) and 20 wt.% (yellow) AM porous gel electrolyte in terms of (a) the tensile stress-strain curves (25 mm $min^{-1}$), (b) the thermal conductivity, (c) Nyquist plots and (d) the electrolyte resistance ($R_{\Omega}$) and the electron transfer resistance ($R_{ET}$) determined by EIS, (e) Cyclic voltammetry (scan rate = 10 mV $s^{-1}$), (f) the linear relationship of peak currents versus square root of scan rates (10 - 125 mV $s^{-1}$), (g) thermo-electrochemical performance at $\Delta T$ = 10 ℃ ($T_c$ = 25 ℃, $T_h$ = 35 ℃), and (h) the long-term performance (short circuit current versus time).

#### *4.3.1.3 Concentration of NaAc on the formation of hydrogel*

A higher concentration of NaAc was attempted to generate gels with different size of pore. The solubility of NaAc increases with temperature. Therefore, increasing the temperature of the precursor solution improves the quantity of NaAc crystallising in the gel. However, attempting to increase the temperature of the synthesis to 70 - 90 ℃ resulted in failure to synthesise gels (Figure 4.6). This is due to NaAc aggregation, which occupies excess internal space of the gels, and decreases the free water content [22]. After removing the NaAc crystals, limited covalent bond formation between the polymer chains and the cross-linker resulted in poor physical properties of these gels.

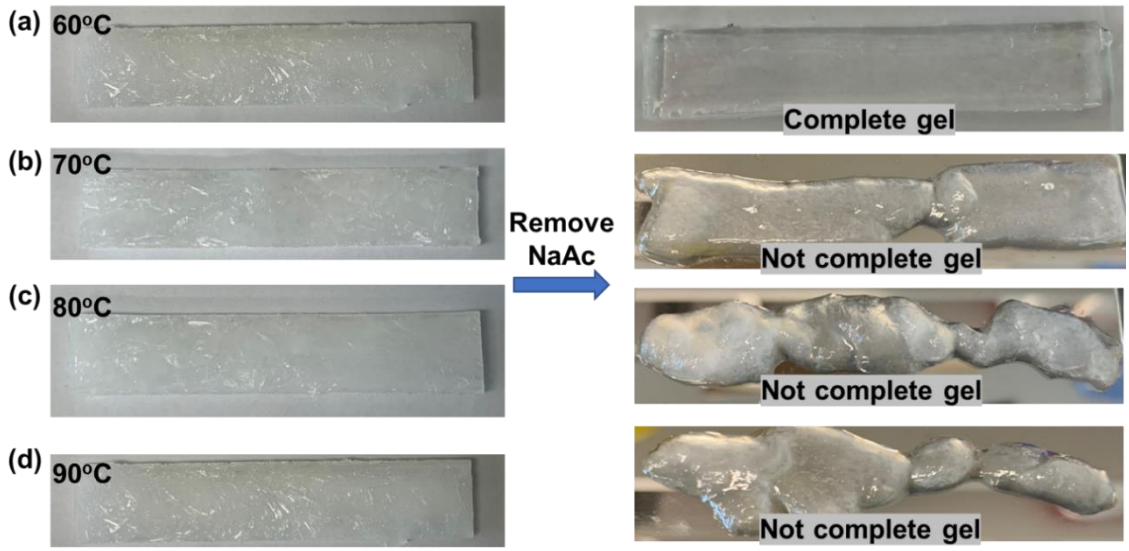


Figure 4.6 Photographs of porous hydrogels mixed with different contents of NaAc (saturated solubility of NaAc at each temperature, (a) 1.39 g NaAc at 60 ℃, (b) 1.46 g NaAc at 70 ℃, (c) 1.53 g NaAc at 80 ℃, (d) 1.61 g NaAc at 90 ℃).

### 4.3.2 Physical properties of gel electrolytes

#### *4.3.2.1 Mechanical properties*

These synthesised gelled electrolytes were tailored into 50 × 10 × 2 mm (L × W × T) rectangles for tensile strength testing (Figure 4.7 a). Figure 4.7 b shows the stress-strain curves of the three gelled electrolytes, tested until the fracture point. All three samples can withstand nearly identical stress (92 - 95 KPa). The strain% of the porous and freeze-dried porous gels were found to be 95% and 97% respectively, which are slightly smaller than that of the non-porous gel (99%), expressing that additional porous structures and freeze-drying treatment had little effect on the mechanical strength of gel electrolytes. Stretchable and durable gelled electrolytes are essential for wearable

devices, which can undergo deformation during practical utilization attached to the human body[1].

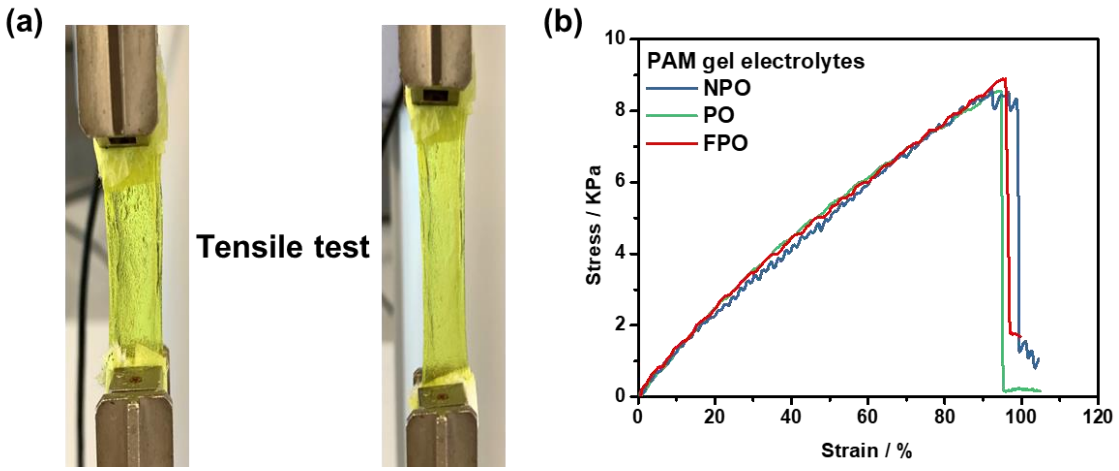


Figure 4.7 (a) PAM gel electrolytes undergoing the tensile test, (b) The tensile stress-strain curves of PAM gel electrolytes.

#### *4.3.2.2 Swelling ratio*

Swelling ratios ($Q$) describes the volume of electrolyte that the gels can absorb. Photographs of gels synthesised in the absence or presence of NaAc and after freeze-dried treatment are shown in Figure 4.8 a, which we describe as “non-porous”, “porous” and “freeze-dried porous” hydrogels, respectively. Gels synthesised by all three methods were soaked in a 0.4 M $K_{3/4}Fe(CN)_6$ solution for 24 h (Figure 4.8 b&c). The non-porous and porous gel electrolyte was found to have swelling coefficients of 118% and 188%. The reduced swelling of the non-porous gel is may due to the higher cross-linking degree [23-25]. The freeze-dried porous gel achieved a $Q$ of 2543%, indicative of a substantial absorption of electrolyte.

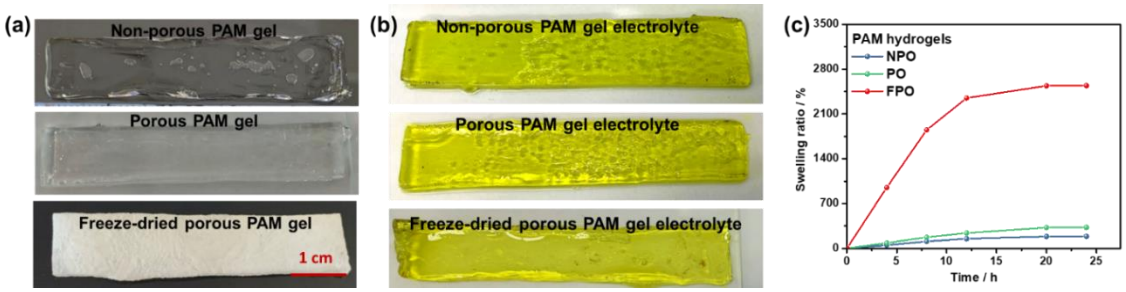


Figure 4.8 (a) Photographs of PAM gels (top: non-porous (NPO); middle: porous (PO), bottom: freeze-dried porous (FPO)), (b) All three gel electrolytes were soaked in $K_{3/4}Fe(CN)_6$ aqueous solution until the equilibrium status (top: non-porous gel; middle: porous gel; bottom: freeze-dried porous gel), (c) The swelling behaviour of gel electrolytes.

### 4.3.3 Electrochemical performance of gel electrolytes

#### *4.3.3.1 Electrochemical activities*

The electrochemical activity of the three gel electrolytes (non-porous, porous and freeze-dried porous hydrogels soaked in 0.4 M $K_{3/4}Fe(CN)_6$ solution) were evaluated using a thin-film platinum electrode (ED-SE1-Pt, Micrux), which contains working, reference, and counter electrodes. Figure 4.9 a displays the cyclic voltammograms (CVs) recorded at a scan rate of 10 mV $s^{-1}$. The freeze-dried gel electrolyte demonstrates the highest peak current, compared to both the non-porous and porous gelled electrolytes. Peak-to-peak separations ($\Delta E_p$) in CVs are indicative of the kinetics of the redox-process[26]. The peak to peak separation of the three gels (non-porous: 101 mV, porous: 105 mV and freeze-dried porous: 108 mV) all show a reversible redox process occurring. CVs were recorded at various scan rates and the peak current plotted *vs* square root of scan rate. A linear relationship was observed (Figure 4.9 b), indicating a

diffusion limited system[26,27]. Unsurprisingly, the $D$ of the three gels followed the same trend as the peak current where the freeze-dried porous gel electrolyte observed the highest $D$ and the non-porous gel observed the lowest $D$ (Figure 4.9 c). The freeze-dried hydrogels have a more porous nature, where retained a greater proportion of redox-active electrolyte, which reflected a higher relative D, meanwhile as expressed by the higher $Q$ value, and thus blocked less of the electrode surface area.

Electrochemical impedance spectroscopy (EIS) was also undertaken on these gels in the same setup as the CVs and are displayed in Figure 4.9 d-e. From this, the electron transfer ($R_{\mathrm{ET}}$) and mass transport ($R_{\Omega}$) resistances can be determined. The freeze-dried porous gel observed the lowest minimum electrolyte resistance of 29.3 Ω (indicated by the intercept at the real axis) among the three gelled electrolytes. With respect to electron transfer resistance (defined by the semicircle diameter at high frequency domain) the freeze-dried porous gel electrolyte (7.4 Ω) observed lower $R_{\mathrm{ET}}$ than in porous (11.1 Ω) and non-porous gel electrolyte (14.2 Ω), likely owing to higher concentration of redox couple in the freeze-dried porous gel electrolyte [28]. The freeze-dried porous gel electrolyte therefore demonstrates superior electrochemical performance (ionic conductivity, apparent diffusion coefficient, and apparent electron transfer kinetics) compared to the other gel electrolytes.

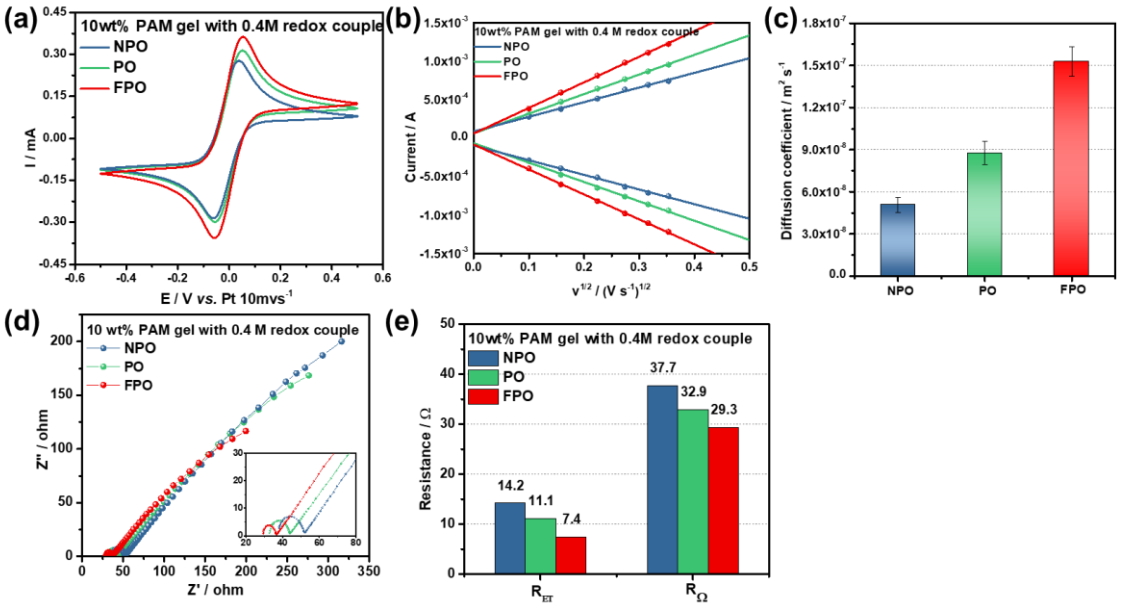


Figure 4.9 A comparison electrochemical activities of non-porous (NPO, blue), porous (PO, green) and freeze-dried porous (FPO, red) gel electrolytes in terms of (a) cyclic voltammetry (scan rate = 10 mV $S^{-1}$), (b) the linear relationship of peak currents versus square root of scan rates (10 - 125 mV $s^{-1}$), (c) diffusion coefficient, (d) electrochemical impedance spectra, and (e) electrolytes resistance ($R_{\Omega}$) and electron transfer resistance ($R_{ET}$).

### *4.3.3.2 Thermo-electrochemical performance*

The fabrication process of thermocells for thermo-electrochemical performance analysis is illustrated in chapter 2.6.2. The acrylic framework (10 × 10 × 2 mm) and Pt electrodes were assembled using epoxy glue (dashed area) to obtain reproducible size, shape and positioning of the gelled electrolytes. The gels themselves were designed to be slightly thicker (2.1 - 2.2 mm) than the frame to ensure a good connection to the Pt electrodes. The thermocell device was then placed between the hot and cold electrodes to provide a temperature gradient. The comparison of thermochemical performance

(current and power density displayed as dashed and solid line respectively) at ΔT = 10 ℃ ($T_c$ = 25 ℃, $T_h$ = 35 ℃) is indicated in Figure 4.10 a. The hot electrode was set to 35 ℃ to simulate the average temperature of human skin, while the cold electrode was varied to simulate the changing ambient environmental temperature. Based on the equation $P = JV$, power density displays a parabola curve *versus* potential with the maximum power density ($P_{max}$) equal to 0.25 $J_{sc}V_{oc}$ [29]. Compared with the non-porous gel electrolyte, the $J_{sc}$ of the freeze-dried porous gel electrolyte was improved from 1.3 to 2.4 A $m^{-2}$ and $P_{max}$ increased from 4.01 to 7.1 mW $m^{-2}$. The $V_{oc}$ of the thermocell describes the $S_e$ at any applied temperature difference, all three gelled electrolytes demonstrated the same $V_{oc}$, equating to equivalent $S_e$. The improved power density of the freeze-dried hydrogel can be attributed to the lower mass transport and electron transfer resistances observed in the EIS measurements, which are also the cause of the higher peak current in the CVs, demonstrating a good correlation between the electrochemical and thermo-electrochemical results. Long-term short-circuit current density outputs (30 mins) of the thermocells is demonstrated in Figure 4.10 b, wherein all samples demonstrate a high initial peak current density, which decreases over time (in line with previous aqueous [30] and gelled [23] thermocells); the current density of these thermocells were found to stabilize after 1000 s. The thermocell with freeze-dried porous gel electrolyte displayed the highest steady-state current density of 1.4 A $m^{-2}$ (*cf.* 1.2 A $m^{-2}$ for the non-porous thermocell). In summary, the freeze-dried porous gel electrolyte with good mechanical properties, lower mass transport and electron transfer resistances and faster diffusion coefficient of redox ions was found to be the optimal host as a solid-state electrolyte, and this was the gel which further testing was performed on.

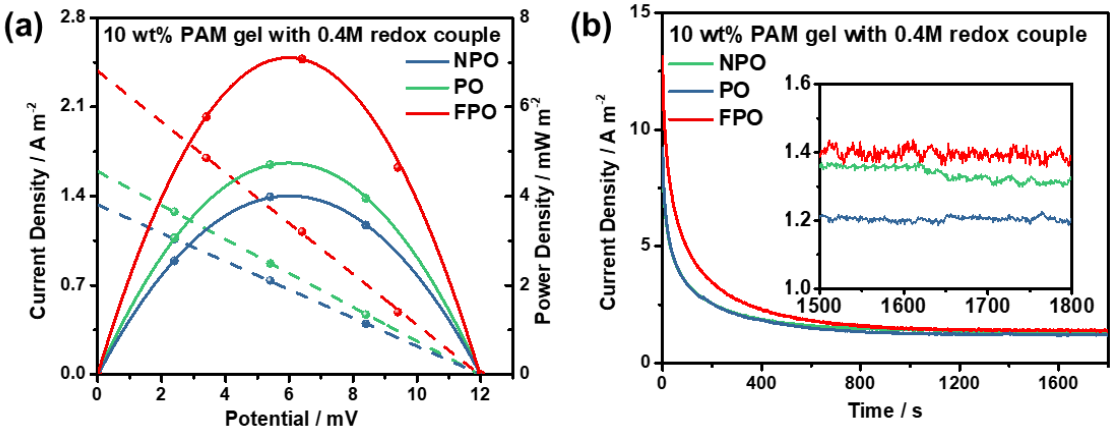


Figure 4.10 A comparison electrochemical activities of non-porous (NPO, blue), porous (PO, green) and freeze-dried porous (FPO, red) gel electrolytes in terms of (a) thermo-electrochemical performance: current (dash) and power (solid) density *versus* voltage, and (b) The long-term short-circuit current density *versus* time (30 mins) at ΔT = 10 ℃ ($T_c$ = 25 ℃, $T_h$ = 35 ℃).

### 4.3.4 Investigation of the introduction of GdmCl in thermocells

#### *4.3.4.1 Open-circuit voltage ($V_{oc}$)*

Under standard conditions within a typical thermocell, the electrolyte concentration is uniformly distributed throughout the solution. When the temperature gradient is applied to the electrodes, this equilibrium is perturbed, as electrolyte migrates toward the electrodes and redox processes are allowed to occur (Figure 4.11 a). The $S_e$ correlates primarily with the solvent-dependent $\Delta S$. Yu *et. al.* [16] have previously reported a significant increase in $S_e$ of a $[Fe(CN)_6]^{3-/4-}$ thermocell with the introduction of guanidinium $[Gdm]^+$. Inspired by this, we introduced a $[Gdm]^+$ salt into our thermocell solution. It was expected that the $[Gdm]^+$ would form complexes with the $[Fe(CN)_6]^{4-}$,

generating crystallization near the cold electrode (top of cell). Simultaneously, $[Gdm]^+$-induced crystallisation occurs, if precipitates and redissolve into $[Gdm]^+$ and $[Fe(CN)_6]^{4-}$ at the hot electrode (bottom of cell). The $[Fe(CN)_6]^{4-}$ associated crystallisation was reported to therefore result in a significant concentration imbalance ($\Delta C_r$) between the two electrodes. Broadly, similar results for the $S_e$ were achieved when measurements were made in the absence of the gel; the $S_e$ was enhanced in the presence of $[Gdm]^+$ due to crystallisation, the $S_e$ was found to be orientation-sensitive, and importantly if the solution was filtered to remove the crystals then the $[Gdm]^+$-induced increase in $S_e$ was decreased significantly.

The experiment was then reproduced in the freeze-dried gel thermocell. The $S_e$ of the thermocell was found to increase with the introduction of GdmCl to the system from 1.2 to 1.5 mV $K^{-1}$ upon addition of 0.5 M GdmCl (Figure 4.11 b&c), reflecting a minor contribution of $\Delta C_r$ relative to $\Delta S$. It is likely that the gel prevented significant contact between the crystals and the electrode, preventing the full increase in $S_e$ expected by the full $\Delta C_r$ effect. Nevertheless, GdmCl addition slightly improved performance.

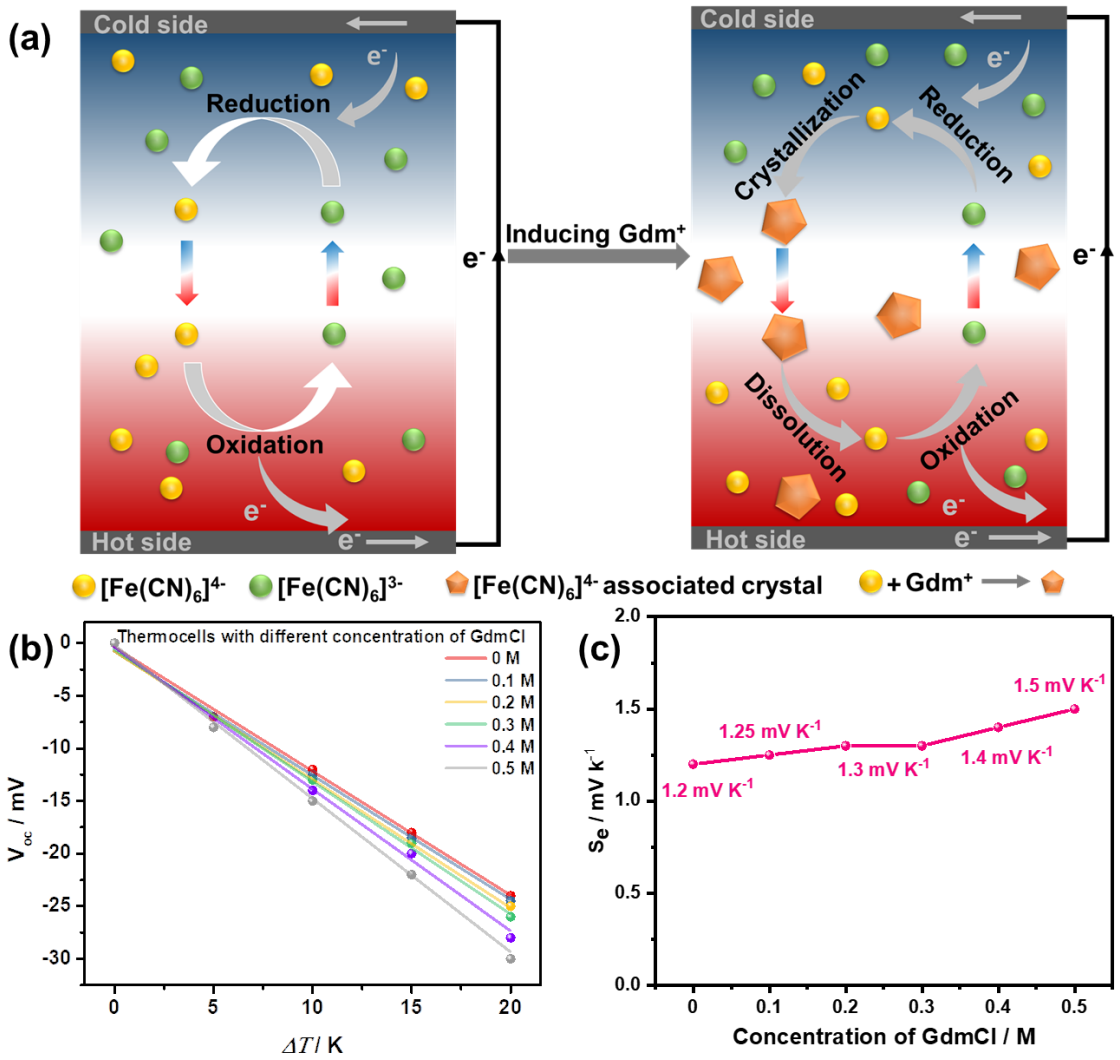


Figure 4.11 (a) A schematic of $Gdm^+$ inducing $[Fe(CN)_6]^{4-}$ crystallization and enhancement of the ΔS in the 0.4 M $K_3Fe(CN)_6/K_4Fe(CN)_6$ system, (b) open-circuit voltage ($V_{oc}$) of thermocells involved various amounts of GdmCl at different values of ΔT, and (c) the Seebeck coefficient ($S_e$) of thermocells involved different amounts of GdmCl.

*4.3.4.2 Thermal conductivity*

In addition, based on a report from Romano *et. al.* [31], [31] the thermal conductivity ($\kappa$) is also an important parameter to consider when evaluating the $V_{oc}$. Therefore, we also

evaluated the relationship between $[Gdm]^+$ crystallization and $\kappa$ (Figure 4.12). The $\kappa$ displays a minor increase from 0.57 W $m^{-1}$ $K^{-1}$ to 0.62 W $m^{-1}$ $K^{-1}$ upon introduction of $[Gdm]^+$. Which demonstrates the increase in $V_{oc}$ (and subsequent $S_e$) was not induced by $\kappa$, and was due to the $\Delta C_r$ effect.

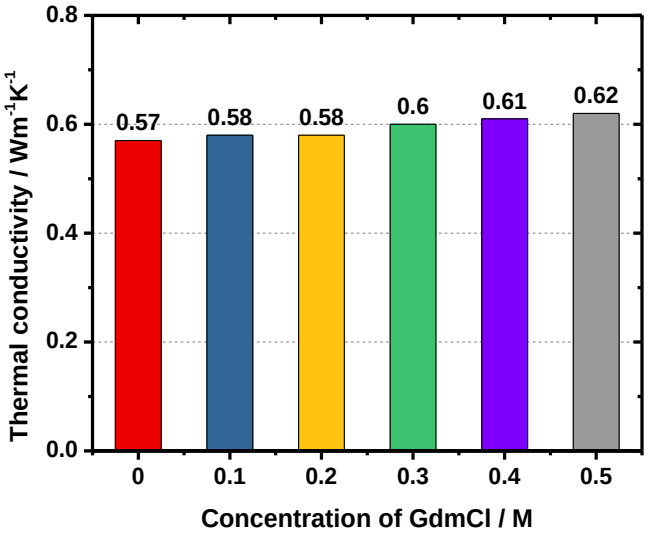


Figure 4.12 The thermal conductivity of gel electrolytes containing varied concentrations of GdmCl.

*4.3.4.3 Thermo-electrochemical performance at different electrode temperatures*

The thermo-electrochemical performance of these systems with various concentration of GdmCl at ΔT = 5 - 20 ℃ ($T_c$ = 15 - 30 ℃, $T_h$ = 35 ℃) was also conducted and are shown in Figure 4.13 a&b. In the range of ΔT = 5 - 10 ℃, 0.2 M GdmCl was found to observe the highest $P_{max}$ (3.02 and 8.33 mW $m^{-2}$ at ΔT = 5 and 10 ℃ respectively). Interestingly, at higher ΔT values, the 0.1 M GdmCl was found to observe the highest power density (17.60 and 29.03 mW $m^{-2}$ at ΔT = 15 and 20 ℃ respectively). The thermocell with 0.5 M GdmCl demonstrated the highest $V_{oc}$, but consistently displayed

some of the worst power densities. This suggests that the crystallisation-improved $V_{oc}$ actually hinders mass transport (through the porous gel), leading to lower $J_{sc}$ and thus $P_{max}$. In contrast, the 0.1 M GdmCl modestly increased $V_{oc}$, but mass transport was not hindered by this process, leading to higher $J_{sc}$ and $P_{max}$ than the system in the absence of $[Gdm]^+$. Therefore, the 0.1 M $[Gdm]^+$ system was taken as the optimised system. Below, we further assess the thermo-electrochemical performance of thermocells with 0.1 M GdmCl.

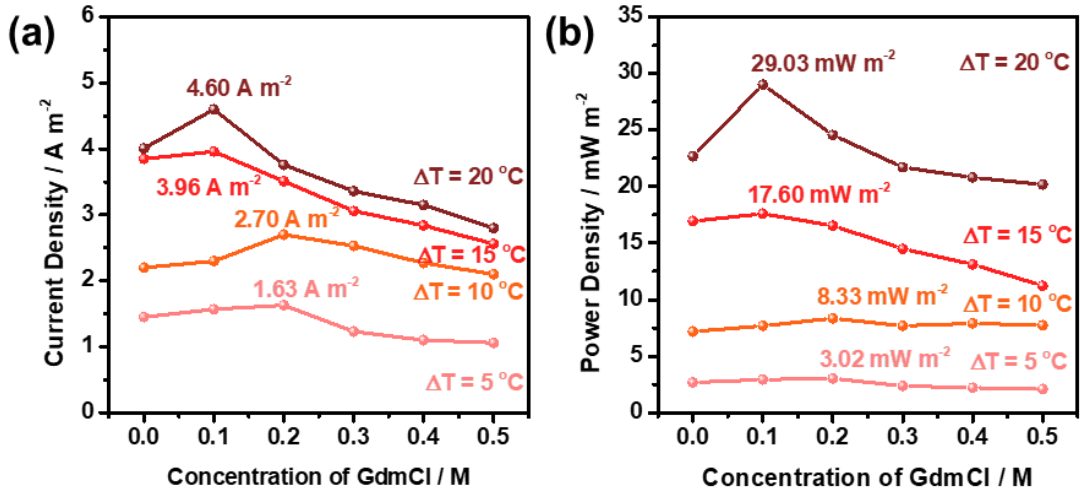


Figure 4.13 The (a) maximum current and (b) power density of thermocells containing variety concentration of GdmCl at different temperature gradients ($T_c$ = 15 - 30 ℃, $T_h$ = 35 ℃).

Figure 4.14 a show the comparison of the thermo-electrochemical performance of thermocells in the presence (black) and absent (red) of 0.1 M GdmCl at ΔT = 10 ℃ ($T_c$ = 25 ℃, $T_h$ = 35 ℃). The system in the presence of $[Gdm]^+$ demonstrates slightly higher $V_{oc}$ from 12 mV to 12.5 mV (driven by 0.1 M GdmCl). The $[Gdm]^+$-containing thermocell also exhibits a corresponding increase in both $J_{sc}$ and $P_{max}$, from 2.2 to 2.4

A $m^{-2}$ and 7.1 to 7.68 mW $m^{-2}$, respectively. The long-time $J_{sc}$ of these thermocells was next measured. As expected, the $[Gdm]^+$-containing system also demonstrates better long-term current density (Figure 4.14 b) that reaches 1.6 A $m^{-2}$ after 30 min, compared to 1.4 A $m^{-2}$ in the absence of $[Gdm]^+$. CVs were also recorded for the $[Gdm]^+$ system; Figure 4.15 shows that despite the crystallisation process occurring because of the $[Gdm]^+$, the electron transfer kinetics is unaffected. The open-circuit voltage of the two systems was also measured over a long time while changing ΔT (5 - 20 ℃), and is shown in Figure 4.14 c. The red and black curves represent the presence or absence of 0.1 M GdmCl, respectively. In the period of 0 - 4800 s, both cold electrode and hot electrodes were both maintained at 35 ℃ (as $T_c$) for 600 s, then the hot electrode temperature was increased in 5 ℃ increments every 600 s up to 55 ℃. Following this, the hot electrode was cooled back to 35 ℃ to re-obtain the ΔT of 0 K. Then, the same electrode that was increased previously was then decreased in temperature in order to increase ΔT (note that this makes the former cold electrode the hot electrode, and is reflected in the change in open circuit voltage from negative to positive). From 5400 s, the (now) hot electrode temperature was fixed at 35 ℃, and the (now) cold electrode temperature reduced until 15 ℃, then return back up to 35 ℃, to reobtain ΔT = 0 ℃. This long-time analysis shows that the $V_{oc}$ of the thermocell containing 0.1 M GdmCl is consistently higher than that of the system in the absence of GdmCl, and with the greatest difference of 24 mV to 26.5 mV at ΔT = 20 ℃. Due to the limitation of 0.1 M $Gdm^+$ on $S_e$ coefficient (1.2 mV $K^{-1}$ to 1.25 mV $K^{-1}$), no significant variation of $V_{oc}$ at ΔT = 5 and 10 ℃ was observed, however, the difference of $V_{oc}$ became obviously with the enlarged temperature differences (ΔT = 15 and 20 ℃). During the period of 0 - 9600 s, $V_{oc}$ improves from 0 mV to 26.5 mV then dropped back to 0 mV, and repeats the cycle again, which demonstrates a quick thermosensitive response of GdmCl in the

thermocells to constantly changing ΔT. This is significant for an ever-changing environmental temperature experienced by a wearable device.

Even though 0.5 M GdmCl improves the $V_{oc}$, $[Gdm]^+$-associated precipitation near the cold electrode weakens the ionic conductivity, and reduces the working area of electrode and/or mobility through the freeze-dried porous gel, resulting in unfavourable thermopower. However, the freeze-dried porous gel thermocell with 0.1 M GdmCl has a similar electroactivity of redox couples, excellent thermo-electrochemical performance and maintains the quick response to changing differences in temperature.

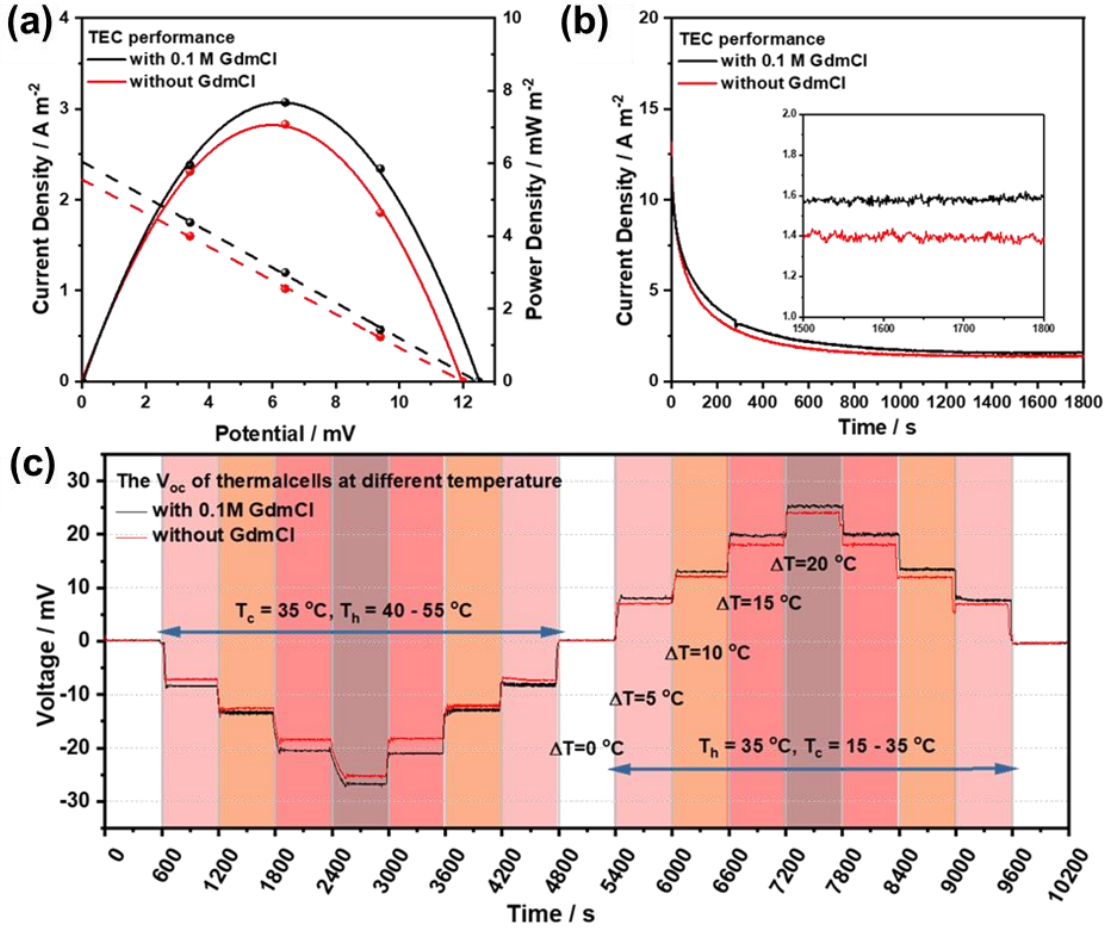

Figure 4.14 Thermo-electrochemical performance (ΔT = 10 ℃, $T_c$ = 25 ℃, $T_h$ = 35 ℃) of thermocells present (black) and absent (red) GdmCl in terms of (a) current (dash) and power (solid) density *versus* voltage, (b) long-term short-circuit current density *versus* time (30 min), and (c) continuous $V_{oc}$ curves under varied temperature differences.

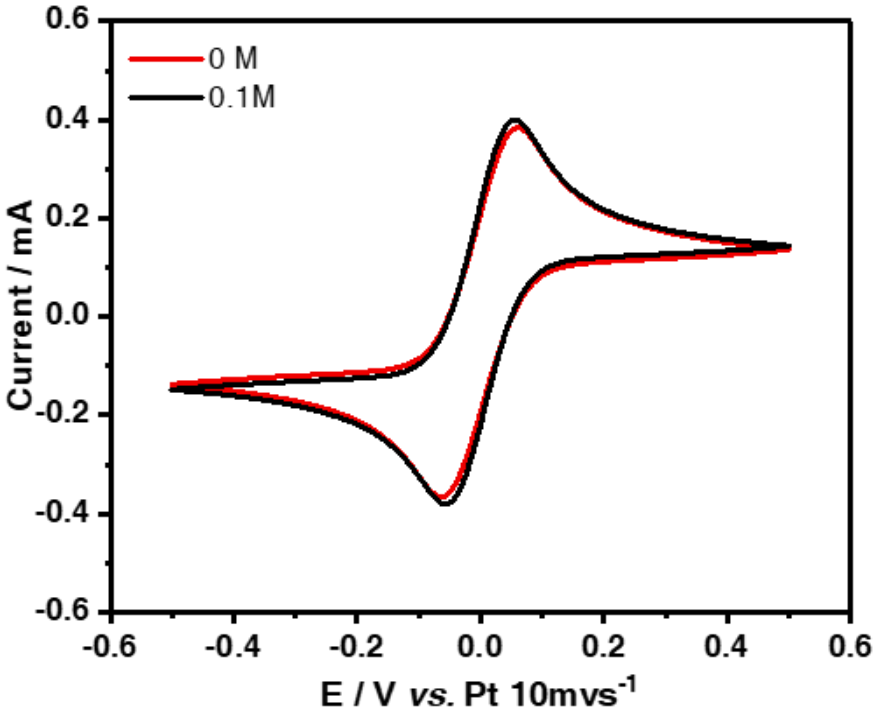


Figure 4.15 Cyclic voltammetry curves (scan rate = 10 mV $s^{-1}$) of gel electrolytes with 0.1 M and without GdmCl.

The difference in temperature applied to the thermocell drives the distinctive precipitation and redissolution process of $[Gdm]^+$-$[Fe(CN)_6]^{4-}$ crystallisation (Figure 4.16). Therefore, we systematically compared the thermo-electrochemical performance of thermocells with varied concentrations of GdmCl at ΔT = 5 - 20 ℃ (Figure 4.17). The blue background indicates the cold electrode ($T_c$) was varied from 15 - 30 ℃ and the hot electrode ($T_h$) was maintained at 35 ℃. Red background refers to the $T_c$ being

maintained at 35 ℃ and $T_h$ varied in the range of 40 - 55 ℃. Both current and power density increased with the ΔT. However, comparing Figure 4.17 c&d, $P_{max}$ is observed to barely change as a function of $T_h$ at ΔT = 5 ℃. However, regardless of the GdmCl concentration, from ΔT = 10 ℃ or more, the thermopower increases with higher $T_h$ values, and the trend is more apparent at greater ΔT values. At ΔT = 20 ℃, the $J_{sc}$ and $P_{max}$ of the thermocell with 0.1 M GdmCl was 4.63 A $m^{-2}$ and 29.03 mW $m^{-2}$ when $T_c$ = 15 ℃. This increases to 5.5 A $m^{-2}$ and 35.2 mW $m^{-2}$ at $T_c$ = 35 ℃, even at an equivalent ΔT of 20 ℃ (Figure 4.18). That is because the higher electrode temperature at the cold electrode accelerates the redox kinetics and reduces the accumulation of crystallised $[Gdm]^+$-$[Fe(CN)_6]^{4-}$ near the cold electrode, resulting in a higher current output.

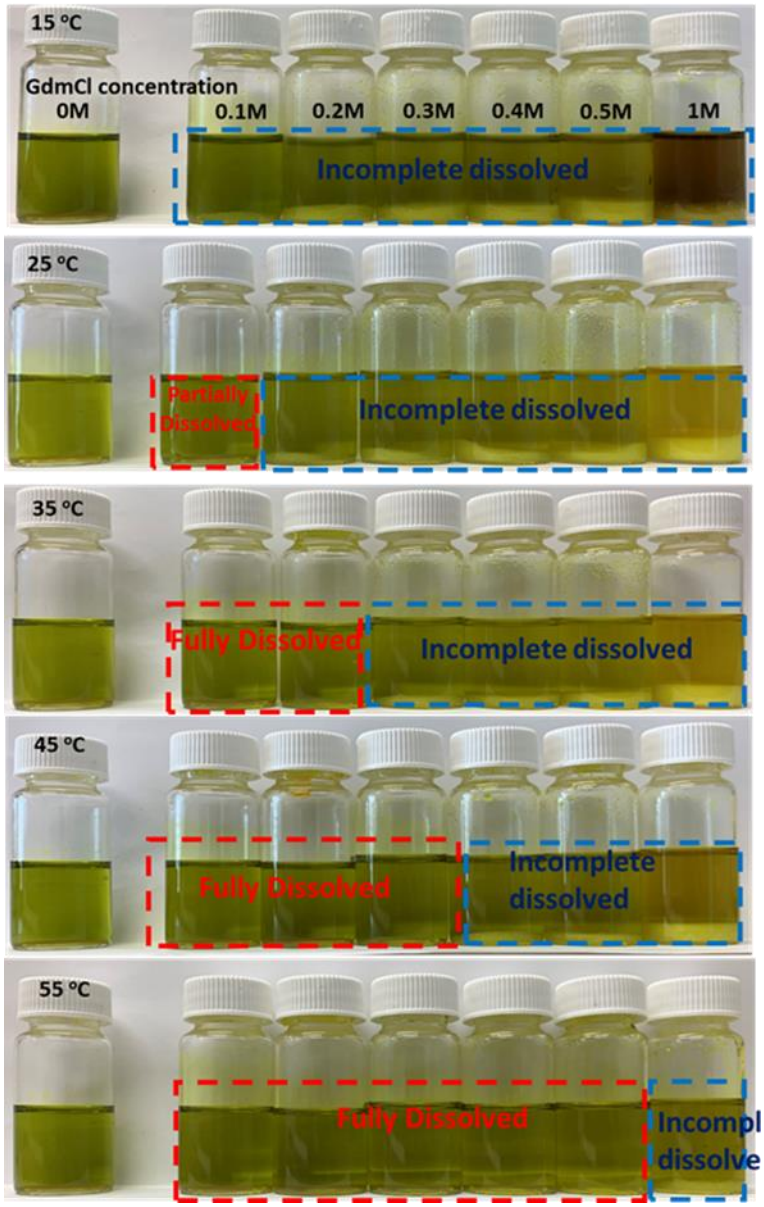


Figure 4.16 The solubility of GdmCl in 0.4 M redox couple aqueous solution at varied temperatures.

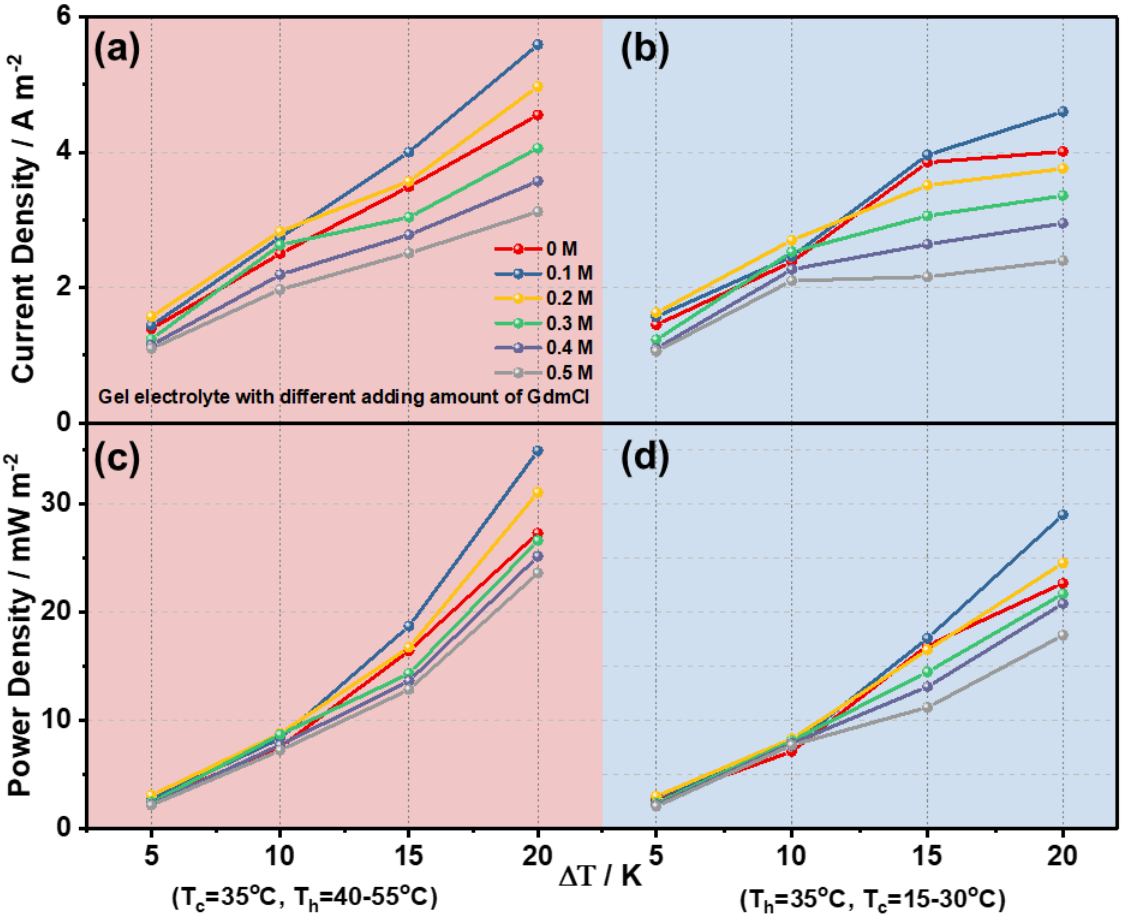


Figure 4.17 The maximum current (a-b) and maximum power (c-d) density of thermocells containing varied concentration of GdmCl at different electrode temperatures (red background: $T_c$ = 35 ℃, $T_h$ = 40 - 55 ℃; blue background: $T_c$ = 15 - 30 ℃, $T_h$ = 35 ℃).

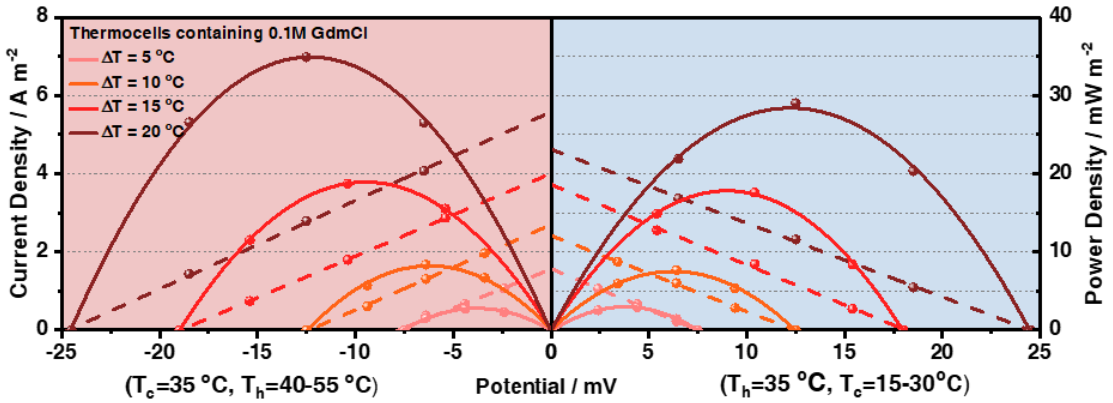

Figure 4.18 Thermo-electrochemical performance of thermocell containing 0.1 M GdmCl showing current (dashed line) and power (solid line) output versus voltage at ΔT = 5, 10, 15, 20 ℃ (red background: $T_c$ = 35 ℃, $T_h$ = 40 - 55 ℃; blue background: $T_c$ = 15 - 30 ℃, $T_h$ = 35 ℃).

### 4.3.5 Fabrication of wearable device

#### *4.3.5.1 Paring the P-N thermocells*

The potential output of individual thermocell is usually limited by the modest range of $S_e$ values (0.1 - 1.5 mV $K^{-1}$) [32] and modest temperature gradient across the single cell. To produce thermocell devices which could power electronic equipment, for example as a wearable device, thermocells are typically arranged electrically in series to significantly increase the output voltage. However, utilising all p-type or all n-type thermocells in series requires complicated wiring to avoid a thermal short-circuit. To avoid these issues, n-type and p-type thermocells are utilised electrically in series but crucially thermally parallel [32-34]. The n-type thermocell used for this was prepared through soaking the freeze-dried porous gel into the optimized $Fe^{2+}/Fe^{3+}$-HCl aqueous solution that we previously reported (Figure 4.19) [35], were fabricated with Pt electrodes, and connected *via* sputter-coated Pt.

Here, a typical pair of p-n thermocells were fabricated and examined, both individually and in series (Figure 4.20 a). As seen in Figure 4.20 b, the voltage of the p-n cells exhibits an effective $S_e$ at 1.93 mV $K^{-1}$, which is approximately 94.6% of the absolute $S_e$ of the combined p-type cell (-1.25 mV $K^{-1}$) and n-type cell (+0.79 mV $K^{-1}$); the slight decrease is due to the increased resistance of the additional electrical connections[36]. As

expected, the comparable current and long-term short-circuit current output of p-n cells equated to almost the combined current from the individual p-type and n-type cells at ΔT = 10 ℃ ($T_c$ = 25 ℃, $T_h$ = 35 ℃) (Figure 4.20 c and Figure 4.21 a). The absolute power was applied because the power output of single N-type and P-type thermocells are different. If the unified the normalized power was used, which represented the average number of the power output of single P-type and single N-type, which can not reflect the actual power output of each type of thermocells. Another reason is that the increased resistance of the additional electrical connections would also slight the power output, which is an inaccurate evaluation for array thermocells connected in series. While the overall power output is theoretically doubled by connecting thermocells in series, here the total $P_{max}$ increased 193% (rather than 200%) due to the internal resistance mentioned above[32,33]. The P-N paired thermocell also produced stable $J_{sc}$ and $V_{oc}$ during 12 h of testing, which suggested that stability of performance can be achieved in long-term operation (Figure 4.21 b). Further, the P-N combined thermocell shows the expected parabolic absolute power output *versus* voltage and a linear current output *versus* voltage relationships under different temperature gradients (ΔT = 5 - 20 ℃) in Figure 4.20 d. These results demonstrate that the P-N systems combine effectively and is an effective combined thermocell at various temperatures, showing the potential to power supply for real self-powered wearable electronics.

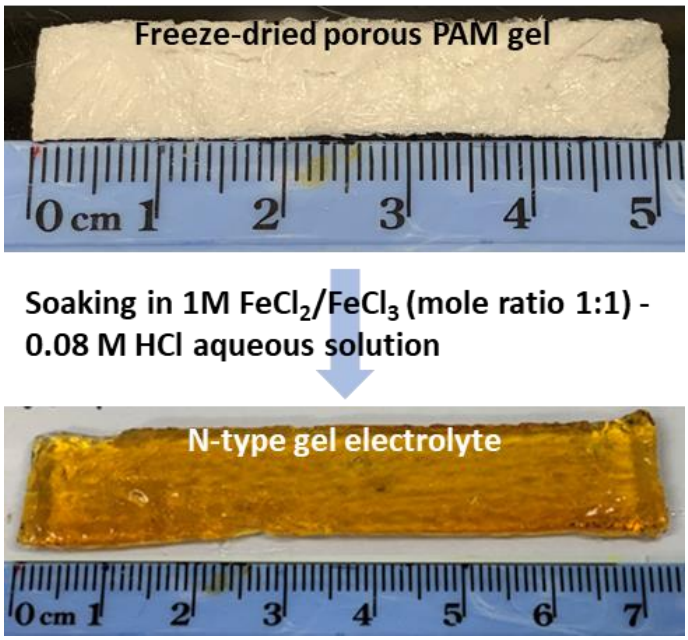


Figure 4.19 An illustration of preparation of the n-type gel electrolyte

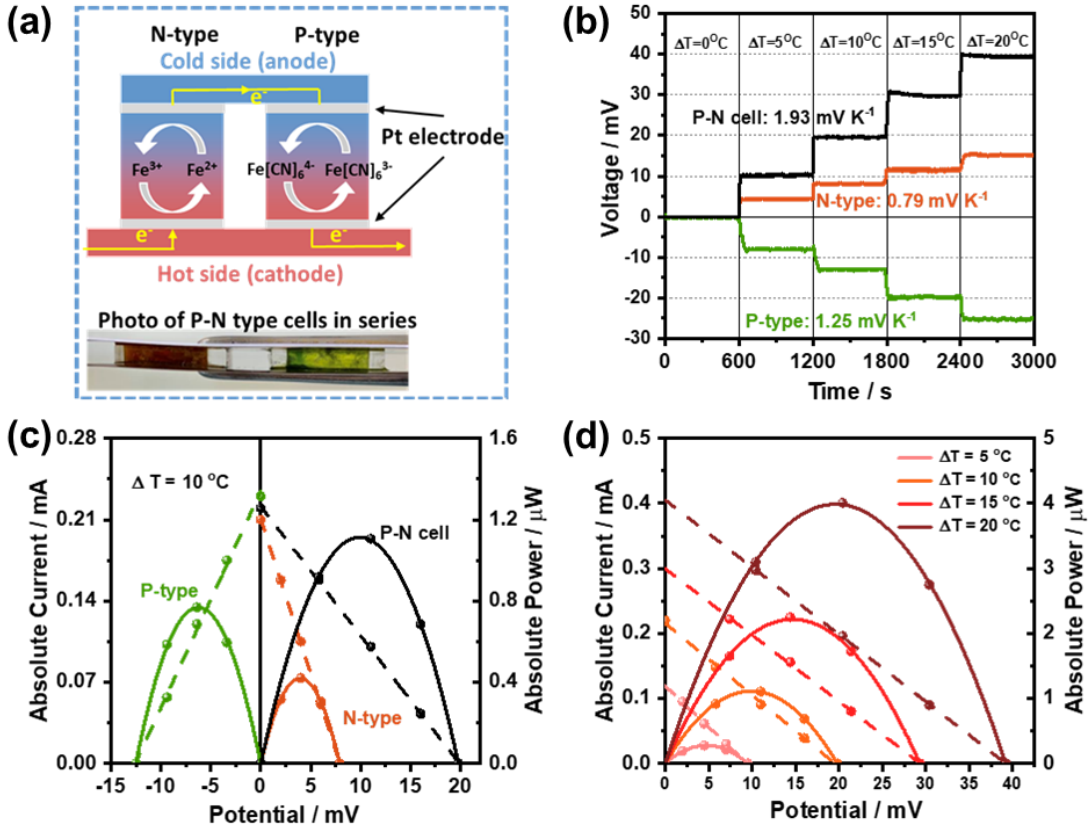

Figure 4.20 A pair of p-n cells. (a) Schematic illustration and photo of the p-type and n-type device connected in series (p-n cell). Thermo-electrochemical performance of the p-type, n-type and p-n cells in terms of (b) voltage at different ΔT (5 - 20 ℃), (c) current (dashed line) and power (solid line) output versus voltage at ΔT = 10 ℃ ($T_c$ = 25 ℃, $T_h$ = 35 ℃), and (d) current (dashed line) and power (solid line) output versus voltage of p-n cell at different ΔT.

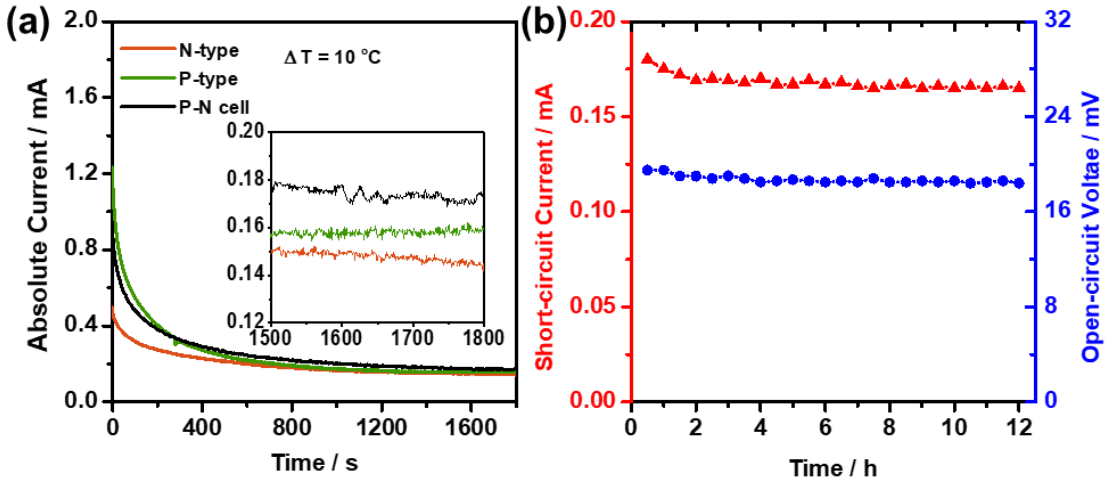


Figure 4.21 (a) The long-term performance (short circuit current versus time) of the n-type (dark yellow), p-type (green) and p-n cell (black). (b) Long-term operation stability of the paired N- and P-type thermocell (red: short-circuit current and blue: open-circuit voltage) for 12 h at ΔT = 10 ℃ ($T_c$ = 25 ℃, $T_h$ = 35 ℃).

### *4.3.5.2 The power conversion efficiency ($\eta_r$)*

The power conversion efficiency ($\eta$) refers to the ratio of the maximum electrical output power ($P_{max}$) to the heat flux through the cell:

$$\eta = P_{max} / \left( kA \cdot \frac{\Delta T}{d} \right)$$

The Carnot-relative efficiency ($\eta_r$) of thermocell is a more standardized method to evaluate the energy conversion efficiency ($\eta$) at different temperature excluding the effect of temperature and temperature itself:

$$\eta_r = \eta / (\Delta T / T_H)$$

Where $k$ is the thermal conductivity ($Wm^{-1}K^{-1}$), $A$ is the electrode surface ($m^2$), $d$ is the electrode separation distance (meter, m), $T_H$ is the hot-side temperature (K), ΔT is the temperature difference (K) [16].

The power conversion efficiency ($\eta$) was calculated in Figure 4.22. The Carnot-relative efficiency ($\eta_r$) of N-type, P-type, and P-N in-series thermocells is 0.008%, 0.004% and 0.006% respectively, which is lower than thermocells used aqueous electrolytes [37,38]. Additionally, the relative conversion efficient largely depends on the electrode separation ($d$). The closer interelectrode separation ensures correspondingly high rates of heat flow and results in a well below optimum power conversion efficiency. A wearable device should satisfy the portable and convenient properties, therefore, the thickness was controlled at 2 mm. The thin wearable thermocell devices cause the lower conversion efficiency than thermocells used in different applications.

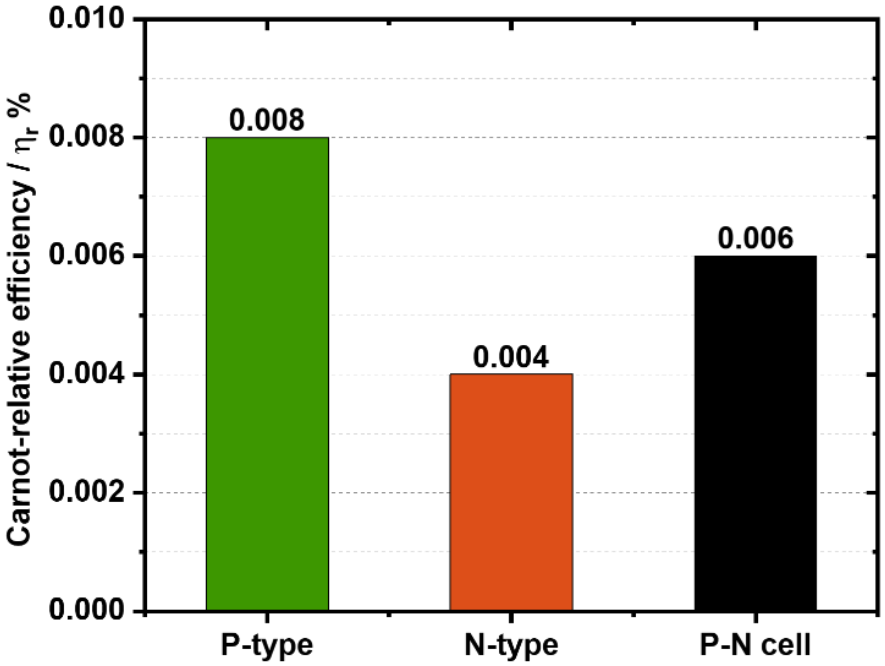


Figure 4.22 The Carnot-relative efficiency ($\eta_r$) of single N-type, P-type, and P-N in-series thermocells.

*4.3.5.3 Prototyping multiple P-N Cells*

To further demonstrate the utility of our combined p-n-thermocells, a larger array was designed (Figure 4.23 a). It used sputter coated Pt as electrodes and interconnection between individual thermocells. PMMA frames (L × W × T = 10 × 10 × 2 mm) were placed as spacers between the two electodes, and held in place by epoxy resin (4 pairs of p-n cells connected in series, Figure 4.23 b). The multiple p-n cell connected in series was fabricated (3 × 4 pairs of p-n cells, Figure 4.23 a) and used to both charge a supercapacitor or light up a LED (whilst in conjunction with a voltage booster) at a 10 ℃ temperature gradient. A supercapacitor and a voltage booster were applied here because temperature gradients are varied during practical applications of wearable devices, which leads to unstable power output. The supercapacitor was used as an energy storage

device here, which can be charged by the array thermocells and output steady current and voltage. Furthermore, the voltage booster used in this experiment is for increasing the voltage in order to light an LED, while the voltage booster is not necessary for all electrical devices. A large array of P-N paired cells could be manufactured to power the electronic devices that need a higher voltage. On the other hand, the voltage booster is a small electrical component (roughly 5 mm × 5 mm), which is easy to incorporate in any equipment. The expandable adaptivity of multiple p-n cells was measured at ΔT = 10 ℃, by expanding up to 12 pairs (Figure 4.23 c and Figure 4.24). The $V_{oc}$ (black curve) of thermocell arrays linearly increase from 19.3 (1 pair) to 228 mV (12 pairs). The absolute current output (red curve) gradually reduces with increasing the number of p-n pairs. Therefore, the rate of increasing power output with increasing pairs (blue curve) is solely due to the increase in output voltage. A device of multiple p-n cells also enables charging of commercial supercapacitors (C = 22, 47, 100 and 470 mF) to >220 mV (Figure 4.23 d). The charge rate of the 22 - 100 mF supercapacitors was fast, and the expected voltage could be reached in 5 mins. The largest capacitor (470 mF) took a longer time to reach the desired voltage (*ca.* 100 min), demonstrating how different capacitors could be applied to reflect the different durations that wearable devices could be worn before being removed (and remaining powered *via* the stored capacitance).

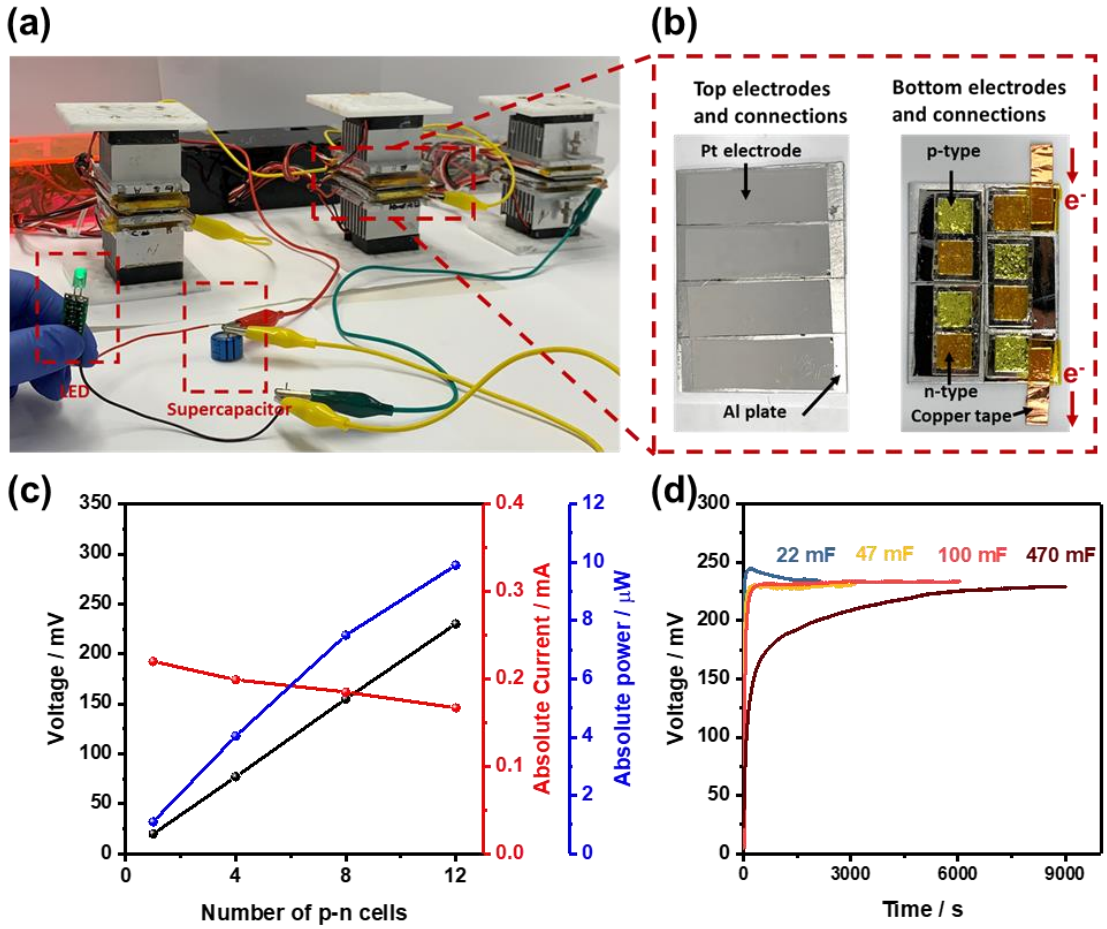


Figure 4.23 (a) Demonstration of thermally charged supercapacitors illuminating a green LED (arrays with 3 × 4 pair p-n cells connected in series), and (b) photographs of 4 pair p-n cells connected in series. (c) Thermoelectrochemical performance of multiple pairs of p-n cells at $\Delta T$ = 10 K, and (d) 12 pair of p-n cells charging capacitors and supercapacitors with different capacitance.

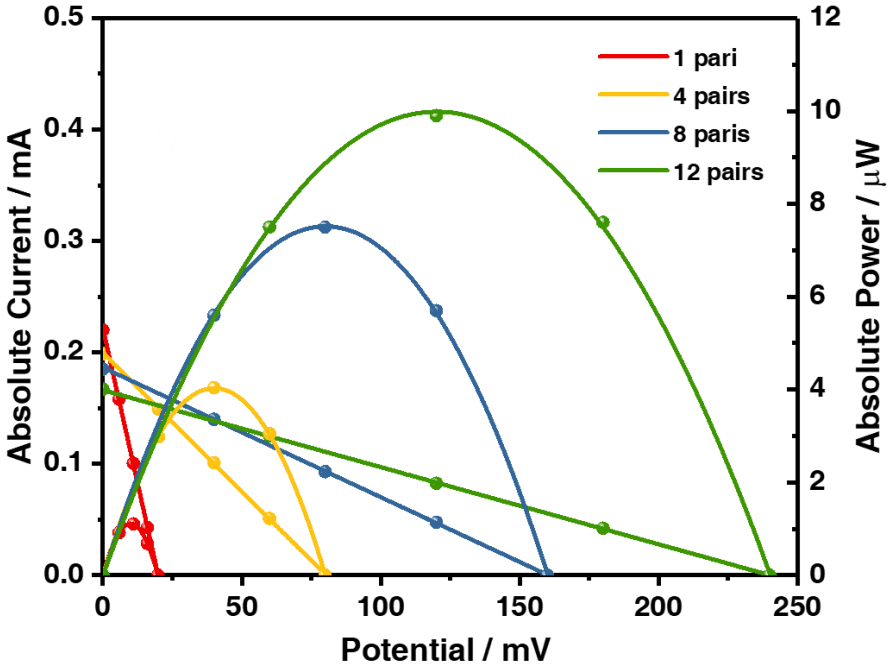


Figure 4.24 1 to 12 serial pairs of n-p cells TEC performance at ΔT = 10 °C.

#### *4.3.5.4 Flexible and wearable P-N Cells*

For harvesting human body heat *via* a wearable thermocell, a flexible strap design that conforms to the surface of the skin is highly desirable and was thus designed and prepared. The ambient air electrodes were slightly more separated than the body heat electrodes, to achieve the degree of curvature required to make this device (Figure 4.25 a). As a demonstration of our device, one of our researchers wore a single strap thermocell array (9 pairs of p-n thermocell) on a wrist. The wearable thermocell device could charge a 100 mF supercapacitor during long-term wear and power a LED when in combination with a voltage booster (Figure 4.25 b). This demonstration illustrated the potential effectiveness of human body heat to supply energy for certain self-powered epidermal electronics.

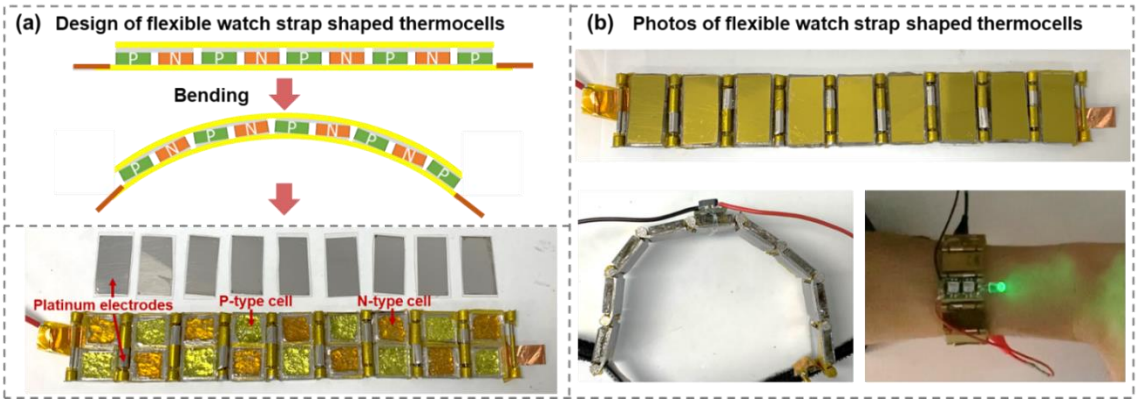


Figure 4.25 Flexible and wearable p-n cells. (a) Design and (b) photographs of the flexible watch-strap shaped thermocell for body-heat harvesting.

## 4.4 Conclusion

In this report, we have designed and synthesised a porous gel as a host for redox-active electrolyte, by using a NaAc template and freeze-drying treatment. This produced a gel that has high ionic conductivity, fast diffusion of electrolyte and acceptable mechanical properties for wearable devices. GdmCl was investigated in this system to induce crystallisation and enhance the $S_e$ and power output of the thermocell. The optimised thermocell contained 0.1 M GdmCl. The long-time measurement of $V_{oc}$, thermogalvanic current and power density was measured at various temperature gradients. By varying the temperature gradient of a single electrode to become both the hot and cold electrode, while maintaining the other electrode at 35 ℃, fast responses were observed with respect to the output voltage, demonstrating the effectiveness of our gels for wearable applications using an altering ambient electrode. N-type gels were also prepared and used in series with the p-type thermocell, demonstrating an output voltage of 0.23 V at $\Delta T$ = 10 ℃, for 12 number of pairs. Finally, we demonstrated a strap-shaped thermocell that can be worn on the wrist. This thermocell device was demonstrated by charging a

commercial supercapacitor and by illuminating an LED light. This thermocell design has therefore been demonstrated as a wearable device and could provide an approach towards future wearable thermocells in the future.

The wearable thermocell on human body heat harvesting is a novel research area, especially in gel electrolytes, which is an ideal candidate for wearable devices due to the safety. However, the ionic conductivity of gel electrolytes is limited compared with aqueous electrolytes. Porous gels are proposed as a potential strategy to address this challenge, which provide the porous channel to facilitate the ions transfer in gel electrolytes. The stretchability of gel electrolytes is essential to evaluate the practical applications of gel electrolytes. Although, the PAM porous structure gel electrolyte can be tensile over 100%, the ultra-stretchable gel electrolytes that can move and be attached to joints or body parts are also urgent to be exanimated in gel systems in the next chapter.

## 4.5 References


[1] Y. Zhou, Y. Liu, M. A. Buckingham, S. Zhang, L. Aldous, S. Beirne, G. Wallace, J. Chen, *Electrochem. commun.* **2021**, *124*, 106938.

[2] M. A. Buckingham, F. Marken, L. Aldous, *Sustain. Energy Fuels* **2018**, *2*, 2717.

[3] D. Wang, H. Li, Z. Liu, Z. Tang, G. Liang, F. Mo, Q. Yang, L. Ma, C. Zhi, *Small* **2018**, *14*, 1.

[4] H. Li, Z. Liu, G. Liang, Y. Huang, Y. Huang, M. Zhu, Z. Pei, Q. Xue, Z. Tang, Y. Wang, B. Li, C. Zhi, *ACS Nano* **2018**, *12*, 3140.

[5] Y. Zhao, Y. Alsaid, B. Yao, Y. Zhang, B. Zhang, N. Bhuskute, S. Wu, X. He, *Adv. Funct. Mater.* **2020**, *1909133*, 1.

[6] G. Shao, D. A. H. Hanaor, X. Shen, A. Gurlo, *Adv. Mater.* **2020**, *32*, 1907176.

[7] X. Liu, O. O. Taiwo, C. Yin, M. Ouyang, R. Chowdhury, B. Wang, H. Wang, B. Wu, N. P. Brandon, Q. Wang, S. J. Cooper, *Adv. Sci.* **2019**, *6*, 1.

[8] J. Wei, C. Yin, H. Wang, Q. Wang, *J. Mater. Chem. A* **2017**, *6*, 58.

[9] E. H. B. Anari, M. Romano, W. X. Teh, J. J. Black, E. Jiang, J. Chen, T. Q. To, J.

Panchompoo, L. Aldous, *Chem. Commun.* **2016**, *52*, 745.

[10] V. Zinovyeva, S. Nakamae, M. Bonetti, M. Roger, *ChemElectroChem* **2014**, *1*, 426.

[11] T. J. Abraham, D. R. MacFarlane, J. M. Pringle, *Energy Environ. Sci.* **2013**, *6*, 2639.

[12] N. Jiao, T. J. Abraham, D. R. MacFarlane, J. M. Pringle, *J. Electrochem. Soc.* **2014**, *161*, D3061.

[13] T. Kim, J. S. Lee, G. Lee, H. Yoon, J. Yoon, T. J. Kang, Y. H. Kim, *Nano Energy* **2017**, *31*, 160.

[14] P. F. Salazar, S. T. Stephens, A. H. Kazim, J. M. Pringle, B. A. Cola, *J. Mater. Chem. A* **2014**, *2*, 20676.

[15] J. J. Fillion, J. F. Brennecke, *J. Chem. Eng. Data* **2017**, *62*, 1884.

[16] B. Yu, J. Duan, H. Cong, W. Xie, R. Liu, X. Zhuang, H. Wang, B. Qi, M. Xu, Z. L. Wang, J. Zhou, *Science (80-. ).* **2020**, *370*, 342.

[17] C. Baldock, L. Rintoul, S. F. Keevil, J. M. Pope, G. A. George, *Phys. Med. Biol.* **1998**, *43*, 3617.

[18] M. K. Gupta, R. Bansil, *J. Polym. Sci. Part A-2, Polym. Phys.* **1981**, *19*, 353.

[19] W. Li, X. Li, X. Zhang, J. Wu, X. Tian, M. J. Zeng, J. Qu, Z. Z. Yu, *ACS Appl. Energy Mater.* **2020**, *3*, 9408.

[20] J. Guo, X. Liu, N. Jiang, A. K. Yetisen, H. Yuk, C. Yang, A. Khademhosseini, X. Zhao, S. H. Yun, *Adv. Mater.* **2016**, *28*, 10244.

[21] X. Sun, F. Yao, C. Wang, Z. Qin, H. Zhang, Q. Yu, H. Zhang, X. Dong, Y. Wei, J. Li, *Macromol. Rapid Commun.* **2020**, *41*, 1.

[22] R. E. Del Sesto, T. M. McCleskey, A. K. Burrell, G. A. Baker, J. D. Thompson, B. L. Scott, J. S. Wilkes, P. Williams, *Chem. Commun.* **2008**, *10*, 447.

[23] J. Wei, G. Wei, Y. Shang, J. Zhou, C. Wu, Q. Wang, *Adv. Mater.* **2019**, *31*, 1.

[24] M. A. Buckingham, S. Zhang, Y. Liu, J. Chen, F. Marken, L. Aldous, *ACS Appl. Energy Mater.* **2021**, *4*, 11204.

[25] K. Ogino, H. Sato, K. Tsuchiya, H. Suzuki, S. Moriguchi, *J. Chromatogr. A* **1995**, *699*, 59.

[26] K. Hu, J. M. Dickson, *J. Memb. Sci.* **2007**, *301*, 19.

[27] A. J. Bard, L. R. Faulkner, *Double-Layer Structure and Adsorption*, **2001**.

[28] O. A. González-Meza, E. R. Larios-Durán, A. Gutiérrez-Becerra, N. Casillas, J. I. Escalante, M. Bárcena-Soto, *J. Solid State Electrochem.* **2019**, *23*, 3123.

[29] J. S. Park, J. H. Choi, J. J. Woo, S. H. Moon, *J. Colloid Interface Sci.* **2006**, *300*, 655.

[30] J. Wu, J. J. Black, L. Aldous, *Electrochim. Acta* **2017**, *225*, 482.

[31] M. A. Buckingham, L. Aldous, *J. Electroanal. Chem.* **2020**, *872*, 114280.

[32] M. S. Romano, S. Gambhir, J. M. Razal, A. Gestos, G. G. Wallace, J. Chen, *J. Therm. Anal. Calorim.* **2012**, *109*, 1229.

[33] M. A. Buckingham, K. Laws, J. T. Sengel, L. Aldous, *Green Chem.* **2020**, *22*, 6062.

[34] Y. Liu, H. Wang, P. C. Sherrell, L. Liu, Y. Wang, J. Chen, *Adv. Sci.* **2021**, *8*, 1.

[35] M. A. Buckingham, K. Laws, E. Cross, A. J. Surman, L. Aldous, *Green Chem.* **2021**, *23*, 8901.

[36] M. Al Maimani, J. J. Black, L. Aldous, *Electrochem. commun.* **2016**, *72*, 181.

[37] T. I. Quickenden, Y. Mua, *J. Electrochem. Soc.* **1995**, *142*, 3985.

[38] R. Hu, B. A. Cola, N. Haram, J. N. Barisci, S. Lee, S. Stoughton, G. Wallace, C. Too, M. Thomas, A. Gestos, M. E. Dela Cruz, J. P. Ferraris, A. A. Zakhidov, R. H. Baughman, *Nano Lett.* **2010**, *10*, 838.

# Chapter 5 Highly stretchable double-network gel electrolytes for wearable thermo-electrochemical cells

## 5.1 Introduction

Chapter 4 describes thermocells comprised of polyvinyl alcohol (PVA), carboxymethyl cellulose (CMCs) [1–5], and polyacrylamide (PAM) [6] as polymer frameworks for gel electrolytes. The $K_3[Fe(CN)_6]/K_4[Fe(CN)_6]$ and $FeCl_2/FeCl_3$ are commonly used as P- and N-type redox couples in thermocells due to their high $S_e$ of -1.4 and 7.8 mV $K^{-1}$, respectively in solid-state electrolytes [3]. However, PVA, CMCs, or PAM based gel electrolytes are also inevitably compromised by their poor tensile properties (strain 100-110%) [3,4,6]. The development of gel electrolytes that exhibit excellent stretchability and acceptable electrochemical performance is one of the most crucial factors for the manufacture of wearable devices. In addition, the selection of a polymer host that is compatible with the redox couples is a key issue to address, including its pH sensitivity, low solubility, thermal stability, and mechanical properties [3,6].

Chitosan (CS) is an attractive neutral polymer and an excellent candidate for biocompatible utilization [7]. However, its drawback is its low water solubility [8]. Carboxymethyl chitosan (CMCs) is a derivative modified from CS, wherein the hydroxyl and amino groups in the CS main chains are replaced by carboxymethyl moieties via chemical modification, which alters the solubility of CS [8]. The numerous free amino and carboxyl groups in CMCs polymers modify their properties and enable gelation via multiple chemical reactions [9]. Moreover, the water-soluble polymer polyacrylamide (PAM) is a popular synthetic polymer that offers a number of advantages, including flexibility, porous structure, thermal stability, non-toxicity, biocompatibility stability in the presence of metal salts, and acceptable ionic

conductivity [10–14], which is favorable in many fields, such as e-skin [15], soft tissue engineering [16], and thermoelectric devices [17].

Despite this, gel electrolytes always encounter challenges, such as poor mechanical properties and unfavorable thermo-electrochemical performance [18,19]. The friability and easily fragmented hydrogels comprised of CMCs and PA are unsuitable for extreme stretching [20] and the network structures of hydrogels are prone to disassociation due to the instability of the dynamic bonds (*e.g.* hydrogen bonds and ionic bonds) in highly concentrated electrolytes [21]. Furthermore, mass transport is restricted in gel electrolytes, resulting in a lower power output density than liquid electrolytes [6,22]. The polymer concentration must achieve a trade-off between mechanical toughness to maintain gel formation and TECs performance [3]. Therefore, the rational design of gel electrolytes not only guarantees robust mechanical properties that can adapt to practical applications, but also minimizes the sacrifice in the TECs power output [21].

The introduction of a dissipation mechanism on a molecular level to increase the total viscoelastic dissipation of 3D network structures is crucial for the synthesis of hydrogels with excellent mechanical properties [23]. Multiple techniques have been proposed for energy dissipation, including interpenetrating network hydrogels [24], double network hydrogels [25–27], nanocomposite hydrogels [28], and topological hydrogels [29]. Among these, double-network (DN) crosslinking is an effective strategy used for a diverse range of applications. Normally, the DN hydrogel is synthesized using a two-step method, wherein rigid and fragile sacrificial bonds are generated in the first network to dissipate energy and the second network provides elasticity to the hydrogels [30]. Numerous contributions have been made to the DN of CMCs and PAM.

The carboxyl groups in CMCs are ionically coordinated with $Fe^{3+}$ to form a rigid network to ameliorate the mechanical properties of the hydrogel [31]. Zhang et al. physically crosslinked CMCs with polyaniline (PANI), which served as the first network [9]. Extra polymer alginate was introduced to form the first ionic network upon crosslinking with $Ca^{2+}$ [20]. The active amino and carboxyl groups in CMCs facilitate the chemical crosslinking reactions involving copolymerization with PAM via covalent bonds in the second network [9,20]. Regardless of the introduction of additional polymers and ions, the formation of gels via physical and ionic crosslinking results in poor TECs performance or dissociation of the gels. With these concerns in mind, the aldehyde groups in glutaraldehyde (GA), which act as crosslinkers, react with the amine groups in CMCs to generate reversible and dynamic covalent imine bonds *via* a Schiff reaction, which replaces the unstable ionic bonds to reinforce the mechanical properties during the first crosslinking process[30,32] and avoid the introduction of extra metal ions and polymers.

Herein, we designed a stretchable and tough CMCs-PAM DN gel electrolyte with a semi-interpenetrating structure and capability to accommodate the N- and P-type redox couple without affecting the gelation process. The excellent mechanical properties of gel electrolytes are beneficial for restoring the structure of the thermocells after deformation. The TECs performance of both the N- and P-cells was boosted using PEDOT:PSS textile electrodes with porous structures and was further examined under deformation to simulate their practical applications. The novel thermocells consist of gel electrolytes integrated with PEDOT:PSS textile electrodes to address the poor mechanical and TECs performance challenges observed in current thermocells.

## 5.2 Experimental

### 5.2.1 Synthesis of double-network CMCs:PAM gel electrolytes

The synthetic processes of the double-network CMCs:PAM gel electrolytes are described in Section 2.5.3.

### 5.2.2 Preparation of PEDOT:PSS textile electrodes

The preparation processes of the PEDOT:PSS textile electrodes are described in Chapter 2.5.5.

### 5.2.3 Electrochemical measurements

All the electrochemical measurements were performed according to the procedures presented in Chapter 2.4

### 5.2.4 Device assembly

The flexible wearable thermocell devices were assembled using gel electrolytes, Pt, and textile electrodes, as described in Chapter 2.6.3.

## 5.3 Results and discussion

### 5.3.1 Investigation of CMCs:PAM double-network gel electrolytes

#### *5.3.1.1 Mechanism*

The synthesis process of the DN CMCs-PAM hydrogel electrolyte is illustrated in Figure 5.1. The mixed CMCs-AM precursor solution (Figure 5.1 a) was placed in an oven heated at 50 ℃ for 4 h to carry out the first crosslinking process (Figure 5.1 b). The CMCs-PAM gels were then soaked in a mixed AM, KPS, and MBA aqueous solutions for free swelling until a penetration equilibrium was reached (Figure 5.1 c). Subsequently, the sufficiently absorbed CMCs-PAM gels were placed in an oven for the second crosslinking process (50 ℃ 4 h), which was carried out in the presence of the 3D network structure of the first crosslinked CMCs-PAM gel. Therefore, highly stretchable CMCs-PAM hydrogels with semi-interpenetrating network structures were synthesized (Figure 5.1 d). The double crosslinking process occurred during the first crosslinking step, including intramolecular crosslinking of the CMCs by GA, free radical polymerization of the AM monomers, and interactions between the CMCs and PAM chains (Figure 5.1 e) [25,30].

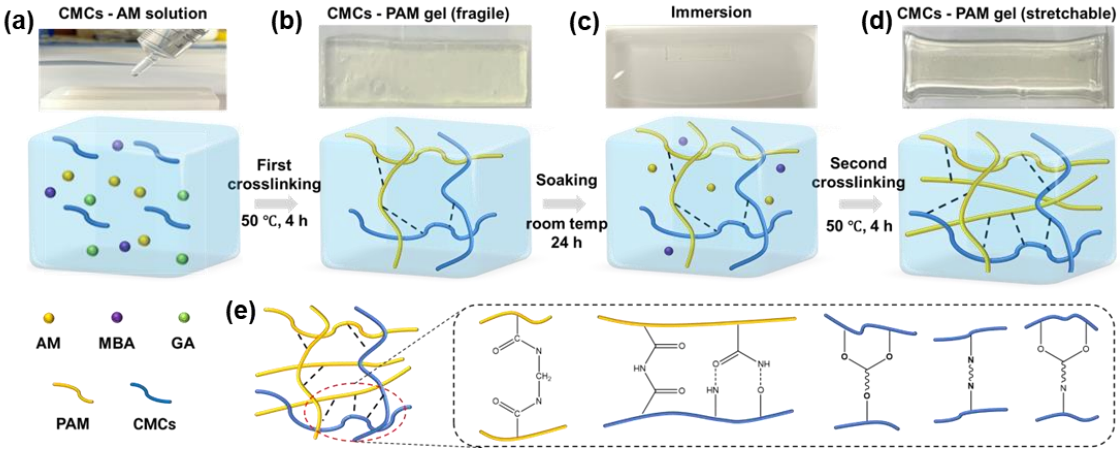


Figure 5.1 Preparation and mechanism of the CMCs-PAM gel electrolytes. (a) Illustration of the CMCs-AM precursor gel solutions. Photographs of CMCs-PAM gels in terms of (b) first crosslinking, (c) immersion process, and (d) second crosslinking. (e) Chemical crosslinking of intramolecular and intermolecular of CMCs and PAM

polymers including CMCs intramolecular crosslinking, PAM 3D network structures, and interactions between CMCs and PAM chains.

In the first crosslinking step, GA is a conventional crosslinker that contains two aldehyde groups at the end of each molecule, which react with amino groups and hydroxyl groups in the branch chains of CMCs to generate imine bonds and either semi-acetals or acetal-type rings, respectively (Figure 5.2 a). [33,34] Furthermore, DN products comprised of CMCs backbones and PAM chains were copolymerized through GA in the first crosslinking step (Figure 5.2 b). [35] Simultaneously, the interaction between the CMCs and PAM chains based on the positively charged amino groups and negatively charged carboxyl groups form electrostatic interactions and hydrogen bonds [9,31,33]. In the second crosslinking, the crosslink mainly occurred through the free radical polymerization of a neutral AM monomer initiated by APS in the presence of an MBA crosslinker (Figure 5.2 c). [6] The resulting polymeric gel is actually IPN of firstly-polymerized PAM and CMC, after which underwent the crosslinking, again, with MBA on the secondly-polymerized PAM chains.

(a)

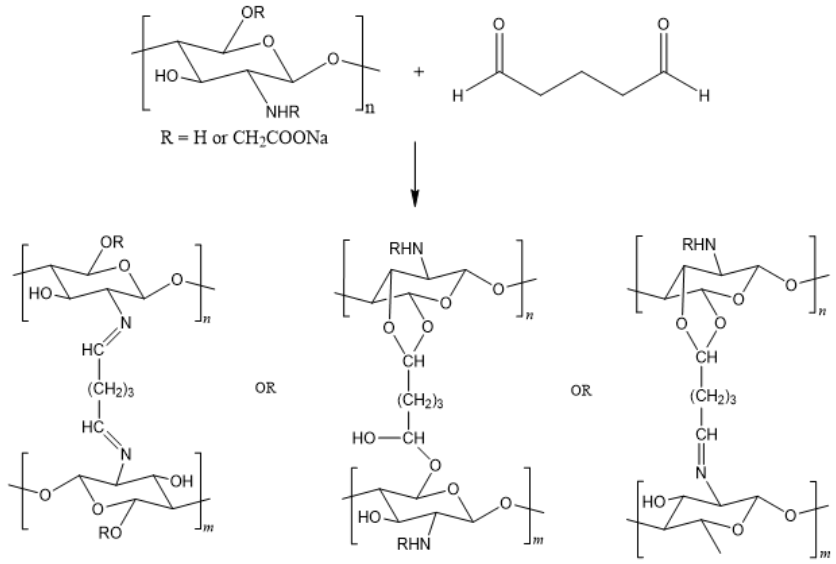
OR
HO
NHR
n
R = H or CH2COONa
RHN
OR
RHN

(b)

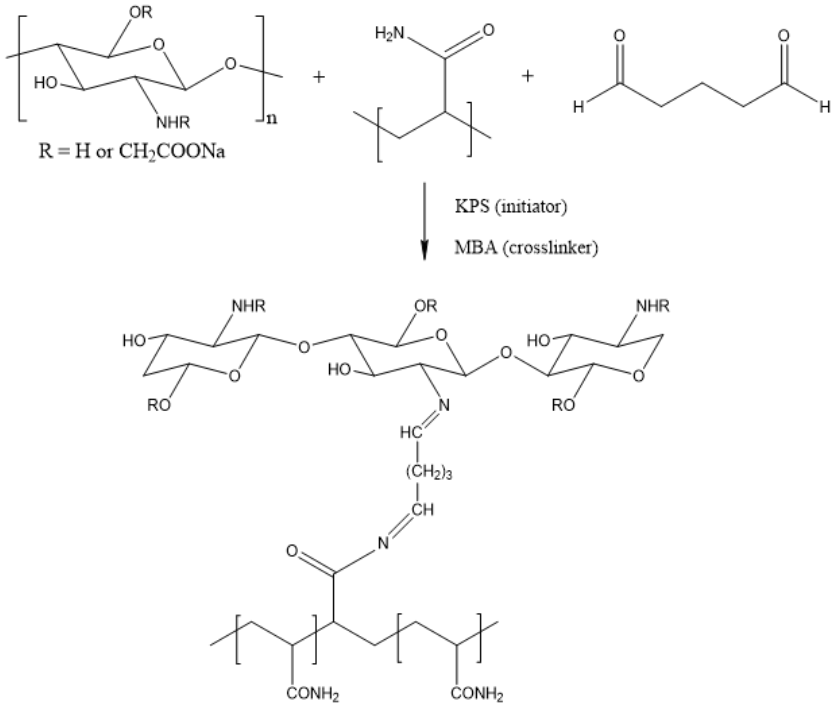
R = H or CH2COONa
KPS (initiator)
MBA (crosslinker)
CONH2

(c)

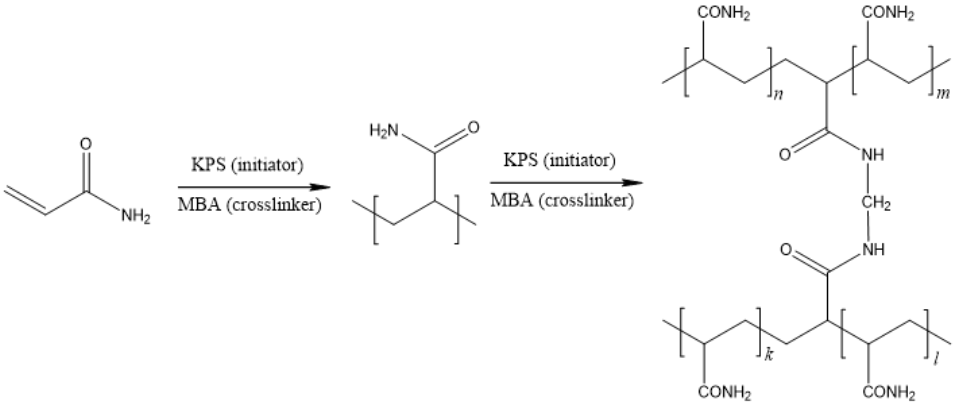
KPS (initiator)
MBA (crosslinker)
KPS (initiator)
MBA (crosslinker)
CONH2

Figure 5.2 The crosslinking mechanism of double-network CMCs-PAM gel electrolytes in terms of (a) the imide bond reaction of CMCs, (b) double-crosslinking between CMCs and PAM.by GA, and (c) the free radical polymerization of AM monomers.

Figure 5.3 shows the Raman spectra obtained for the samples of the PAM gel and the first and second crosslinking CMCs-PAM gels. The PAM gel exhibited weak bands at 3348 and 3205 $cm^{-1}$ representing the stretching vibrations of the N-H bonds. The sharp peak observed at 2924 $cm^{-1}$ was assigned to C-H stretching vibrations. The peaks located at 1663 and 1609 $cm^{-1}$ represent the C=O vibration and N-H deformation of the primary amide on the side chains in PAM. The bands at 1456 $cm^{-1}$ ($CH_2$ in plane scissoring), 1422 $cm^{-1}$ (C-N stretching for primary amide), 1322 $cm^{-1}$ (C-H deformation), and 1105 $cm^{-1}$ ($NH_2$ in plane rocking) were also detected. The bands at 835, 635, and 482 $cm^{-1}$ correspond to the C-C skeletal stretching, C-C skeletal bending, and C-O bending vibrations, respectively. The first crosslinked CMCs-PAM gel exhibited sharp peaks at 975 and 1072 $cm^{-1}$, which were assigned to the C-O stretching in the C-O-C structures and C-O stretching in the CH-OH structures, respectively. PAM further penetrated the previous gels after the second crosslinking step, resulting in the intensities of the absorption bands being amplified. However, the intensities of the peaks associated with the C-O stretching vibrations in the C-O-C structure (975 $cm^{-1}$) and C-O stretching vibrations in the CH-OH structure (1072 $cm^{-1}$) decreased. Moreover, a new weak peak was observed at 1212 $cm^{-1}$ was assigned to the C-N stretching of the secondary amide. These results illustrate new C-N bonds were generated between the-$NH_2$ groups of PAM and the carboxyl groups of CMCs [25].

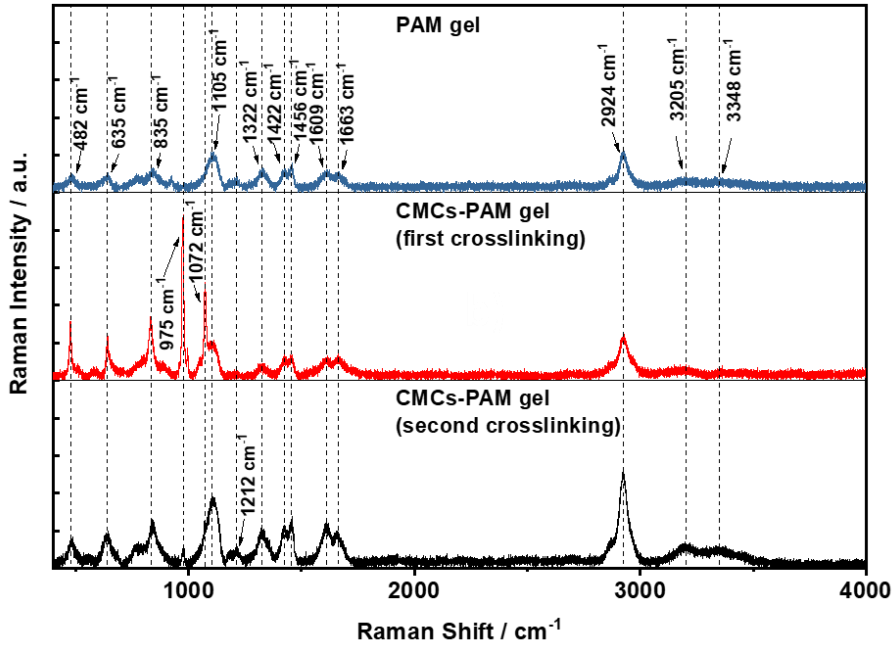


Figure 5.3 Raman spectra of PAM, CMCs-PAM (first crosslinking), and CMCs-PAM (second crosslinking) gels.

*5.3.1.2 Content and weight ratio of CMCs and AM*

Gel electrolytes prepared using various polymers (including CMCs and AM synthesized at 5-20 wt.%) and weight ratios of CMCs and AM (1:2, 1:3, 1:4, and 1:5) were also systematically investigated for their gel-forming ability (Figure 5.4). The mixed CMCs-AM precursor solution was poured into a PDMS model (L × W × T : 50 × 10 × 2 mm) using a syringe (Figure 5.4 a). The gels were prepared using polymer concentrations of 10, 15, and 20 wt.% (Figure 5.4 c-e), and decreasing the polymer concentration to 5 wt.% resulted in loose 3D network structures and a failure to synthesize gels after the first crosslinking step (Figure 5.4 b). Thereafter, the CMCs-PAM gels were cooled to room temperature and soaked in the PAM precursor solution containing the AM monomer, KPS initiator, and MBA crosslinker for 24 h, which is a free swelling process until

equilibrium. Subsequently, the sufficiently absorbed CMCs-PAM gels were deposited in an oven heated at 50 ℃ for 4 h for the second crosslinking step (Figure 5.4 f-i). The hybrid DN hydrogel was transparent and homogenous, indicating the uniform dispersion of CMCs in the PAM polymer chains [31].

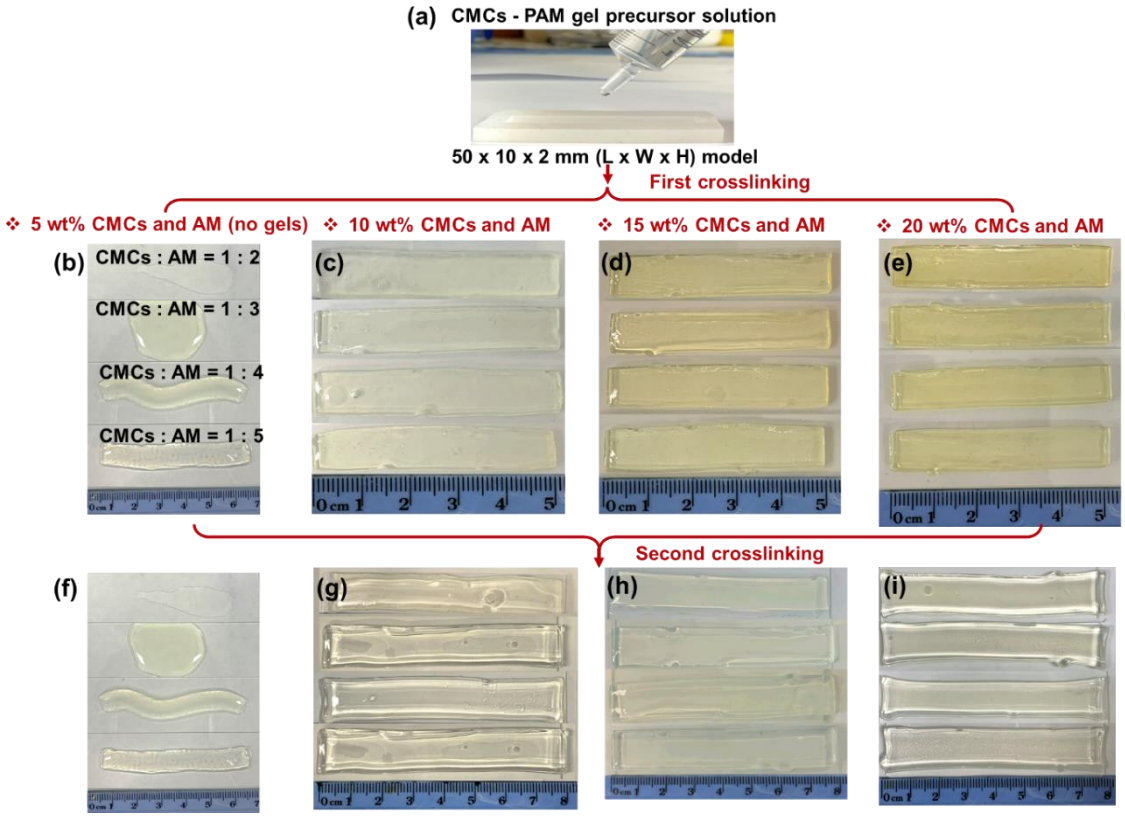


Figure 5.4 Photographs of the gel-forming ability of DN hydrogels prepared using various CMCs:AM weight ratios (1:2, 1:3, 1:4, 1:5) and concentrations of polymers (5 wt.%, 10 wt.%, 15 wt.% and 20 wt.%).

The mechanical properties including the stretchability and compressibility of the DN gel electrolytes prepared with various polymer concentrations (10, 15, and 20 wt.%) and weight ratios of CMCs:AM (1:2, 1:3, 1:4, and 1:5) were systematically evaluated and

referred to as 1-2, 1-3, 1-4 and 1-5 gel electrolytes, respectively. The hydrogel without the redox couple was marked as “blank.”

The strain-stress test reflects the elongation properties of the gel electrolytes tested until the fracture point (Figure 5.5 a). The strain-stress curves of the blank hydrogels prepared with various polymer weight ratios and concentrations are illustrated in Figure 5.5 b-d. The maximum strain (725%) of the 10 wt.% 1-2 DN gel was observed in Figure 5.5 b, whose stretchability gradually decreased with an increase in the PAM percentage (626% strain for 1-5). Conversely, the tensile strength increased upon increasing the PAM ratio at each polymer concentration studied. Moreover, for the 1-2 gels, the increase in polymer concentration generally decreased the breaking point of elongation, as shown in Figure 5.5 c&d (628% strain for the 15 wt.% sample and 532% strain for the 20 wt.% sample). These results were caused by the increase in the molecular weight and density of the PAM chains, leading to the increased rigidity, stiffness, and lower elasticity of hydrogels [23]. Higher CMCs concentrations lead to more dynamic bond formation, including ionic coordination and hydrogen bonds between the CMCs and PAM chains, which assist in dissipating energy and improving tensile strain [31].

Elongation processes require pathways for energy dissipation in the hydrogel. The excellent strain tolerance of the DN hydrogel was attributed to multiple interactions. Unlike conventional double-network gels, the identical monomer (AM) used in both crosslinking processes was beneficial toward reducing the interfacial energy, providing a synergistic effect between them and thus, assisting energy dissipation to promote toughness. The neutral AM monomer forms a loose network in the second crosslinking step and provides mechanical strength due to interweaving and entanglement with the

existing 3D network structure of the gels and via physical and chemical interactions to significantly boost the mechanical properties [21]. In addition, due to the intramolecular bonding in PAM and CMCs, the intersections of the PAM and CMCs networks and non-covalent interactions, such as van der Waals forces and hydrogen bonds, can be formed between PAM and CMCs. The hydrogen bonds formed between the hydroxyl groups in CMCs and the amide groups in the PAM polymer chains effectively dissipate energy during deformation, which contributes to the excellent mechanical properties of the gel electrolytes [36]. Therefore, stretchable CMCs-PAM hydrogels were synthesized (Figure 5.5 e) [23], which can be attached to human skin, twisted at the elbow joint (Figure 5.5 f), and exhibit high stretchability (Figure 5.5 g).

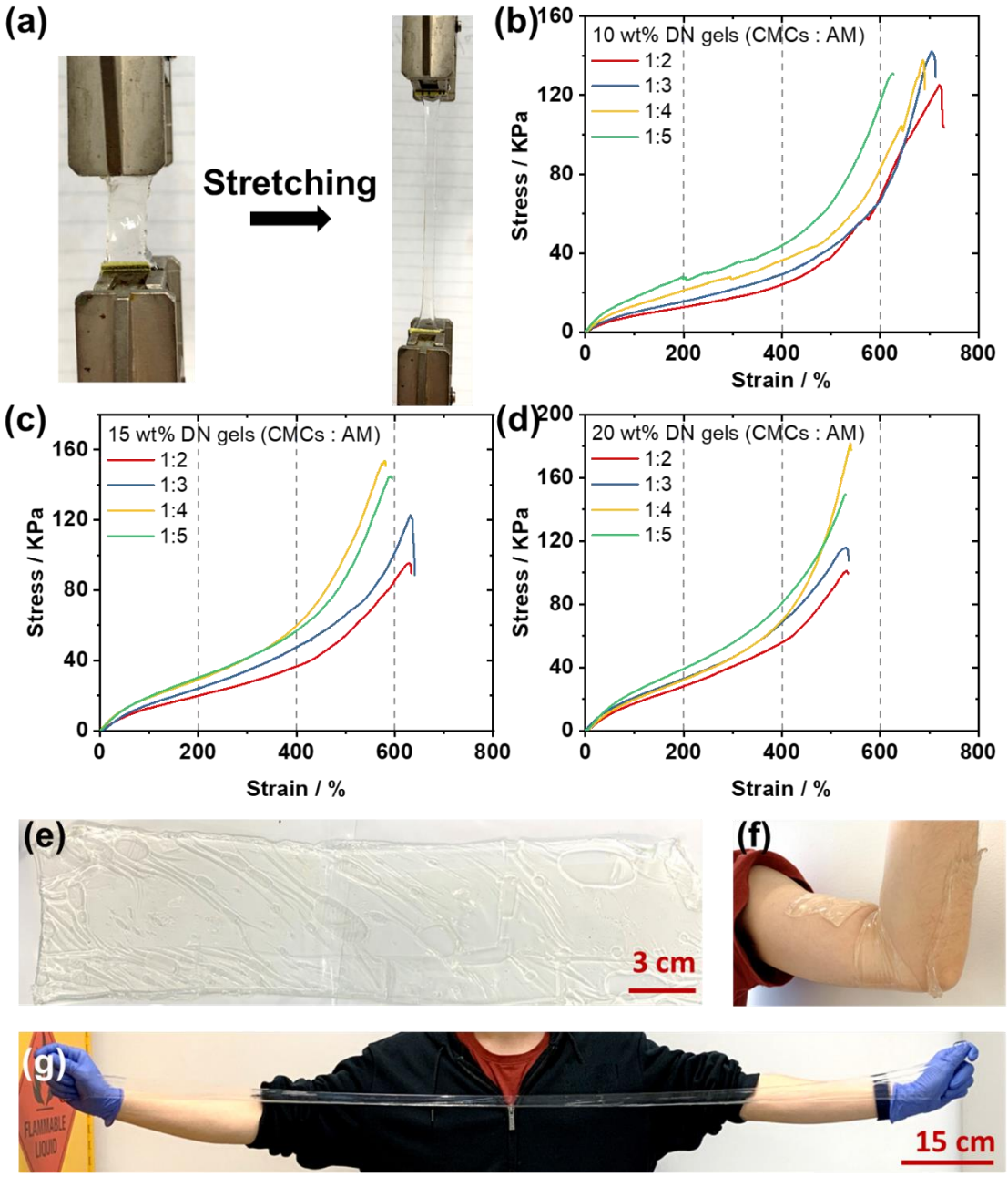


Figure 5.5 (a) Photographs of the CMCs: PAM gels undergoing the tensile test. Stress-strain curves of (b) 10 wt.%, (c) 15 wt.%, and (d) 20 wt.% CMCs: PAM gels with varied weight ratios. Photographs of the DN hydrogel in terms of (e) original state, (f) twisted and attached to an arm, and (g) highly stretchable state.

*5.3.1.3 Compatibility of both N- and P-type redox couple*

In the final state, highly stretchable CMCs-PAM gels were immersed and solvent exchanged with N-type (0.08 M HCl, 1 M $FeCl_2$, and 1 M $FeCl_3$) or P-type (0.4 M $K_3[Fe(CN)_6]$ and 0.4 M $K_4[Fe(CN)_6]$ [3,4,6]) redox couple aqueous solutions for 48 h until swelling equilibrium and the gel electrolytes were ready to use (Figure 5.6 a-f).

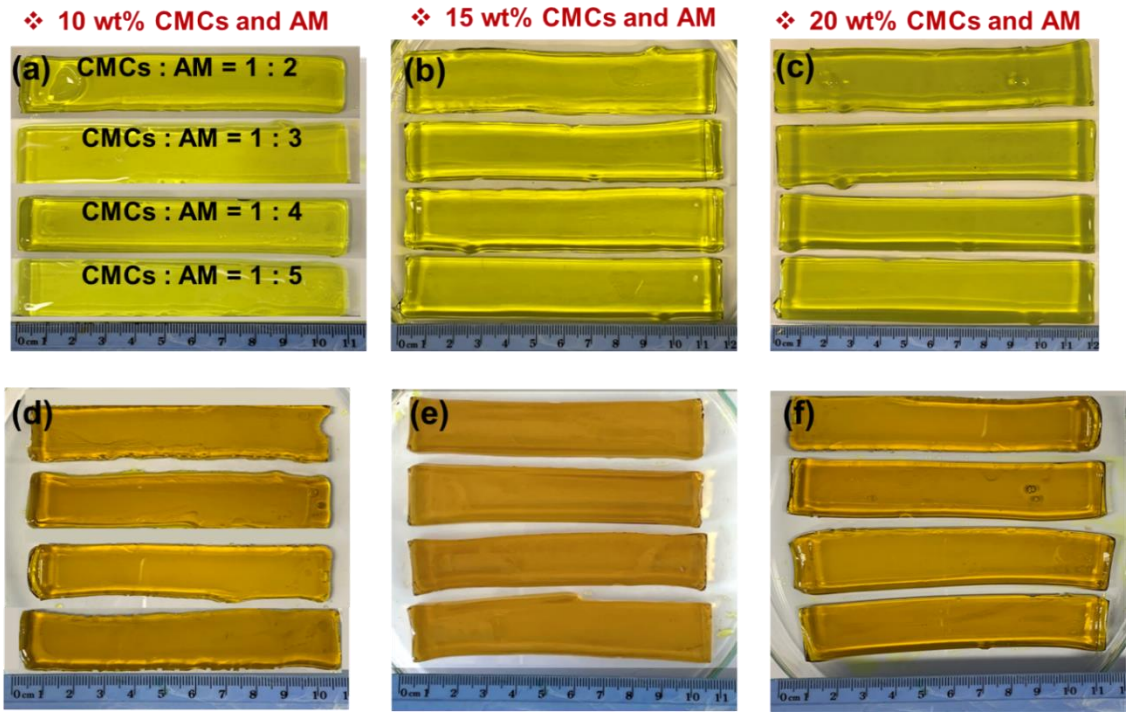


Figure 5.6 Photographs of the of (a-c) P and (d-f) N-type gel electrolytes prepared in varied CMCs:AM weight ratios (1:2, 1:3, 1:4, 1:5) and concentrations of polymers (10 wt.%, 15 wt.% and 20 wt.%).

### 5.3.2 Physical properties of gel electrolytes

#### *5.3.2.1 Mechanical properties*

Photographs of the N- and P-type gel electrolytes under the tensile test are shown in Figure 5.7 a&d, respectively. The strain-stress curves for the various contents of CMCs

and AM in the N- and P-type gel electrolytes were also investigated. Figure 5.7 b shows the 10 wt.% 1-2 N-type gel electrolyte can largely withstand 330% elongation and nearly 40 KPa stress, and the% strain decreased to 250% with an increase in the weight ratio of AM to CMCs:AM = 1:5. Meanwhile, the% stress was slightly improved to 45 KPa. The 10 wt.% 1-2 P-type gel electrolyte also remained integrated until a maximum 368% strain when compared with the various weight ratios studied (Figure 5.7 e). The effect of the polymer host concentrations of the N- and P-type gel electrolytes was also comprehensively investigated in order to optimize the mechanical properties (Figure 5.7 c&f). Similar to the blank gels, the% strain of the breaking point of both the N- and P-type gel electrolytes decreased upon increasing the polymer concentration, while stress was promoted.

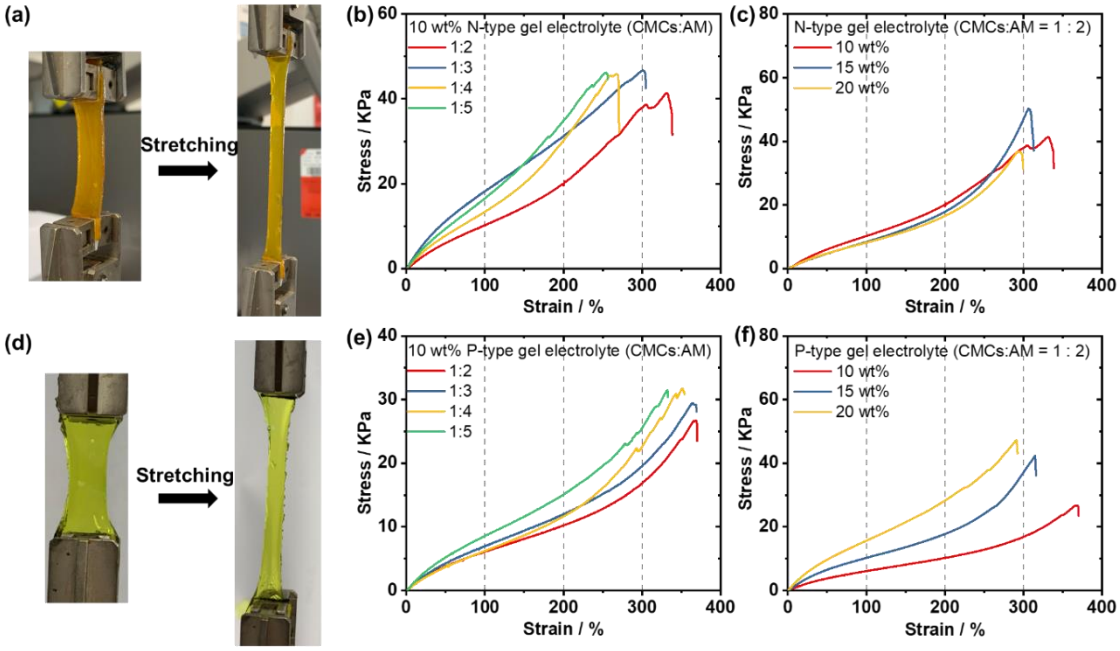


Figure 5.7 (a) Photographs of the of N-type gel electrolytes undergoing the tensile test. Stress-strain curves of N-type gel electrolytes with (b) CMCs:AM weight ratios, and (c) different polymer concentrations (10 wt.%, 15 wt.% and 20 wt.%). (d) Photos of P-type

gel electrolytes undergoing the tensile test. Stress-strain curves of P-type gel electrolytes with (e) CMCs:AM weight ratios, and (f) different polymer concentrations (10 wt.%, 15 wt.% and 20 wt.%).

Figure 5.8 shows the comparison of the tensile ability among the 10 wt.% 1-2 DN gel with N-type, P-type, and without redox couples. A sharp decline in the mechanical properties was observed. The tensile strength of the blank gel (125 KPa) was nearly three times that of the N- and P-type gel electrolytes (30-40 KPa), and the elongation ability (725% strain for the blank sample) was also roughly double that of the redox couple (367-331%), which presents a typical swelling-weakening phenomenon caused by the dilution of the network [37]. Nevertheless, both the N- and P-type gel electrolytes can be stretched >300%, which is sufficient to satisfy the requirements of wearable devices.

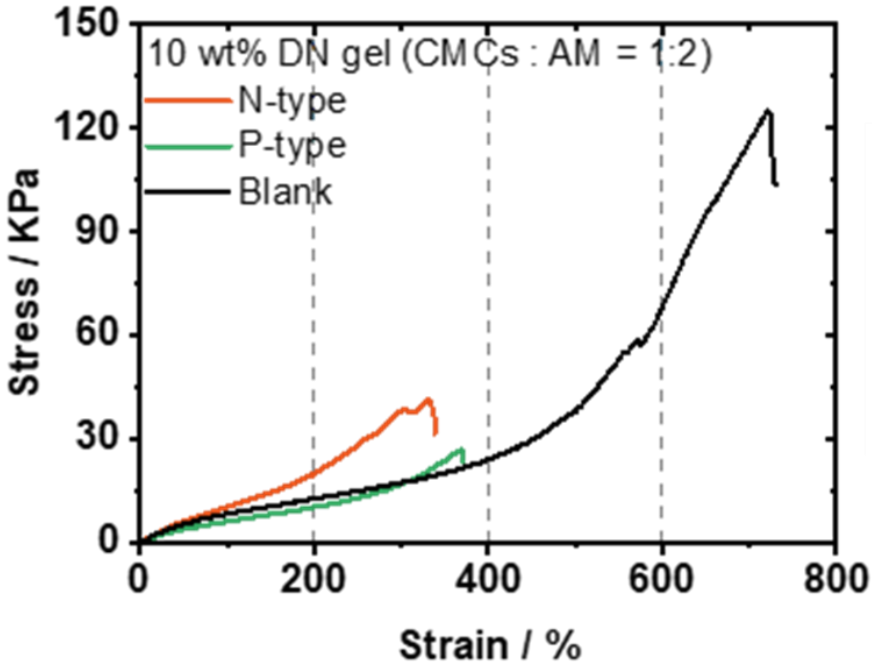

Figure 5.8 A comparison of stress-strain curves among N-type, P-type and blank double-network gels (10 wt.%, mass ratio CMCs:AM = 1:2).

Both of the optimized N- and P-type gel electrolytes have excellent mechanical properties (Figure 5.9), which can maintain their shape after being stretched over 300% with twisting over 720° and exhibited ultra-high recovery properties under >95% compression (Figure 5.9 c-e). These excellent mechanical properties emphasize the potential of gel electrolytes in wearable applications and complicated fields. These outstanding mechanical properties, such as flexibility, elastic stability, and recoverability after compression, highlight their potential for wearable applications [38]. Furthermore, we assumed that hydrogels without redox couples will probably be mixed with the desired salt-based electrolyte and adapted to a wide range of diverse utilization fields.

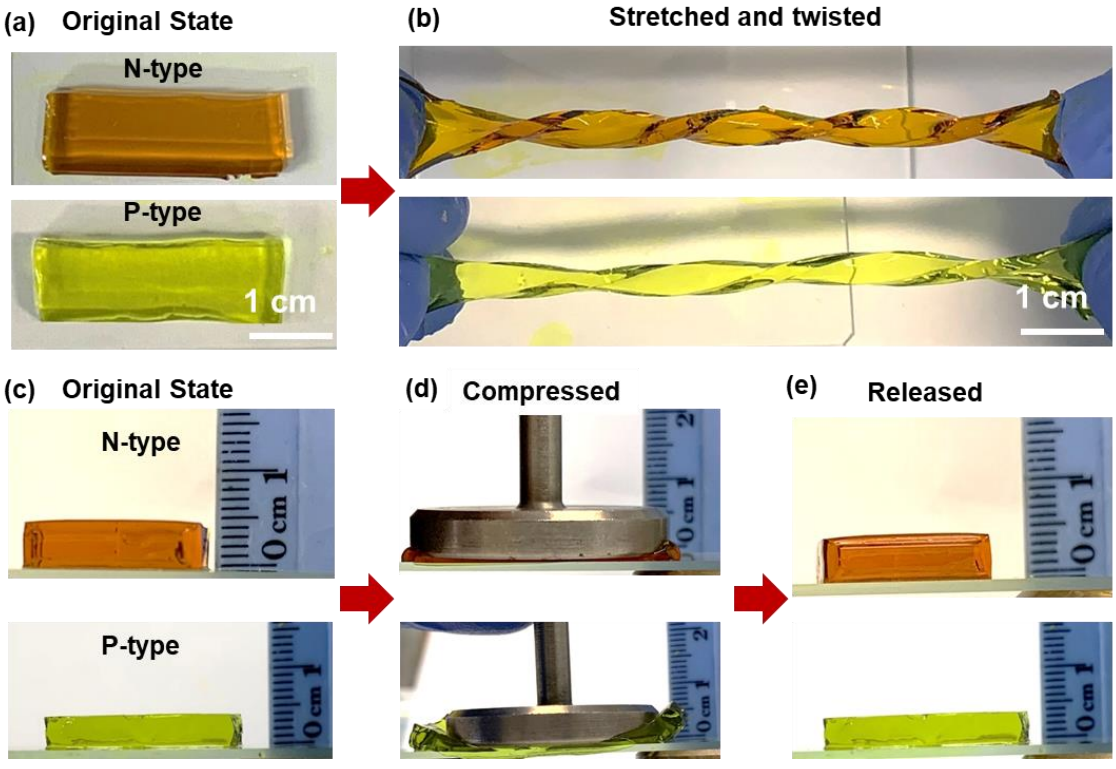

Figure 5.9 (a-e) Digital images of N and P-type gel electrolyte that demonstrates outstanding stretchability and recoverability from >95% compression.

*5.3.2.2 Swelling ratio*

The swelling ratio ( $S_r$ ) of the gel electrolytes was calculated using $S_r = (W_s - W_o)/W_o \times 100\%$, where $W_s$ is the original weight (before soaking) of the gel and $W_o$ is the weight of the swelled gel. Figure 5.10 a shows the $S_r$ values of the DN hydrogels prepared with various polymer concentrations and weight ratios before and after immersion in the PAM precursor aqueous solution. Hydrogels consisting of 10 wt.% CMCs and AM had the highest $S_r$ of up to 220% and the absorbent ability of the 20 wt.% hydrogel decreased to ~150%. Meanwhile, the $S_r$ slightly decreased upon decreasing the percentages of CMCs. A similar tendency was observed when soaking in the redox couple aqueous solutions (Figure 5.10 b&c). As expected, the 20 wt.% DN gel achieve more substantial absorption in the redox couple solutions, in which the $S_r$ progressively decreases with the weight ratio of CMCs to AM from 1:2 to 1:5 and decreases with a higher weight ratio of AM monomer. The absorbent ability of the hydrogels was significantly affected by the weight ratio and concentration of polymers used, in which a greater swelling ratio was observed with an increase in the polymer concentration or at higher percentage of CMCs. The negatively charged carboxylic groups that are abundant in CMCs accumulate inside the hydrogels, resulting in chain relaxation via strong electrostatic repulsion.[39–41] In addition, the absorbent ability of gels was dramatically influenced by the hydrophilic environment created by the branched chains in the 3D network structures.[42] At a higher weight ratio of AM monomer units in the DN hydrogel, more radicals were triggered by the initiators and facilitate the

termination step via intermolecular collisions, which elongate the backbone of the PAM chains and weakens the molecular weight of the branched chains, leading to a reduction in the swelling ratio.[43]

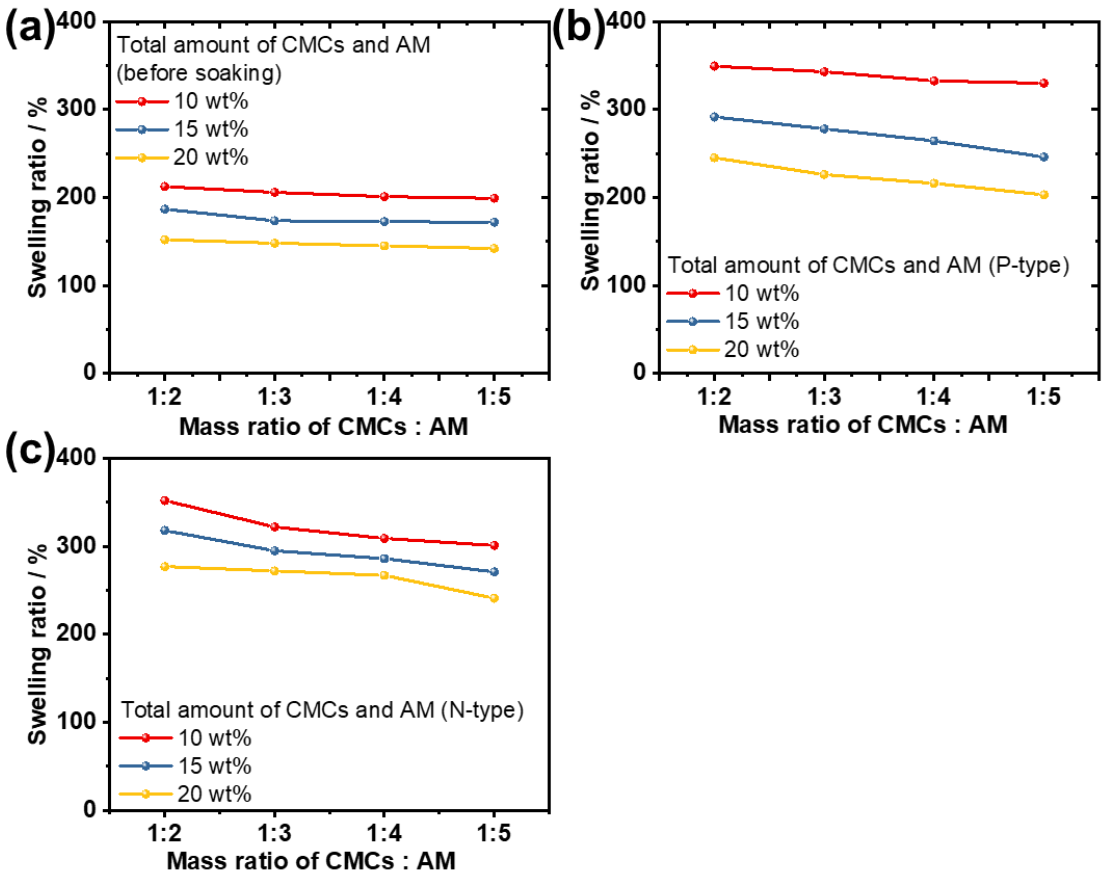


Figure 5.10 Swelling ratio of gel electrolytes in terms of (a) before and after second crosslinking, and (b) before and after soaking in P-type redox couple aqueous solutions, (c) before and after soaking in N-type redox couple aqueous solutions.

### 5.3.3 Electrochemical performance of gel electrolytes

#### *5.3.3.1 Electrochemical activity*

The electrochemical activity of the gel electrolytes prepared with various weight ratios of CMCs and AM (1:2, 1:3, 1:4, and 1:5) was systematically investigated. Figure 5.11 a shows the cyclic voltammograms (CVs) of the N-type gel electrolytes recorded at a scan rate of 10 mV $s^{-1}$. The 1-2 and 1-3 gel electrolytes exhibited a higher peak current when compared to the 1-4 and 1-5 gel electrolytes. The peak-to-peak separations ($\Delta E_p$) observed in the CVs are indicative of the kinetics of the redox processes [44]. The peak-to-peak separation of the four gels (100-110 mV) indicated a reversible redox process. The CVs curves were recorded at various scan rates and the peak current was plotted *vs* the square root of the scan rate. A linear relationship was observed (Figure 5.11 b), indicating a diffusion-limited system [44,45]. The diffusion coefficient ($D$) was estimated using the Randles-Sevcik equation (Equation S1, all shown in Figure 5.11 c) and unsurprisingly, the $D$ values of the four gels followed the same trend as the peak current, in which all of the samples displayed nearly similar $D$ values.

$$ip = (2.69 \times 10^5) n^{\frac{3}{2}} A D^{\frac{1}{2}} C v^{\frac{1}{2}}$$

where $ip$ is the peak current, $n$ is the number of electrons, $A$ is the electrode surface area ($cm^2$), $C$ is the redox couple concentration ($mol/cm^3$), $v$ is the scan rate (V/s), and $D$ is the electrolyte-diffusion coefficient ($cm^2/s$).

Electrochemical impedance spectroscopy (EIS) was also performed on the gels using the same setup as that used for the CV curves and displayed in Figure 5.11 d. The electron transfer resistance ($R_{ET}$) and mass transport ($R_{\Omega}$) resistance were determined from the EIS spectra. The 1-2 gel exhibited the minimum electrolyte resistance of 42.5 Ω (indicated by the intercept on the real axis) among the four gelled electrolytes studied.

The 1-2 gel electrolyte (45.6 Ω) exhibited a lower $R_{ET}$ than the 1-5 gel electrolyte (110 Ω) with respect to the electron transfer resistance (defined by the semicircle diameter in the high-frequency domain), which was likely due to the slightly higher concentration of the redox couple in the 1-2 gel electrolyte [46].

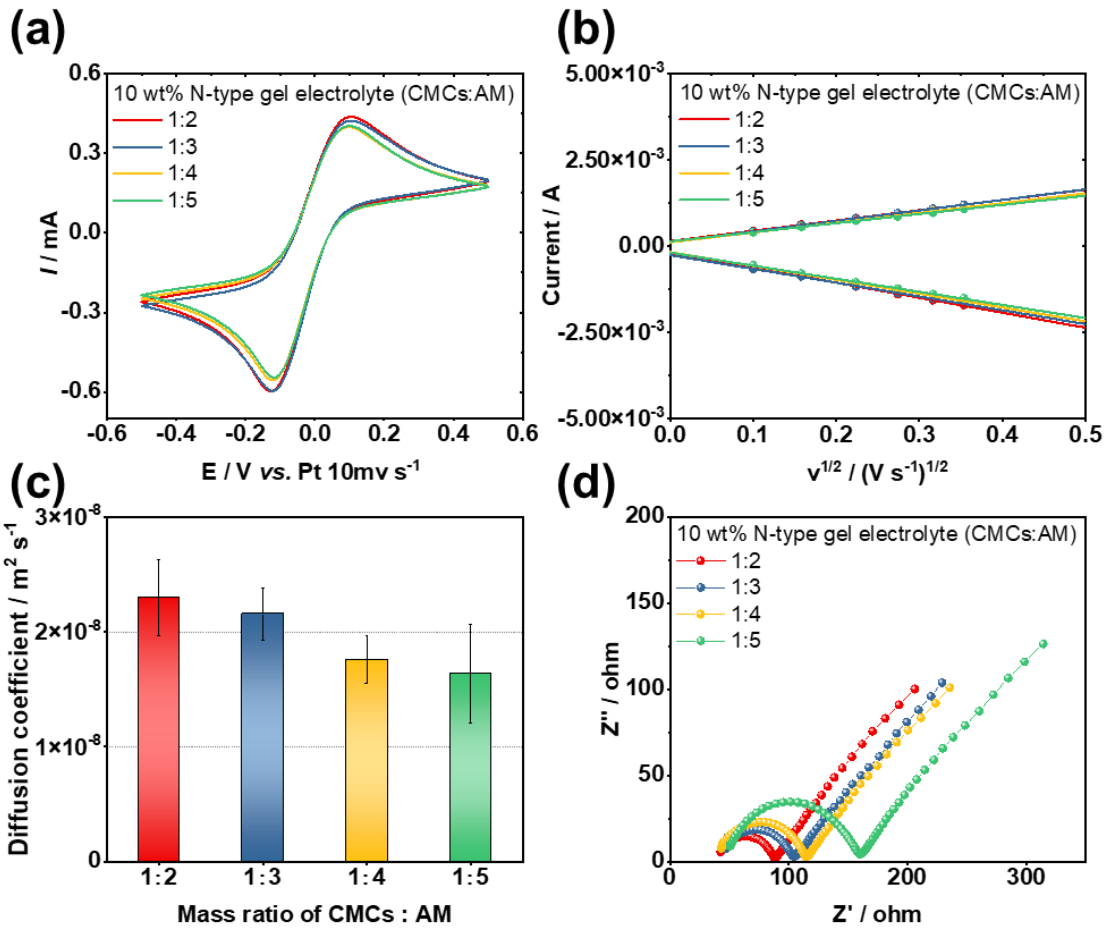


Figure 5.11 A comparison of the electrochemical activities of 10 wt.% N-type gel electrolyte with different CMCs : AM weight ratio in terms of (a) cyclic voltammetry (scan rate = 10 mV $s^{-1}$), (b) the linear relationship of peak currents *versus* square root of scan rates (10 - 125 mV $s^{-1}$), (c) diffusion coefficient, and (d) electrochemical impedance spectra.

The electrochemical characteristics of the p-type gel electrolytes show an identical tendency (Figure 5.12). The similar peak current of the gel electrolytes prepared with different weight ratios in the CVs curves (Figure 5.12 a) contribute significantly to $D$, as shown in Figure 5.12 b and c. The EIS results shown in Figure 5.12 d also indicated that the 1-2 gel electrolyte has the lowest electrolyte resistance. The 10 wt.% 1-2 gel electrolyte demonstrated an advantageous electrochemical performance (ionic conductivity, apparent diffusion coefficient, and electron transfer kinetics) when compared to the other gel electrolytes studied.

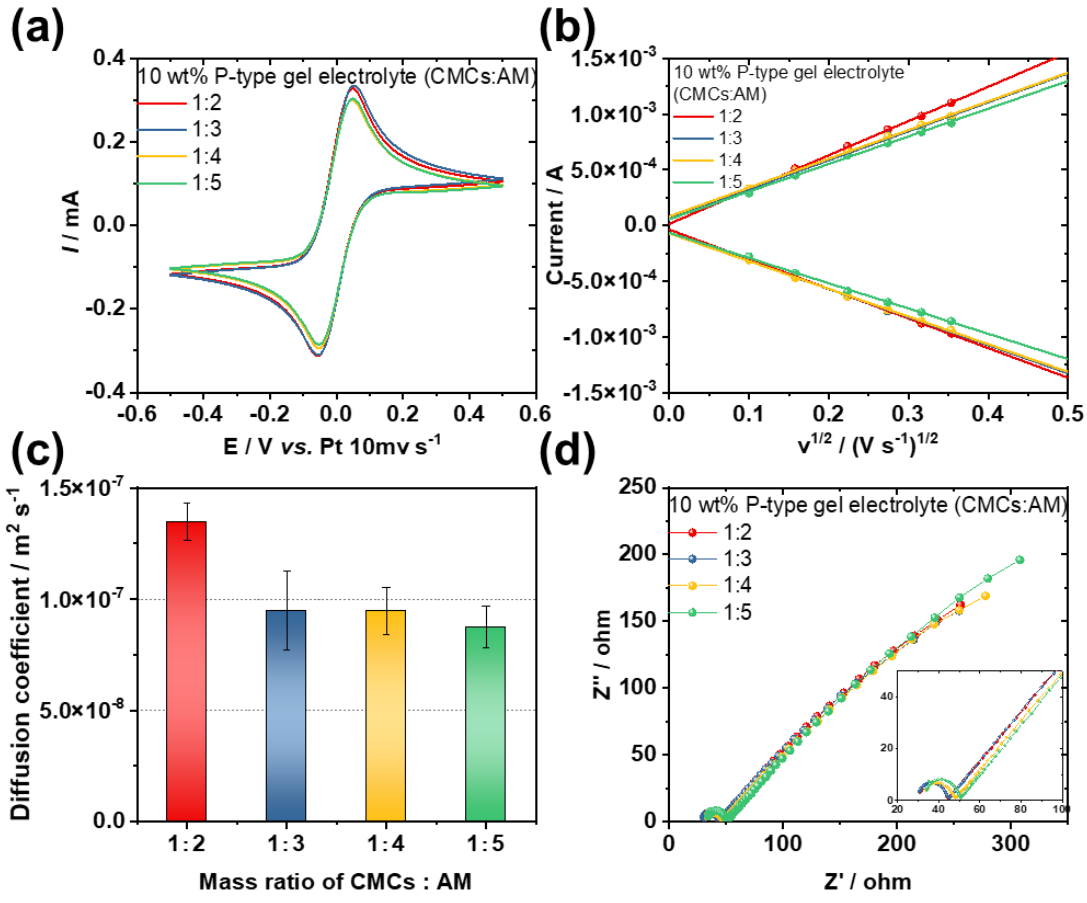


Figure 5.12 A comparison of the electrochemical activities of 10 wt.% P-type gel electrolyte with different CMCs: AM weight ratio in terms of (a) cyclic voltammetry

(scan rate = 10 mV $s^{-1}$), (b) the linear relationship of peak currents *versus* square root of scan rates (10 - 125 mV $s^{-1}$), (c) diffusion coefficient, and (d) electrochemical impedance spectra.

### *5.3.3.2 Thermo-electrochemical performance*

The fabrication process of the thermocells used for our thermo-electrochemical performance analysis is illustrated in Figure 5.13. Reproducible size, shape, and positioning of the gelated electrolytes were obtained using an acrylic spacer (2 mm thickness). The slightly thicker (2.1-2.2 mm) gel electrolytes compared to the spacer guaranteed the good connection to the Pt electrodes. The thermocell devices were then placed between the hot and cold electrodes to provide temperature gradients.

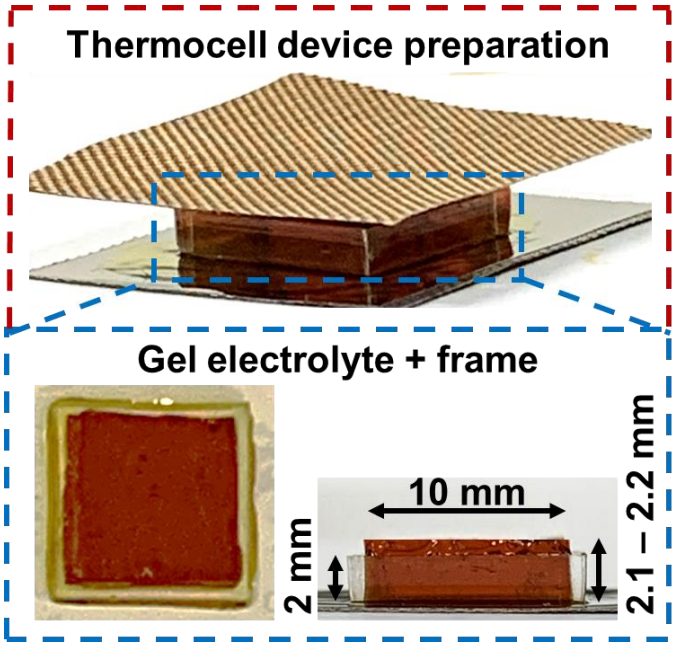


Figure 5.13 An illustration of the fabrication of thermocell devices.

A comparison of the TECs performance observed at ΔT = 10 ℃ ($T_c$ = 25 ℃, $T_h$ = 35 ℃) is shown in Figure 5.14. The hot electrode was set at 35 ℃ to simulate the average temperature of human skin and the cold electrode was modified within the range of 15-30 ℃) to simulate changes in the ambient environmental temperature. The power density exhibits a parabolic relationship *versus* the potential using $P = JV$ and the maximum power density ($P_{max}$) was equivalent to 0.25 $J_{sc}V_{oc}$ [47]. Figure 5.14 a shows the $P_{max}$ values of the N-type thermocells generally decrease upon increasing the weight percentage of AM. When compared with the 1-5 gel electrolyte, the $J_{sc}$ of the 1-2 gel electrolyte was improved from 1.7 to 2.3 A $m^{-2}$ and $P_{max}$ increased from 3.8 to 5.3 mW $m^{-2}$. The $V_{oc}$ of the thermocells was related to the $S_e$ at the applied temperature gradients and all four gelated electrolytes exhibited the same $V_{oc}$, equating to equivalent $S_e$. A similar tendency was observed in the P-type thermocells, where the $P_{max}$ and $J_{sc}$ were improved by roughly 27% (5.6 to 7.1 mW $m^{-2}$ and 1.5 to 2.0 A $m^{-2}$, respectively) upon varying the weight ratio of CMCs:AM from 1:5 to 1:2 (Figure 5.14 b). The enhanced power density and higher peak current observed in the CVs curve obtained for the 10 wt.% 1-2 gel electrolytes can be attributed to the greater mass transport and lower electron transfer resistance, which indicates a good correlation between the electrochemical and thermo-electrochemical results.

Figure 5.14 c&d show the long-term short-circuit current density outputs (30 min) observed for the thermocells, which indicate a higher initial peak current density and then decrease over time and stabilize after 1000 s (in line with previous aqueous [48] and gelated [49] thermocells). Both N and P-type thermocells prepared with the 1-2 gel electrolytes exhibit the highest steady-state short-circuit current densities of 1.9 and 1.6 A $m^{-2}$, respectively (*cf.* 1.5 and 1.4 A $m^{-2}$ for the 1-5 gel electrolytes). In conclusion, 10

wt.% 1-2 gel electrolyte was determined as the optimal gel host with good mechanical properties, mass transport, lower electron transfer resistances, and faster diffusion coefficient of redox ions. Consequently, this gel was subjected to further testing.

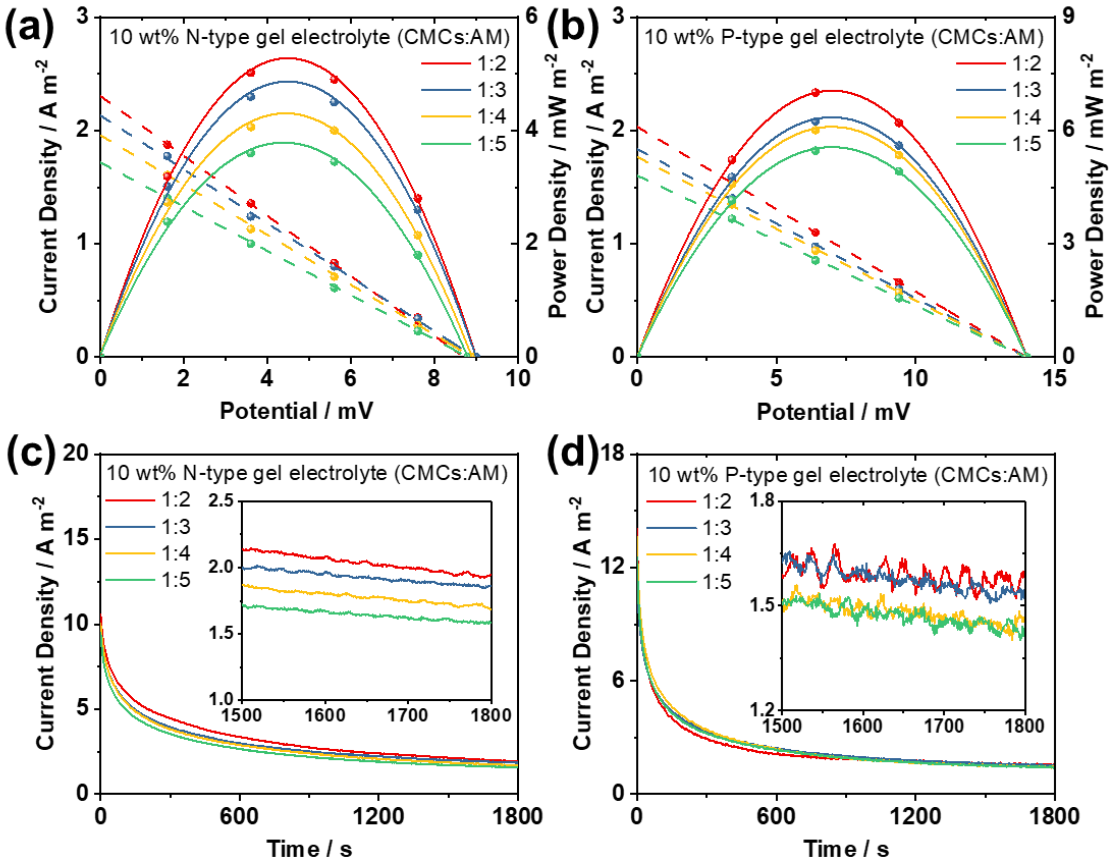


Figure 5.14 A comparison of the thermo-electrochemical performance of N-type and P-type gel electrolytes with different CMCs: AM weight ratios at $\Delta T$ = 10 ℃ ($T_c$ = 25 ℃, $T_h$ = 35 ℃) in terms of (a) & (b) current (dash) and power (solid) density *versus* voltage, and (c) & (d) the long-term short-circuit current density *versus* time (30 min).

### *5.3.3.3 Paring the N-P thermocells*

Based on the above results, the 10 wt.% 1-2 gel was selected for further investigation. A typical pair of N-P thermocells was fabricated and examined, both individually and in

series (Figure 5.15 a), which were fabricated using Pt electrodes and connected *via* sputter-coated Pt. Figure 5.15 b shows the voltage of the N-P cells exhibits an effective $S_e$ of 2.1 mV $K^{-1}$, which is ~95% of the absolute $S_e$ of the combined P-type cell (-1.35 mV $K^{-1}$) and N-type cell (+0.86 mV $K^{-1}$); the slight decrease was attributed to the increased resistance of the additional electrical connections [50]. As expected, the comparable current and long-term short-circuit current output of the N-P cells was almost equal to the combined current from the individual P-type and N-type cells observed at $\Delta T$ = 10 ℃ ($T_c$ = 25 ℃, $T_h$ = 35 ℃) (Figure 5.15 c). While the overall power output was theoretically doubled by connecting the thermocells in series, the total $P_{max}$ increased by 193.6% (rather than 200%) due to the internal resistance mentioned above [51,52]. Furthermore, the N-P combined thermocell shows an expected parabolic absolute power output *versus* voltage and a linear current output *versus* voltage relationship under the different temperature gradients studied ($\Delta T$ = 5-20 ℃), as shown in Figure 5.15 d. These results demonstrate that the N-P systems were combined effectively and are an effective combined thermocell at various temperatures, showing potential as a power supply for real self-powered wearable electronics.

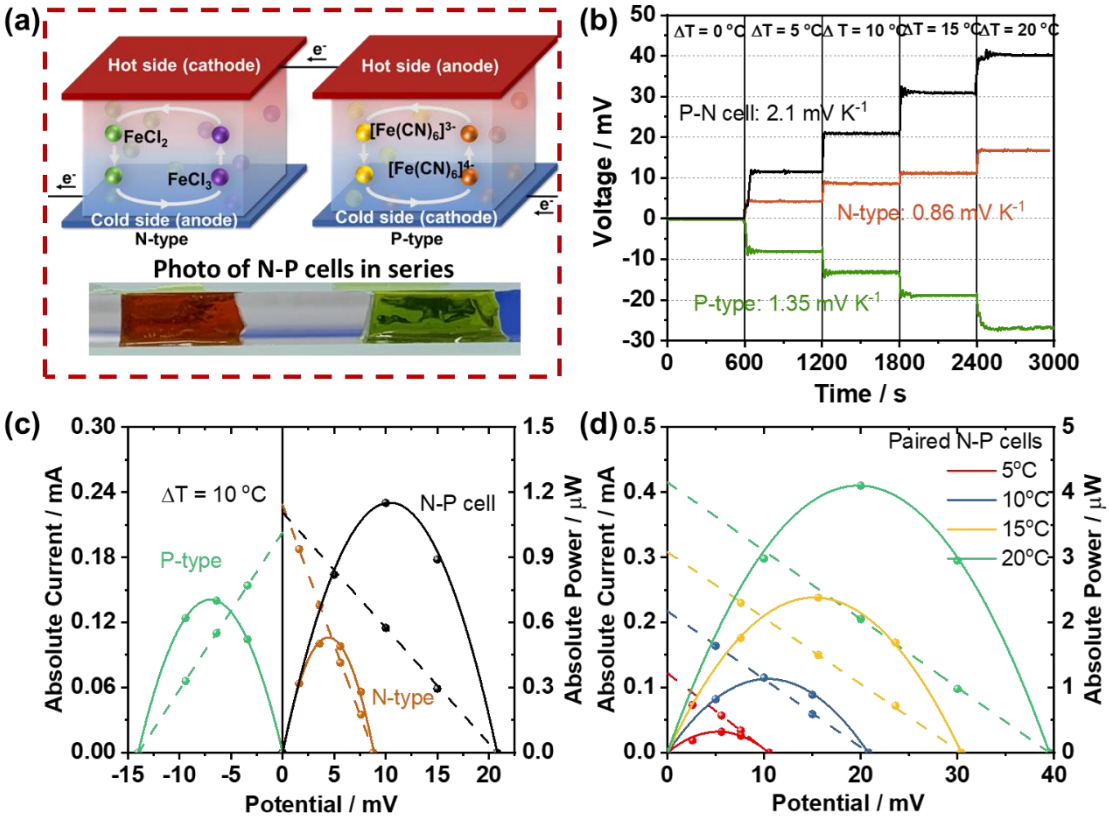


Figure 5.15 A pair of N-P cells. (a) Schematic illustration and photograph of the P-type and N-type device connected in series (N-P cell). Thermo-electrochemical performance of the P-type, N-type and N-P cells in terms of (b) voltage at different ΔT (5 - 20 °C), (c) current (dashed line) and power (solid line) output versus voltage at ΔT = 10 °C ($T_c$ = 25 °C, $T_h$ = 35 °C), and (d) current (dashed line) and power (solid line) output *versus* voltage of P-N cell at different ΔT.

### 5.3.4 Design of textile electrodes and integration with gel electrolytes

#### *5.3.4.1 Dipping times*

Textile electrodes were prepared by repeatedly dipping hydrophilic polyester fibers into PEDOT:PSS aqueous solutions and drying them in an oven, in which the PEDOT:PSS

was fully absorbed by the textile materials and unified encapsulation of each thread of polyester, and the textile electrodes can still retain the porous structure for further penetration with the gel electrolyte (details in Chapter 2.5.5).

The coating conditions used for the textile fibers with different dipping times before and after stretching were compared (Figure 5.16 - Figure 5.21). The SEM graphs of 1-6 times dipping PEDOT:PSS coated textile electrodes after strain were summarized in Figure 5.22. The PEDOT:PSS did not fully encapsulate the polyester fibers after 1-2 immersion steps and peeled off after stretching (Figure 5.16 c and Figure 5.17 c). However, after the fifth immersion step, the dried PEDOT:PSS obstructed the porous structures of the polyester textiles, which was detrimental to its integration with the gel electrolytes (Figure 5.20 b and Figure 5.21 b). Only the electrodes immersed 3- and 4-times not only retained the pristine porous textile, but also maintained acceptable electrical properties. The porous structure resulted in a geometric structured contact area instead of a flat surface, which decreased the resistance and enlarged the electrochemically active area.

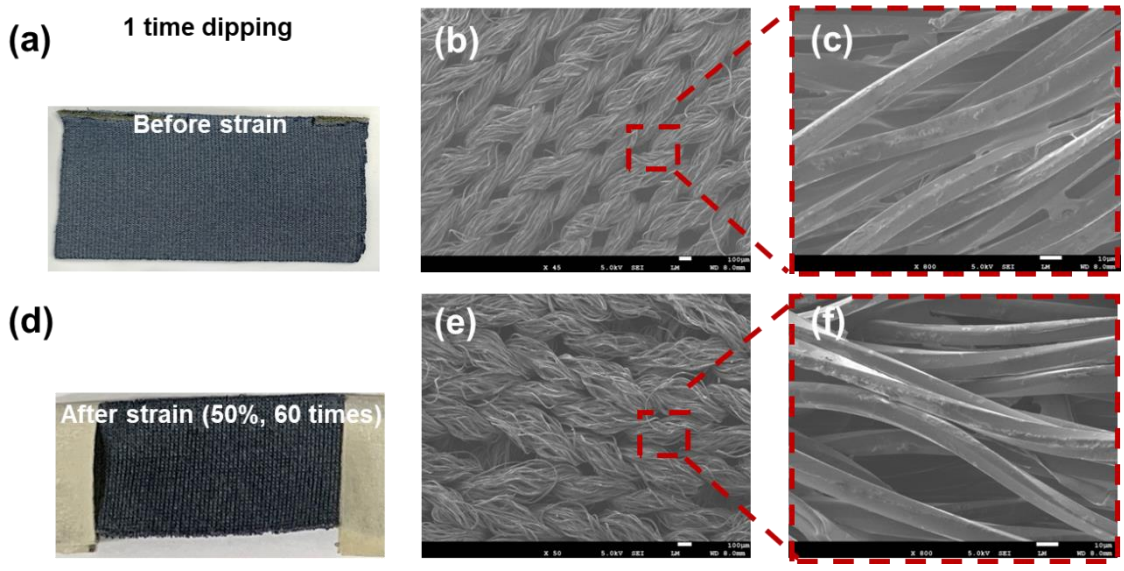

Figure 5.16 Photographs and SEM images of 1 time dipping PEDOT:PSS coated textile electrodes in terms of (a) - (c) before and (d) - (f) after strain.

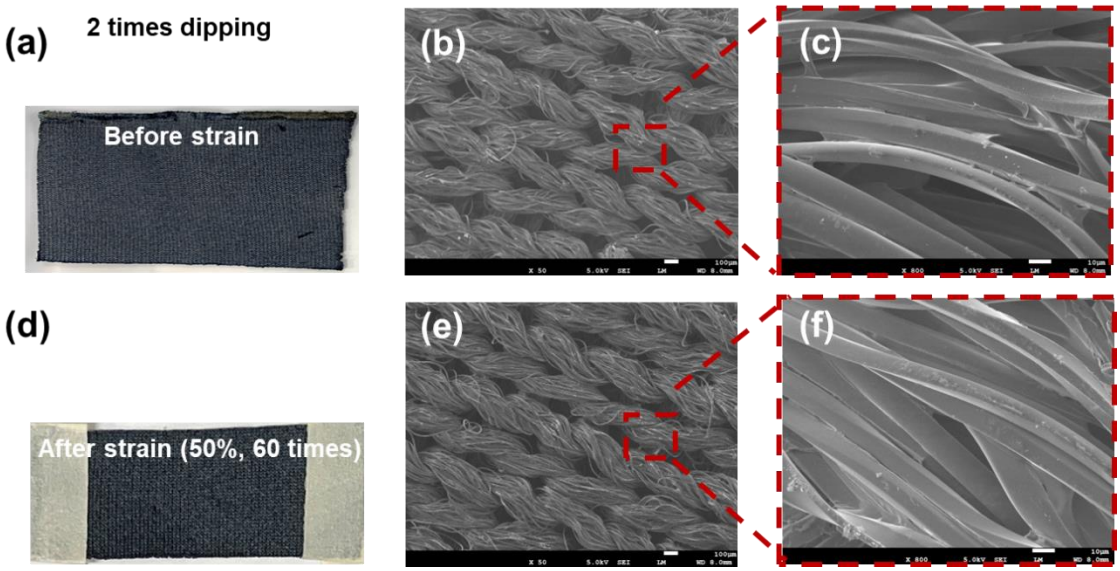


Figure 5.17 Photographs and SEM images of 2 times dipping PEDOT:PSS coated textile electrodes in terms of (a) - (c) before and (d) - (f) after strain.

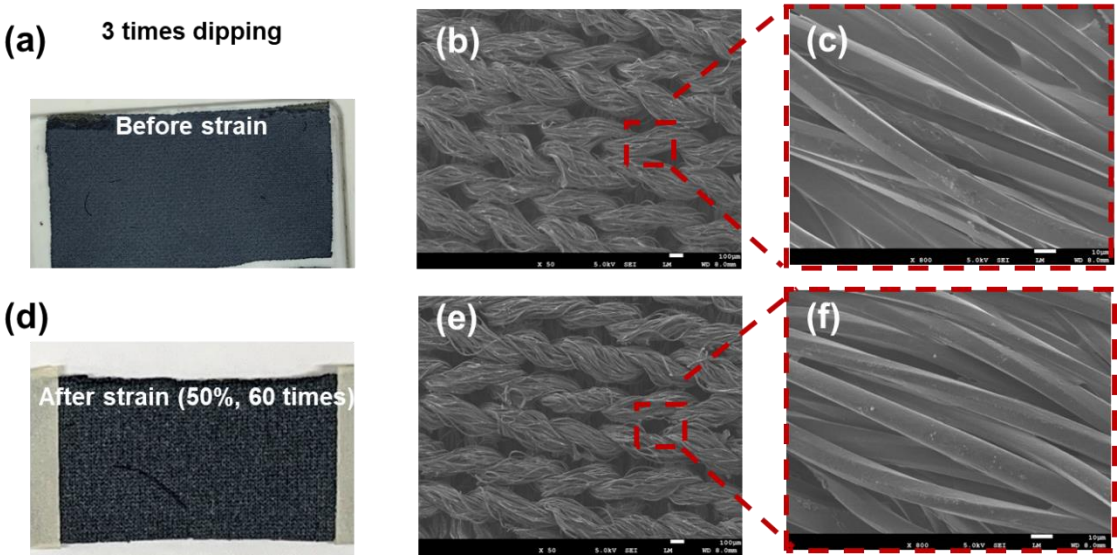

Figure 5.18 Photographs and SEM images of 3 times dipping PEDOT:PSS coated textile electrodes in terms of (a) - (c) before and (d) - (f) after strain.

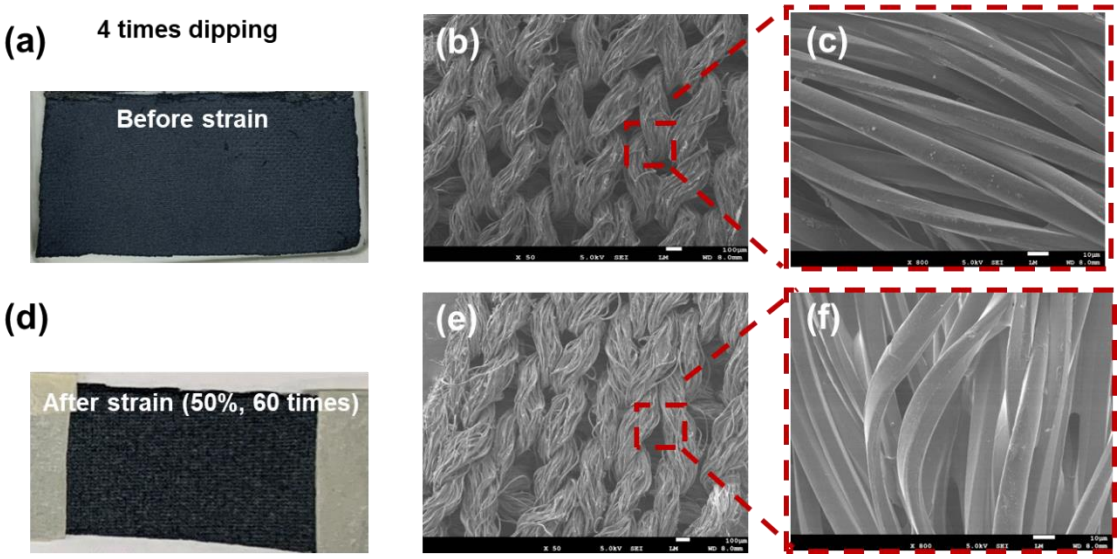


Figure 5.19 Photographs and SEM images of 4 times dipping PEDOT:PSS coated textile electrodes in terms of (a) - (c) before and (d) - (f) after strain.

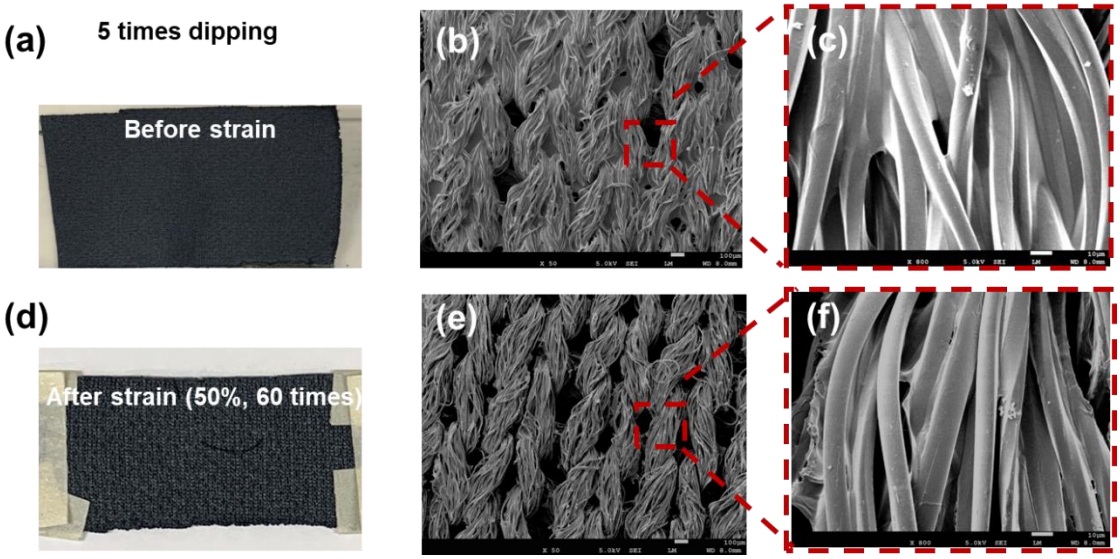


Figure 5.20 Photographs and SEM images of 5 times dipping PEDOT:PSS coated textile electrodes in terms of (a) - (c) before and (d) - (f) after strain.

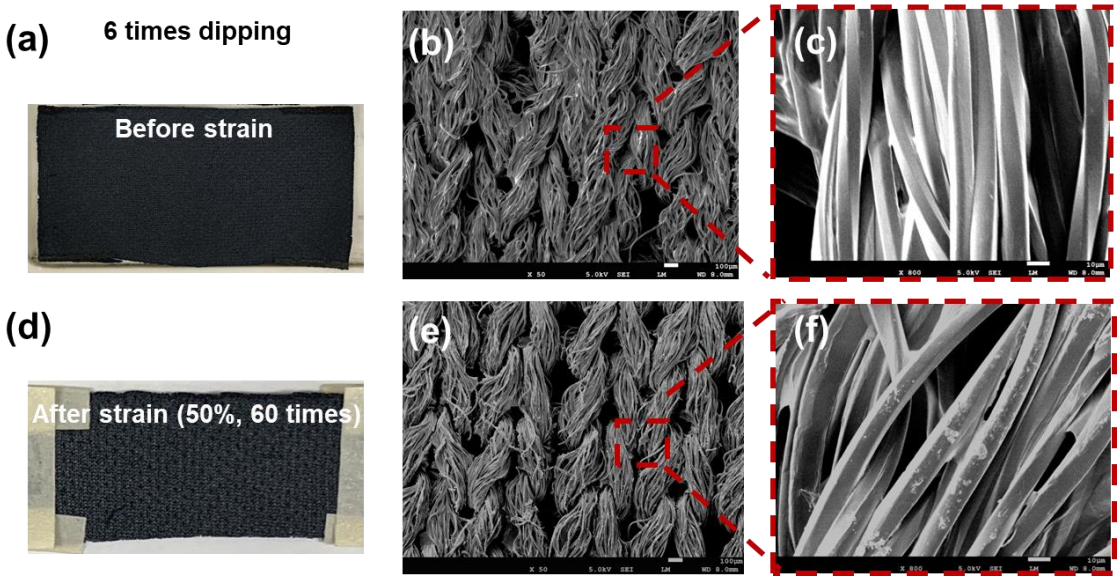


Figure 5.21 Photographs and SEM images of 6 times dipping PEDOT:PSS coated textile electrodes in terms of (a) - (c) before and (d) - (f) after strain.

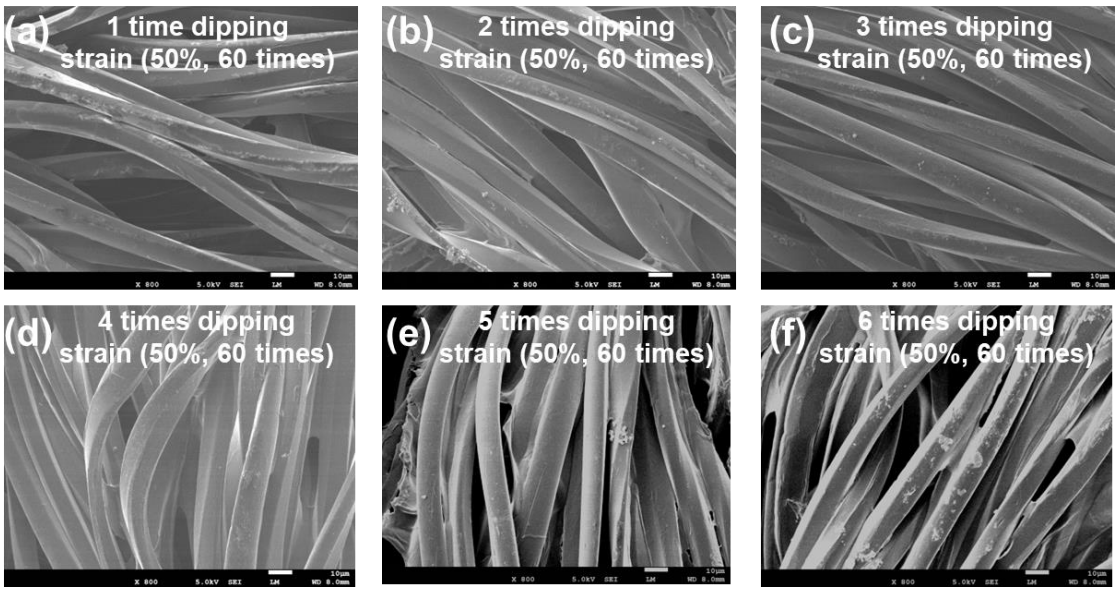


Figure 5.22 Photographs and SEM images of 1-6 times dipping PEDOT:PSS coated textile electrodes after strain.

In order to evaluate the electric conductive ability after deformation, the textile electrodes prepared with different numbers of dipping cycles (1-6 times) were compared using a multimeter at a distance of 1 cm, as shown in Figure 5.23 a. The textile electrodes were progressively stretched from the original state to 50% strain, and the resistance was recorded every 10 times stretching. Predictably, all of the samples show a similar trend in that the initial conductivity increases with the number of dipping cycles and then decreased considerably after 10 stretching cycles. Subsequently, the conductivity was almost equal after continuous stretching and was measured 20, 40, and 60 times, in which the textile electrodes immersed for 4, 5, and 6 cycles exhibited nearly identical conductivity values to those observed in their original state (no stretching). Moreover, the electrodes immersed 5- and 6-times exhibited higher conductivity (6.9 S/cm) than the electrodes immersed 4-times (5.9 S/cm) after 60 stretching cycles (Figure 5.23 b). 0-100% stretching was performed over 50 cycles and the conductivity was measured every 10 cycles (Figure 5.23 c). The conductivity progressively degraded with the% strain and the number of stretching cycles, which was less varied after 20 stretching cycles and was maintained at a stable level.

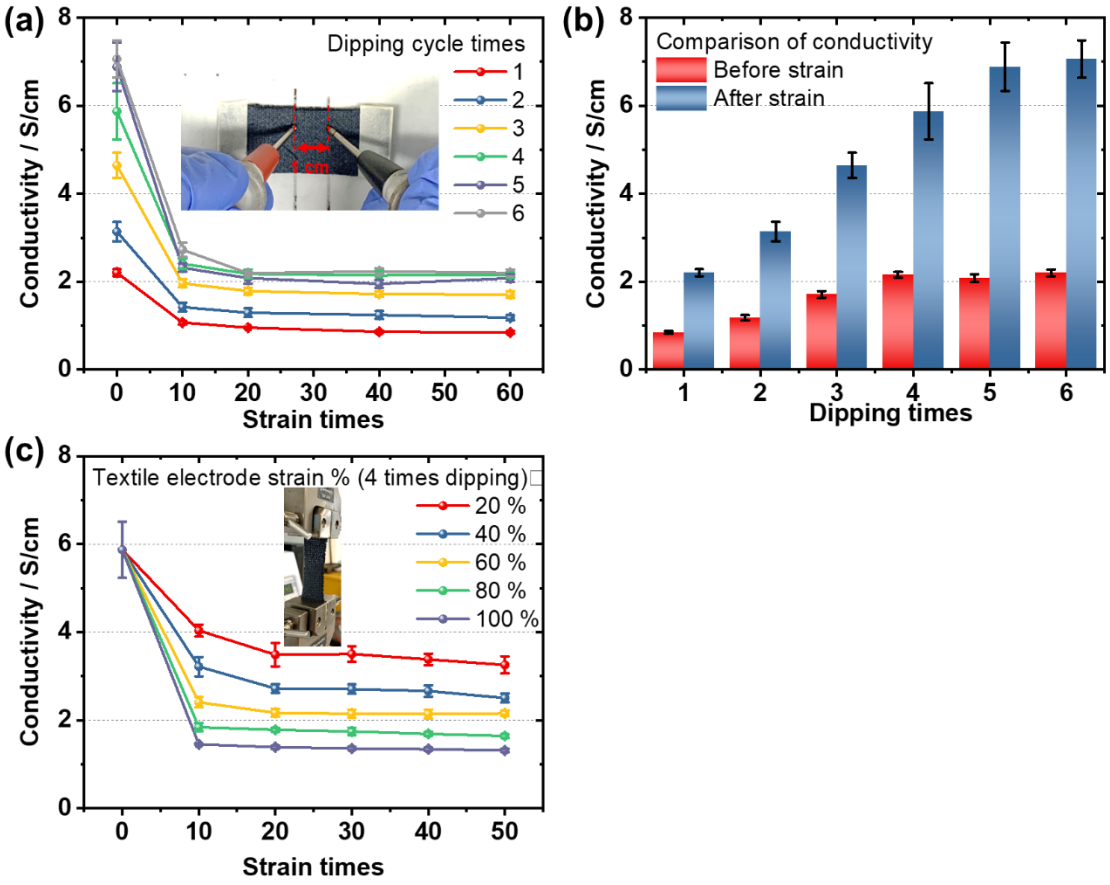


Figure 5.23 The comparison of conductivity of PEDOT:PSS textile electrodes in terms of (a) dipping cycle times, (b) before and after 50% strain for 50 times, and (c) stretching at different strain (20% - 100%).

### *5.3.4.2 Integration with gel electrolytes*

The first crosslinked CMCs-PAM gel was placed between two textile electrodes as a sandwich-structured device (Figure 5.24 a) and the entire device was placed in an oven for the second crosslinking step (Figure 5.24 b). The soft gel penetrated the pores and enveloped the textile electrodes during the second polymerization process, after which the stretchable device was separated into N- and P-type redox couple aqueous solutions (Figure 5.24 c&d) for 48 h prior to use.

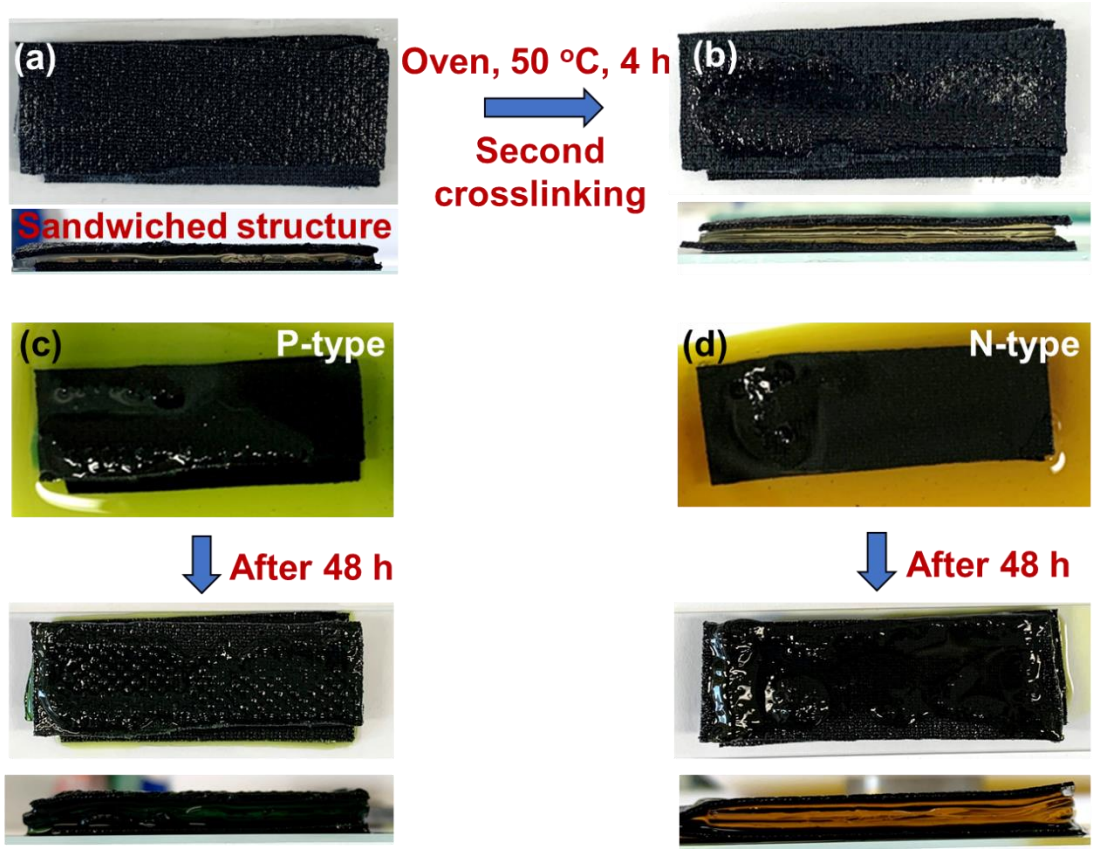


Figure 5.24 Photographs of integration of PEDOT:PSS textile electrodes and gel electrolytes in terms of (a) original state, (b) after second crosslinked, after soaking into (c) P-type and (d) N-type redox couple aqueous solutions.

### 5.3.5 Fabrication of a wearable device

#### *5.3.5.1 Thermo-electrochemical performance upon thermocell deformation*

Once the gel electrolytes and textile electrodes were optimized, the thermocell was subjected to thermo-electrochemical performance analysis; the fabrication process illustrated in Chapter 2.6.3. The thermocell prepared with the textile electrodes was tailored into a 1 × 1 cm squares and assembled with Pt electrodes (as Pt-textile). Two acrylic frameworks (1-4 mm) were placed on the side of the thermocells to control the

distance between the electrodes. The thermocell device was then placed between the hot and cold Peltier instruments, which provided the temperature gradient (Figure 5.25). For the thermocell prepared without the textile electrodes, all procedures were similar with the exception that the textile electrodes were replaced by Pt electrolytes. To simulate the working conditions of the wearable device, the hot electrode was maintained at 35 ℃ as the temperature of the human skin, whereas the cold electrode was changed from 15 to 30 ℃ as the ambient environmental temperature.

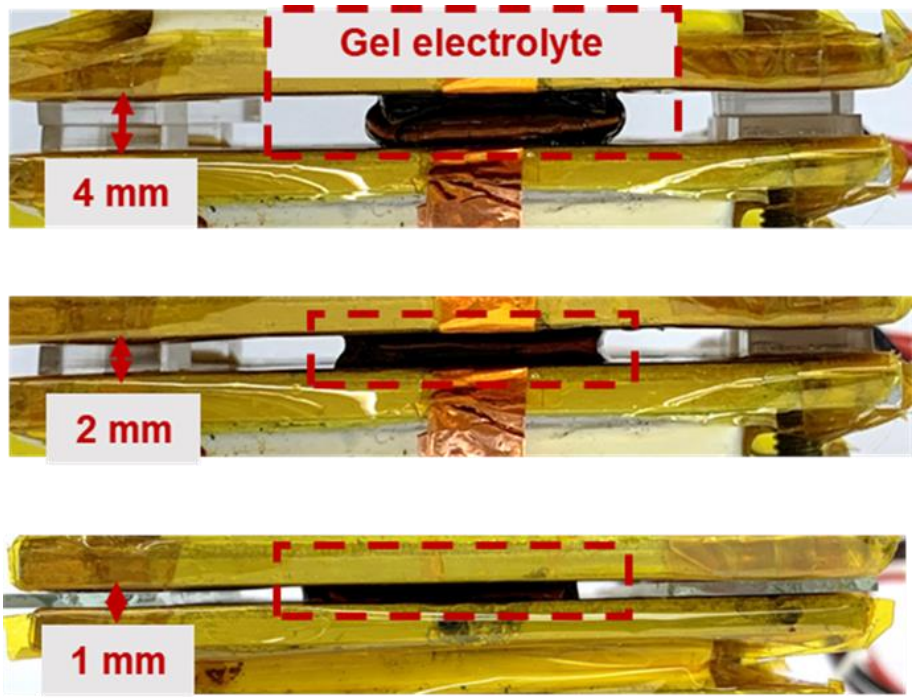


Figure 5.25 An illustration of the compressed thermocells during the thermo-electrochemical test.

The thermo-electrochemical performance under deformation (release: 4 mm; compression: 1 and 2 mm) of the individual thermocells integrated with Pt-textile electrodes and pristine Pt electrodes was systematically studied (Figure 5.26 - Figure 5.28). Figure 5.26 a and b show the optimized TECs performance (the current and

power density are displayed as dashed and solid lines, respectively) of the N- and P-type thermocells at the original thickness (4 mm), respectively. For the N-type gel electrolytes (Figure 5.26 a), Pt-textile electrodes improved the $P_{max}$ from 2.5 to 4.36 mW $m^{-2}$ when compared with the pristine Pt electrode. Surprisingly, the $V_{oc}$ not only failed to decrease with the thermal resistance of the textile fabrics, but also increased from 8.5 to 11 mV. This obvious increase in the $V_{oc}$ of the N-type gel electrolytes was probably caused by the electrochemical catalytic activity of the $Fe^{2+}/Fe^{3+}$ and PEDOT:PSS materials. The $Fe^{2+}/Fe^{3+}$ redox couple is easily drawn around the electrode surface of PEDOT:PSS due to the strong electrostatic attraction from the highly affinitive functional groups in PSS [53,54], which would be further facilitated by the microporous textile electrodes with large electrochemically active surfaces [3,55]. On the contrary, the $V_{oc}$ of the P-type thermocell decreased from 14 to 12.5 mV due to the decrease in the temperature difference between the electrodes. Consequently, swift ion diffusion and electron transfer in the PEDOT:PSS electrodes also promoted the $P_{max}$ from 3.8 to 4.8 mW $m^{-2}$ due to the abundant micronized pores in the textile electrodes (Figure 5.26 b). The long-term (30 min) short-circuit current density of the thermocell was also investigated (Figure 5.26 c&d). Pt-textile electrodes as expected to lead to a significantly improved long-term current density for both the N- (from 1.5 to 2.0 A $m^{-2}$) and P- (from 1.0 to 1.5 A $m^{-2}$) type thermocells. A comparison of the TECs performance under compression (2 and 1 mm) is also shown in Figure 5.27 and Figure 5.28, respectively. When compared with the pristine Pt electrodes, Pt-textile electrodes effectively enhance the $P_{max}$ and long-term current output of both the N- and P-type gel electrolytes under deformation. Pt-textile electrodes have advantages over Pt electrodes under different deformation conditions, which can fully work and effectively improve the thermoelectrochemical performance of thermocells.

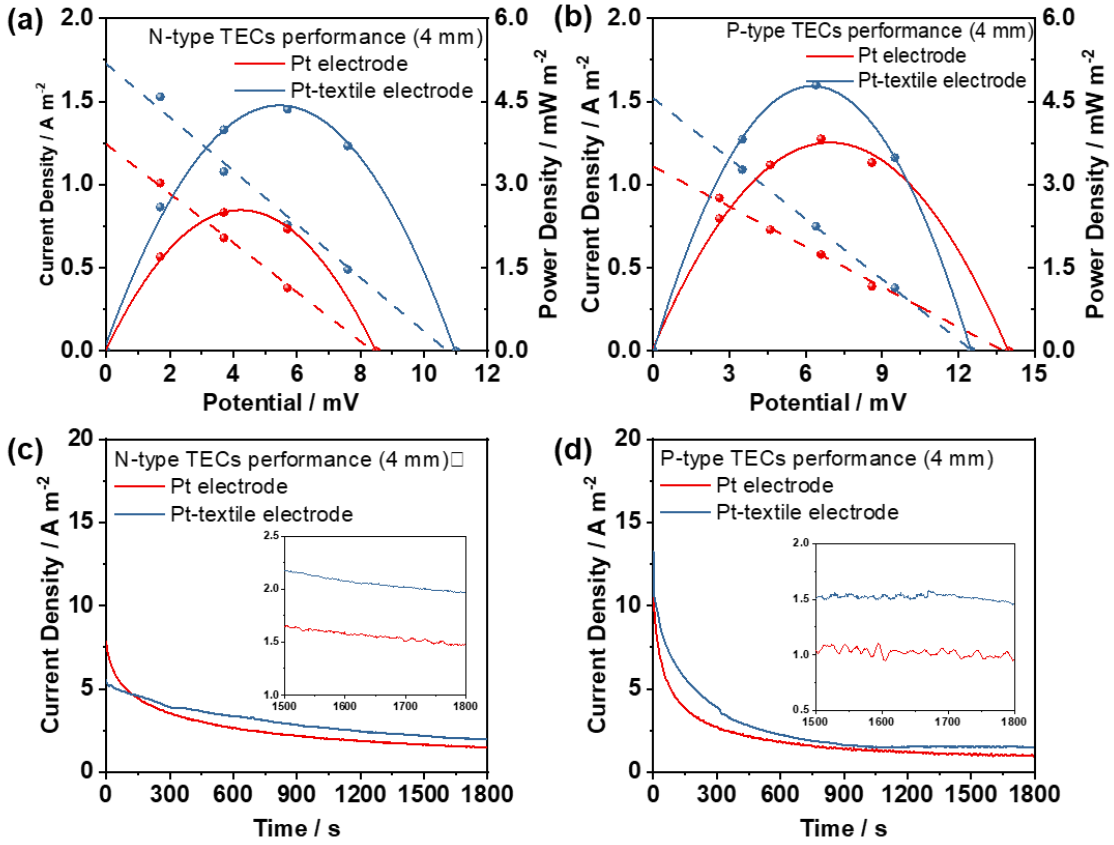


Figure 5.26 A comparison of the thermo-electrochemical performance of N-type and P-type thermocells using Pt electrodes and Pt-textile electrodes under 4 mm thickness at $\Delta T$ = 10 ℃ ($T_c$ = 25 ℃, $T_h$ = 35 ℃) in terms of (a) & (b) current (dash) and power (solid) density versus voltage, and (c) & (d) the long-term short-circuit current density versus time (30 min).

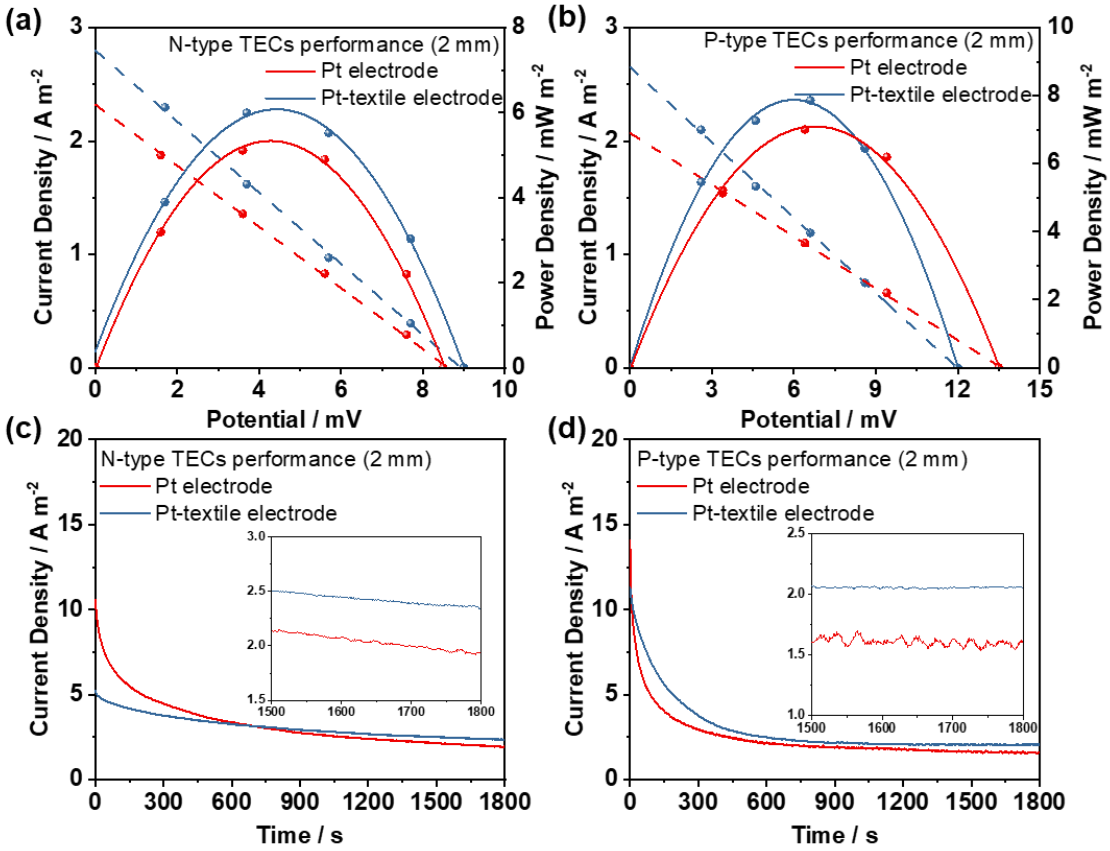


Figure 5.27 A comparison of the thermo-electrochemical performance of N-type and P-type thermocells using Pt electrodes and Pt-textile electrodes under 2 mm thickness at $\Delta T$ = 10 ℃ ($T_c$ = 25 ℃, $T_h$ = 35 ℃) in terms of (a) & (b) current (dash) and power (solid) density versus voltage, and (c) & (d) the long-term short-circuit current density versus time (30 min).

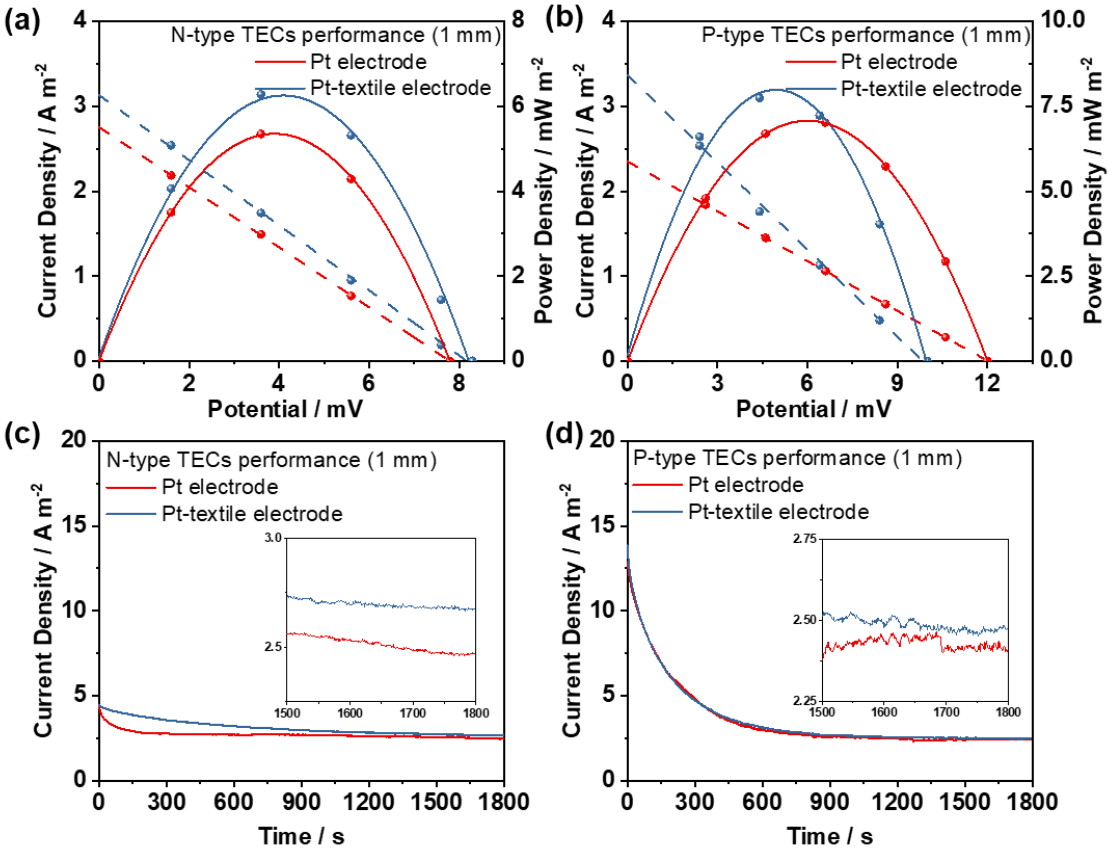


Figure 5.28 A comparison of the thermo-electrochemical performance of N-type and P-type thermocells using Pt electrodes and Pt-textile electrodes under 1 mm thickness at $\Delta T$ = 10 °C ($T_c$ = 25 °C, $T_h$ = 35 °C) in terms of (a) & (b) current (dash) and power (solid) density versus voltage, and (c) & (d) the long-term short-circuit current density versus time (30 min).

In addition, the $P_{max}$ of both the N- and P-type thermocells prepared with Pt-textile electrodes was strongly altered by reducing the electrode distance. Initially, the $P_{max}$ of the N-type thermocells constructed with the electrodes separated by 4 mm (releasing state) was measured to be 4.42 mW $m^{-2}$, which then increased in the range of 6.07-6.26 mW $m^{-2}$ upon compressing the thermocell to 2 and 1 mm, respectively (Figure 5.29 a). A similar tendency was observed for the P-type thermocell, as shown in Figure 5.29 b;

$P_{max}$ was observed to be 4.79 mW $m^{-2}$ in the original state (4 mm), which increased by 64% to 7.86 mW $m^{-2}$ upon reducing the thickness to 2 mm and slightly increased to 7.98 mW $m^{-2}$ at 1 mm (1.5% improvement). The long-term current output densities are also shown in Figure 5.29 c&d, which both decrease upon decreasing the distance between the electrodes. When compared with the thickness of the thermocells in the range of 1-4 mm, the maximum $V_{oc}$ values of the N- and P-type thermocells were observed at 11 and 12.5 mV for a separation of 4 mm, which decreased to 8.3 and 10 mV, respectively when two electrodes were separated by 1 mm (Figure 5.29 a&b). The change in $V_{oc}$ represents a reduction in the electrode spacing, which intensifies the heat diffusion and reduces the temperature differences between the anode and cathode. Consequently, the enlarged current output of the compressed thermocells contributes to the minimization of the distance of ionic diffusion between the two electrodes and larger contact surface after compression [56].

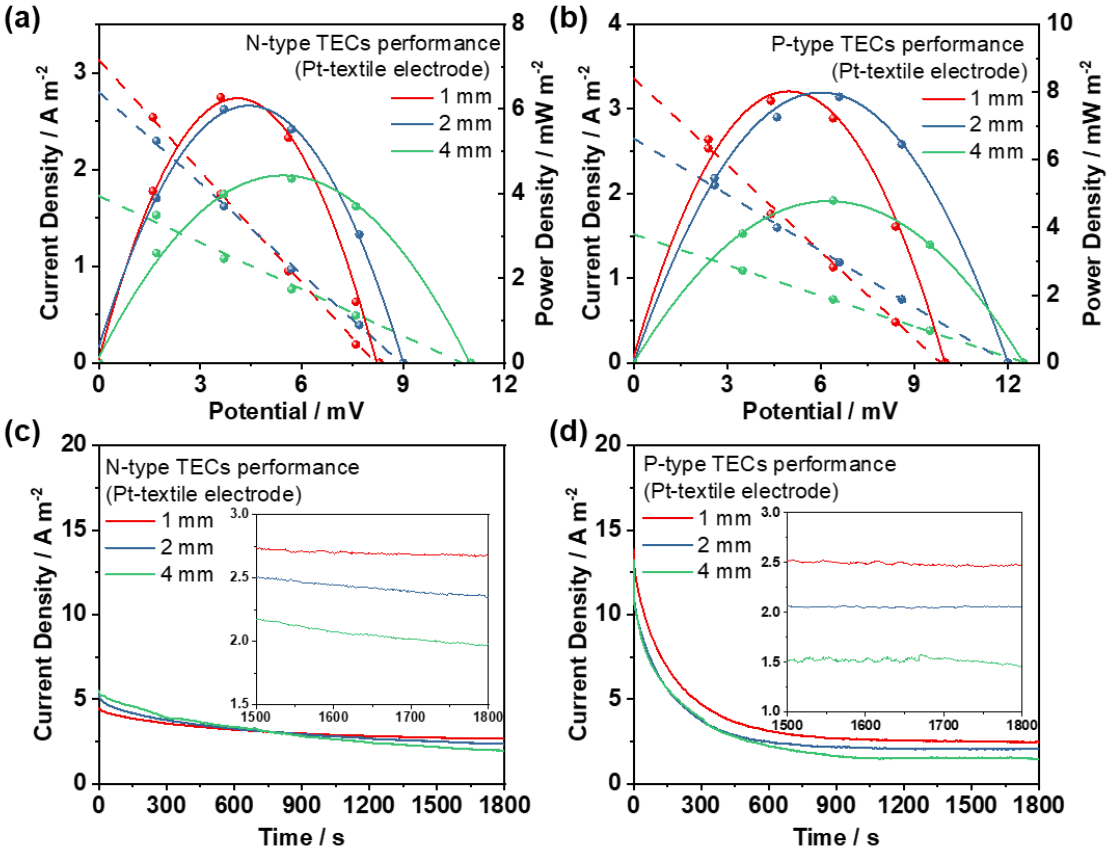


Figure 5.29 A comparison of the thermo-electrochemical performance of N-type and P-type gel electrolytes under the deformations (1 - 4 mm) at $\Delta T$ = 10 °C ($T_c$ = 25 °C, $T_h$ = 35 °C) in terms of (a) & (b) current (dash) and power (solid) density versus voltage, and (c) & (d) the long-term short-circuit current density versus time (30 min).

Furthermore, the current density with deformation of the thermocells is displayed in Figure 5.30. The short-circuit current density quickly responds with alternating compression and recovery every 300 s. The short-circuit current density of the N-type thermocell increased to 2.87 A $m^{-2}$ during compression (2 mm) and decreased to 1.77 A $m^{-2}$ when released (4 mm). The P-type thermocell also displayed a two-fold improvement in the short-circuit current density from 1.15 (4 mm) to 2.35 A $m^{-2}$ (2 mm), implying that the thermocells exhibit practicality under deformation conditions and can

generate electrochemical signals with external physical forces, which indicates their potential in wearable devices and gel electrolytes used for other sensor applications.

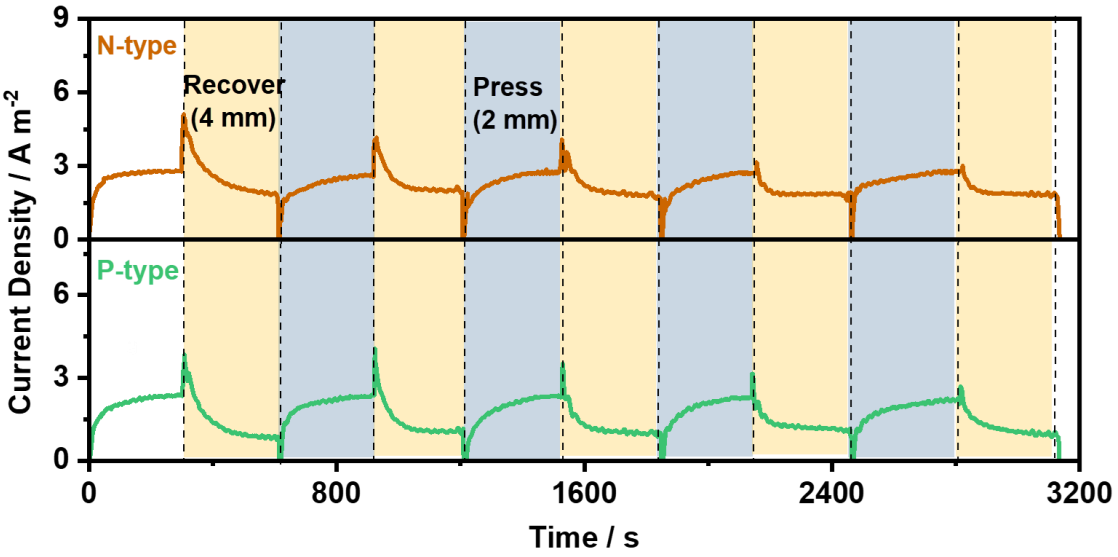


Figure 5.30 The continual electric signal response of current density under deformations.

*5.3.5.2 Combining N- and P-type thermocells*

To satisfy the voltage output requirements of electronic equipment, such as microsensors and wearable devices, N- and P-type thermocells are generally designed alternatively in series to boost the voltage output rather than in parallel to avoid thermal short-circuits [50–52,57]. In this study, the optimized individual N- and P-type thermocells, which were interconnected by sputter-coated Pt, were manufactured in series and analyzed (Figure 5.31 a). Figure 5.31 b shows the voltage of the P-N cells exhibits an effective $S_e$ of 1.9 mV $K^{-1}$, which was ~91% of the absolute $S_e$ of the combined P-type (-1.2 mV $K^{-1}$) and N-type (+0.89 mV $K^{-1}$) cells. This slight decrease was due to the increased resistance of the additional electrical connections [50].

Comparable current outputs were observed at $\Delta T$ = 10 ℃ ($T_c$ = 25 ℃, $T_h$ = 35 ℃) for the single N- and P-types cells (2 mm thickness) due to the unique electrochemical catalysis of PEDOT:PSS on the N-type thermocell (Figure 5.31 c), which were expected to be nearly equal to that of the combined N-P-type cell (0.26 mA). The total absolute power output of the N-P-type cell (1.27 μW) increased by ~191% (rather than 200%) when compared with the sum of the individual N- (0.6 μW) and P- (0.79 μW) type cells due to the interconnection resistance [50–52]. The absolute power was employed instead of the unified normalized power in the combined thermocell investigation because of the different power output and increased connection electrical resistance of the individual N- and P-type thermocells, which deviate from the single thermocells. The N-P-type cell showed predictable relationships of parabolic power output *versus* voltage and linear current output *versus* voltage at $\Delta T$ = 5-20 ℃ ($T_h$ = 35 ℃, $T_c$ = 15-30 ℃) in Figure 5.31 d, which indicated the stability of thermocells at various temperature gradients. These results illustrate that the effectively combined N-P-type cell fully operates under deformation and a broad temperature range, showing its potential for utilization under a variety of complicated conditions.

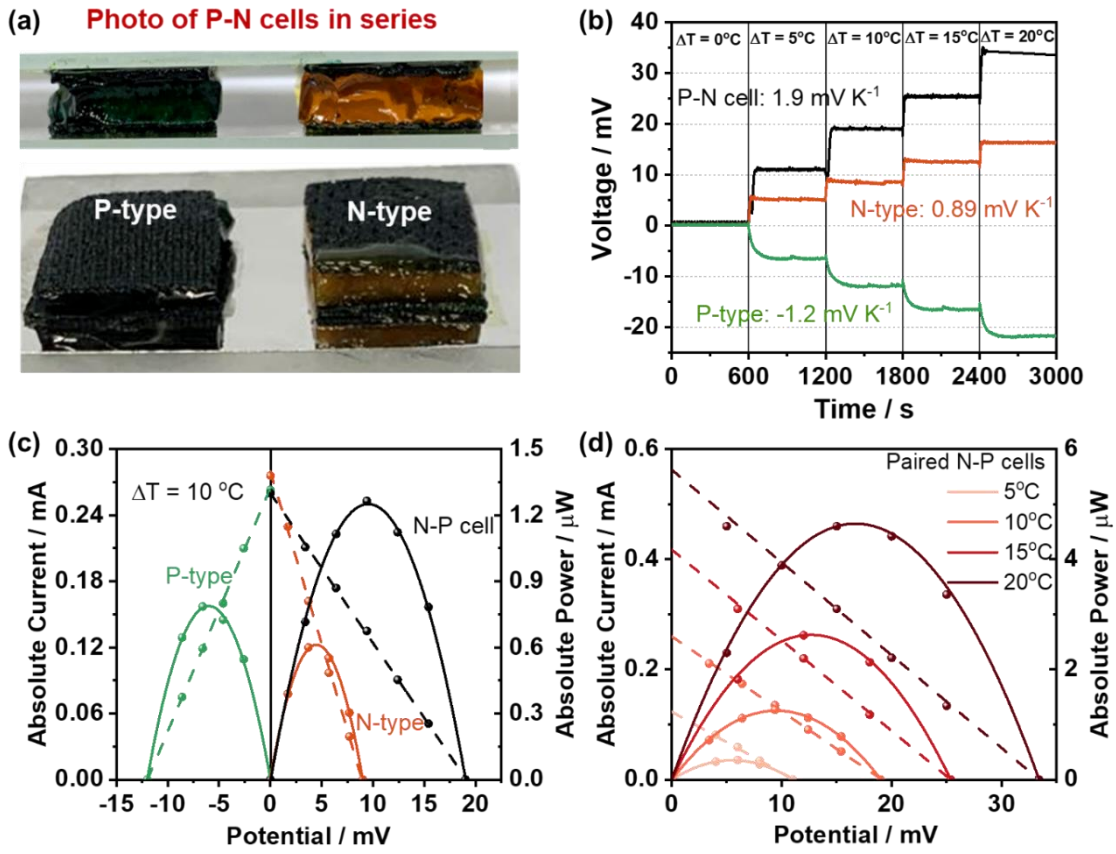


Figure 5.31 A pair of P-N cells. (a) Schematic illustration and photograph of P-N-type cells in series. Thermo-electrochemical performance of the P-type, N-type and P-N cells in terms of (b) voltage at different ΔT (5 - 20 ℃), (c) current (dashed line) and power (solid line) output versus voltage at ΔT = 10 ℃ ($T_c$ = 25 ℃, $T_h$ = 35 ℃), and (d) current (dashed line) and power (solid line) output versus voltage of P-N cell at different ΔT.

Furthermore, the thermo-electrochemical performance of the combined N-P-type cells was also tested under deformation, as shown in Figure 5.32. The identical trend observed for the absolute power and current output increased as the distance between the electrodes decreased and the $P_{max}$ of the combined N-P-type cell could achieve 1.32 μW at a thickness of 1 mm, which was a 59% improvement when compared with that of the thermocells at 4 mm (0.83 μW) (Figure 5.32 a). Figure 5.32 b shows the long-time

$J_{sc}$ values of the thermocells. As expected, the thermocell under compression to 1 mm also demonstrated an improved long-term current density that reached 0.22 mA after 30 min when compared to 0.15 mA in the released state (4 mm).

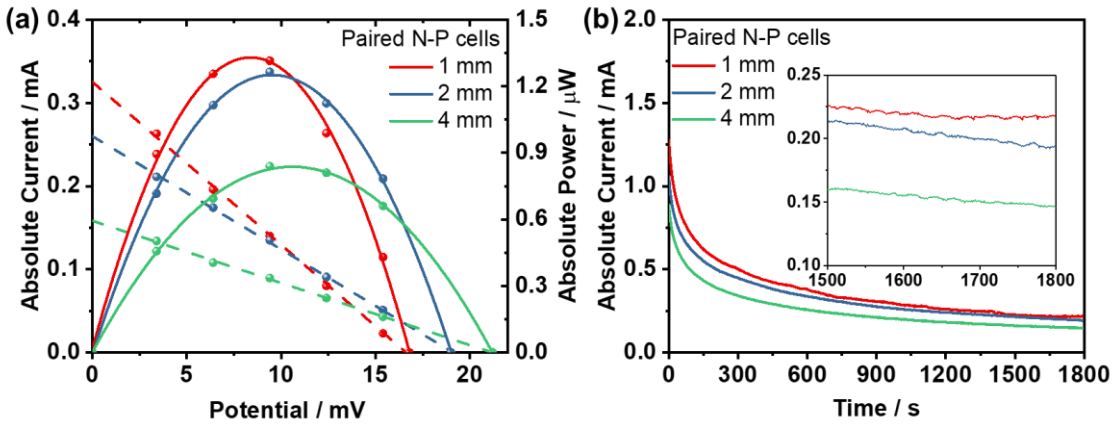


Figure 5.32 Thermo-electrochemical performance of combined N-P-type cells under deformations ΔT = 10 ℃ ($T_c$ = 25 ℃, $T_h$ = 35 ℃) in terms of (a) current (dashed line) and power (solid line) output versus voltage and (b) long-term short-circuit current density versus time (30 min).

### *5.3.5.3 Prototyping multiple N-P cells*

A larger array was designed to further confirm the effectiveness of the N-P-type cells (Figure 5.33 a). Sputter-coated Pt was used as the connection of the inter-individual alternative N- and P-types cells and the electrode separation was also maintained through the PMMA spacers, as mentioned above. Two pairs of N-P-types cells were combined in series (Figure 5.33 b) and multiple N-P-types cells connected in series were prepared, as shown in Figure 5.33 a (2 × 2 pairs), which can charge a commercial supercapacitor and light up an LED *via* a voltage booster at a temperature gradient of

10 ℃ (Figure 5.33 a). The thermo-electrochemical performance of the thermocell arrays (1-4 pairs, 2 mm thickness) was measured at ΔT = 10 ℃ (Figure 5.33 c). $V_{oc}$ linearly increased from 19 mV for one pair of cells to 74.3 mV for four pairs. The absolute current output of the four pairs of thermocell arrays was less diminished by the connection resistance and the power output gradually increased with the number of N-P pairs. A device with multiple N-P-type cells also enables the charging of commercial supercapacitors (C = 47, 100, 470, and 100 mF) to ~74 mV (Figure 5.33 d). The charge rate of the 47-470 mF supercapacitors was fast and the expected voltage was reached within 5 min. The largest capacitor (1000 mF) took a longer time to reach the desired voltage (~12 min), demonstrating how different capacitors can be applied to reflect the different durations that wearable devices may be worn before being removed (and remaining powered by the stored capacitance).

As also in Chapter 4, the device apparently needs the voltage booster to work with. The voltage booster used here could amplify voltage for satisfying the electrical devices. For equipping voltage boosters in actual wearable device, some points need to be considered. Firstly, the available area within the wearable device to accommodate the voltage booster need to be considered. It should not hinder the functionality or comfort of the device for the user. Develop or procure a compact voltage booster that can easily fit within the constraints of the wearable device. It should have the necessary specifications suitable for the specific power requirements of the device. Next, thermocells as the power source that need to optimize and management. Ensure that the wearable device has efficient power management capabilities to support the voltage booster. Then, thermocells integrate with voltage boosters accordingly. It should be connected in a way that ensures a stable power supply to the device, considering factors like voltage

fluctuations and load variations. Finally, conduct thorough testing to verify that the voltage booster performs as intended and functions seamlessly with the wearable device. Validate its effectiveness, efficiency, and durability under various usage scenarios. We believe the voltage booster can be successfully equipped in the upcoming wearable devices, ensuring stable operation and optimal power supply.

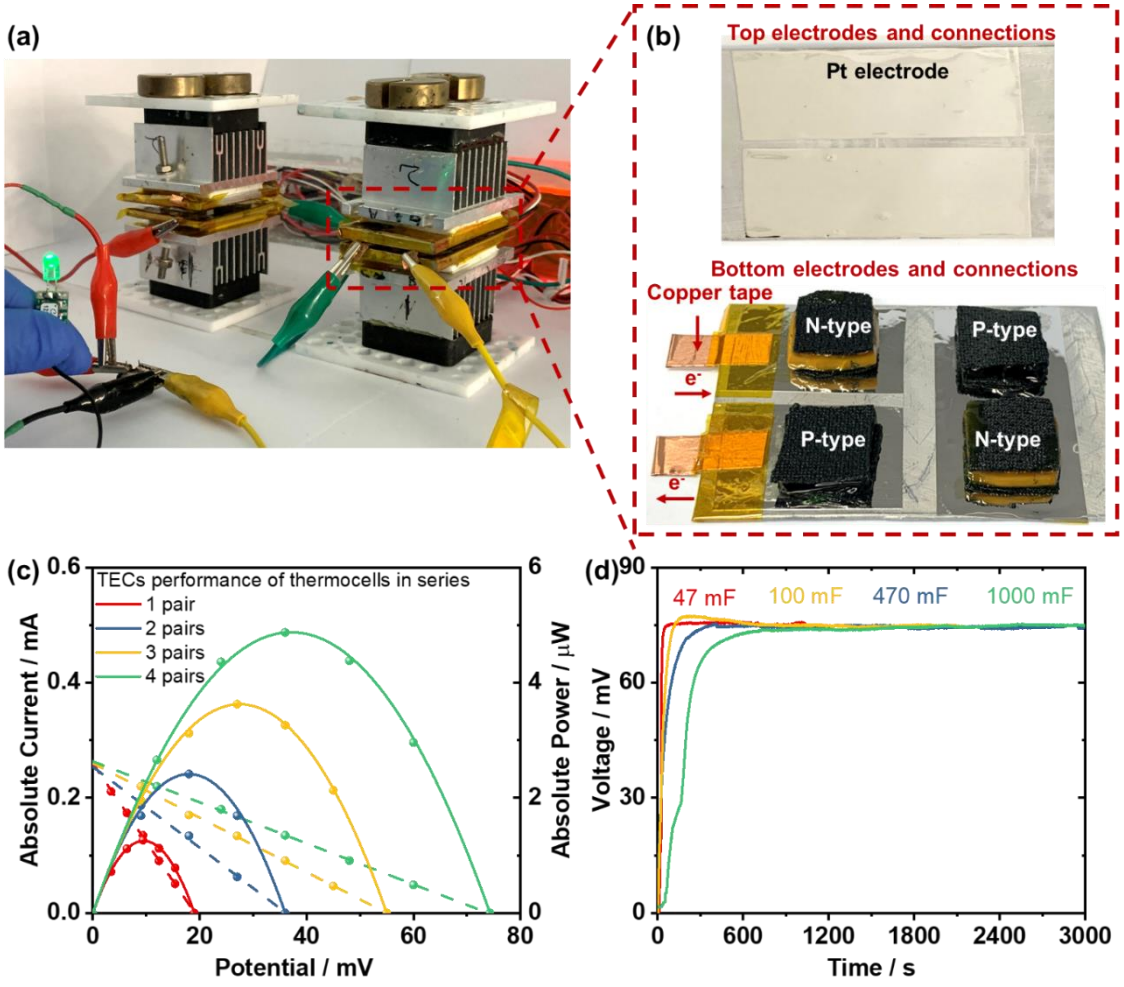


Figure 5.33 (a) Demonstration of thermally charged supercapacitors illuminating a green LED (arrays with 2 x 2 pair N-P cells connected in series), and (b) photograph of 2 pair N-P cells connected in series. (c) Thermo-electrochemical performance of multiple pairs of N-P cells at $\Delta T$ = 10 °C, and (d) 4 pairs of N-P-type cells charging supercapacitors with different capacitances.

*5.3.5.4 Flexible and wearable N-P-type cells*

A flexible soft pack thermocell that conforms to the surface of the skin was fabricated to harvest human body heat. The Pt electrode and thermocell (10 × 50 mm) were encapsulated by Al-laminated film and the tab electrode was fixed on the Pt electrode using Kapton tape (Figure 5.34 a). The individual N- and P-type soft-pack thermocells were connected in series, as shown in Figure 5.34 b. As a demonstration of wearable devices, a soft pack thermocell array (two pairs of N- and P-type cells) was connected in series and wore on the arm. The flexible thermocell device could be a 100 mF commercial supercapacitor after long-term wear and illuminated an LED *via* a voltage booster (Figure 5.34 c). This prototype wearable thermocell device is an effective potential energy source for self-powered devices.

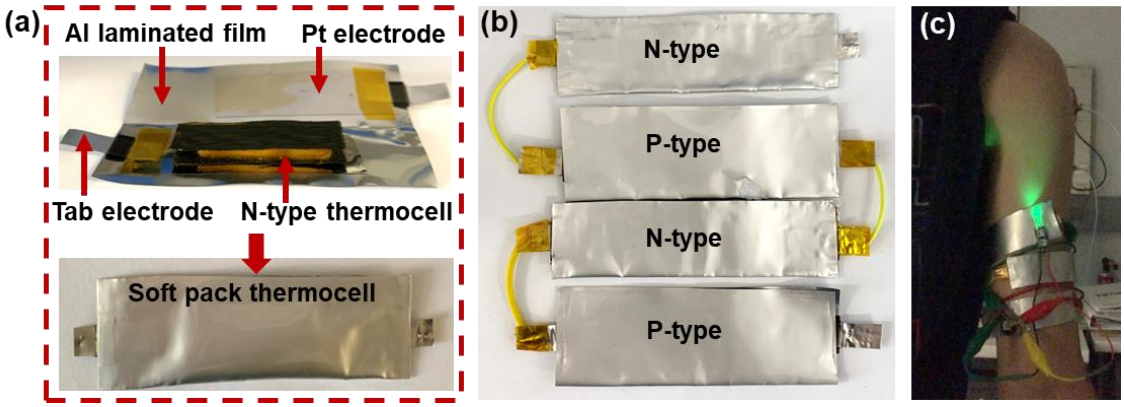


Figure 5.34 (a) Design of soft-packing N-P-type cells, (b) the soft-packing N-P cells array, and (c) photographs of the wearable thermocell for body-heat harvesting.

## 5.4 Conclusions

In summary, we have designed stretchable and biocompatible double-network CMCs-PAM gel electrolytes that were adapted to accommodate both N- and P-type redox couples to address the challenges encountered by the poor mechanical properties and compatibility issues observed between the polymer and redox couples. Gel electrolytes can be maximally stretched up to 368% and recover their original state immediately after compression, which satisfies the requirements of wearable devices. Moreover, textile electrodes with porous structures were integrated with gel electrolytes to boost their electrochemical performance by expanding the electrochemical reaction surface and coordination of PSS and $Fe^{3+}$. Fast response and restoration of the current density were observed with respect to the compression test, demonstrating the effectiveness of the thermocells utilized in realistic applications. Finally, N- and P-type soft packing thermocells were manufactured and connected in series, which could be worn on the arm to illuminate an LED light by charging a supercapacitor. This work is the first to report novel double-network hydrogels with excellent mechanical properties that can be used as solid-state electrolytes in wearable thermocells. Porous textile electrodes were initially employed in combination with solid-state electrolytes in thermoelectrochemical fields to fabricate integral stretchable thermocells. We believe that the mechanism of crosslinking and the proportion of polymers will provide inspiration to address the difficulties encountered in multidisciplinary applications. The design of thermocells has proven the practical feasibility of wearable devices and provides an approach toward advanced self-powered devices in the future.

## 5.5 Reference

[1] Y. Liu, S. Zhang, S. Beirne, K. Kim, C. Qin, Y. Du, Y. Zhou, Z. Cheng, G. Wallace, J. Chen, *Macromol. Rapid Commun.* **2022**, *43*, 1.

[2] S. Zhang, Y. Zhou, Y. Liu, G. G. Wallace, S. Beirne, J. Chen, *iScience* **2021**, *24*, 103466.

[3] R. E. Del Sesto, T. M. McCleskey, A. K. Burrell, G. A. Baker, J. D. Thompson, B. L. Scott, J. S. Wilkes, P. Williams, *Chem. Commun.* **2008**, *10*, 447.

[4] Y. Zhou, Y. Liu, M. A. Buckingham, S. Zhang, L. Aldous, S. Beirne, G. Wallace, J. Chen, *Electrochem. commun.* **2021**, *124*, 106938.

[5] S. Zhang, Y. Liu, J. Hao, G. G. Wallace, S. Beirne, J. Chen, *Adv. Funct. Mater.* **2021**, *2103092*, 1.

[6] Y. Zhou, S. Zhang, M. A. Buckingham, L. Aldous, S. Beirne, C. Wu, Y. Liu, G. Wallace, J. Chen, *Chem. Eng. J.* **2022**, *449*, 137775.

[7] S. S. Vaghani, M. M. Patel, C. S. Satish, K. M. Patel, N. P. Jivani, *Bull. Mater. Sci.* **2012**, *35*, 1133.

[8] Z. Shariatinia, *Int. J. Biol. Macromol.* **2018**, *120*, 1406.

[9] H. Zhang, H. Shen, J. Lan, H. Wu, L. Wang, J. Zhou, *Carbohydr. Polym.* **2022**, *295*, 119848.

[10] Y. Sun, J. Gao, Y. Liu, H. Kang, M. Xie, F. Wu, H. Qiu, *Chem. Eng. Sci.* **2019**, *207*, 516.

[11] Y. Yue, X. Wang, J. Han, L. Yu, J. Chen, Q. Wu, J. Jiang, *Carbohydr. Polym.* **2019**, *206*, 289.

[12] M. Moztahida, D. S. Lee, *J. Hazard. Mater.* **2020**, *400*, 123314.

[13] D. Wang, H. Li, Z. Liu, Z. Tang, G. Liang, F. Mo, Q. Yang, L. Ma, C. Zhi, *Small* **2018**, *14*, 1.

[14] H. Li, Z. Liu, G. Liang, Y. Huang, Y. Huang, M. Zhu, Z. Pei, Q. Xue, Z. Tang, Y. Wang, B. Li, C. Zhi, *ACS Nano* **2018**, *12*, 3140.

[15] F. L. Yi, F. L. Guo, Y. Q. Li, D. Y. Wang, P. Huang, S. Y. Fu, *ACS Appl. Mater. Interfaces* **2021**, *13*, 32084.

[16] H. Xue, L. Hu, Y. Xiong, X. Zhu, C. Wei, F. Cao, W. Zhou, Y. Sun, Y. Endo, M. Liu, Y. Liu, J. Liu, A. Abududilibaier, L. Chen, C. Yan, B. Mi, G. Liu, *Carbohydr. Polym.* **2019**, *226*, 115302.

[17] X. Mu, J. Zhou, P. Wang, H. Chen, T. Yang, S. Chen, L. Miao, T. Mori, *Energy Environ. Sci.* **2022**, *15*, 3388.

[18] C.-G. Han, X. Qian, Q. Li, B. Deng, Y. Zhu, Z. Han, W. Zhang, W. Wang, S.-P. Feng, G. Chen, W. Liu, *Science (80-. ).* **2020**, *368*, 1091.

[19] D. G. Mackanic, M. Kao, Z. Bao, *Adv. Energy Mater.* **2020**, *10*, 2001424.

[20] D. J. Liua Y, L. L. Jianga J, *J. Mol. Genet. Med.* **2015**, *09*, 9.

[21] Z. Lei, W. Gao, P. Wu, *Joule* **2021**, *5*, 2211.

[22] W. Gao, Z. Lei, C. Zhang, X. Liu, Y. Chen, *Adv. Funct. Mater.* **2021**, *31*, 2104071.

[23] Z. Jing, X. Dai, X. Xian, X. Du, M. Liao, P. Hong, Y. Li, *RSC Adv.* **2020**, *10*, 23592.

[24] G. Du, L. Nie, G. Gao, Y. Sun, R. Hou, H. Zhang, T. Chen, J. Fu, *ACS Appl.*

*Mater. Interfaces* **2015**, *7*, 3003.

[25] J. Y. Sun, X. Zhao, W. R. K. Illeperuma, O. Chaudhuri, K. H. Oh, D. J. Mooney, J. J. Vlassak, Z. Suo, *Nature* **2012**, *489*, 133.

[26] Q. Chen, D. Wei, H. Chen, L. Zhu, C. Jiao, G. Liu, L. Huang, J. Yang, L. Wang, J. Zheng, *Macromolecules* **2015**, *48*, 8003.

[27] X. Huang, J. Li, J. Luo, Q. Gao, A. Mao, J. Li, *Mater. Today Commun.* **2021**, *29*, 102757.

[28] C. W. Chang, A. Van Spreeuwel, C. Zhang, S. Varghese, *Soft Matter* **2010**, *6*, 5157.

[29] Y. Okumura, K. Ito, *Adv. Mater.* **2001**, *13*, 485.

[30] W. Huang, Y. Wang, L. M. McMullen, M. T. McDermott, H. Deng, Y. Du, L. Chen, L. Zhang, *Carbohydr. Polym.* **2019**, *222*, 114977.

[31] R. Zeng, S. Lu, C. Qi, L. Jin, J. Xu, Z. Dong, C. Lei, *J. Appl. Polym. Sci.* **2022**, *139*, 1.

[32] J. Xu, Y. Liu, S. Hsu, *Molecules* **2019**, *24*, 1.

[33] G. Buhus, M. Popa, J. Desbrieres, *J. Bioact. Compat. Polym.* **2009**, *24*, 525.

[34] L. Upadhyaya, J. Singh, V. Agarwal, R. P. Tewari, *Carbohydr. Polym.* **2013**, *91*, 452.

[35] I. Dmitriev, I. Kuryndin, N. Bobrova, M. Smirnov, *Mater. Today Commun.* **2015**, *4*, 93.

[36] R. Wang, M. Yao, S. Huang, J. Tian, Z. Niu, *Sci. China Mater.* **2022**, *65*, 2189.

[37] F. Wu, Y. Pang, J. Liu, *Nat. Commun.* **2020**, *11*, 1.

[38] Y. Wang, C. Zhu, R. Pfattner, H. Yan, L. Jin, S. Chen, F. Molina-Lopez, F. Lissel, J. Liu, N. I. Rabiah, Z. Chen, J. W. Chung, C. Linder, M. F. Toney, B. Murmann, Z. Bao, *Sci. Adv.* **2017**, *3*, 1.

[39] J. Lei, J. H. Kim, Y. S. Jeon, *Macromol. Res.* **2008**, *16*, 45.

[40] T. Q. Bui, V. D. Cao, W. Wang, A. L. Kjøniksen, *Polymers (Basel).* **2021**, *13*, 1.

[41] M. A. Elblbesy, T. A. Hanafy, M. M. Shawki, *E-Polymers* **2022**, *22*, 566.

[42] N. V. Gupta, H. G. Shivakumar, *Iran. J. Pharm. Res. IJPR* **2012**, *11*, 481.

[43] B. Cheng, B. Pei, Z. Wang, Q. Hu, *RSC Adv.* **2017**, *7*, 42036.

[44] A. J. Bard, L. R. Faulkner, *Double-Layer Structure and Adsorption*, **2001**.

[45] O. A. González-Meza, E. R. Larios-Durán, A. Gutiérrez-Becerra, N. Casillas, J. I. Escalante, M. Bárcena-Soto, *J. Solid State Electrochem.* **2019**, *23*, 3123.

[46] J. S. Park, J. H. Choi, J. J. Woo, S. H. Moon, *J. Colloid Interface Sci.* **2006**, *300*, 655.

[47] J. Wu, J. J. Black, L. Aldous, *Electrochim. Acta* **2017**, *225*, 482.

[48] M. A. Buckingham, L. Aldous, *J. Electroanal. Chem.* **2020**, *872*, 114280.

[49] M. A. Buckingham, S. Zhang, Y. Liu, J. Chen, F. Marken, L. Aldous, *ACS Appl. Energy Mater.* **2021**, *4*, 11204.

[50] M. Al Maimani, J. J. Black, L. Aldous, *Electrochem. commun.* **2016**, *72*, 181.

[51] M. A. Buckingham, K. Laws, J. T. Sengel, L. Aldous, *Green Chem.* **2020**, *22*, 6062.

[52] Y. Liu, H. Wang, P. C. Sherrell, L. Liu, Y. Wang, J. Chen, *Adv. Sci.* **2021**, *8*, 1.

[53] A. K. Sundramoorthy, B. S. Premkumar, S. Gunasekaran, *ACS Sensors* **2016**, *1*, 151.

[54] M. Sobkowiak, R. Gabrielsson, O. Inganäs, G. Milczarek, *Synth. Met.* **2014**, *194*, 170.

[55] R. Hu, B. A. Cola, N. Haram, J. N. Barisci, S. Lee, S. Stoughton, G. Wallace, C. Too, M. Thomas, A. Gestos, M. E. Dela Cruz, J. P. Ferraris, A. A. Zakhidov, R. H. Baughman, *Nano Lett.* **2010**, *10*, 838.

[56] Y. Huang, F. Cui, J. Bao, Y. Zhao, J. Lian, T. Liu, H. Li, *J. Mater. Chem. A* **2019**, *7*, 20778.

[57] M. A. Buckingham, K. Laws, E. Cross, A. J. Surman, L. Aldous, *Green Chem.* **2021**, *23*, 8901.

# Chapter 6 Conclusion and Perspectives

## 6.1 General conclusions

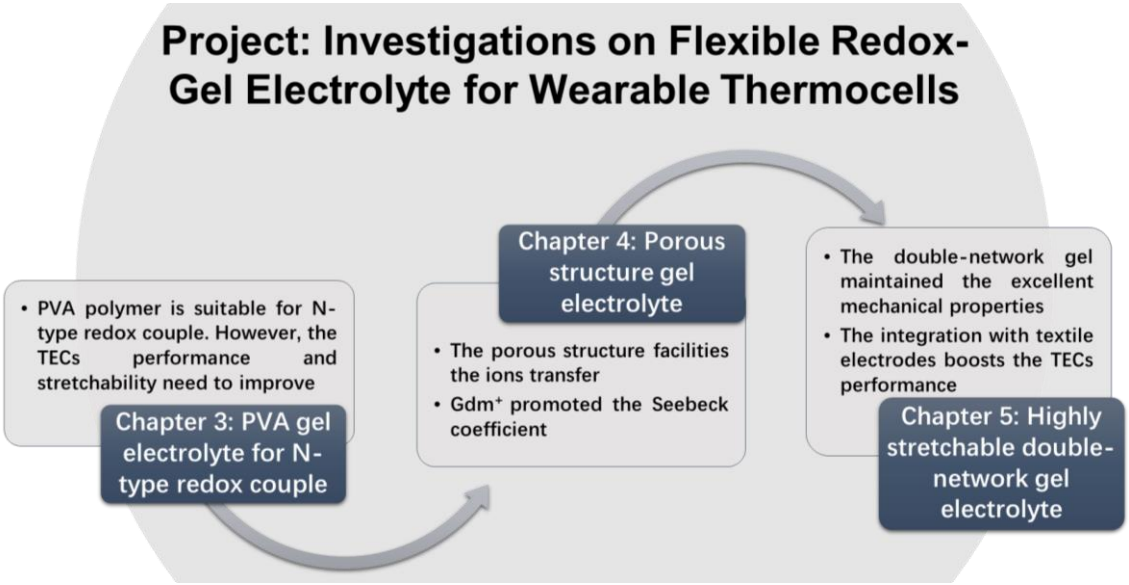


Figure 6.1 An illustration of thesis project outline.

This thesis has focused on the synthesis of multifunctional gel electrolytes for thermogalvanic cells and the manufacturing of flexible wearable thermocell devices. In Figure 6.1, progress was made in terms of hydrogel hosts with multifunctional properties, gel electrolytes compatible with redox couples and suitable technologies to achieve advanced device performance step-by-step.

Specifically, this thesis started with the preparation of novel PVA-$FeCl_{2/3}$-HCl gel electrolytes and CMC-$K_{3/4}[Fe(CN)_6]$ quasi-solid electrolytes. The CMC was selected to be compatible with chemically active P-type redox couple because of its neutrality and solubility for $K_{3/4}[Fe(CN)_6]$. In the N-type gel electrolyte, PVA gel is firstly reported as the polymer matric for acidic $FeCl_{2/3}$ redox couple solution, coincidentally, acidity is also indispensable for gelation reactions. Moreover, HCl was initially used as the acidic

supporting electrolyte in thermocells fields to provide the extra ions to reduce the charge transfer resistance from 113 Ω to 57 Ω and improved the elastic performance of PVA gel electrolytes from 110% to 180%. Optimized PVA-$FeCl_{2/3}$-HCl gel electrolytes exhibited a similar redox reaction process with the liquid electrolyte systems. The N-type thermocell also delivered excellent TECs performance with a $S_e$ of 0.8 ± 0.02 mV $K^{-1}$, $J_{sc}$ of 16.1 A $m^{-2}$ and $P_{max}$ of 63.7 mW $m^{-2}$ at ΔT = 20 K. The parallel connected N-type thermocell set a solid foundation for thermocells (either N- or P-type) connection in series for increased power output kinetics. However, ions transfer suffered from the limitation in the gel electrolytes system in this work and each polymer host was only suitable for one kind of type redox couple individually. Therefore, the hydrogel host that is compatible with both types of redox couple is necessary to explore.

To address the above noted issue, we also prepared the neutral PAM hydrogel host that is suitable for both N and P-type redox couple with porous structures. Furthermore, $Gdm^+$ ions were also initially introduced in gel electrolytes for improving the $S_e$, because repeated crystallization and dissolution in the vicinity of hot and cold electrodes rise to concentration differences. In this project, the long-term TEC performance was used to simulate the realistic utilization of thermocells. The optimized PAM-$K_{3/4}[Fe(CN)_6]$ gel electrolyte performed the $V_{oc}$ of 12 mV, $J_{sc}$ of 2.4 A $m^{-2}$ and $P_{max}$ of 7.1 mW $m^{-2}$ at ΔT = 10 K. The N-type gel electrolyte PAM-$FeCl_{2/3}$-HCl showed a comparable current density, which enabled the N and P cells to alternatively be connected 12 pairs resulting in an output voltage of 0.23 V when ΔT = 10 K. The band shape thermocells array containing 9 pairs of N-P cells was worn on the wrist for harvesting human body heat and charged a 100 mF commercial supercapacitor or illuminated a LED. Consequently, we expect that these heat harvesting devices in this

project have great potential in realistically applying portable wearable electrical systems.

However, challenges still remain in the fabrication of flexible and tough gel electrolytes and their compatibility with redox actives. We have developed a novel robust, neutral and biocompatible hydrogel with outstanding stretchability and recoverability *via* double network crosslinked carboxymethyl chitosan (CMCs) and polyacrylamide (PAM) by covalent bonds, which accommodates both N-type ($FeCl_2/FeCl_3$) and P-type ($K_3[Fe(CN)_6]$/ $K_4[Fe(CN)_6]$) redox couple. Moreover, PEDOT:PSS textile electrodes with porous structure are integrated into gel electrolytes that effectively boost the $P_{max}$ of N- and P-type thermocell by 76% and 26%, respectively, under the larger electrochemical active area and the ionically coordination effect with $Fe^{3+}$. The optimized thermocell exhibits a quick current density response and is continually fully operational under deformations, which satisfies the working conditions of wearable devices. The multiple thermocells (4 pairs) were fabricated in alternating single N and P-type cells in series and output nearly 74.3 mV at $\Delta T$ = 10 ℃. The wearable device was manufactured into a soft pack thermocells to successfully harvest human body heat and illuminate an LED, demonstrating the potential of the actual application of the thermocell device. We believe that the cross-linking mechanism and the proportion of polymers are a source of inspiration for addressing the challenges of multidisciplinary interactions. Wearable thermocells design has proven the practical feasibility of portable wearable devices and has provided an approach toward advanced self-powered devices in the future.

## 6.2 Perspectives

We introduced recent remarkable progress of wearable thermo-electrochemical cells made in the last decades, which benefited from the fundamental theoretical principles and advanced material technologies. Despite multiple crosslinking strategies for high-performance flexible gel electrolytes discussed in this thesis, challenges of gel electrolytes are still remained in intrinsic limitations and fabrication techniques aspects to achieve comparable performance with liquid systems. Following, we discussed the elaborated four directions for future applications of multifunctional gel electrolytes for wearable devices (Figure 6.2).

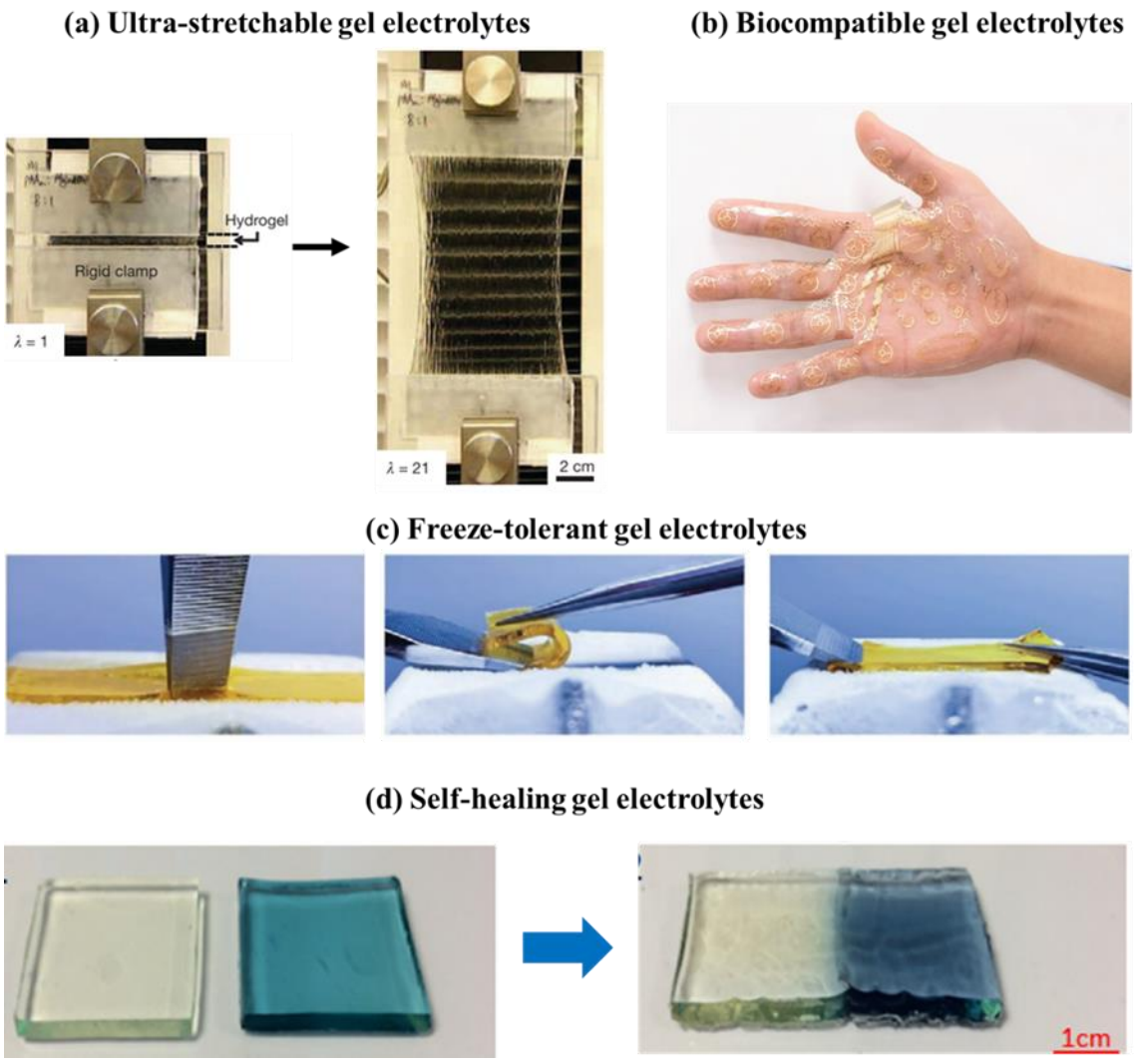

Figure 6.2 (a) A strip of the undeformed gel was glued to two rigid clamps and was stretched to 21 times its initial length in a tensile machine [1]; (b) Photograph showing the wearable devices based on biocompatible hydrogel worn on the hand [2]; (c) A photograph of the organohydrogel thermocell being pressed, bent and stretched on an ice surface of -20 ℃ [3]; (d) A photograph of freshly cut κ-carrageenan and polyacrylamide double-network hydrogel samples with a sheet shape and the self-healed sheet-shaped sample [4].

**Ultra-stretchable gel electrolytes**

The challenge associated with gel electrolytes that needs to be addressed is the mechanical strength of hydrogels. Although the highly stretchable gel electrolyte was introduced in chapter 5, the gel electrolytes with ultra-mechanical strength can be further developed, because a wider range of activities, including sports and other physical activities, which requires that gel electrolytes tolerant durable and repeated bending and twisting. Its exceptional stretchability and recoverability after stretching lead the ideal candidate for use in wearable devices that need to conform to the body and withstand repeated bending and twisting. Further research is needed to focus on the mechanical strength gel electrolytes. It is important to note that the synthesis process for ultra-stretchable gel electrolytes can be complex and typically requires careful control of the polymer synthesis, crosslinking, and electrolyte incorporation [4]. Additionally, optimization of the synthesis process is often necessary in order to achieve the balance between stretchability and conductivity (e.g. double-network) [5], as well as to ensure that the material is stable and does not degrade over time. The synthesis of ultra-stretchable gel electrolytes is an active area of research, and new synthesis methods and

materials are being developed to improve the properties and performance of these materials in flexible wearable devices.

**Biocompatible gel electrolytes**

Additionally, the biocompatibility is also should be concerned, which is an important factor for wearable devices that are worn for extended periods of time, as it reduces the risk of discomfort and skin irritation for users. In chapter 5, CMCs was introduced into double-network hydrogel electrolyte, however, the crosslinker (N,N'-Methylenebisacrylamide) is harmful in contact with skin, therefore, the biocompatible gel electrolyte is urgent to develop. Biocompatible gel electrolytes can be synthesized through several methods, including physical crosslinking (e.g. H-bonding [6]) and solvent evaporation [7,8]. Regardless of the method used, it is important to choose polymers (e.g. cellulose, starch, chitosan, gelatin [6] and dough [9]) and solvents (e.g. deep eutectic solvents [10]) that are biocompatible, meaning that they do not cause harm or damage to human bodies in which they will be used. In addition, the synthesis process should be controlled to ensure that the final electrolyte material has the desired properties, meantime, it may also be necessary to add other materials, such as salts or nanofillers, to enhance the electrochemical performance of the gel electrolyte.

**Freeze-tolerant gel electrolytes**

Freeze-tolerant gel electrolytes are designed to maintain their properties even after exposure to low temperatures, which makes them suitable for use in extreme environments where conventional gel electrolytes may freeze and lose their properties, such as in cold storage or during transportation in cold weather conditions. Freeze-

tolerant gel electrolytes are suitable for use in wearable and implantable devices, where low temperatures can affect the performance and safety of conventional gel electrolytes. For example, in the healthcare sector, freeze-tolerant gel electrolytes find applications in medical devices that require power sources, which require consistent monitoring of vital signs, such as body temperature, blood pressure, or glucose levels. Freeze-tolerant gel electrolytes can be incorporated in the sensors and battery packs of these devices, allowing patients in cold environments to receive accurate and reliable readings for effective healthcare management. Furthermore, wearable navigation devices, such as smart glasses or headsets, often rely on battery power for location tracking and displaying route information. By utilizing freeze-tolerant gel electrolytes, these devices can maintain their battery life and performance in extreme cold temperatures, ensuring continuous and accurate navigation guidance for users. By maintaining their properties even at low temperatures, freeze-tolerant gel electrolytes can help to improve the performance and reliability of these devices. Freeze-tolerant gel electrolytes can be synthesized by the addition of organic solvents soluble ions with high concentrations, which limits the crystallization of water and decrease in the freezing point of electrolytes [11]. Additionally, various additives, such as plasticizers and stabilizers (e.g. ionic liquids), can be added to improve the performance and stability of the gel electrolytes [12]. Overall, freeze-tolerant gel electrolytes have the potential to play an important role in a wide range of applications, from energy storage to wearable and implantable devices. Their continued development is likely to lead to new and exciting applications in the years to come.

**Self-healing gel electrolytes**

Self-healing gel electrolytes have emerged as a promising solution for enhancing the durability of wearable thermo-electrochemical cells. With the growing demand for portable and wearable electronic devices, there is a need for reliable and long-lasting power sources that can withstand the rigors of daily use. Traditional gel electrolytes used in thermo-electrochemical cells normally suffered from mechanical degradation, leading to reduced efficiency and shorter lifespan. However, self-healing gel electrolytes offer a groundbreaking solution to overcome these limitations. By incorporating self-healing properties into gel electrolytes, the overall performance and lifespan of wearable thermo-electrochemical cells can be significantly improved. The self-healing process helps to maintain the structural integrity of the gel electrolyte, preventing leakage and promoting efficient ion transport within the cell. Moreover, self-healing gel electrolytes can withstand mechanical stresses and strains associated with everyday use, such as bending, twisting, or stretching. This ensures the durability and reliability of thermo-electrochemical cells in wearable devices, even in challenging conditions. Self-healing gel electrolytes can be achieved by appropriate molecular design of the hydrogel network, such as chemically self-healing hydrogels (phenylboronic ester complexation, dynamic imine bond and disulfide bond) and physically self-healing hydrogels (hydrogen bond, hydrophobic interaction and host-guest Interaction) [13]. As research in this field progresses, self-healing gel electrolytes hold great potential to revolutionize the wearable technology industry by providing longer-lasting and more efficient power sources for various applications.

In summary, the porous structure and highly stretchable gel electrolytes that showed in this work pioneered the application of multifunctional hydrogels in the thermal-electrochemical cells field. However, the gel electrolytes still require further

improvements like ultra-stretchability, biocompatibility, freeze-tolerant and self-healing gel electrolytes areas. With the extraordinary and dedicated investigation of wearable technology and materials, versatile solid-state electrolytes for various wearable devices will be developed soon.

## 6.3 Reference


[1] J. Y. Sun, X. Zhao, W. R. K. Illeperuma, O. Chaudhuri, K. H. Oh, D. J. Mooney, J. J. Vlassak, Z. Suo, *Nature* **2012**, *489*, 133.

[2] K. Yao, J. Zhou, Q. Huang, M. Wu, C. K. Yiu, J. Li, X. Huang, D. Li, J. Su, S. Hou, Y. Liu, Y. Huang, Z. Tian, J. Li, H. Li, R. Shi, B. Zhang, J. Zhu, T. H. Wong, H. Jia, Z. Gao, Y. Gao, Y. Zhou, W. Park, E. Song, M. Han, H. Zhang, J. Yu, L. Wang, W. J. Li, X. Yu, *Nat. Mach. Intell.* **2022**, *4*, 893.

[3] W. Gao, Z. Lei, C. Zhang, X. Liu, Y. Chen, *Adv. Funct. Mater.* **2021**, *31*, 2104071.

[4] S. Liu, L. Li, *ACS Appl. Mater. Interfaces* **2017**, *9*, 26429.

[5] S. Bashir, M. Hina, J. Iqbal, A. H. Rajpar, M. A. Mujtaba, N. A. Alghamdi, S. Wageh, K. Ramesh, S. Ramesh, *Polymers (Basel).* **2020**, *12*, 2702.

[6] G. Li, K. Huang, J. Deng, M. Guo, M. Cai, Y. Zhang, C. F. Guo, *Adv. Mater.* **2022**, *34*, 1.

[7] H. Qin, R. E. Owyeung, S. R. Sonkusale, M. J. Panzer, *J. Mater. Chem. C* **2019**, *7*, 601.

[8] S. Y. Xiao, Y. Q. Yang, M. X. Li, F. X. Wang, Z. Chang, Y. P. Wu, X. Liu, *J. Power Sources* **2014**, *270*, 53.

[9] Y. J. Jo, H. Kim, J. Ok, Y. Shin, J. H. Shin, T. H. Kim, Y. Jung, T. Kim, *Adv. Funct. Mater.* **2020**, *30*, 1909707.

[10] R. Wang, M. Yao, S. Huang, J. Tian, Z. Niu, *Adv. Funct. Mater.* **2021**, *31*, 2009209.

[11] J. Lan, B. Zhou, C. Yin, L. Weng, W. Ni, L. Y. Shi, *Polymer (Guildf).* **2021**, *231*, 124111.

[12] R. Wang, M. Yao, S. Huang, J. Tian, Z. Niu, *Sci. China Mater.* **2022**, *65*, 2189.

[13] W. Ren, C. Ding, X. Fu, Y. Huang, *Energy Storage Mater.* **2021**, *34*, 515.

[14] W. Wang, R. Narain, H. Zeng, *Front. Chem.* **2018**, *6*, 1.